EFFECT OF WELDING PROCESSES ON THE WELD ATTRIBUTES OF 9Cr-1Mo STEEL WELD JOINTS

By

S.NAGARAJU

Enrollment Number: ENGG02201104042

Indira Gandhi Center for Atomic Research, Kalpakkam, India

A thesis submitted to the

Board of Studies in Engineering Sciences

In partial fulfillment of requirements for the Degree of

DOCTOR OF PHILOSOPHY

of

HOMI BHABHA NATIONAL INSTITUTE

January, 2018

Recommendations of the Viva Voce Board

As members of the Viva Voce Board, we certify that we have read the dissertation prepared by **S. Nagaraju** entitled "**Effect of Welding Processes on the Weld Attributes of 9cr-1mo Steel Weld Joints**" and recommend that it may be accepted as fulfilling the thesis requirement for the award of Degree of Doctor of Philosophy.

(G.SASIKALA, Dean-Academic)

Chairman	**Dr.M.Sai Baba** (Retired)	**Date:** 11/01/2018
Guide / Convener	**Dr. M.Vasudevan**	**Date:** 10/01/2018
Member	**Dr.Shaju K Albert**	**Date:** 10/01/2018
Member	**Dr. Saroja Saibaba**	**Date:** 10/01/2018
External Examiner	**Prof. S. Ganesh Sundara Raman** **IIT, Madras.**	**Date:** 10/01/2018

Final approval and acceptance of this thesis is contingent upon the candidate's submission of the final copies of the thesis to HBNI.

I hereby certify that I have read this dissertation prepared under my direction and recommend that it may be accepted as fulfilling the dissertation requirement.

Date: 11/01/2018
Place: Kalpakkam

(Dr. M.Vasudevan)
Guide

STATEMENT BY AUTHOR

This dissertation has been submitted in partial fulfillment of requirements for an advanced degree at Homi Bhabha National Institute (HBNI) and is deposited in the Library to be made available to borrowers under rules of the HBNI.

Brief quotations from this dissertation are allowable without special permission, provided that accurate acknowledgement of source is made. Requests for permission for extended quotation from or reproduction of this manuscript in whole or in part may be granted by the Competent Authority of HBNI when in his or her judgment the proposed use of the material is in the interests of scholarship. In all other instances, however, permission must be obtained from the author.

S.NAGARAJU

DECLARATION

I, S. NAGARAJU, hereby declare that the investigation presented in the thesis entitled "**Effect of Welding processes on the Weld Attributes of 9Cr-1Mo Steel Weld Joints**" submitted to **Homi Bhabha National Institute (HBNI)**, Mumbai, India, for the award of **Doctor of Philosophy** in **Engineering Sciences** is a record of work carried out by me under the guidance of **Dr. M.Vasudevan**, Head, Advanced Welding Processes &Modeling Section, Metallurgy and Materials Group, Indira Gandhi Centre for Atomic Research, Kalpakkam. The work is original and has not been submitted as a whole or in part for a degree/diploma at this or any other Institution/ University.

S.NAGARAJU

List of Publications Arising from the Thesis

Published

1. S.Nagaraju, P.Vasantharaja, N.Chandrasekhar, M.Vasudevan and T.Jayakumar, Optimisation of A-TIG Welding Process parameters for 9Cr-1Mo steel using Response surface methodology and Genetic Algorithm, 2016, **Materials and Manufacturing Processes**, 31:3, pp. 319-327.
2. S.Nagaraju, J.Ganeshkumar, P.Vasantharaja, M.Vasudevan and K.Laha, Evaluation of Strength Property Variations across 9Cr-1Mo Steel Weld Joints Using Automated Ball Indentation (ABI) Technique, 2017, **Materials Science and Engineering A**, 695, pp. 199-210.
3. S.Nagaraju, P.Vasantharaja, G.Brahadees, M.Vasudevan and Mahadevan, Effect of Welding Processes on the Microstructure, Mechanical Properties and Residual Stresses of 9Cr-1Mo Steel Weld Joints, 2017, **Journal of Materials Engineering and Performance**, 26, pp. 5938–5953.
4. Surya DeoYadav, P. Vasantharaja, Florian Riedlsperger, S. Nagaraju and M. Vasudevan, Zone wise investigation of creep behaviour in 9Cr-1Mo steel weld joints, **Materials Science and Technology**, 2019, Vol 35, No 2, pp. 155-172.

Conferences

5. S.Nagaraju, P.Vasantharaja, N.Chandrasekar, M. Vasudevan and T. Jayakumar, Optimization of A-TIG welding Process Parameters for 9Cr-1Mo Steel using Response Surface Methodology and Genetic Algorithm, April 2014, IIW IC-2014, New Delhi.
6. S. Nagaraju, J. Ganesh Kumar, P. Vasantharaja, M. Vasudevan and K. Laha, Evaluation of Mechanical Property across 9Cr-1MoSteel Weld Joints Using Automated Ball Indentation (ABI) Technique, October, 2016, IWS-2K16, Mumbai.
7. P. Vasantharaja, S. Nagaraj and M. Vasudevan, Zone wise Evaluation of Impression creep Behaviour of 9Cr-1Mo Steel Weld Joints, December 2017, IIW IC-2017, Chennai.

(S. Nagaraju)

Dedicated to my loving parents

Late Smt Vellammal S

&

Late Shri Srinivasan S

ACKNOWLEDGEMENTS

Many astonishing people have influenced my professional life, over the years. This acknowledgement is for all of them. I am sure; I won't be able to mention many of them even after next few paragraphs. My sincere thanks to all of them.

My deepest gratitude goes first and foremost to **Dr.M.Vasudevan**, my supervisor, for his constant encouragement, unstinted inspiration, keen interest, and invaluable guidance for academic research that has greatly affected my attitude towards the acquisition of knowledge. I am grateful to him for critically reviewing this thesis. His professional, systematic and down-to-earth approach to research, clarity of writing and presentation, are among the many things that I always proudly try to imitate. His giving of concern for my professional and personal development in these years is appreciated.

I thank **Dr. M. Sai Baba, Dr. Shaju K Albert** and **Dr.Saroja Saibaba** for being active members in my doctoral committee, and providing their inputs, encouragement and support during the regular committee meetings.

I am extremely thankful to **Dr. T. Jayakumar**, former Director, MMG, IGCAR and my guide for the initial period of my research work for his support and encouragement during my research work. My sincere thanks goes to him for providing excellent environment and giving a free hand to carry out my research work. It gives me immense pleasure to acknowledge to **Shri.P.Vasantharaja** who has supported my entire research work as colleague and co-author of all my publications. I am extremely grateful to **Shri. K.V.Ravi,** Chief executive, NRB for constant support, encouragement and counseling through the difficult times during this period.

I take this opportunity to specially thank all the co-authors, **Shri N.Chandrasekar, Shri J.Ganesh Kumar, Shri K.Laha, Dr. S. Mahadevan** and **Shri G.Brahadees** of technical papers originated out of this research work, for extending professional supervision and impetus throughout my research work. I would like to thank **Shri T.Sakthivel, Shri David Vijayanand, Shri V. Maduraimuthu, Dr B. Arivazhagan** and **Shri M.Ragavendran** for various useful discussions. I am highly obliged to **Dr. Amirthapandian** for his timely support and courtesies towards completion of my TEM work in time. I would also like to thank all the colleagues of **MTD, MMD,** and **NDED** for their help and support.

I am thankful to **Dr V Chandramouli, Shri S. Sriram, Dr R Sudha, Dr R Mythili, Dr. K.C.Ganesh** and **S.Arun Kumar** for many useful discussions and support during the course of thesis work.

I would like to extend my regards to **Shri R.Balakrishnan**, **Ms S. PaneerSelvi,** and **Ms N. Sreevidya,** for technical assistance extended by them. I express my special appreciation to **Shri D. Manokaran, Shri M. Munivel, Shri P. Babu** and **Mrs Gauri** for their dedication towards carrying out welding and metallography sample preparations. I extend special appreciation and regards to the work force of Central Workshop, Zonal Workshop, RCL and all other technical laboratories without whose contribution towards various test specimen preparation and conduct of experiments/ analysis, present research studies would not have been possible.

Above all, I owe it to the **Almighty** for granting me health, strength and wisdom to undertake this research work and enabling me to take it to successful completion.

CONTENTS

ABSTRACT

Key words: 9Cr-1Mo steel, Arc Welding, A-TIG Welding, Optimization, Response Surface methodology, Genetic algorithm, Microstructure, Mechanical properties, Residual Stresses, Automated Ball Indentation, Impression Creep.

9Cr-1Mo steel in the normalized and tempered condition is used for steam generator fabrication in the conventional and nuclear power plants. It is being considered as a candidate material for wrapper application for Fast Breeder Reactor fuel elements. This steel is popular because of its properties which include high temperature creep strength, adequate corrosion resistance and long-term microstructural stability etc. Shielded Metal Arc Welding (SMAW) and Tungsten Inert Gas (TIG) welding processes are the main welding process being employed for welding of 9Cr-1Mo steel. The limitation associated with TIG welding process is obtaining penetration beyond 3 - 4 mm in single pass welding. For welding plates thicker than 4 mm, welding consumables or filler wires are needed along with edge preparation. The above operations increase the fabrication time, cost of welding and enhance the possibility of defects. A Novel variant of TIG welding with activated flux called A-TIG welding process has been reported to overcome the above limitations. However, it is essential to set up the optimum process parameters for achieving the desired depth of penetration and Heat Affected Zone (HAZ) width in this steel during welding.

Design of Experiments (DOE) approach was employed using Response Surface Methodology (RSM) and Genetic Algorithm (GA) to optimize the welding parameters for achieving maximum Depth of Penetration (DOP) in A-TIG welding process. Design matrix was generated using DOE

techniques and bead on plate experiments were carried out to generate data regarding influence of welding process variables on DOP and HAZ width. The four input variables considered were current, torch speed, electrode tip angle and arc gap. The DOP and HAZ were considered as the response variables. The multiple regression equations correlating depth of penetration with the process parameters were developed for both the optimization techniques. The identified optimum process parameters were validated by carrying out bead on plate experiments. Using the generated data based on DOE, regression models correlating the process variables with the weld bead shape parameters were developed. The developed models were used for evaluating the objective function in GA. GA code was executed considering two different selection processes. Genetic Algorithm employing tournament selection technique was found to predict more accurate welding process parameters for achieving maximum DOP during A-TIG welding process.

Three 9Cr-1Mo steel weld joints were fabricated using shielded metal arc welding (SMAW), Tungsten Inert gas welding (TIG), and Activated Tungsten Inert gas welding (A-TIG) processes. A-TIG weld joint was fabricated using the optimized process parameters. All the three weld joints passed radiographic examination. X-Ray Diffraction (XRD) was used to experimentally measure the residual stress variations across the weld joints. In the SMA joint, the stresses were compressive at all measured locations on both sides of the weld centre. A peak compressive stress of 280 MPa was observed at 7 mm from the weld centre. The presence of compressive stresses may be attributed to dominance of phase transformation (martensite formation) induced stresses over that of the shrinkage stresses. In the TIG joint, tensile stress of 75 MPa was observed at the weld centre which dropped to ~ zero at 10 mm form the weld centre. A peak tensile stress of 300 MPa was observed at 15 mm from the weld centre on both sides. In the A-

TIG weld joint, the stresses were tensile up to 30 mm from the weld centre. A peak tensile stress of 520 MPa was observed at 10 mm from the weld centre. All the three weld joints showed typical ‘M’ shaped characteristic residual stress profile across the line of measurement with an elevation at the weld centre.

The microstructure study of the base 9Cr-1Mo steel and the three weld joints was undertaken using optical microscope, SEM and TEM. The microstructure of 9Cr-1Mo steel exhibited tempered martensitic microstructure with $M_{23}C_6$ precipitates in the weld metal and HAZ in all the three weld joints. The grain size of the TIG weld metal are relatively finer compared to that the other weld joints. TEM studies showed that after PWHT, lath structure is broken up and substructures had formed in the weld metal and HAZ for all the tree weld joints. $M_{23}C_6$ precipitates are seen in the prior austenite grain boundaries and sub grain boundaries.

The hardness values measured across the weld joints were found in Post Weld Heat Treated (PWHT) condition in the range of 220 to 260 VHN. The hardness of weld metal was observed to be higher than the base metal. The micro-hardness values gradually increase from base metal to HAZ and a minor decrease in the hardness value was observed near the fusion zone followed by higher hardness values in weld metal. Hardness variations correlate very well with the microstructural observations described earlier for all the three weld joints. Higher hardness observed in the weld metal of A-TIG weld joint is attributed to higher carbon dissolved in martensite.

The A-TIG welding process being unique for 9Cr-1Mosteel, 180° bend test was carried out for A-TIG joint. No cracks observed on application of dye penetration testing confirmed the integrity and adequate ductility. Standard procedures were followed for evaluating the mechanical properties of the weld joints. The tensile test and impact tests were performed on cross weld joint specimen. The yield strength, ultimate tensile strength and % of elongation are comparable for all the three joints. The tensile fracture of the cross weld specimen occurred in the base metal region away from weld metal implying that weld metal is stronger. The impact toughness values of base steel was 241 J at RT whereas SMA, TIG and ATIG welds exhibited 70, 241 and 112 J respectively. The toughness values at sub-zero temperature were 8, 16 and 7 J respectively compared to base steel of 18 J. However all three weld joints possess the minimum toughness required of 47 J as per the European specification EN1599:1997.

For the first time zone wise evaluation of strength properties across the SMAW, TIG and A-TIG weld joints in 9Cr-1Mo steel were carried out using automatic ball indentation (ABI) technique. The yield strength and tensile strength were observed to vary significantly across the 9Cr-1Mo steel weld joints. The YS and UTS decreased systematically from weld metal to base metal except at Inter Critical Heat Affected Zone (ICHAZ) which exhibited least strength values. The incomplete phase transformation during the weld thermal cycle caused the softening in the ICHAZ of the weld joints. The A-TIG weld metal exhibited higher strength values followed by TIG and SMA weld metals respectively. A-TIG weld joint exhibited higher strain hardening values while SMA weld joint exhibited the least strain hardening values. High carbon martensite in the weld metal and HAZ of the A-TIG weld joint caused the higher strength and strain hardening values compared to that of the other two weld joints in 9Cr-1Mo steel. Hence, among the three welding processes used for welding of 9Cr-1Mo steel, weld joint fabricated by A-TIG welding process exhibited the higher strength and strain hardening exponent values and similar ductility values compared to that of the weld joints fabricated by TIG and SMA welding processes. In terms of strength properties, A-TIG welding process is found to be a better for fabricating components made of 9Cr-1Mo steel.

Impression creep technique has been employed to characterize creep behavior of distinct microstructural regions such as the weld metal, the heat-affected zone and the base metal of 9Cr-1Mo steel weld joints fabricated by various welding processes at 848, 873 and 898 K under punching stress levels in the range of 100 to 300 MPa. Smaller prior austenitic grain size, lower density of precipitates and dislocations resulted in faster recovery and higher creep rate of HAZ in comparison to the weld and base metal. Compared to base metal, shielded metal arc weld (SMAW) and activated tungsten inert gas (A-TIG) weld of the P9 steel weld joints exhibited better resistance to creep and displayed higher activation energy due to their coarser prior austenite grain size. A-TIG HAZ exhibited superior creep properties compared to the SMAW and TIG HAZ due to the presence of higher number density of precipitates. Activation energy for creep was in range of 334-448 KJ/mol for various zones and dislocation creep is identified as the governing creep mechanism in the tested range and the creep deformation is controlled by climb and glide motion of dislocations. A-TIG welding process exhibited strongest HAZ in terms of creep deformation.

Effect of welding processes on the weld attributes of 9Cr-1Mo steel weld joints was successfully studied and it was found that A-TIG welding process exhibited many advantages over SMA and TIG welding processes for welding of 9Cr-1Mo steel. Hence A-TIG welding process is recommended for fabrication of 9Cr-1Mo steel components.

LIST OF FIGURES

LIST OF TABLES

ABBREVIATIONS

ABI	Automated Ball Indentation	M_s	Martensite Start Temperature
ANOVA	Analysis of Variance	NDT	Non Destructive Testing
A-TIG	Activated flux Tungsten Inert Gas	PWHT	Post Weld Heat Treatment
CCD	Central Composite Design	RSM	Response Surface Methodology
CCT	Continuous cooling transformation	SAD	Selected area diffraction
CGHAZ	Coarse-grained Heat Affected Zone	SEM	Scanning Electron Microscope
DBTT	Ductile Brittle Transition Temperature	SMAW	Shielded Metal Arc Welding
DOE	Design of Experiments	TCST	Thermal Co-efficient of Surface Tension
DOP	Depth of penetration	TEM	Transmission Electron Microscope
EDS	Energy Dispersive Spectroscopy	TF	Tempered Ferrite
GA	Genetic Algorithm	TIG	Tungsten Inert gas
HAZ	Heat Affected Zone	TTT	Time Temperature Transformation
HV	Vickers Hardness	UTS	Ultimate Tensile Strength
ICHAZ	Inter critical heat affected zone	XRD	X-ray Diffraction
LVDT	Linear Variable Differential Transformer	YS	Yield Strength

CHAPTER 1

INTRODUCTION

The need to reduce fuel costs as well as environmental pollution from fossil fuels by significantly decreasing carbon dioxide emissions from power-generating plants has led to efforts to increase the thermal efficiency of power plants [1]. Power plants, chemical, petro - chemical, fertiliser and nuclear industry widely use 9Cr-1Mo steel in the normalized and tempered condition for the steam generator and its structural components during high temperature applications [2-7]. The plain 9Cr-1Mo steel is suitable for applications in the temperature range 773-823 K. Ferritic-Martensitic (FM) steels are attractive candidate materials for core components of future Generation IV reactors as they exhibit excellent void swelling resistance, far superior to that of austenitic stainless steels and possibility to reach high fuel burn-ups. Fuel assemblies fabricated using commercial FM steels including EM 10 have been irradiated in fast reactors to high doses up to 155 dpa and have demonstrated high dimensional stability. 9Cr – 1Mo steel offers high resistance to void formation during ion, electron and neutron irradiations in the temperature range 673 – 898 K and their good high temperature properties has rendered them suitable for application as fuel element components, such as wrappers, and also in the steam circuitry in the sodium-cooled fast reactors [8-11]. 9Cr – 1Mo steels are being seriously considered for Fast Breeder Reactor (FBR) applications for the following reasons [12]: Acceptable mechanical properties at service temperature, achieved by the fine substructure generated during martensitic transformations; Easy control of microstructure and microstructural stability during long term service; Reduced tendency for temper embrittlement due to a lesser degree of segregation of impurity elements; Resistance to decarburization; Better corrosion resistance (stress corrosion cracking); Better oxidation resistance; Excellent resistance to thermal stresses. 9Cr-1Mo steels have been used for super heater components in steam generator circuits and as a wrapper material in the prototype fast reactor in the United Kingdom [12]. The envisaged applications of FM steels in Generation IV reactors is at present mainly restricted to wrapper as conventional 9-12 Cr FM steel grades used so far in fission reactors have maximum operating temperatures limited to 823 K. However, Plain 9Cr-1Mo steel is chosen as a candidate material for hexcan wrapper fuel subassembly components of fast breeder reactor to be loaded with metallic fuel in India.

Components made of 9Cr-1Mo steel are generally fabricated by the common arc welding processes such as shielded metal arc welding (SMAW) and Tungsten Inert Gas (TIG) welding processes. SMAW process is normally chosen due to its adaptability, simplicity of equipment and wide range of availability of electrodes. The quality of the weld joint depends on the expertise of the welder and hence welder must be qualified. TIG welding is one of the welding processes normally used for fabrication of 9Cr-1Mo steels. TIG welding is in general used in thin sections for single pass full penetration joints and also root pass of multi-pass welds for thicker sections. The advantages of TIG welding are good metallurgical and mechanical properties. The limitations include limited depth of penetration (DOP) achievable in single pass welding, slow welding speed, larger number of passes required for welding of thicker components. A variant of the TIG welding called as activated TIG welding process has been reported to overcome the above limitations [13-15]. In plain 9Cr-1Mo steel, Activated flux Tungsten inert Gas (A-TIG) welding has been reported to enhance the penetration by more than two times. The A-TIG process eliminates the requirement of edge preparation and has been reported to reduce the residual stresses in the weld joints significantly. In addition, there is very little degradation in the microstructure and mechanical properties of 9 Cr-1Mo steel weld joints produced by A-TIG welding process and it is negligible [16]. Improvement in creep-rupture behaviour has been reported for FM steels fabricated by A-TIG welding process [17]. Therefore, A-TIG welding process has been considered as one of the candidate processes for welding of 9Cr-1Mo steel hexcan with top head portion and bottom foot assemblies made of same steel during the fabrication of fuel subassembly components.

Depending on the welding process, residual stress distribution in the weld joint may differ due to variation to the extent of shrinkage, cooling rate and phase transformations. The residual stresses generated due to shrinkage in the weld metal are generally tensile in nature. Residual stresses generated due to phase transformation involving martensite are compressive in nature. Measurement of residual stresses is important to optimise the welding process conditions so that magnitude of residual stresses is reduced. X-ray diffraction is the common technique used for residual stress measurements in FM steels.

Structural materials used for high temperature service in nuclear power plants undergo changes in microstructure during service resulting in degradation in their mechanical properties. Small specimen testing methods which are non-destructive are required for directly evaluating the mechanical properties for the success of any materials ageing and life management program. Automated Ball Indentation (ABI) technique [18] has clearly demonstrated the feasibility of obtaining the true stress-true strain behaviour of several metals and alloys including ferritic steels and their weldments exhibiting microstructural variations in different regions. One of the advantages of ABI technique is that it is nearly non-destructive since no material is removed from the material surface. It is proposed to use ABI for evaluating the strength properties zone wise across the 9Cr-1Mo steel weld joints.

Impression creep testing [19] has gained attention of several researchers as an innovative tool to study the creep deformation behaviour of materials. It has several advantages over conventional creep tests which include (i) the test requires very small amount of material (ii) it is possible to evaluate the creep behaviour of narrow microstructural regions such as heat affected zones (HAZ) in ferritic steels (iii) As small spherical indentation is left in the sample, the testing in a sense is nearly non-destructive. It is proposed to use impression creep testing for zone wise evaluation of creep behaviour in 9Cr-1Mo steel weld joints.

1.1 Scope of Investigation

A-TIG welding process requires setting up of process parameters in order to achieve the desired DOP during autogenous welding. Hence, it is necessary for Optimization of A-TIG welding process parameters for 9Cr-1Mo steel. For optimization of the welding process parameters, response surface methodology (RSM) of design of experiment (DOE) approach and genetic algorithm (GA) have been reported to provide good solutions [20]. RSM is one of the suitable methods for the identification of the relevant parameters and their interactions especially when the relationships are very complex and highly non-linear. GA based methodology is another method for selection of optimum process parameters to achieve the target weld bead geometry in 9Cr-1Mo steel welds produced by A-TIG welding. The scope of this study includes optimisation of welding parameters for achieving maximum DOP during A-TIG welding. However, literature is very limited on the comparison of the performance of RSM and GA in welding process optimization. Comparison of the performance of the optimization techniques is also envisaged.

This study includes residual stress measurements, microstructure characterization and evaluation of mechanical properties of weld joints fabricated by SMAW, TIG and A-TIG welding processes. Residual stress measurements across the 9Cr-1Mo steel weld joints employing X-ray diffraction fabricated by various welding processes is envisaged. It is proposed to employ cross weld specimens for evaluating tensile and impact toughness properties of 9Cr-1Mo steel weld joints. It is proposed to characterize zone wise variation in microstructures employing optical microscopy (OM), scanning electron microscope (SEM) and transmission electron microscope (TEM) for 9Cr-1Mo steel weld joints fabricated by various welding processes. Evaluation of zone wise variation in strength properties using ABI and zone wise variation in creep behaviour using Impression creep testing technique is also envisaged for the 9Cr-1Mo steel weld joints fabricated by various welding processes.

1.2 Outline of Thesis

The thesis comprises of the following chapters:

1. Introduction
2. Literature Review
3. Objective and Scope
4. Experimental procedure
5. Results and Discussion
6. Conclusions
7. Future Directions
8. References

The highlights of each chapter are given below: -

Chapter 1 gives a brief introduction to 9Cr-1Mo steel and arc welding processes. Scope of investigations and organisationof the thesis is also included.

Chapter 2 provides a detailed literature survey on 9Cr-1Mo steel, applications of this steel, physical and welding metallurgy aspects, effects of post weld heat treatment(PWHT) on the microstructure and mechanical properties. The survey includes discussions about the welding processes such as SMAW, TIG and A-TIG welding. It also provides detailed survey on mechanism of penetration enhancement and factors affecting the DOP during A-TIG welding. Optimization techniques such as RSM & GA and its applications in welding process optimization are discussed. The literature review of studies carried out for understanding and measurement of residual stresses in weld joints, strength measurements using ABI and evaluation of creep behaviour using impression creep testing procedure is also included.

Chapter 3 provides the objectives and scope of this study.

Chapter 4 provides experimental details of design of experiments (DOE) carried out to optimise the weld process parameters for achieving desired DOP. The process parameters used for fabricating the weld joint by three different welding processes (SMAW, TIG, A-TIG) are given. Procedure for measuring residual stresses using X-ray Diffraction (XRD) technique is discussed. The specimen dimensions and the testing standards for tensile and impact testing on cross weld specimens are provided. Metallography sample preparation details are provided for Optical, SEM, and TEM studies. Details of small specimen testing using ABI and Impression creep testing machines are provided.

Chapter 5 presents the results and discussions of this study carried out.

5.1 Provides details of DOE carried out to optimise the weld process parameters for achieving desired DOP by RSM and GA methods and comparison of their performance. The square butt weld joints were fabricated with 10 mm thick plates employing A-TIG welding using the optimized process parameters.

5.2 Presents the results of hardness variation and residual stresses variation across the weld joints. Strength properties and impact toughness of the weld joints evaluated using the cross weld specimens is presented. The chapter also discussesin detail on the microstructure evolution zone wise in 9Cr-1Mo steel weld joints using optical microscopy, SEM and TEM studies.

5.3 Zone wise variation in strength properties in 9Cr-1Mo steel weld joints estimated using ABI technique is presented. It is found that ABI can be effectively used to determine the variation of mechanical properties across the weld jointquite rapidly and by using a small amount of test materials compared to that of conventional testing method.

5.4 Presents the zone wise variation in the impression creep behaviour of 9Cr-1Mo steel weld joints fabricated by SMA, TIG and A-TIG welding processes. Assessment of steady state creep rate and activation energy across the various zones of the weld joints is also presented.

Chapter 6 Presents the Conclusions on the research findings

Chapter 7 Gives the scope for future directions.

Chapter 8 Presents the list of references used for this study.

CHAPTER 2

LITERATURE SURVEY

2.1 Introduction to Cr-Mo Steels

Cr-Mo steels were developed mainly for applications in fossil power plants and petrochemical industry because of their superior oxidation and creep resistance [21,22]. Stainless steels are not preferred for the above applications because of their high cost, poor thermal conductivity and susceptibility to stress corrosion cracking. Cr-Mo steels also find application as steam generator materials in liquid metal cooled fast breeder reactors [23] and are candidate materials for reactor core applications [24]. Such a wide range of applications for this class of steels has resulted in their continued modification in the alloy composition and further developments.

The basic and classic CrMo steels are alloyed with 0.5%Mo – 1%Cr/0.5% Mo – 2.25%Cr/ 1%Mo – 5%Cr/ 1%Mo – 9%Cr/1%Mo and 12%Cr/1%Mo. From these steels further development has taken place by adding elements such as V, W, Ni, Ti, Nb, B and/or N to arrive at the new grades of steels which are used today such as T/P22V, T/P23, T/P24, T/ P91, T/P92 and VM 12-SHC. Many of these new grade steels have been applied successfully in industry but the development continues.

The development of 9–12% chromium steels (Fig.2.1) [25] is reported to have originated in 1912 with the manufacture of a 12% Cr:2–5% Mo steel for steam turbine blades by Krupp and Mannesmann in Germany [26,27]. However, in 1912–13 Brearley in the U.K., while attempting to develop high-temperature steels for gun barrels, accidentally discovered that martensitic steels containing 13% Cr and 0.2% C did not rust [28]; the stainless characteristics of high-chromium steels were also recognized by Haynes in the USA and by Strauss and Maurer in Germany at about the same time. The high-chromium, high-carbon martensitic steels were hard and had a sharp cutting edge and were subsequently developed commercially for applications such as cutlery knives and tableware in competition with austenitic stainless steels as well as for razors, scalpel blades, and heat-resisting tools and bearings [29]. The 9 and 12% Cr transformable steels with lower carbon (0.1% max) contents and additions of Mo, W, V, Nb, N and other elements, possessing higher creep-rupture strengths combined with good oxidation and corrosion resistance at elevated temperatures, have subsequently been developed. These steels have been used or considered for use in petrochemical and chemical plants, gas turbine engineering, aircraft and aerospace industries, electrical power plants, nuclear fission and fusion reactor components. The petrochemical and chemical processing industries utilize the steels in the form of thin tubular products in hydrogen desulfurization systems and in plants for the combustion of oil and the containment of various chemical products. The 9Cr-1Mo (T9) type of steel [30], possessing fairly moderate creep-rupture strength, was initially developed in the 1930s for such applications. However, the principal uses of the high-chromium martensitic steels are currently for components in gas turbines and in the boilers and turbines in steam power plants. The development and usage of the 9–12% Cr steels for these applications, as well as the 7–12% Cr steels for core components in fast breeder reactors and as potential first wall and breeder blanket structural materials in fusion reactor systems were reported.

Mo was added to C-Mn steels to improve its creep resistance, raising the temperature of application to around 450°C [31]. However, such steels had poor ductility and a tendency to graphitisation on prolonged service at high temperature, which were overcome with the addition of Cr up to 1 wt.%. It was also found that Mo could be increased to 1 wt. % to further improve the creep resistance without resulting in any form of embrittlement, if sufficient amount of Cr was present.

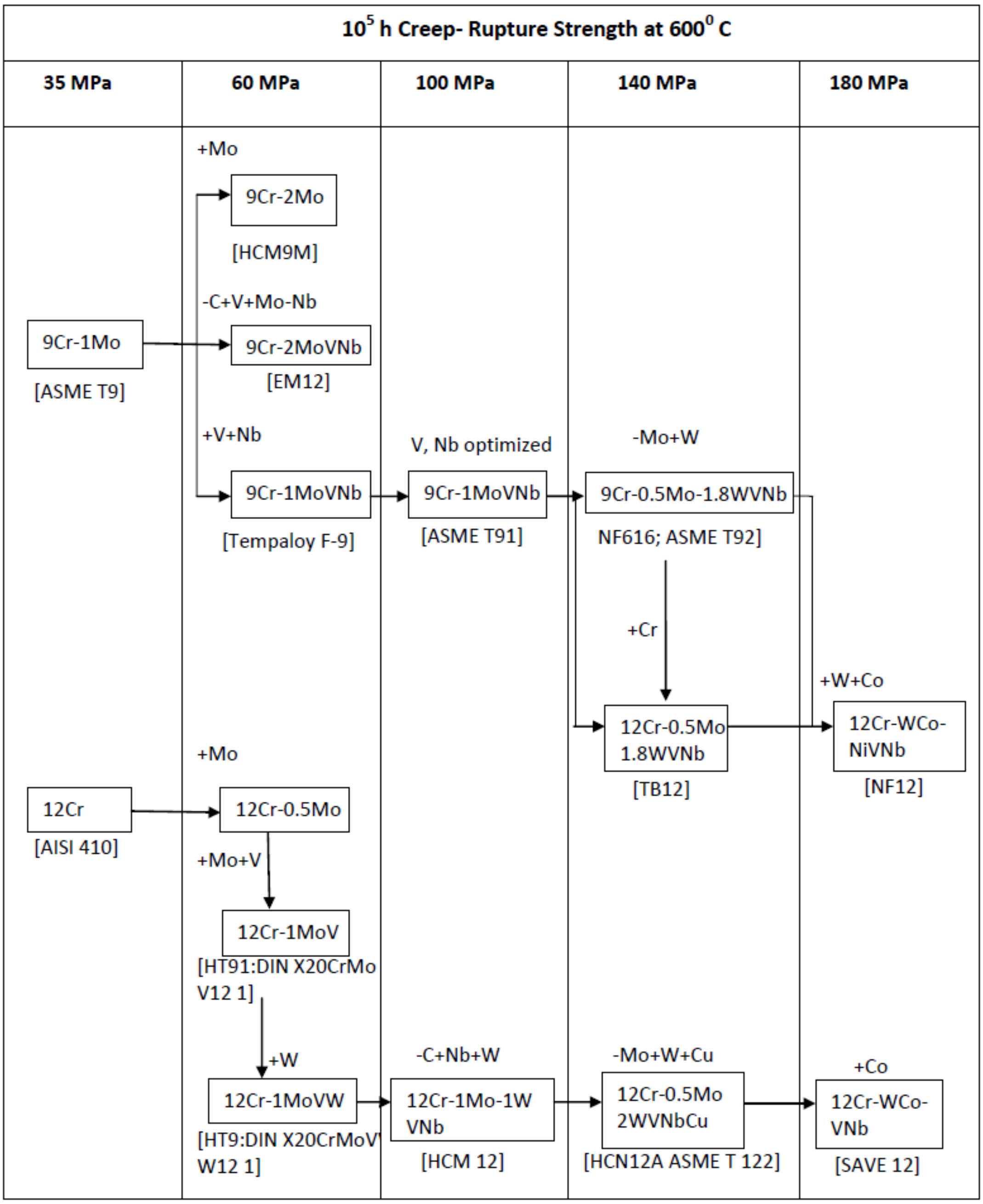

Fig.2.1 Development of 9-12% Chromium Ferritic/martensitic steels [30]

Hence the Cr-Mo steels contained Cr up to 1 wt. % and Mo up to 0.5 wt. %, with creep resistance better than that of C-Mn steels. However, there was no substantial improvement in their oxidation resistance over the C-Mn steels. The Cr content was further increased to improve oxidation resistance and this led to the development of 2.25Cr-1Mo steel, the most widely used alloy among this class of steels. A slightly modification of this alloy is the 3Cr-1 Mo steel in which Cr content was increased to provide resistance to hydrogen attack at high temperatures [32].

The need for steels with higher Cr content than 2.25 wt. %, because of the demands for materials to operate at temperatures higher than 550°C or in corrosive environments such as the oil processing industry, led to the development of 9Cr-1 Mo steels.

2.2 Applications of 9Cr-1Mo Steel

2.2.1 Petrochemical and Power Generation

Typical components of these industries are boilers, heaters, heat exchangers, reactors, and hydrocrackers, usually built as heavy wall pressure vessels. In a continuous strive for optimizing the economics in the various process installations in these industries, the service pressures and/or temperatures have increased. This implied that the respective base materials either had to be made available in heavier thicknesses or they had to be developed to meet higher strength and impact toughness requirements.

Improved mechanical properties will reduce or at least restrict the necessary wall thickness which generates an additional economical advantage in production, handling and installation of heavy process equipment. The petrochemical and chemical processing industries utilized the steels in the form of thin tubular products in hydrogen desulfurization systems and in plants for the combustion of oil and the containment of various chemical products [25].

2.2.2 Steam Power Plants

The majority of large fossil-fired power plants were operated at sub-critical steam conditions (pressures 22 MPa) prior to about 1990; the main steam temperature was standardized at 540°C worldwide, although 565°C was the standard for coal fired plants in Europe, particularly in the U.K., with the steam pressure being typically 18 MPa. However, the need to develop fossil-fired power plants with reduced generating costs and acid rain and greenhouse gas productions was widely recognized in the late 1970s and early 1980s and subsequently led to the design and construction of super-critical or ultra super-critical (USC) and combined cycle power plants with improved thermal efficiencies.

2.2.3 Nuclear Reactors

The 12Cr (AISI 403) and wrought 9Cr-1Mo steels have been used for the pressure tube end fittings in the Canadian CANDU reactors [33] and in the evaporators and parts of the super heaters in the UK Advanced Gas-Cooled Reactors (AGRs) [34], respectively. 9Cr-1Mo steel is now established as a structural material for steam generator units by the UK nuclear industry following its successful service in the evaporators and parts of the super heaters of the Advanced Gas Cooled Reactor. Furthermore, the steel is also being used for the replacement super heater and re heater tube bundles for the UK Prototype Fast Reactor. The high-chromium martensitic steels have found few other applications in thermal reactors, their main development having been directed towards fast breeder reactor usage.

The 9Cr-1Mo steel has been utilized as internal sleeves for the repair of leaks in the welds between the 2.25Cr-1MoNb steel steam tubes and 2.25Cr-1Mo steel tube plates in the evaporator units and also for the replacement super heater and re heater tube bundles in PFR [34,35]. However, the successful operation of fast reactors is also dependent on the performance of the materials used in the construction of the fuel and breeding blanket assemblies. Thus, the subassembly fuel pin cladding and wrappers (or ducts) in a commercial fast reactor have to endure prolonged service at elevated temperatures and a maximum displacement per atom (dpa) dose of 150 to 200 dpa, if the fuel is to achieve an economic target burn-up of 15 to 20% of the heavy atoms.

The prototype fast breeder reactors usually commenced operation with conventional austenitic steels as the core component structural materials. However, these steels exhibited significant irradiation-induced void swelling and irradiation creep that could lead to dimensional instability and core distortion [36]. These problems may be exemplified by reference to the PFR [600 MW(th), 250 MW(e)] fuel element subassembly shown in Fig. 2.2 [37]. PFR employed a nominally free-standing core design in which 78 subassemblies were cantilevered from the bottom core support structure. Each subassembly consisted of 325 or 265 fuel pins with outside diameters of 5.84 and 6.60 mm, respectively, containing a stack of mixed-oxide (UO_2:PuO_2) annular pellets; the pins were held in grids spaced at intervals along their length and enclosed within a hexagonal wrapper approximately 2.75 m long, 142 mm across the flats, and 3 mm wall thickness. The wrapper served to channel the sodium coolant flow (inlet and outlet temperatures of 400 and 560°C, respectively) over the fuel pin bundles and provided the structural strength and stiffness of the assemblies. The design temperature ranges for the wrapper and cladding (mid-wall) for the fuel element subassemblies in PFR (Row 1) were 420 to 550°C and 430 to 700°C, respectively.

The void swelling produced both axial and radial expansion of the cladding and wrapper so that, in the extreme, the coolant flow between the pins would be reduced, resulting in increases in temperature and possible failure, together with difficulties in removal or insertion during refueling unless sufficient clearance was allowed. In addition, differential void swelling due to gradients in neutron flux and temperature across a subassembly caused wrapper bowing, while the wrapper faces dilated (or bulged) due to irradiation creep under the influence of the internal coolant pressure. The subassembly bowing, dilatation and length, illustrated (Fig. 2.3) were important in determining the design, operation, and burn-up limits for the fuel elements. However, irradiation creep could be beneficial in certain circumstances by reducing interaction loads between neighboring subassemblies in the free-standing PFR core design or between the subassemblies and the core restraint structure in constrained core designs, such as those adopted for FFTF, PHÉNIX, and BN-350.

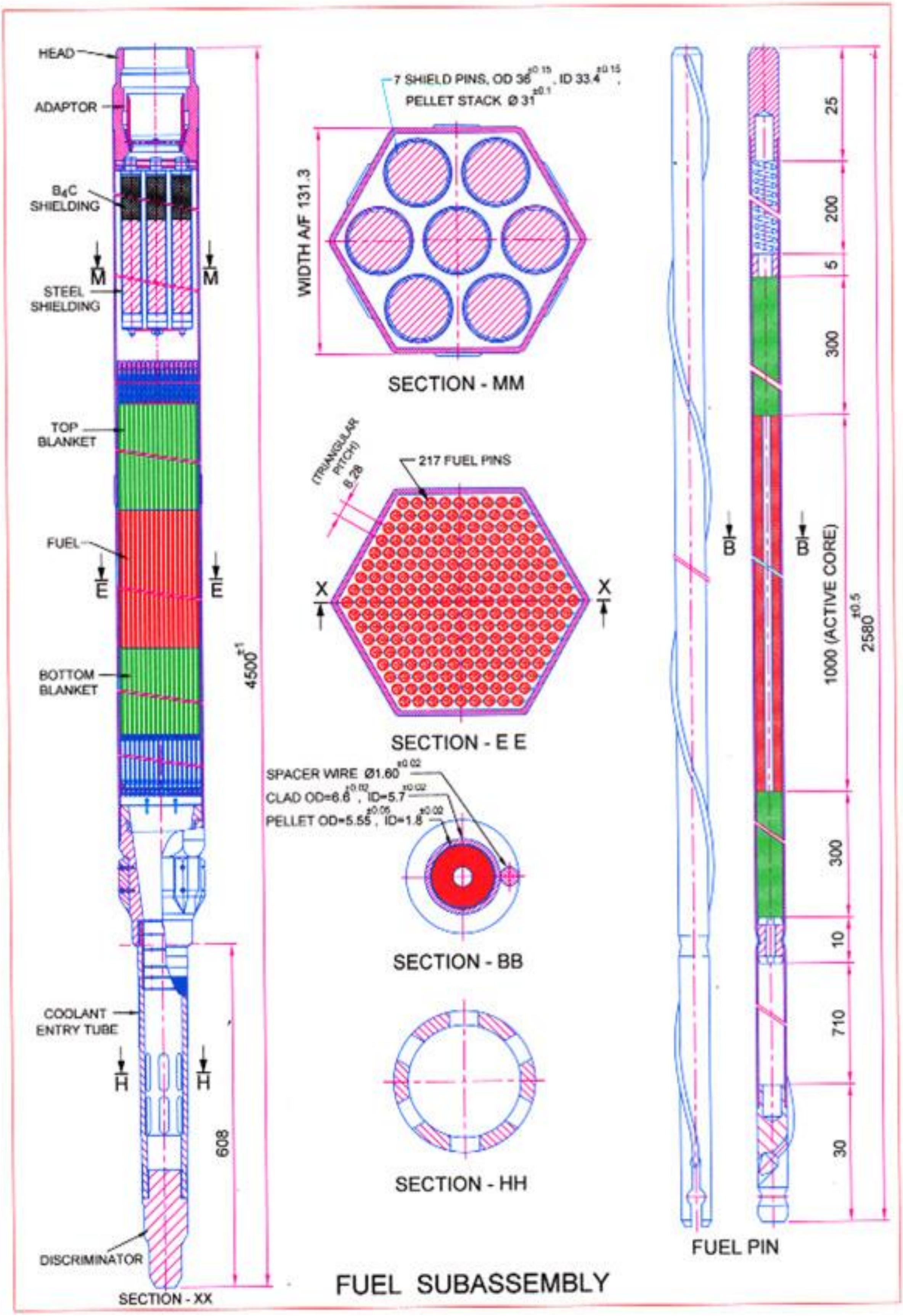

Fig 2.2 PFBR Standard Core Sub-assembly [37]

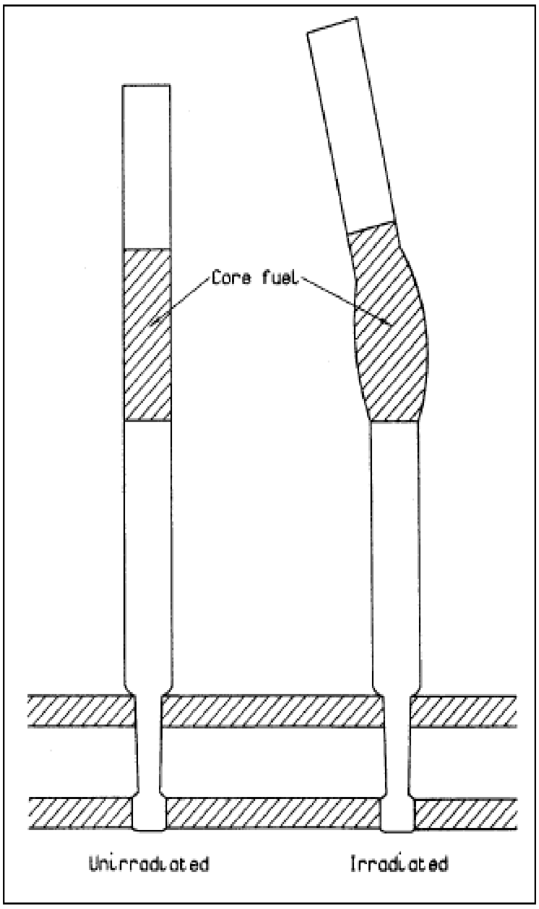

Fig 2.3 Unirradiated and Irradiated
Fast Reactor Fuel Sub-assembly

It became essential, therefore, to select or develop wrapper materials exhibiting consistently low void swelling and irradiation creep rates that were not excessively high if the burn up targets in the fuel were to be achieved [36]. Furthermore, the fuel pin cladding had to retain sufficient “in-reactor” creep strength and ductility to avoid premature failure under the stresses imposed by fission product gas release and fuel clad mechanical interaction.

These requirements led to extensive post-irradiation examination and test programs on the subassembly components, as well as on specimens irradiated in rigs in experimental fast reactors, such as DFR, RAPSODIE, EBR II, FFTF, BR-10, BOR-60, and JOYO, and in the prototypes being undertaken in Europe [38–42], the USA [43,44], Russia [45,46], and Japan

[46]. The data obtained in these studies enabled component material design rules to be formulated and materials with progressively increased resistance to void swelling, such as cold-worked un stabilized (based on Type 316: 0.08% C max.; 16.0–18.0% Cr; 10.0–14.0% Ni; 2.0–3.0% Mo) and Ti- or Nb-stabilized austenitic steels, precipitation-hardened intermediate nickel-base alloys and the high-chromium ferritic/martensitic steels, to be identified.

Many wrought ferritic/martensitic steels have been employed or considered for application as wrappers (ducts) and, to a lesser extent, cladding in the core fuel element subassemblies in sodium-cooled fast reactors in Europe, the USA, Russia, and Japan [39–50]. They include: plain 12Cr (FI) in the U.K. and a fully ferritic, non transformable 17Cr (F17) in France, 9Cr-1Mo (EM10) and duplex 9Cr-2Mo (EM12) in France, 12Cr-1MoV (FV607 and CRM12) in the U.K., 1.4923 in Germany and EP450 in Russia), 9Cr-1MoVNb [modified 9Cr-1Mo (T91) in the USA and France], 12Cr-MoVNb (FV448 in the U.K. and 1.4914 in Germany), 12Cr-1MoVW (HT9) in the USA, and 12Cr-MoVNbW (PNC-FMS) in Japan.

Due to their limitations in terms of high temperature thermal creep strength as compared for instance to austenitic steels, the main applications of 9Cr-1Mo steels was for wrappers or ducts whose maximum operating temperature in sodium cooled fast reactors does not exceed about 550° C. Based on their excellent resistance to void swelling and on operating experience gained from past reactors, 9Cr-1Mo steel has been selected as wrapper material for several future reactors currently under development.

The heat treatments specified for the 9–12% Cr ferritic-martensitic steels for non-nuclear conventional engineering applications are aimed at maximizing the tensile proof and creep-rupture strengths. However, high thermal creep strength has not been a primary requirement for the wrappers, as the operating temperatures are below or at the lower end of the creep range for these materials and the components are not highly stressed during normal operation. Reduced creep strength was therefore acceptable, provided that increased fracture toughness and good high-temperature ductility, coupled with adequate formability and weldability, could be achieved. Consequently, extensive studies, involving modifications of the compositions and initial heat treatments, were carried out to develop the optimum combination of properties for some of the steels intended for use as wrappers [41, 49, 50].

The high-chromium ferritic/martensitic steels have shown excellent dimensional stability (void swelling-0.5%) at high displacement doses 132 dpa for an FV448 steel wrapper in PFR and 142 and 115 dpa for EM10 and 1.4914 steel wrappers, respectively, in PHÉNIX based on length and across flats measurements on irradiated wrappers and density determinations on specimens machined from irradiated wrappers or exposed in irradiation rigs [42]. In addition, 20 subassemblies consisting of STA Nimonic PE16 clad pins in FV448 steel wrappers loaded. A major limitation of the high-chromium ferritic/martensitic steels, in common with other body-centered-cubic (bcc) steels, is that they exhibit a ductile-brittle transition temperature (DBTT) in which the energy of fracture increases with increasing temperature on passing through the transition, followed by an upper-shelf region of relatively constant or slightly decreasing high fracture energies. The steels also suffer radiation embrittlement in that the DBTT increases and the upper-shelf energy is reduced by neutron irradiation; these changes correspond to a reduction in fracture toughness in fracture mechanics terminology, with decreased resistance to crack initiation in the transition region and ductile crack growth from preexisting flaws in the upper-shelf region. However, it has been established that the DBTT of the irradiated high-chromium steels are not markedly dependent on the steel type and displacement dose (10 to 100 dpa) in the wrapper operating temperature range of 400 to 560°C, the irradiation- induced shifts being relatively small [42].

2.3 Physical Metallurgy of Cr-Mo Steels

The presence of alloying elements like Cr and Mo in significant quantities makes the hardenability of these steels fairly high. They are mostly used in the normalised and tempered condition. In the normalised condition, the structure varies from a mixture of bainite and ferrite in the low alloy steels to fully martensitic in the high alloy steels [24]. For 1Cr-0.5Mo steel, the structure is typically a mixture of bainite and ferrite, for 2.25Cr-1Mo steel it is predominantly bainite and for 9Cr-1Mo steel it is fully martensitic. The martensite start (Ms) temperatures are in the range of 400-500°C and decrease with alloy content. The Ms temperature for2.25Cr-1Mo steel determined from continuous cooling transformation (CCT) data is close to 500°C [51, 52] while for 3Cr-1Mo steels it is around 450°C. For 9Cr-1Mo steel, Ms temperature was estimated to be close to 400°C from time temperature transformation (TTT) diagrams by Pickering and Vassiliou [53].

It can be seen that depending on the temperature, an alloy with 9 wt.% Cr can exist in different sub-liquidus phase fields like, γ+ δ-ferrite, γ, γ + α.-ferrite + carbides and α.-ferrite + carbides. The presence of other alloying elements modifies the phase fields shown in the Fig. 2.4. Hence, the extent of the phase fields crossed by a particular alloy while cooling from high temperature is dependent on the alloy composition which has been represented in terms of net Cr equivalent (equation 2.1) as suggested by Patriarcaet. al. [54]:

$$Cr_{eq} = Cr + 6Si + 4Mo + 1.5W + 11V + 5Nb + 12Al + 8Ti - 40C - 2Mn - 4Ni - 2Co - 30N - Cu \quad (2.1)$$

(All elements in wt. %)

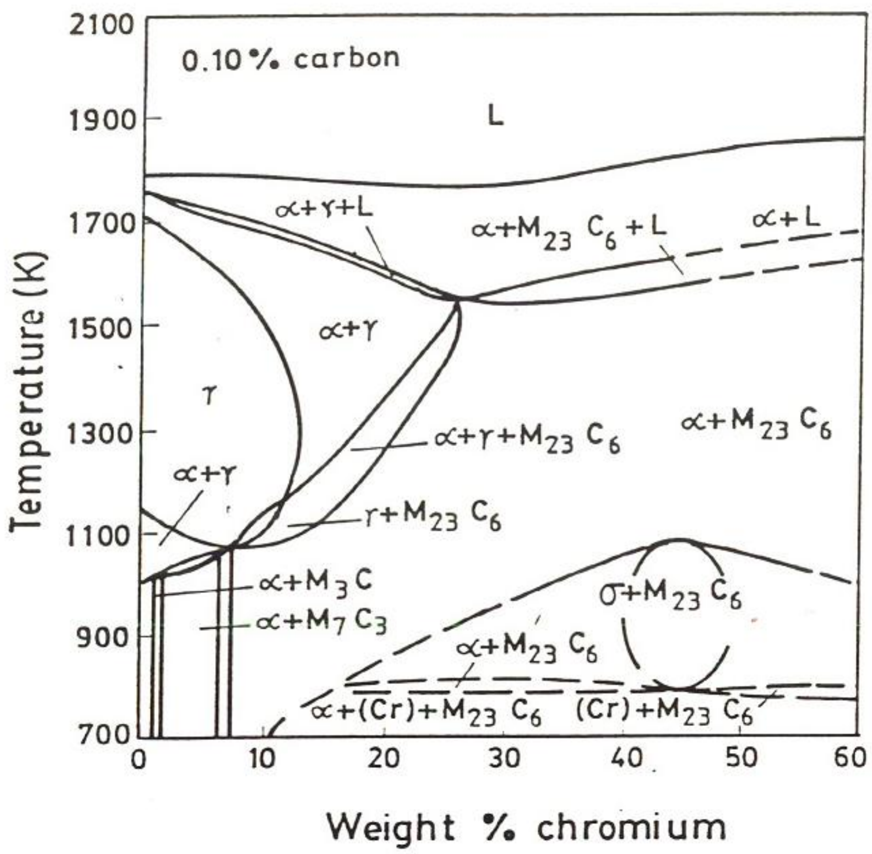

Fig. 2.4. Pseudo Binary Fe-Cr phase Diagram with 0.1 wt.%. Carbon [55]

The above equation has been developed specifically for 9Cr-1Mo (P9) and Modified 9Cr-1Mo (P91) steels and it reveals the potent effect of Si, Mo and C in fixing the phase fields for 9Cr-1Mo steels. This equation was developed to predict the delta ferrite formation tendency in high chromium ferritic steels. In the standard P9 steel the elements such as Al, Ti and N are not present in significant amount. The effects of these elements were considered insignificant in P9 steel and hence not discussed. However, Al and Ti have a dual role in the weld pool. Al is ferrite stabilizer and de-oxidizer and Ti is ferrite stabilizer and carbide former. Nitrogen is always kept low in this type of steel to avoid retained austenite in the weld metal.

2.3.1. Tempering Behaviour

Tempering treatment for normalised steels is chosen in order to obtain a microstructure that would provide the best creep and oxidation resistance under the service conditions. In the case of normalized 9Cr- 1Mo steels, the microstructure is martensitic and harder, hence tempering is required. This steel cannot be used in the as-welded condition. For these steels, creep strength is provided by the presence of finely dispersed carbide particles. Precipitates formed in 9Cr-1Mo steel are $M_{23}C_6$ type carbides and Cr_2X type precipitates during the initial stages of tempering [56]. These particles not only hinder the movement of dislocations but also retard the recovery of structure, thus retaining the creep resistance. The optimum microstructural conditions occur when the carbides are fine and numerous and have just lost the coherency with the matrix [57]. The conditions for producing such fine and numerous carbides usually occur when the steels are heat treated or subjected to service at 0.4-0.5 Tm (where Tm is the temperature of melting in K) and have a carbon content of 0.1-0.2 wt. %. In the case of many low alloy steels, these conditions are met during tempering in the range of 650-750°C and during subsequent service at 450-600 °C. The creep resistance of these steels is attributed to the strengthening effect of these carbides.

The sequence of reactions taking place during normalising and tempering in 9Cr-1 Mo steels can be represented as follows

$$\text{Martensite} \longrightarrow \alpha + M_2X + M_{23}C_6 \longrightarrow \alpha + M_{23}C_6$$

Depending on the alloy level and the heat treatment(s), specific types of precipitations will be formed in a specific amount. The governing parameters for the heat-treatment are temperature and time. The variety of precipitations that can be expected and that are mainly used in the design of classic and modern creep resistant CrMo steels are listed in Table 2.1.

Table 2.1 Precipitations that can be found in CrMo Steels

Precipitations and possible phases in CrMo steels		
Graphite		
Epsilon	= $Fe_{2.4}C$	
Cementite	= Fe_3C	
Chi	= Fe_2C	
M_2X	M_6C	$M_{23}C_6$
M_7C_3	Laves	
M_5C_2	Z-phase	
Mo_2C	Cr_3C	
NbC	NbN	VN

2.3.2 Post Weld Heat Treatment

The heat treatments for the base materials are reasonably complex but are required to obtain the optimal mechanical properties. Depending on the alloy content a Normalising, Tempering and Annealing treatment at various temperatures for several hours with a controlled cooling rate have to be executed according strict procedures. The same is valid for the weld metal, with increasing alloy content the PWHT for welded joints gets more complicated.

As both the weld metal and the HAZ of Cr-Mo steel weldments are harder than that of the base metal which is in the normalised and tempered condition, it is required to subject the weld to proper PWHT to temper the microstructure and thus improve its toughness. In addition to tempering of the HAZ and the weld metal microstructures, it also reduces the residual stresses that are present in the welds. The recommended temperature range of PWHT for different Cr-Mo steels is in the range of 650- 760^{0}C. The time of treatment is determined by the combined thickness of the joint; usually it is 1h per 25.4 mm (1") of thickness [58].

The hardness of the weld metal of Cr-Mo steels decreases substantially during PWHT due to tempering of martensite or bainite. The PWHT is similar to tempering treatment given to the normalised steel.

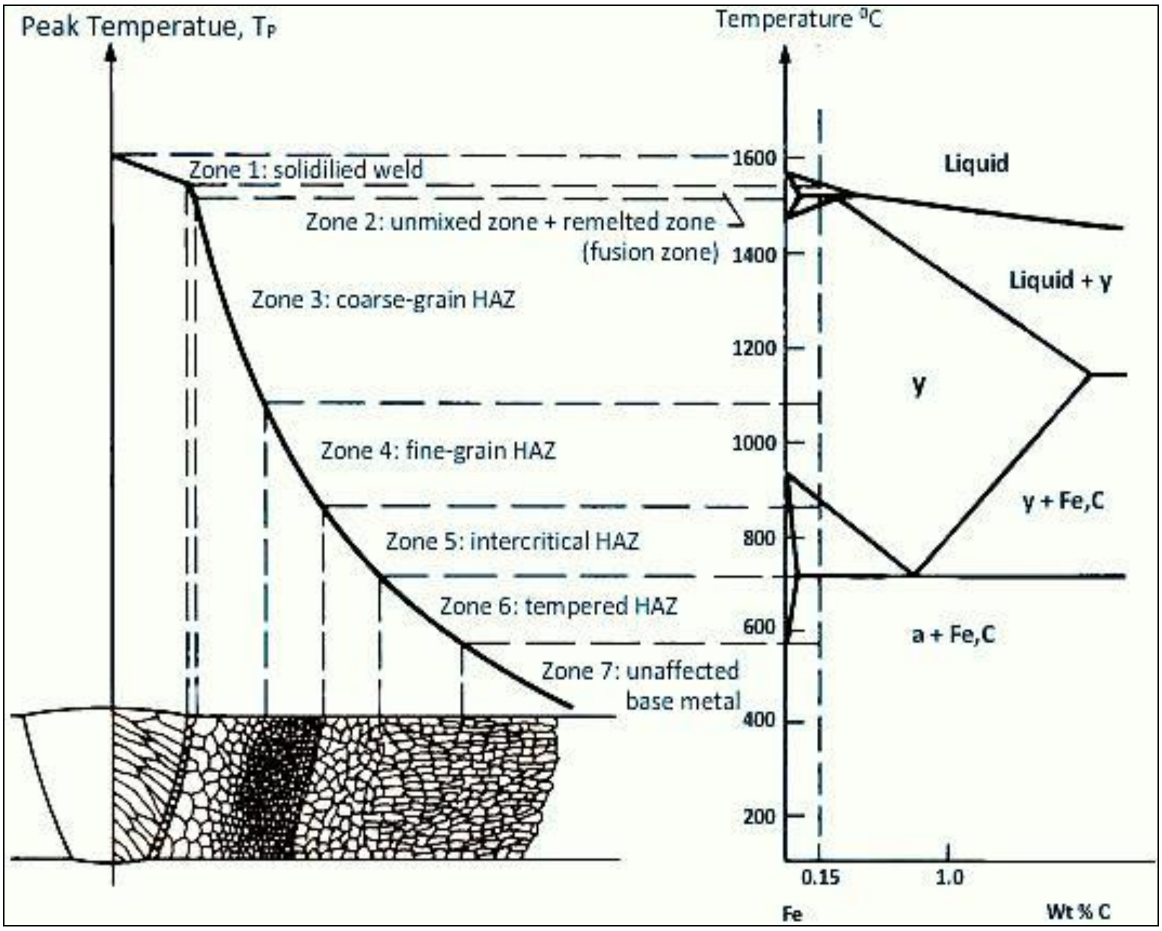

Fig. 2.5 Schematic Representation of Different Regions of HAZ Microstructure [58]

2.4 Welding Metallurgy of Cr-Mo Steels

Welding is a process of joining two similar or dissimilar materials such that a metallurgical bond is established between them. Fusion welding is the most widely used technique applied for joining metallic materials and in this process the faces to be joined are fused and joined with or without the help of molten filler metal. Hence, in this welding process weld metal exhibits a cast microstructure which is vastly different from the wrought microstructure of the base metals that are joined. The base metal adjacent to the weld metal also undergoes microstructural changes due to the rapid heating and cooling cycle experienced by this region during welding. The part of the base metal which undergoes substantial microstructural changes during the weld thermal cycle is called the HAZ. The microstructural changes in the HAZ are more pronounced in steels which undergo transformations during heating and cooling.

Depending on the peak temperature experienced and the amount of grain growth, the HAZ of steels can be broadly divided into three different regions [58]. The region close to the fusion line which experiences temperatures around and above 1200°C where extensive growth of the austenite grains takes place during the heating part of the thermal cycle is called the coarse-grained heat affected zone (CGHAZ). The grain coarsening temperature strongly depends upon the alloy type and its composition. The region of the HAZ which is heated to temperatures high enough for transformation of ferrite to austenite but not sufficient for the growth of the austenite grains is called the fine grained heat affected zone (FGHAZ). Similarly, the region of the base metal which is heated to a temperature range in which both austenite and ferrite are stable (between the two critical temperatures A 1 and A3) is called the inter-critical heat affected zone (ICHAZ). A schematic representation of the different regions of the HAZ is shown in Fig. 2.5. In addition to these three distinct regions in HAZ, a fourth region called subcritical HAZ is also defined. This region experiences temperatures below the critical temperature, A_1, and hence no matrix transformation takes place. However, heating results in tempering of this zone which may result in a slight softening.

While the peak temperature experienced determines the grain size of the different regions of the HAZ, it is the cooling part of the weld thermal cycle along with the chemical composition that determines the final microstructure of both the weld metal and the HAZ. Austenite formed in the HAZ during heating and that produced in the weld metal during weld solidification transforms into ferrite, martensite, bainite or a mixture of these depending on the cooling rate and alloy composition. In order to predict the transformations taking place during the cooling part of the weld thermal cycle, cooling rate is represented as $T_{8/5}$(time required by the weld to cool from 800 to 500°C) while alloy composition is represented as carbon equivalent (CE) which normalises the effect of various elements into a single parameter [59]. In general, the higher the cooling rate and higher the alloy content, higher is the probability that HAZ or weld metal would transform into a martensitic or bainitic microstructure. CrMo steels exhibit significant variations in microstructure across the weld joint. It is essential to understand zone wise variations in microstructure.

The plain 9Cr-1Mo steel being the candidate material for FBR wrapper and steam circuit components and the main fabrication method to be employed is welding, literature review of welding processes used for fabrication the above steel was carried out.

2.5 Welding Processes

The components made of plain 9Cr-1Mo steel are generally fabricated by the most common arc welding processes such as SMAW and TIG welding. SMAW process is normally chosen due to its adaptability, simplicity of equipment and wide range of availability of electrodes. The above requirements are vital for field welding applications. SMAW is a manual welding process. The quality of the weld joint depends on the expertise of the welder and hence welder must be qualified. TIG welding is one of the welding processes normally used for fabrication of 9Cr-1Mo steels. TIG welding is in general used in thin sections for single pass full penetration joints and also root pass of multi-pass welds for thicker sections. The advantages of TIG welding are good metallurgical and mechanical properties. However, there are number of limitations associated with TIG welding. The limitations include limited DOP achievable in single pass welding, slow welding speed, larger number of passes required for welding of thicker components. A-TIG welding process said to conquer the above limitations [13-15]. In plain 9Cr-1Mo steel, A-TIG welding has been reported to enhance the penetration by more than two times. The A-TIG process eliminates the requirement of edge preparation and has been reported to reduce the residual stresses in the weld joints significantly.

2.5.1 Shielded Metal Arc Welding

It is also known as manual metal arc welding (MMA or MMAW), flux shielded arc welding or informally as stick welding, is a manual arc welding process that uses a consumable electrode covered with a flux to lay the weld.

An electric current, in the form of either alternating current or direct current from a welding power supply, is used to form an electric arc between the electrode and the metals to be joined. The work piece and the electrode melt forming the weld pool that cools to form a joint. The electrode consists of a solid metal core covered by a mixture of mineral and metallic compounds. The composition of the coating depends on the type of electrode and welding polarity. As the weld is laid, the flux coating of the electrode disintegrates, giving off vapours that serve as a shielding gas and providing a layer of slag, both of which protect the weld area from atmospheric contamination and remove impurities from the weld deposit and providing the desired weld mechanical properties by controlling the weld deposit chemistry. SMAW can be performed in areas of limited access and in all positions. It is a viable process for joining most metals and alloys, and the equipment needed is both portable and low in cost. The schematic welding set up of SMAW welding process is shown in Fig. 2.6.

Because of the versatility of the process and the simplicity of its equipment and operation, SMAW is one of the world’s first and most popular welding processes. It dominates other welding processes in the maintenance and repair industry.

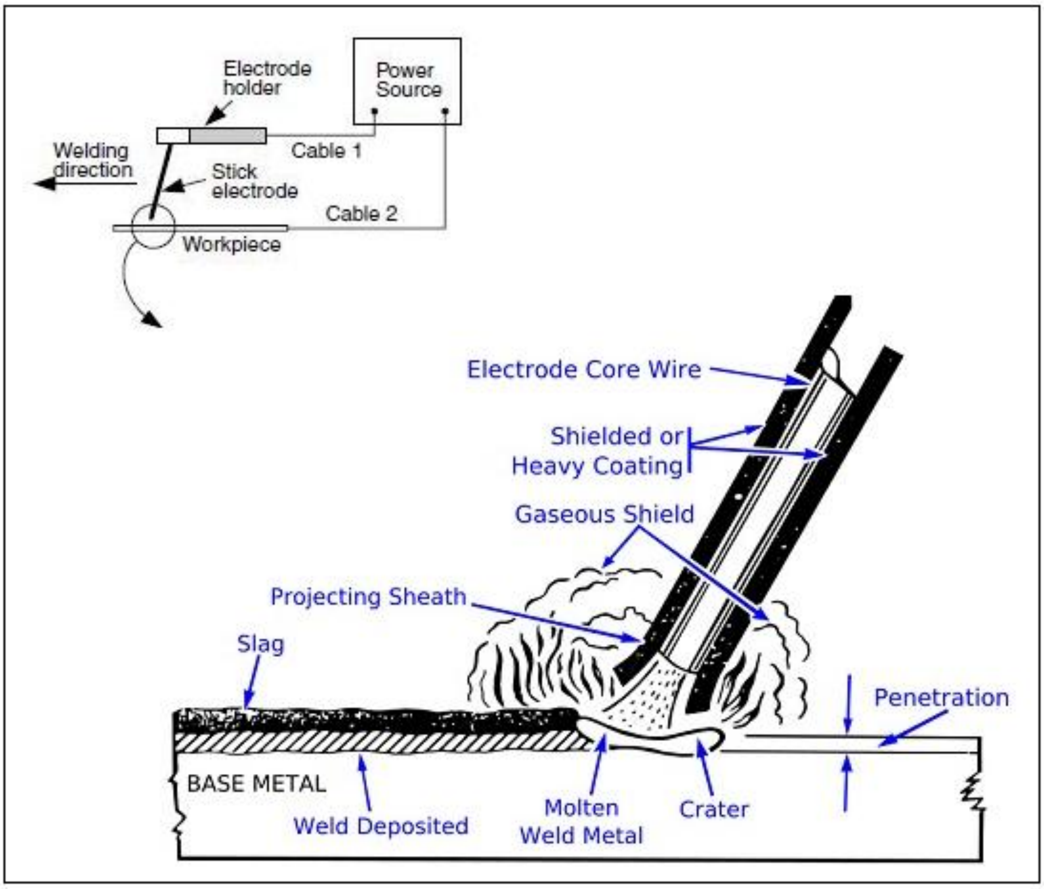

Fig. 2.6 Schematic SMAW Welding Setup [60]

The most common quality problems associated with SMAW include weld spatter, porosity, poor fusion, shallow penetration, and cracking.

Weld spatter, while not affecting the integrity of the weld, damages its appearance and increases cleaning costs. It can be caused by excessively high current, a long arc, or arc blow, a condition associated with direct current characterized by the electric arc being deflected away from the weld pool by magnetic forces. Arc blow can also cause porosity in the weld, as can joint contamination, high welding speed, and a long welding arc, especially when low-hydrogen electrodes are used.

Porosity, often not visible without the use of advanced non destructive testing (NDT) methods, is a serious concern because it can potentially weaken the weld. Another defect affecting the strength of the weld is poor fusion, though it is often easily visible. It is caused by low current, contaminated joint surfaces, or the use of an improper electrode.

The preferred polarity of the SMAW system depends primarily upon the electrode being used and the desired properties of the weld. Direct current with a negatively charged electrode (DCEN) causes heat to build up on the electrode, increasing the electrode melting rate and decreasing the depth of the weld. Reversing the polarity so that the electrode is positively charged (DCEP) and the work piece is negatively charged increases the weld penetration. With alternating current, the polarity changes over 100 times per second, creating an even heat distribution and providing a balance between electrode melting rate and penetration.

The choice of electrode for SMAW depends on a number of factors, including the weld material, welding position and the desired weld properties. The electrode is coated in a metal mixture called flux, which gives off gases as it decomposes to prevent weld contamination, introduces deoxidizers to purify the weld, causes weld-protecting slag to form, improves the arc stability, and provides alloying elements to improve the weld quality. The composition of the electrode core is generally similar and sometimes identical to that of the base material. But even though a number of feasible options exist, a slight difference in alloy composition can strongly impact the properties of the resulting weld.

2.5.2 TIG Welding Processes

TIG welding developed in 1938 is one of the most currently used techniques in applications for aerospace, nuclear, petroleum & chemical industries. Besides being very simple and requiring low investment, the excellent end results regarding the weld quality with TIG processing have all contributed to its success in manual & automatic welding.

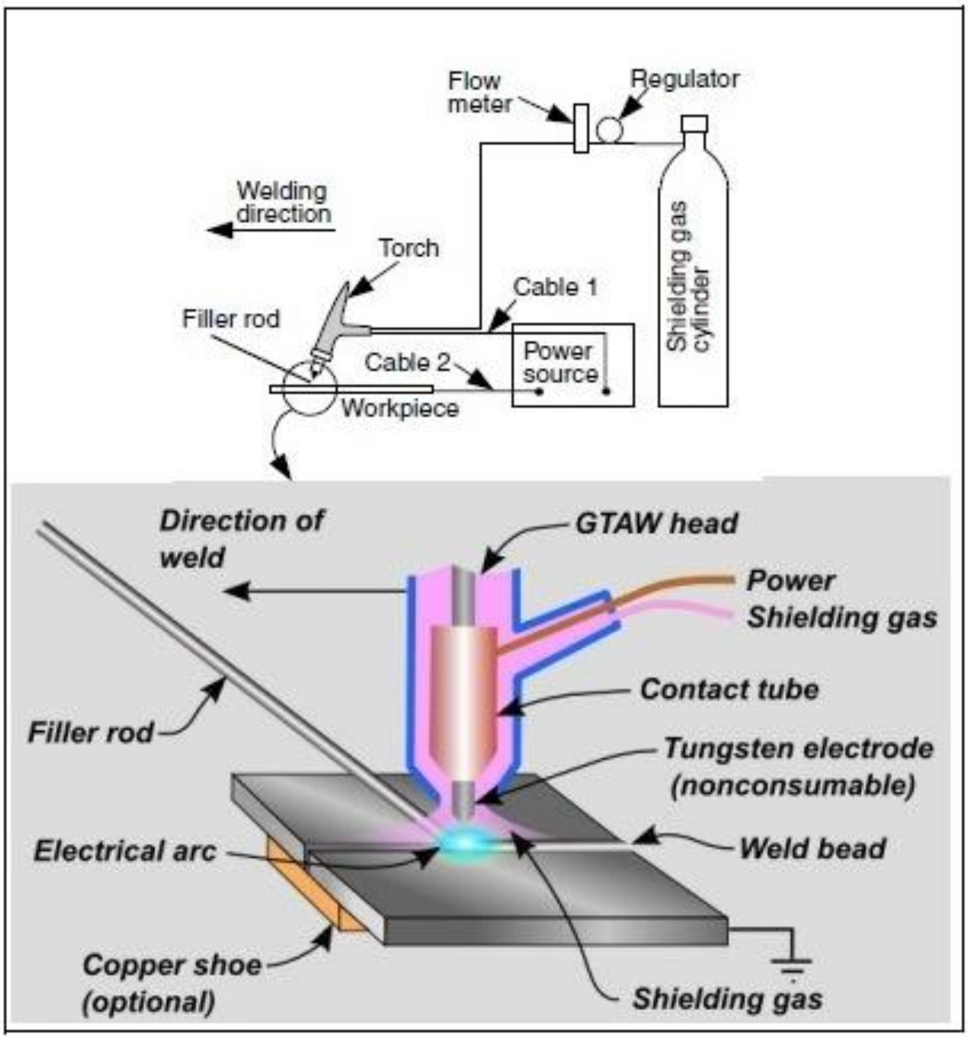

Fig. 2.7 Schematic of TIG Welding Setup [61]

Since the early days of the invention, numerous improvements have been made to the process and equipment. Welding power sources have been developed explicitly for the process. Some provide pulsed DC and variable polarity AC welding power. Water-cooled and gas-cooled torches were developed. The tungsten electrode has been alloyed with small amounts of active elements to increase its emissivity; this has improved arc starting, arc stability and electrode life. Shielding gas mixtures have been identified for improved welding performance.

2.5.2.1 Principles of Operation

The schematic arrangement of TIG welding set up is shown in Fig. 2.7. The process uses a non-consumable tungsten (or tungsten alloy) electrode held in a torch. The use of a non-consumable tungsten electrode and inert shielding gas produces the highest quality welds of any open arc welding process. Shielding gas is fed through the torch to protect the electrode, molten weld pool, and solidifying weld metal from contamination by the atmosphere. The electric arc is produced by the passage of current through the conductive, ionized shielding gas. The arc is established between the tip of the electrode and the work. Heat generated by the arc melts the base metal. Once the arc and weld pool are established, the torch is moved along the joint and the arc progressively melts the faying surfaces. Filler wire, (if used) is usually added to the leading edge of the weld pool to fill the joint. Four basic components are common to all TIG welding setups.

(1) Torch

(2) Electrode

(3) Welding power source

(4) Shielding gas

2.5.2.2 Factors Affecting DOP

There are several welding variables which affect the degree of weld penetration. The following points, in no particular order, highlight the effects that welding process parameters have on penetration depth (assuming all other variables are held constant) [62-63].

2.5.2.2.1 Current

The welding variable that has the greatest effect on the degree of weld penetration is current (measured in amperage or amps). Quite simply, as welding current increases (i.e., more amperage), weld penetration increases. With arc welding processes which use constant current (CC) output, current is the main, presettable welding variable. However, with processes that use constant voltage (CV) output, voltage and wire feed speed (WFS) are the main, presettable welding variables, with current being a result of WFS. As WFS increases, the corresponding current level for that particular electrode type and diameter also increases.

2.5.2.2.2 Travel Speed

How fast the electrode travels down the joint affects how much time the arc energy has to transfer into the base plate at any particular point along the joint. As travel speed increases, the amount of time that the arc is over a particular point along the joint is less and the resulting level of penetration decreases.

2.5.2.2.3 Arc Gap Variations

With the constant voltage (CV) power sources and running at a set travel speed and voltage, as the contact tip to work distance is increased, more resistance to the flow of electricity through the electrode occurs, because the electrode (i.e., the metal electrical conductor) is longer. At a constant voltage level, this increase in resistance causes current to decrease (i.e. Ohms Law), which results in a decrease in penetration level.

2.5.2.2.4 Electrode Tip Angle

The torch position plays an important role in determining the weld pool quality. Similarly, different groove geometries (narrow to shallow) are welded effectively by using appropriate electrode tip angle. Different researchers studied the electrode tip geometry in stationary, ax symmetric TIG process to investigate the arc and weld pool behavior. Tsai and Kou [64] presented a steady state, two- dimensional model for TIG to describe heat transfer and fluid flow in the arc produced by the flat and sharpened electrodes. Current density distribution, electromagnetic force, velocity and temperatures were investigated in the arc plasma. It was found that with flat tip, the arc velocity and pressure was low as compared to the sharp tip. The temperature distribution in the arc column was constricted in case of flat tip and it was found that the presence of the gas nozzle did not produce any change in the velocity and temperature distribution. A study [65] experimentally determines the effect of tip angle on the arc temperatures. For tip angles greater than 60^0, the tip area was more uniform and hence the resultant plasma temperatures were more uniformly distributed and found to be less than 60^0 tip angle. Similarly, for tip angles less than 60^0, the heating was more due to the sharp tip area. This heating produced thermionic emission which resulted in a more uniform temperature on sharp tips. The maximum plasma temperatures were therefore found the maximum for 60^0tip. The effect of tip geometry and torch angle on high speed DCEN TIG welding of ultra-thin aluminum sheets were experimentally investigated [66]. The tip geometries were conical, conical e spherical and ball end. It was concluded that in ultra high speed welding of ultra-thin aluminum sheets, a conical tip angle of 30^0, a spherical surface ratio of 25% and a backward inclination angle of 15^0 were the most effective welding parameters. The effect of electrode tip angle on arc pressure is studied in Ref. [67]. The pressure found to increase with decrease in tip angle had a peak at 45^0. The pressure then decreased with decrease in tip angle. A mathematical model to investigate the welding arc by considering different electrode shapes and turbulent arc flow was developed in Ref. [68]. The calculated velocity was observed the maximum with sharp electrode tip.

2.5.2.3 Advantages

(1) It produced superior quality welds, generally free of defects

(2) It is free of the spatter which occurs with other arc welding process

(3) It can be used with or without filler metal as required for the specific application.

(4) It allows excellent control of root pass weld penetration

(5) It can produce inexpensive autogenous welds at high speeds

(6) It can use relatively inexpensive power supplies.

(7) It allows precise control of the welding variables

(8) It can be used to weld almost all metals, including dissimilar metal joints

(9) It allows the heat source and filler metal addition to be controlled independently.

2.5.2.4 Limitations

(1) Deposition rates are lower than the rates possible with consumable electrode arc welding process

(2) There is a need for slightly more dexterity and welder coordination than with gas metal arc welding or SMAW for manual welding

(3) It is less economical than the consumable electrode arc welding processes for thicker sections greater than 10mm

(4) There is difficulty in shielding the weld zone properly in drafty environments Potential problems with the process include:

(5) Tungsten inclusions can occur if the electrode is allowed to contact the weld pool

(6) Contamination of the weld metal can occur if proper shielding of the filler metal by the gas stream is not maintained

(7) There is low tolerance for contaminants on filler or base metal

(8) Possible contamination or porosity is caused by coolant leakage from water-cooled torches

(9) Arc blow or arc deflection, as with other processes.

2.5.2.5 Applications

TIG welding process offers advantages to many industries, ranging from the high quality required in the aerospace and nuclear industries and the high-speed autogenous welds required in tube and sheet metal manufacturing, to the ease and flexibility of TIG welding which is so welcome in repair shops.

TIG welding provides precise control of heat input. For that reason, it is preferred for joining thin gauge metals and for making welds close to heat sensitive components. It is also used for small jobs and repair welding in many fabrication shops because of the ease of control of the process and the ability to add filler metal as necessary. TIG welding is used with or without filler metal to produce high-quality welds with smooth, uniform shapes. The TIG welding process can also be used for spot welding in sheet metal applications.

2.5.3 Overview of A-TIG Welding

A-TIG process first developed by the E. O. Paton Electric welding institute in the 1960s [69]. The penetration capability of the arc in TIG welding can be significantly increased by application of a flux coating containing certain inorganic compounds on the joint surface prior to welding [70-81]. The use of flux is also claimed to reduce the susceptibility to changes in penetration caused by cast-to-cast variability in material composition and reported to produce consistent penetration regardless of heat-to-heat variations in base metal compositions [76, 82]. In this process, the activated fluxes are prepared with combinations of SiO_2, TiO_2, NiO, CuO_2 and combinations of oxide powders. The prepared mixtures of oxide powders are mixed with acetone and binder material to form a paste. The flux in the form of paste is manually applied on the bead on plate surface using a brush prior to welding (Fig. 2.8). The acetone is evaporated leaving flux on the surface and autogenous A-TIG welding is carried out.

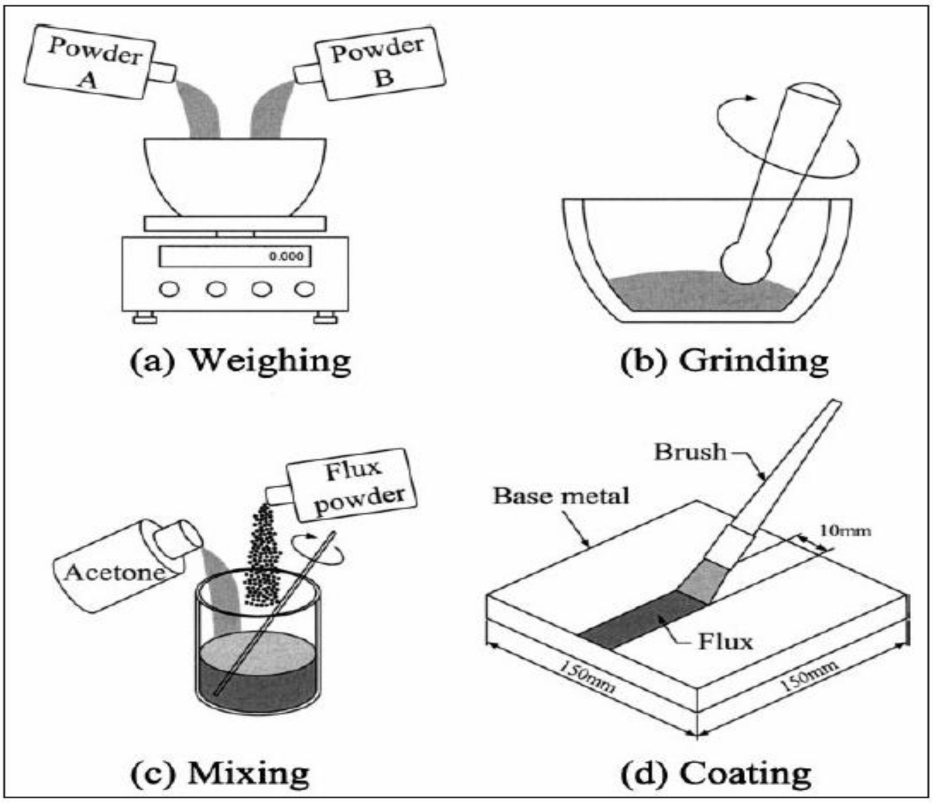

Fig. 2.8 Preparation and Application of Flux on Weld Joint Line [83]

It has been claimed that the A-TIG process can achieve in a single pass a full penetration welding steels and stainless steels up to 12mm thickness without using a bevel preparation or filler wire [82]. Furthermore, the weld joint mechanical properties and soundness are claimed to be unaffected. A series of A-TIG fluxes that produce consistent penetration regardless of heat-to-heat variations in base metal compositions have been developed validated and commercialized. These fluxes can overcome the low deposition rates and shallow penetration common in most TIG process applications. Specific fluxes have been developed for stainless steels (types 304,316,347,409,410), nickel-based alloys (alloys 600,625,690,718,800), carbon and low alloy steels, copper-nickel and titanium (CPandTi-6AL-4V).

2.5.3.1 Mechanism for Increasing Penetration due to Flux

Many investigations have been made to understand the mechanism of increased weld penetration in TIG welding due to flux [81-82, 84-88]. Considering the theoretical basis, the only one difference between TIG and A-TIG is the use of activating fluxes (Fig. 2.9). In the last four decades, four different theories on the explanation of the mechanism of the activating fluxes were published [80, 89].

2.5.3.2 Theory of Savitskii and Leskov 1980[90]**:** This theory indicates that the activating flux decrease the surface tension of the weld pool. This enhances the arc pressure to cause a deeper penetration into the pool and the arc pressure to reach a deeper penetration.

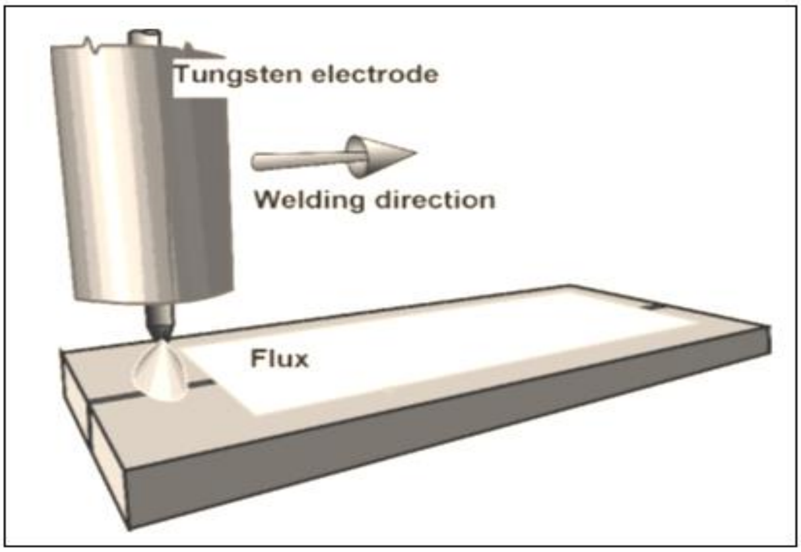

Fig.2.9 Schematic of A-TIG Welding Process [83]

2.5.3.3 Theory of Heiple and Roper 1982 [89]**:** The convective flowing of the molten metal from the centre towards the edge is the phenomenon that is called Marangoni-effect (gradient of the surface tension of the weld pool is negative). This theory explains the high penetration with the reversed Marangoni-convection. It says that the activating fluxes change the gradient of the surface tension from negative to positive that results in the flowing of the molten metal inwards towards the centre.

2.5.3.3.1 Reversal of Marangoni Convection Flow

A change in Marangoni flow has been used to explain variable penetration in weld. This change in fluid flow in weld pool is related to the thermal coefficient of surface tension. Whenever surface tension gradients prevail over a system, liquid flows from the region of lower surface tension to regions of higher surface tension. The resulting liquid flow is designated as thermo-capillary flow and is a dominant phenomenon in welding and joining due to the existence of thermal or composition gradients [91]. When TCST is negative, the cooler peripheral regions of the pool will have higher surface tension than the center of the weld pool and the flow will be outwards, creating a wide, shallow weld pool in Fig.2.10. In A-TIG welding, the TCST changes from negative to positive, owing to the surface-active elements such as oxygen, sulphur, selenium and tellurium contained in the flux.

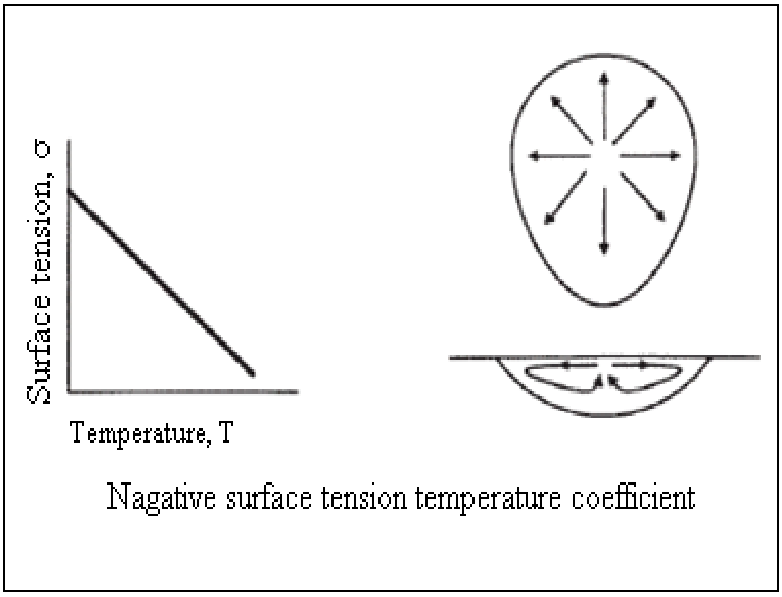

Fig. 2.10 Convective Circulation of Weld Pool Radially Outward [92]

The dissolved flux in the weld pool changes the temperature dependence of the surface tension to increase rather than decrease with temperature, the direction of convective circulation within the weld pool can change radially outwards to radially inwards (contrary to the caused by Marangoni convection), leading to an increased weld depth. For the positive TCST the flow is reversed towards the center of the weld pool and in the centre, the molten material flows downwards creating a narrower, deeper weld pool for exactly the same welding condition Fig.2.11 [93].

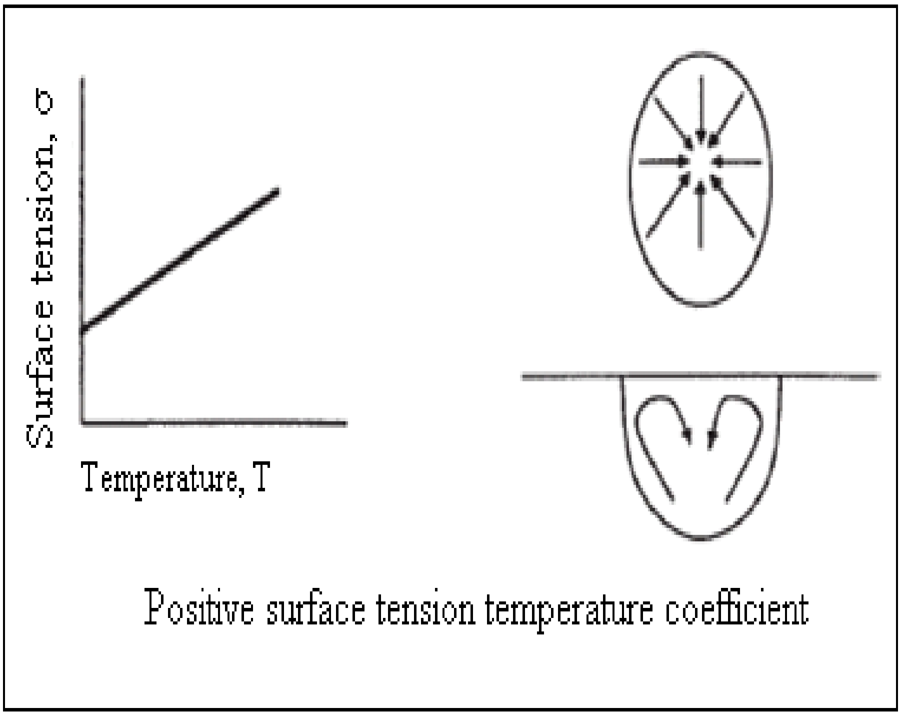

Fig. 2.11. Convective Circulation of Weld Pool Radially Inward [93]

The increase in penetration depth can be explained by the rise in the electromagnetic (Lorentz) forces, which are proportional to the square of current density. The high electromagnetic forces and, consequently, arc pressure can create an inward flow in the weld pool, which tends to produce deeper weld penetration. As the result of this inward flow, the heat input from the arc should transfer from the surface to the depth of the weld pool. This heat transfer causes a steep gradient of surface temperature of the weld pool, which also leads to the metal plasma distribution being localized at the center of the pool surface. This in turn leads to a constricted anode root, which can withstand a higher current density at the anode, promoting the inward re-circulatory flow driven by the electromagnetic force (Lorentz force). Thus the multiplication effect of the Lorentz force and the Marangoni convection appears to cause strong inward re-circulatory flow in the weld pool. Also, the difference in flow direction in the weld pool changes the geometry or depth/width ratio of weld bead penetration [93].

2.5.3.4 Theory of Simonik 1976 [94]***:*** Simonik says that oxide and fluorine molecules present in the activating fluxes have affinity to focus the free electrons at the edge of the plasma of the arc. The ions formed this way have substantially lower mobility than the free electrons. This leads to increased current density in the centre of the arc by means of the higher movement of the free electrons which leads to the deeper penetration.

2.5.3.4.1 Mechanism of Arc Constriction

The TIG arc is comprised of the following four regions.

1. Plasma column, through which the current is carried by the electron and ions produced by the thermal ionization of the shielding gas.

2. Anode/Cathode, for high potential drop to maintain the current flow as the gas is cooled by the electrode.

3. Cathode, under the bombardment by positive ions the high temperature creates the condition for the thermionic emission of electrons.

4. Anode, under the influence of the anode potential drop, the electrons accelerate but then kinetic energy is transferred to the anode.

Lucas and Howse [80] proposed a mechanism which is based on the concept that the constriction of arc will increase the temperature at the anode because of the increase in current density and higher arc voltage. In the A-TIG process, it is proposed that arc constriction is produced by the effect of the vaporized molecules capturing electrons in the outer regions of the arc which results in a constricted plasma similar to the effect produced by the nozzle in the conventional plasma arc system. In the central regions of the arc, the temperature is higher than the dissociation temperature of the molecules and the gas and flux atoms are ionized to generate electrons and positive ions. In the cooler peripheral regions of the arc column, the vaporized material still exists as molecules and dissociated atoms, which are large enough for the electrons to become attached to form negatively charged particles. Consequently, the numbers of electrons in the peripheral regions of the arc, which are the main charge carriers are reduced. This forces the arc to constrict to a new equilibrium state with a higher current density in the plasma and at the anode. Fig. 2.12 shows the arc and its constriction due to negative irons. It has been observed that particular halogen compounds with similar electron affinity but higher temperature of dissociation are more effective at constricting the arc; fluorine was more effective than chlorine in constricting the arc. It should be noted that although metal oxides generally have a low electron affinity than

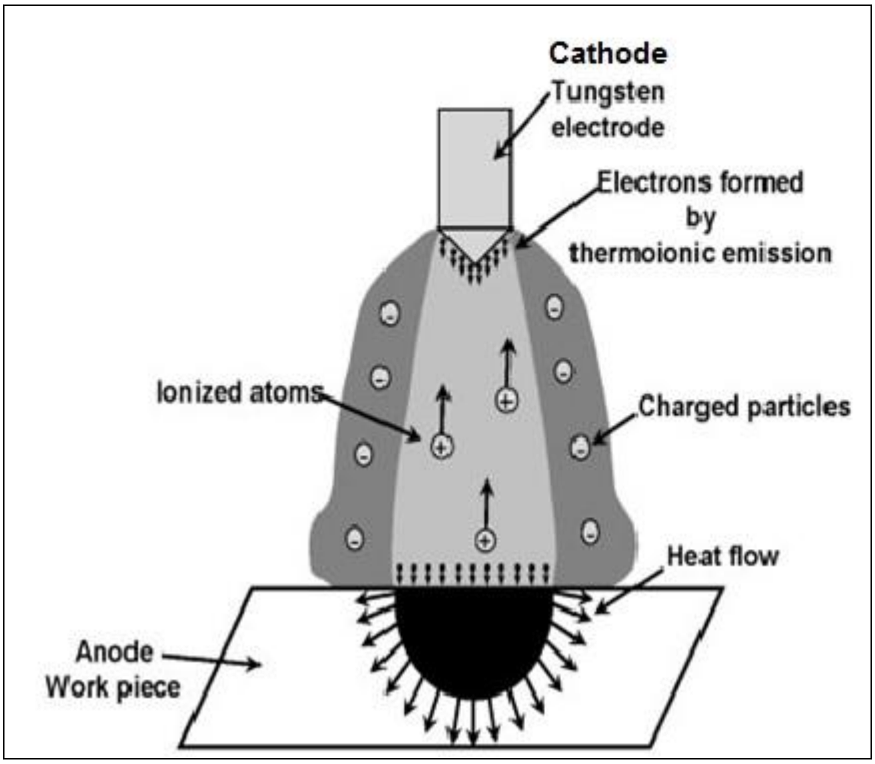

Fig. 2.12 Schematic Representation of Arc Constriction [80]

halogen compounds, their dissociation temperatures are higher which will promote their effectiveness in absorbing electrons in the peripheral regions of the arc and hence in constricting the high temperature plasma. The oxide melting point plays an important role in the activating effect. An oxide with a low melting point is more efficient than an oxide with a high melting point. The oxides V_2O_5, MoO_3 and $B_4Na_2O_7$ have a great number of dissociation of O^{2-} ions and liberate metallic ions with a high degree of ionization.

Electron absorption is affected by the attachment of electrons to vaporized molecules and dissociated atoms to form negatively charged particles. Electron attachment can only take place in the cooler peripheral regions where the electrons have low energy in a weak electric field. Towards the center of the arc, where there is a strong electric field, temperature is high, and there are very high-energy electrons, ionization will dominate. Thus restricting current flow to the central region of the arc will increase the current density in the plasma and at the anode, resulting in a narrower arc and a deeper weld pool. Sulphur added to a metal will cause an inward flow and consequently a deeper penetrating weld, which is due to the formation of FeS at the surface of the weld pool, which has significantly lower surface tension than pure iron. The critical level of sulphur in the weld pool (the point where Thermal co-efficient of Surface tension (TCST) changes from negative to positive) was said to be 60 ppm. Oxygen has slightly lesser effect on the TCST than sulphur. Calcium is a reactive element that tends to cause poor penetration by reacting with free oxygen and sulphur in the molten weld pool. Less than 10 ppm Ca reduces the levels of Oxygen and sulphur to the point that the TCST becomes negative and reduces weld penetration.

2.5.3.5 Theory of Lowke, Tanaka and Ushio 2005 [95]**:** They explain the deep penetration by means of the higher electric insulation of the activating fluxes. Because of the higher electric insulation, the arc is able to break through the surface (and the flux on it) at a narrower area. The focus of the arc increases which leads to higher current density in the arc spot and this causes the deep penetration.

Although the activating flux effect is well known, the mechanisms controlling it are not well understood. Number of investigations on the mechanisms for increase in depth of weld penetration due to use of flux have proposed many theories which include constriction of the arc [76-77, 96-97] and reversal of Marangoni convection in the molten weld pool [90,98-103]. But there is still no common agreement about the Activated TIG mechanism.

2.5.3.5.1 Effect of Arc Constriction due to Insulating Effect of Surface Flux

This is one of the further possible mechanisms. The fluxes that are used are generally metallic oxides, which are good electrical insulators. This flux layer acts as an insulation barrier to the arc current. Temperatures at the center of the weld pool will be sufficient enough to melt the flux so that the electrical current can penetrate the flux to the weld pool and work piece. The arc diameter at the weld pool surface will be reduced by the insulating effect of the flux for the outer regions of the arc. For a given current, the current density at the center of the weld pool will be increased, leading to the increased magnetic pinch forces and pressure in the pool, resulting in strong convective flow downwards in the weld pool and an increased weld depth [95].

2.5.3.6 Advantages of Using Activated Flux

Specific advantages claimed for the activating flux process, compared with the conventional TIG process include: Increases DOP up to 300% in single pass autogenous TIG welding. It overcomes the problem of cast-to-cast variation for example; deep penetration welds can be produced in low sulphur (less than 0.002%) content stainless steels, which would normally form a wide and shallow weld bead with conventional TIG. It reduced weld shrinkage and distortion for example; the deep narrow weld in a square edge closed butt joint will produce less distortion than a multi-pass weld in the same thickness material but with a V-joint. It increases the productivity. The claims for a substantial increase in productivity are derived from the reduction in the welding time either through the reduction in the number of passes or the increase in welding speeds.

The weld pool size is such that it is small enough to be supported by surface tension without the weld sagging which in turn has eliminated the need for the addition of filler wire during welding and for grinding the weld flush post welding. These factors have resulted in product improvements and an overall cost saving.

The mechanical properties, weldability, corrosion resistance and safe use of these fluxes have been extensively tested and found suitable for a wide range of applications.

Due to increase in penetration, it is possible to reduce heat input, if necessary and still achieve penetration levels twice that resulting from conventional TIG welding. Standard TIG welding equipment, shielding and backing gases and consumables are sufficient for carrying out flux assisted TIG welding. Using flux, weld bead width is only half or two thirds of that resulted with traditional TIG welding process.

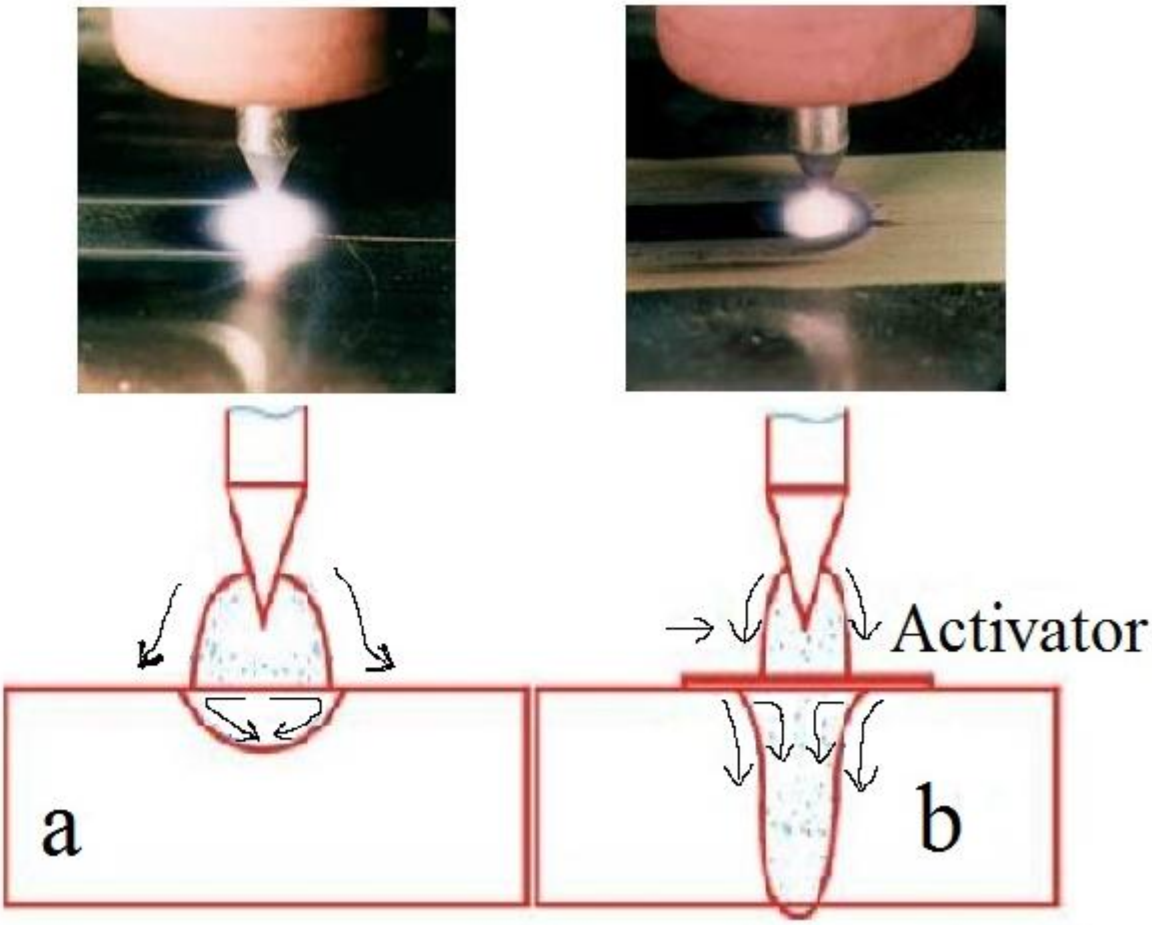

Fig. 2.13 Schematic Sketch of Penetration in (a) Conventional TIG (b) A-TIG welding [13]

The mechanical properties of the TIG weld made with flux should be nominally identical to a conventional TIG weld as long as the consumables and shielding gases are same. The reduction in welding time is significant with flux and applying the flux is relatively easy in the shop or field. Therefore, it is very useful to develop specific activated flux for ferritic steel. However certain disadvantages of using activated fluxes include the rougher surface appearance of the weld bead and the need to clean the weld after welding it often requires rigours wire brushing to remove the slag residue.

Fig. 2.13 compares the characteristic appearances of the arc in argon shielding gas for conventional TIG (Fig. 2.13a) and A-TIG (Fig. 2.13b). It can be seen that the A-TIG (flux) welding arc shows a constriction of the plasma (Fig. 2.13b) column diameter compared with the conventional TIG welding arc at the same current level. Constriction of the plasma column increases the current density in the anode root and a more focused arc increase in the penetration of TIG flux welds can be achieved compared with conventional TIG welds. The Fig. 2.14 and Fig. 2.15 compares the conventional TIG and A-TIG welding in terms of penetration depth Vs time as well as single pass and multi pass welding performances. It is evident that A-TIG welding is cost and time saving.

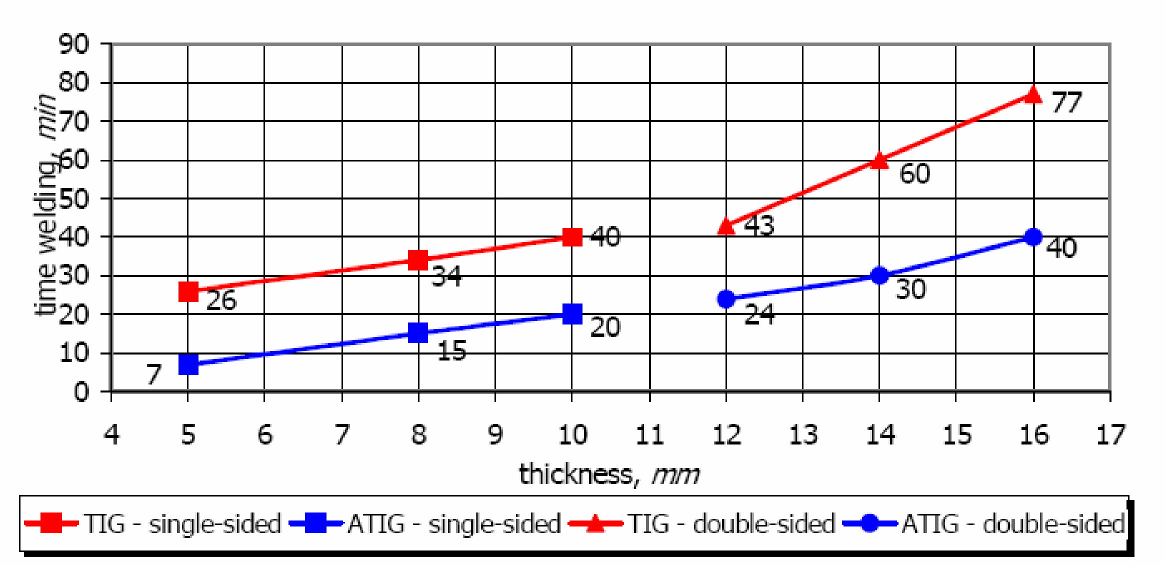

Fig. 2.14 Comparison of Time Required for Welding Vs Thickness for TIG & A-TIG [104]

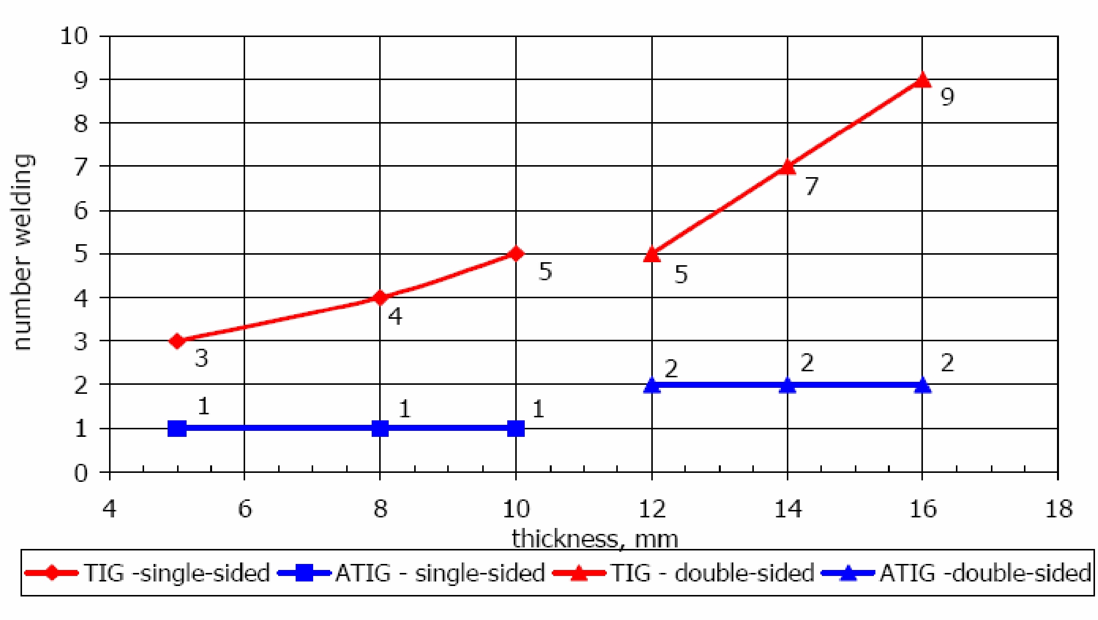

Fig. 2.15 Comparison of No. of Passes Vs Thickness for TIG & A-TIG Welding [104]

As A-TIG welding is an autogenous process, prior setting up of process parameters is required to achieve the desired DOP. Optimization of process parameters is required to achieve the desired weld bead shape parameters during A-TIG welding. Though there are several optimization techniques, the most common optimization techniques used for A-TIG welding process optimization include RSM of DOE and GA [105-112]. Literature survey on the applications of RSM and GA in welding process optimization is discussed below.

2.6 Design of Experiments

An experiment can be considered as a process seeking to answer one or more carefully formulated questions. It should have carefully described goals which will be used to choose the appropriate factors and their range, as well as the relevant procedure. The factors studied should not be covered by other variables, with the chosen experimental sequence removing the effects of the uncontrolled variables. Replication of the experiments will help to randomise the results taken, to limit bias from the experiments. While replication ensures a measure of precision, randomisation provides validity of the measure of precision. By using this technique, many evaluations are usually needed to get sufficient information which can be a time-consuming process. The term “design of experiments” was originated around 1920 by Ronald A. Fisher, a British scientist who studied and proposed a more systematic approach in order to maximize the knowledge gained from experimental data [113] since then, DOE has become an important methodology that maximizes the knowledge gained from experimental data by using a smart positioning of points in the space. This methodology provides a strong tool to design and analyse experiments; it eliminates redundant observations and reduces the time and resources to make experiments. In general, we can say that a good distribution of points achieved through a DOE technique will extract as much information as possible from a system, based on as few data points as possible. Ideally, a set of points made with an appropriate DOE should have a good distribution of input parameter configurations. This equates to having a low correlation between inputs. The DOE approach is important to determine the behavior of the objective function we are examining because it is able to identify which factors are more important. The choice of DOE depends mainly on the type of objectives and on the number of variables involved. Usually, only linear or quadratic relations are detected. However, and fortunately, higher-order interactions are rarely important and for most purposes it is only necessary to evaluate the main effects of each variable. This can be done with just a fraction of the runs, using only a “high” and “low” setting for each factor and some center points when necessary. Therefore, DOE statistical techniques are especially useful in complex physical processes, such as welding. These processes usually involve a large number of interrelating parameters, which range from applied pressure to operating temperature and material properties that are related with complex laws not fully described to the extent necessary for successful industrial implementation of such processes.

2.6.1 Response Surface Methodology

RSM is a collection of mathematical and statistical techniques for empirical model building. By careful DOE, the objective is to optimize a response [114] (output variable) which is influenced by several independent variables (input variables). An experiment is a series of tests, called runs, in which changes are made in the input variables in order to identify the reasons for changes in the output response. Originally, RSM was developed to model experimental responses (Box and Draper, 1987), and then migrated into the modelling of numerical experiments. The difference is in the type of error generated by the response. In physical experiments, inaccuracy can be due, for example, to measurement errors while, in computer experiments, numerical noise is a result of incomplete convergence of iterative processes, round-off errors or the discrete representation of continuous physical phenomena. It has been proved by several researchers that efficient use of statistical design of experimental techniques allows development of an empirical methodology to incorporate a scientific approach in the fusion welding procedure. [115]. In RSM, the errors are assumed to be random. The response can be represented graphically, either in the three-dimensional space or as contour plots that help visualize the shape of the response surface. Contours are curves of constant response drawn in the xi, xj plane keeping all other variables fixed. Each contour corresponds to a particular height of the response surface. With this technique, the effect of two or more factors on quality criteria can be investigated [116-117] and optimum values are obtained. In RSM design there should be at least three levels for each factor. The empirical relationship to predict the tensile strength of friction stir welded AA2219 Aluminium alloy of 6mm thickness joints by incorporating welding parameters and tool profiles was developed by researchers [118]. Another study in Ref. [119] vary the thickness of the aluminium alloy plate welding from 4 to 8 thickness and develop empirical relationship to predict the yield strength (YS) and hardness of joint. Tool rotational speed, welding speed and tool shoulder diameter are also taken into consideration. Yet another Ref. [120] identify a set of friction stir welding parameters to join aluminium matrix composites which will give higher tensile strength, ductility and wear resistance.

RSM is a most capable mathematical approach generally used in the optimization process. It can give information about the interaction between the variables. It also gives required information for design and process optimization and gives multiple responses [121]. When all independent variables can be measurable, controllable with negligible error, the response (y) can be expressed (equation 2.1) as

$$Y = f(x_1, x_2, ..., x_k) \tag{2.1}$$

Where x_k is the number of independent variables called factors. In the general applications of RSM to optimize the response "*y*", a regression model is developed. The second order polynomial equation 2.2 can be given as

$$Y = b_0 + \sum^{k}_{i=1} b_i x_i + \sum^{k}_{i=1} b_{ii} x_i^2 + \sum^{k-1}_{i=1} \sum^{k}_{j=2} b_{ij} x_i x_j \tag{2.2}$$

Where, parameters b_{ij} = 0,1…k are called the regression co-efficients.

2.6.2 Genetic Algorithm

GA is a family of computational models inspired by evolution. GAs are search procedures based on the mechanics of natural selection and natural genetics and work as an iterative optimization procedure [122-125] Instead of working with a single solution in each iteration, a GA works with a number of solutions (collectively known as a population) in each iteration as shown in Fig. 2.16. In the absence of any knowledge of the problem domain, a GA begins its search from a random population of solutions. If the termination criterion is not satisfied, three different operators – reproduction, crossover and mutation operators are applied to update the population of solutions. One iteration of these operators is known as a generation in the parlance of GAs. Since the representation of a solution in a GA is similar to the natural chromosome and GA operators are similar to genetic operators, the above procedure is called a GA.

A flow chart of the working principle of a simple GA is shown in Fig. 2.17. The initial population means the possible solutions of the optimization problem, and each possible solution is called an individual. Each individual can be represented by binary string consisting of combinations of randomly generated zeroes and ones. Decoding is the process of changing the input variables that are coded by the binary string into a real number. The fitness evaluation is a procedure necessary to decide the survival of each individual. Individuals with large fitness values represent better solutions. The next step is to use each individual's fitness and the genetic operators (production, crossover and mutation) to produce the next generation of the population. Reproduction is the process in which each individual may be duplicated according to its fitness.

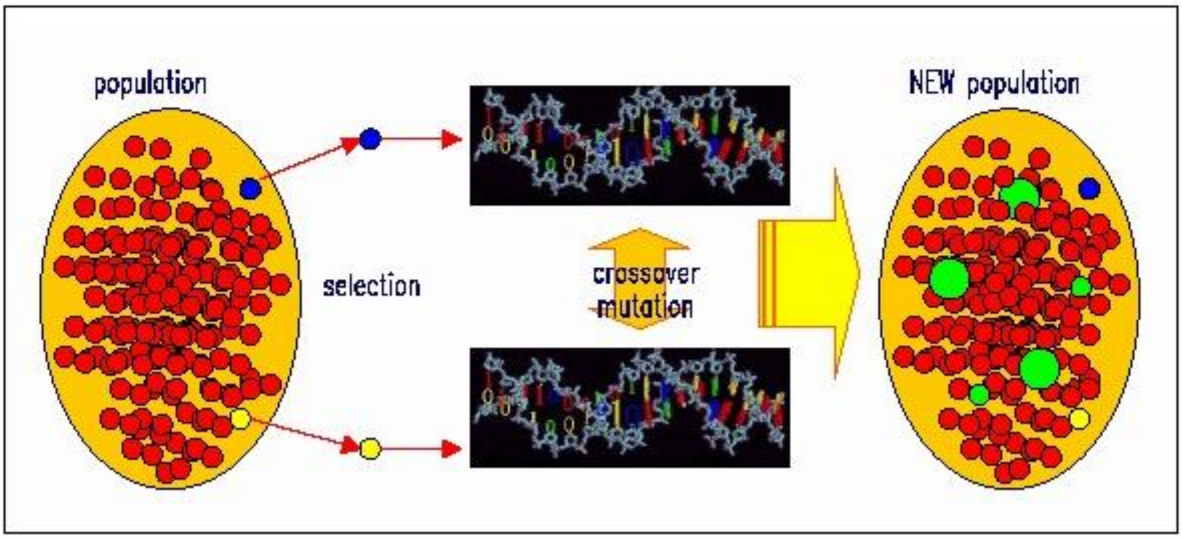

Fig. 2.16 Schematic Sketch Showing the Procedure Followed in the GA [13]

Through this operation process, individuals with higher fitness levels produce more offspring in the next generation than those with lower fitness levels. Crossover is the process by which the strings are able to mix and match their attributes through random process. Crossover proceeds in three steps. First two parent strings are selected randomly from the mating pool. Second, an arbitrary location called crossover site in both strings is selected randomly. Third, the portions of the strings following the crossover site are exchanged between two parent strings to from two offspring strings. This process is applied to the other strings in the mating pool. This process is limited by the crossover rate. For example, if the crossover rate is 0.75, then 75% of the pairs are crossed, whereas the remaining 25% are added to the next generation without crossover. Mutation is performed by occasionally altering the value of a string position. In other words, a bit value of 0 is reversed to 1 and a bit value of 1 is reversed to 0. Selection of the location is determined by the mutation rate. The mutation rate is usually set at a low value to avoid losing good strings. Mutation has the effect of tending to inhibit the possibility of converging to a local optimum rather than the global optimum. After reproduction and mutation, then the individual strings are then if necessary decoded, the objective function evaluated, a fitness value assigned to each individual and individual selected for mating according to their fitness and so the process continues through subsequent generations. The GA is terminated when some criteria are satisfied, e.g. certain number of generations, a mean deviation in the population or when a particular point in the search space is encountered.

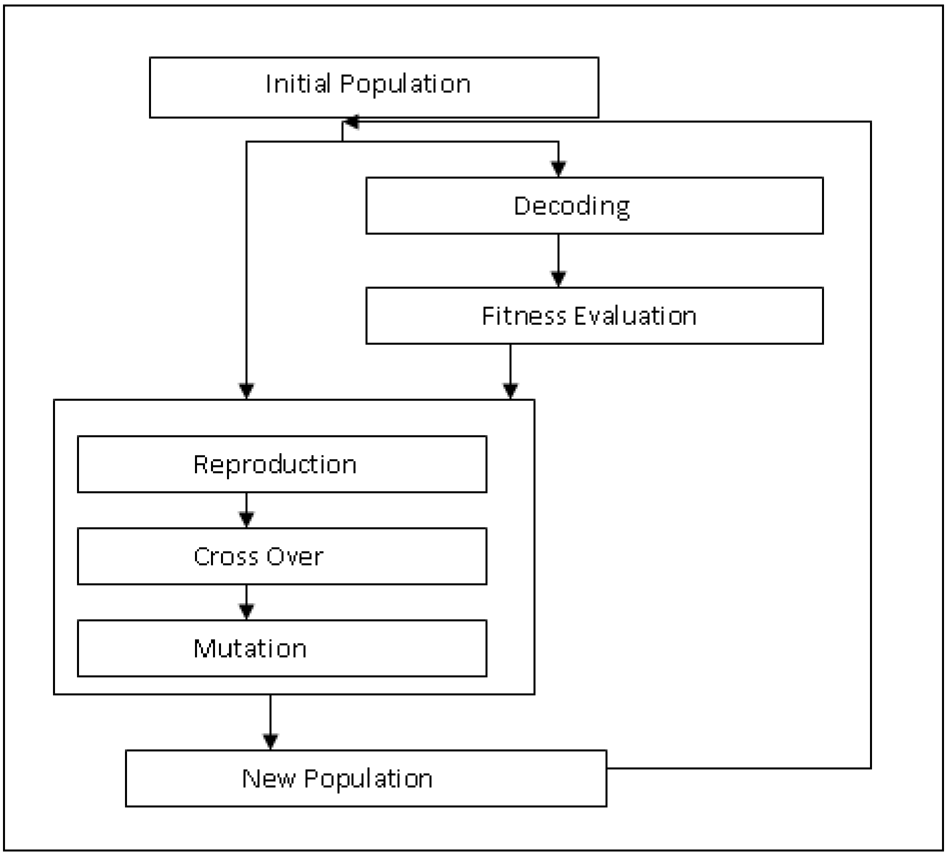

Fig. 2.17 A General Procedure of a GA

In GA the population size, crossover rate and mutation rate are important factors in the performance of the algorithm [126-129]. A larger population size or higher crossover rate allows exploration of more of the solution space and reduces the chances of settling for poor solutions. If it is too large, leads to wastage of computation time. If the mutation rate is too low, many binary bits that may be useful are never tried, but if it is too high there will be much random perturbation, and the offspring will lose the good information of the parents.

GAs is very different from most of the traditional optimization methods. The fundamental differences are listed below.

- GAs work with a population of solutions instead of a single solution

- GAs do not require derivative information or other auxiliary knowledge; only the objective function and corresponding fitness levels influence the directions of search
- GAs use the probabilistic transition rules, not deterministic ones

GAs work on an encoding of the parameter set rather than the parameter set itself (except in where real-valued individuals are used) GAs are finding increasingly applied in the field of welding in recent times. Few examples of the application of GA in welding are discussed below.

2.6.2.1 Applications of GA in Welding

GA was used for determining the optimal/near optimal settings of the GMA welding process parameters to achieve the target geometry [130]. The output variables were the bead height and the DOP of the weld bead. These output variables were determined according to the input variables which are the root opening, wire feed rate, welding voltage and welding speed. The study demonstrated how to obtain neat optimal welding conditions over a wide search space, conducting a relatively small number of experiments. Modeling and optimization of GMA welding process by GA and RSM has been studied by researchers [131,132]; In this study the dual response approach is adopted to determine the welding process parameters which produce the target value with minimal variance. First regression models are generated. Subsequently GA based on the regression models and constraints is applied to determine the welding process parameters which generate the desired penetration with minimum variance. For optimizing the process parameters during welding of brass plates, GA based models [133] were applied for estimating the current and velocity in order to minimize the evaporation of brass material. Good quality weld bead could be obtained by employing GA based models.

GA was applied for obtaining near optimal settings of GMA welding process [134]. In this study the search for near-optimal was carried out step by step with the GA predicting the next experiment based on the previous and without the knowledge of the modeling equations between the inputs and outputs of the GMA welding process. By using GA, it was possible to locate near-optimum conditions with relatively small experiments. The performance of GA was compared in GMAW process optimization with RSM [135] and found that the RSM provided good results over regular experimental regions, i.e., with no irregular points. However, it was found often very difficult to establish an arc, and melt-through may occur under certain experimental points needed to satisfy the specific experimental design. They reported that the GA can be powerful tool in experimental optimization even in the absence of any model. However, the optimization of GA requires a good setting of its own parameters such as population size, number of generations, etc. Otherwise, there is risk of an insufficient sweeping of the search space.

The bi-directional capability of the heat transfer and fluid-flow models is attained by coupling the heat-transfer and fluid flow calculations with a GA [136-137]. In addition, the capability to determine alternate paths to achieve target geometry is demonstrated by estimating the various sets of welding variables current, voltage, welding speed and wire feed rate that can all produce target weld geometry. Researchers first time demonstrated that the coupling of numerical heat and fluid flow model [138] with a GA to arrive at the optimum process parameters in order to achieve the target geometry in GMA welding of low alloy steel fillet welds. The study provided hope that weld attributes can be tailored reliably through multiple routes based on heat transfer and fluid flow calculations and evolutionary algorithms. GA was applied [138] for optimization of the Jhonson-Mehl-Avarami equation parameters for α - Ferrite to γ - Austenite transformation in steel welds. The GA based determination of all three JMA equation parameters resulted in better agreement between the calculated and the experimentally determined austenite phase fractions than was previously achieved. Another researcher [139] used an artificial neural network model for evaluating the objective function in GA to optimize the SMA weld metal composition that will maximize the toughness at - 60°C. Using the model, it could predict the weld metal composition that will give a improved toughness of 87± 20 J at - 60°C in steel welds. It was demonstrated the applicability of coupled optimization and forward models to design weld metal composition.

2.7 Residual Stresses in Weld Joints

The residual stresses in a component or structure are stresses caused by incompatible internal permanent strains. They may be generated or modified at every stage in the component life cycle, from original material production to final disposal. Welding is one of the most significant causes of residual stresses. It typically produces large tensile stresses whose maximum value is approximately equal to the YS of the materials being joined, and balanced by lower compressive residual stresses elsewhere in the component. This phenomena leads to distortion. The distortion causes the degradation of the product performance and the increase of the manufacturing cost due to the poor fit-up, so that it needs to be eliminated or minimised below a critical level.

Tensile residual stresses may reduce the performance and ultimately cause failure of manufactured products. They may increase the rate of damage by fatigue due to the increase of the average stress applied or environmental degradation. They may reduce the load bearing capacity by contributing to failure by brittle fracture, or cause other forms of damage such as shape change. Compressive residual stresses are generally beneficial, but cause a decrease in the buckling load.

2.7.1 Residual Stress Consequences and Parameters

One of the main consequences of residual stresses is warping of thin components upon welding. There are a number of distortion control strategies. They can be mainly classified into two:

(a) Design-related and process-related variables, that include weld joint details, plate thickness and thickness transition if the joint consists of plates of different thicknesses, stiffeners spacing and number of attachments, corrugated construction, mechanical restraint conditions, assembly sequence and overall construction planning.

(b) Welding process, there are important variables including method, travel speed and welding sequence.

Distortion mitigation techniques are implemented to counteract the effects of shrinkage during cooling, which distorts the fabricated structure. One common problem associated with welding is the finished products dimensional tolerance and stability. Fig 2.18a.shows the typical profiles of residual stresses induced during a welding process [140-141]. Fig. 2.18b and Fig. 2.18c shows the typical thermal stress distribution after welding and Change of residual stress due to metallurgical processes during welding respectively.

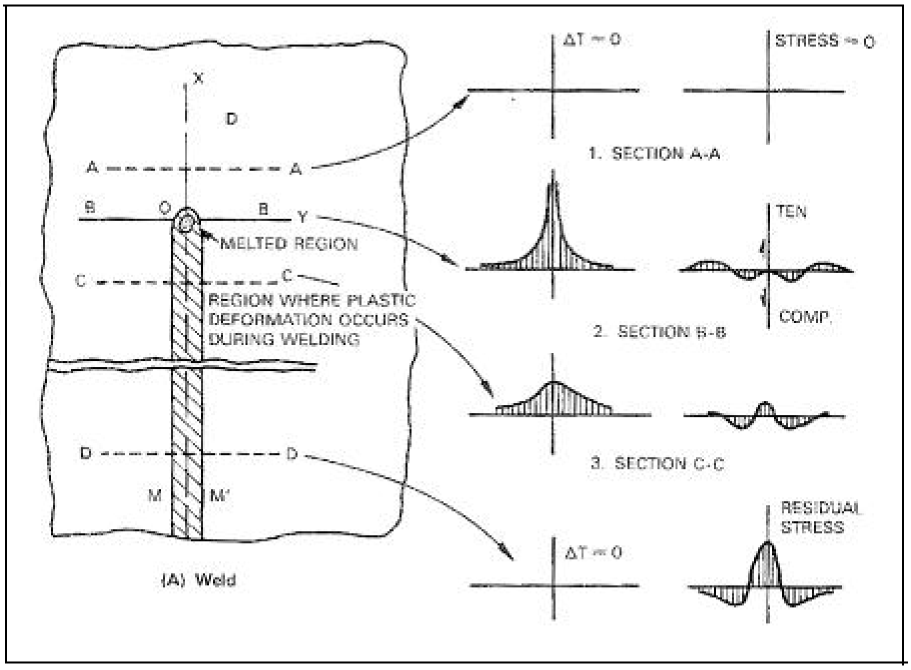

Fig 2.18 (a) Thermal Stress Distribution Before, During and After Welding [140]

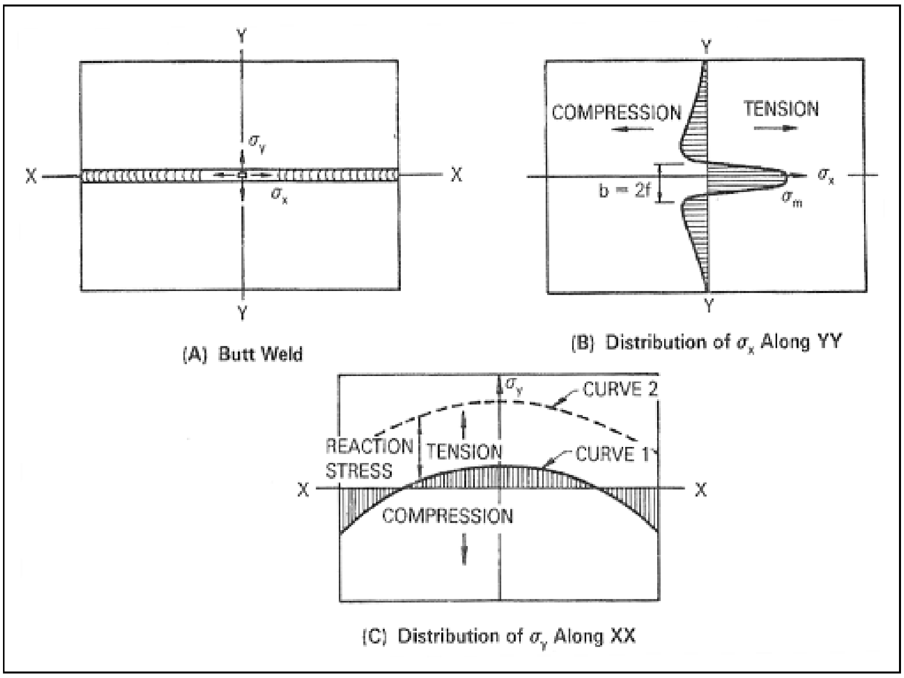

Fig 2.18(b) Thermal Stress after the Welding [140]

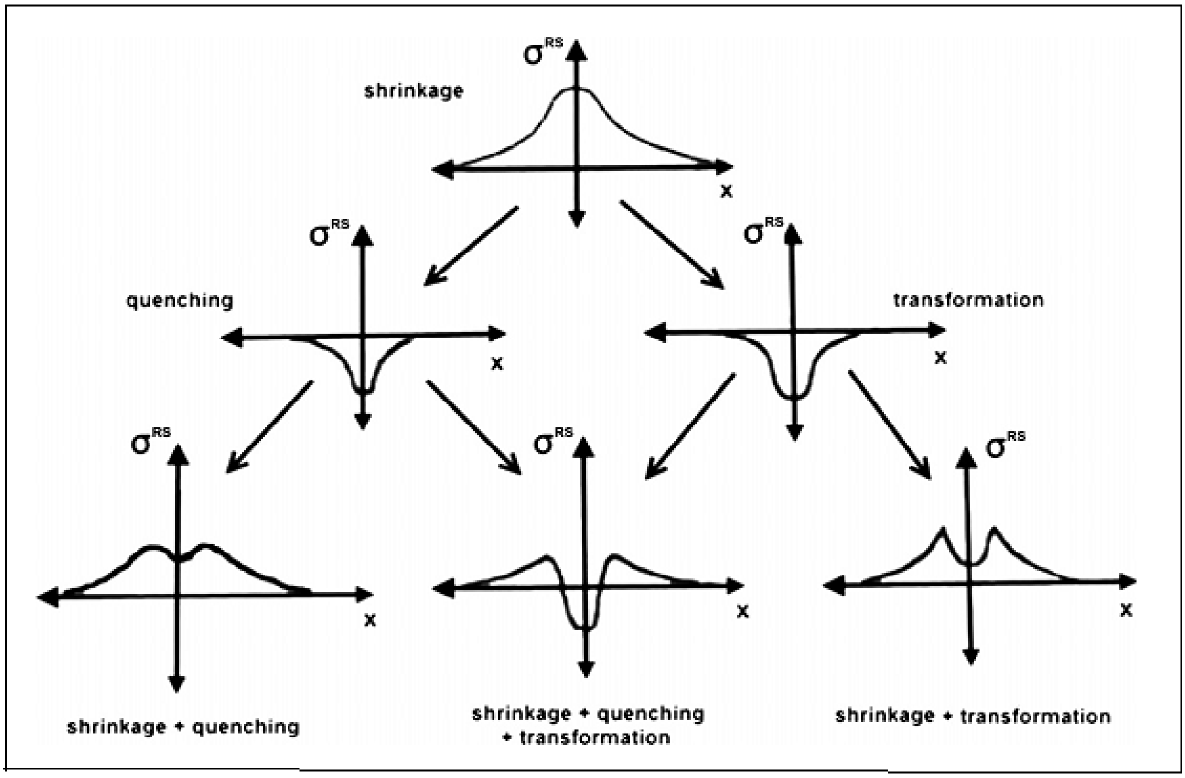

Fig 2.18 (c) Change of Residual Stress due to Metallurgical Processes During welding [141]

2.7.2 Residual Stress Measuring Techniques

Residual stresses may be measured by non-destructive techniques; or by locally destructive techniques and by sectioning methods. The selection of the measurement technique should take into account volumetric resolution, material, geometry, accessibility and if the component needs to be used after the testing or not. The various measurement techniques can be classified into non-destructive, semi-destructive and destructive techniques [142-144] as shown in Fig 2.19.

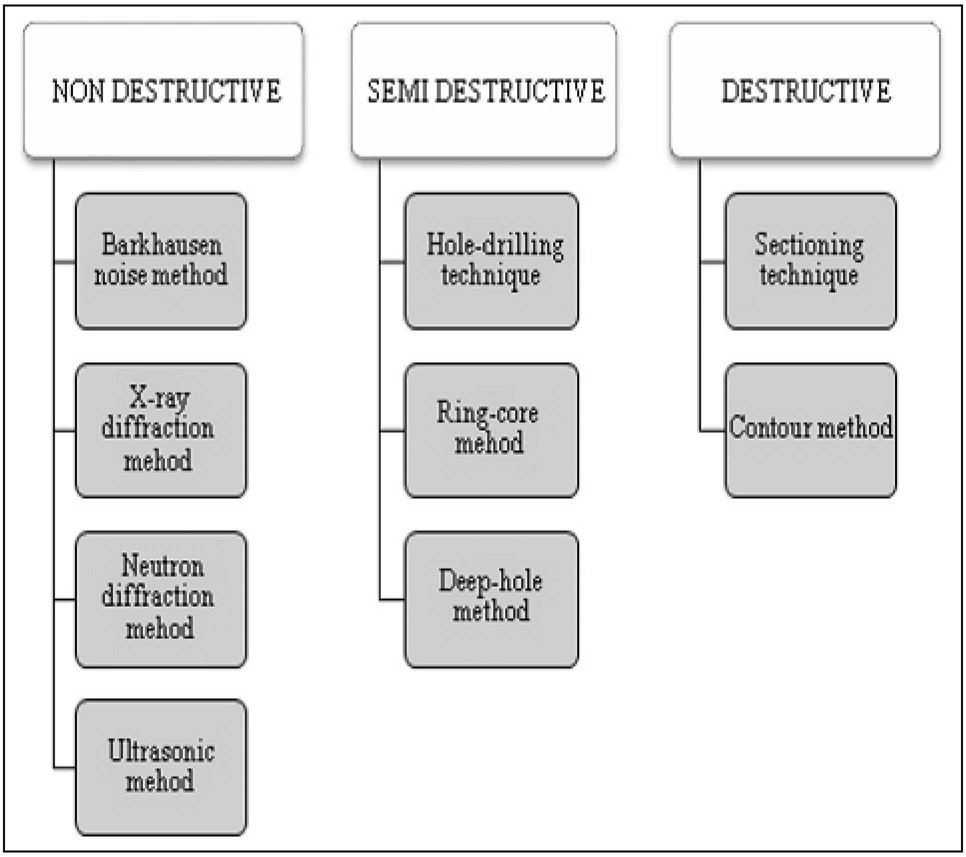

Fig. 2.19 Residual Stresses Measuring Techniques [144]

2.7.3 XRD Technique for Residual Stress Measurement

The XRD technique uses the change in inter planar spacing at different psi angles as a tool to estimate the strain. The presence of residual stresses in the material produces a shift in the XRD peak angular position that is directly measured by the detector [142-145]. The depth of penetration of X-rays is of the order of 5 to 30 microns. Diffraction occurs at an angle 2θ, defined by Bragg's Law: $n\lambda = 2d \sin \theta$, where n is an integer denoting the order of diffraction, λ is the X-ray wavelength, d is the lattice spacing of crystal planes, and θ is the diffraction angle. Any change in the lattice spacing, d, results in a corresponding shift in the diffraction angle 2θ. Measuring the change in the angular position of the diffraction peak for at least two orientations of the sample defined by the angle enables calculation of the stress present in the sample surface lying in the plane of diffraction, which contains the incident and diffracted X-ray beams. To measure the stress in different directions at the same point, the sample is rotated about its surface normal to coincide the direction of interest with the diffraction plane.

Fig. 2.20(a), shows the sample in the $\psi = 0$ orientation. The presence of a tensile stress in the sample results in a Poisson's ratio contraction, reducing the lattice spacing and slightly increasing the diffraction angle, 2θ. If the sample is then rotated through some known angle ψ (Fig. 2.20(b)), the tensile stress present in the surface increases the lattice spacing over the stress-free state and decreases 2θ.

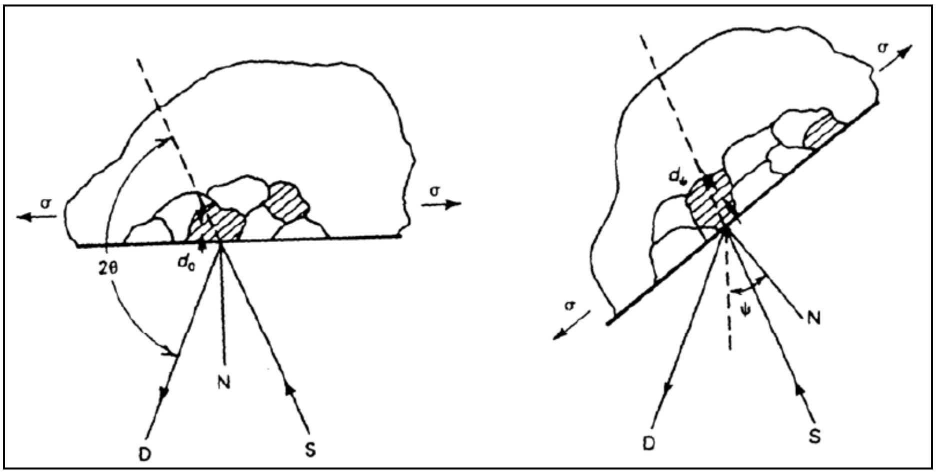

(a) (b)

Fig. 2.20 Principles of X-ray Diffraction Stress Measurement [143]

(a) $\psi = 0$. (b) $\psi = \psi$ (sample rotated through some known angle ψ

D-X-ray detector; S- X-ray source; N-normal to the surface

2.7.4 Advantages of Prediction of Residual Stresses

Controlling the fabrication-induced residual stress state can significantly enhance the structure service life. The advantages of prediction of residual stresses [142-144] are enumerated below:

(a) Understand consequences of fabrication/manufacturing process.

(b) It can lead to quality enhancement.

(c) It can minimize costly service problems.

(d) It can help to improve and optimise welding process parameters and techniques employed for reduction in residual stress build up.

(e) To enhance the service life of welded components and lowering risk of failure by predicting the influence of residual stresses on fatigue, corrosion and other detrimental surface related phenomena.

2.8 Small Specimen Testing:

Engineering structures are generally designed to withstand the anticipated loads and environmental conditions. However, safety margin provided in the design are reduced during service due to degradation in the microstructure and mechanical properties caused by service exposure. Periodic determination of mechanical properties of in-service structural components is therefore necessary for optimizing the operating procedures as well as for residual life assessment. Full scale mechanical tests require large volume of material and extracting them from operating component may impair the integrity of the structure. In such situations, mechanical property evaluation using small specimens are promising. Small specimen testing is gaining importance due to need for evaluating mechanical properties from limited volume of the samples produced from processing and scoop extraction of materials from the in-service components. There are number of testing techniques which include miniature tensile testing, ABI, Shear punch testing, Impression creep, etc. A pre-requisite for using the above techniques is to establish a good correlation between small specimen testing and standard full scale test methods.

The advantages of small specimen testing include;

1. It is near NDT method.

2. It is a very useful tool in new alloy development (small quantity of material required)

3. This can be used in-situ measurements of components in service.

4. It is very useful method for remaining life assessment of components.

5. This technique will be useful where material shortage is there.

In addition to the above advantages, this technique will be very useful especially for evaluating the irradiated components. Evaluation of tensile and creep behaviour in small regions like weld metal, coarse HAZ and fine HAZ in ferritic steel weldments is possible only by employing small specimen testing techniques. The ABI technique and Impression creep techniques are commonly employed for zone wise evaluation of strength and creep properties respectively.

2.8.1 ABI Technique

The ABI testing machine was developed and patented by Advanced Technology Corporation to test minimal material, and determine key mechanical properties of metallic structures including welds and heat-affected zones [146]. ABI technique involves strain-controlled multiple indentations at a single penetration location on a polished metal surface by a small spherical indenter. The applied indentation loads and the associated penetration depths are measured during the test, and are used to calculate the incremental stress–strain values from a combination of elastic and plastic analyses, and semi-empirical relationships which govern material behavior under multi axial indentation loading. By analysing the flow curve, tensile deformation parameters of the material such as YS, tensile strength, strength coefficient and strain hardening exponent as well as fracture toughness parameters like K_{IC} and indentation energy to fracture are evaluated [147-150]. Correlation of indentation hardness and indentation strain associated with a spherical indenter to uniaxial flow stress and flow strain is based on three premises [150]: (i) monotonic true stress-true plastic strain curves obtained from uniaxial tension and compression testing are reasonably similar, (ii) indentation automated strain correlates with true plastic strain in a uniaxial tensile test, and (iii) mean ball indentation pressure correlates with true flow stress in a uniaxial tensile test. These three premises are well established for several materials [151]. The ABI technique of loading followed by partial unloading during indentation enables a proper evaluation of indentation depth (*h*p) associated with plastic deformation of the material. The plastic diameter can then be determined from *h*p if the sinking-in and piling-up of the test material around the indentation are not pronounced [152]. The photograph of the ABI testing machine is shown in Fig. 2.21.

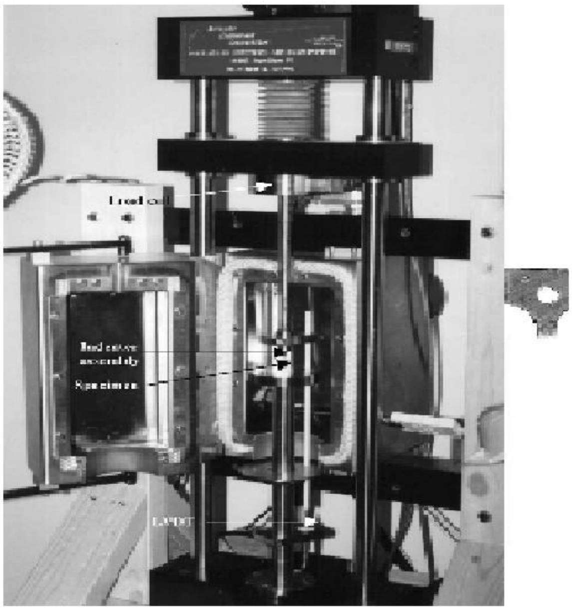

Fig. 2.21. Photograph of Typical ABI Testing Machine [153]

2.8.1.1 ABI Analysis

In a standard tensile test, the uniaxial deformation is almost confined to the constant volume of the specimen's gauge section. Initially, the material is deformed elastically, following which, plastic yielding and work hardening commence, and these processes continue homogeneously until the onset of necking. In contrast, in an ABI test, the elastic and plastic deformations are not distinctly separated. With increasing indentation penetration depth, an increasing volume of test material is forced to flow under multi axial compressive stresses generated by the advancing indenter. Hence, in an ABI test, both elastic and plastic deformation takes place simultaneously during the entire course of the test. An accurate determination of YS should hence be based on the entire load–displacement curve from the ABI test. It should be emphasized that in an ABI test consisting of seven loading and unloading cycles, as shown in Fig. 2.22(a), there will be seven consecutive processes of work hardening of both previously deformed and new material. Hence, the YS analysis is carried out by taking into account simultaneous occurrence of yielding and strain hardening of the material under conditions of multi axial compression. As seen from Fig. 2.22(a), ABI load increases approximately linearly with penetration depth. The linear increase is the consequence of two non-linear but opposing processes occurring simultaneously, i.e. the non-linear increase in the applied load with penetration depth because of the spherical geometry of the indenter, and non-linear increase in load required for further penetration because of work hardening of the material. Hence, ABI tests do not exhibit the traditional segmented behavior, i.e. linear elastic followed by non-linear work-hardening of the material. Fig. 2.22(b) is a schematic representation of the indentation profile in an ABI test.

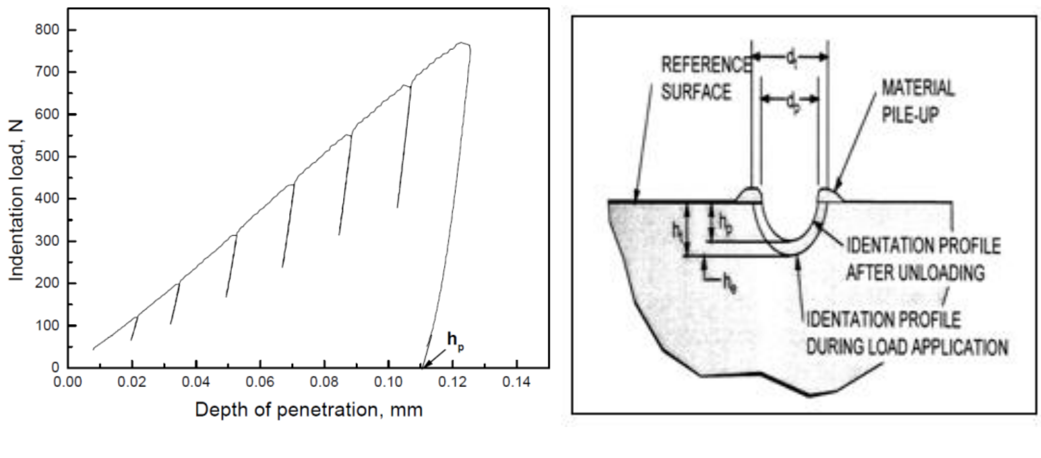

(a) (b)

Fig. 2.22 a) Schematic of Load Vs Depth of Penetration b) Indentation.[154]

2.8.1.2 Correlation of ABI-derived σ–ε Curves with Uniaxial Tensile Curves

Two examples are shown in Fig. 2.23a and 2.23b demonstrating the correlation of the true σ–ε curves derived from ABI tests and tensile data obtained from sub size miniature tensile specimens of aged cast stainless steel (CF-8) and ASTM grade A533B steel weld. The ABI data on A533B pressure vessel steel submerged arc weldment from Oak Ridge National Laboratories (ORNL) Heavy Section Steel Irradiation (HSSI) series are compared with the tensile results for the base and weld metals in Fig. 2.23b that also illustrates a good correlation between ABI and tensile data [18]. Due to the relatively low ductility of A533B, the tensile data are at the lower end of the curve [147].

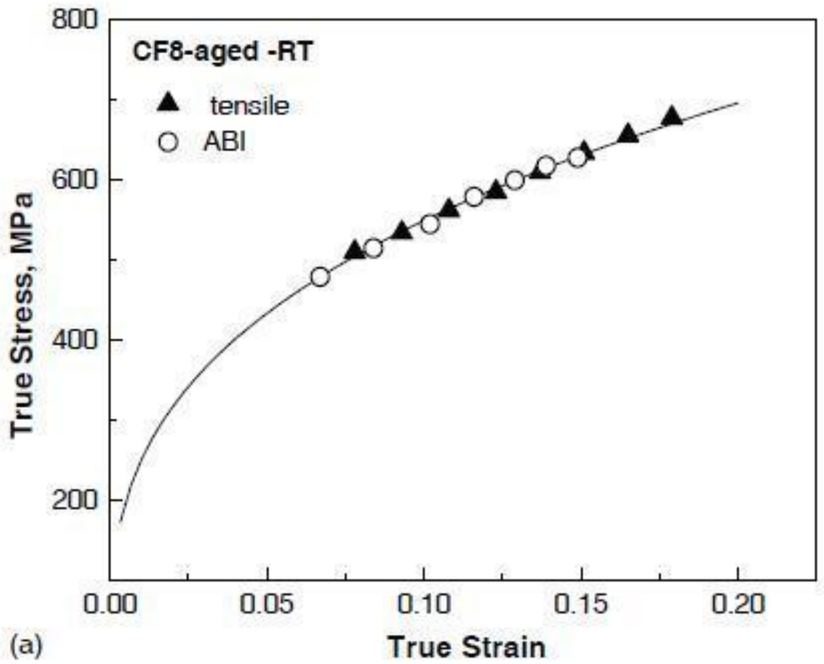

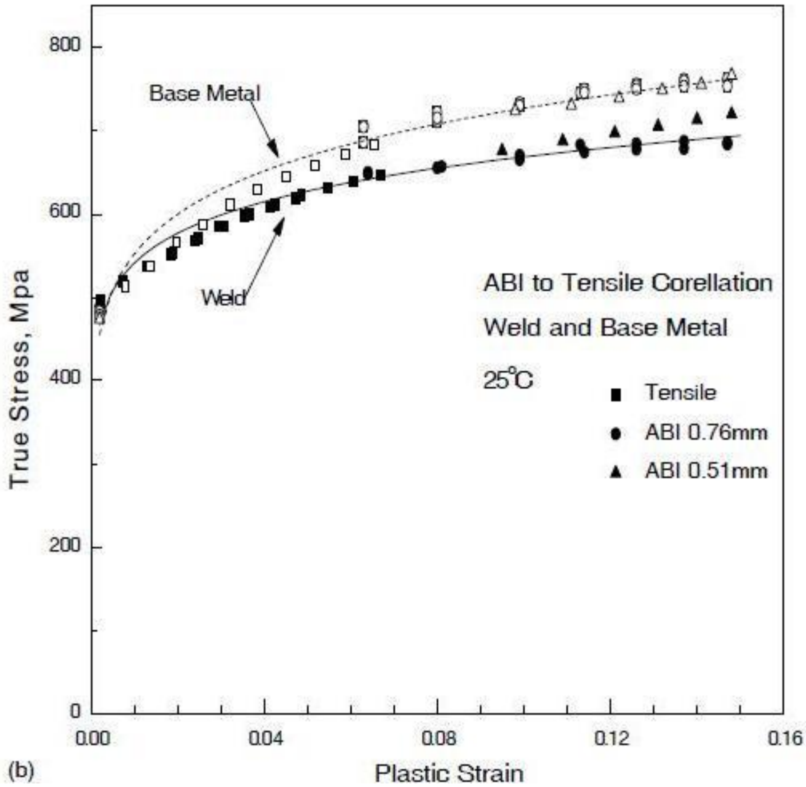

Fig. 2.23(a) Aged CF-8 Stainless Steel [154] (b) A533B Steel (Weld, Base and HAZ) [18]

By analysing the flow curve, tensile parameters of the material such as YS, ultimate tensile strength (UTS), strength coefficient and strain hardening exponent are evaluated [155]. Determination of the integrity of any metallic structure is required either to ensure that failure will not occur during the service life of the components (particularly following any weld repair) or to evaluate the lifetime extension [156] of the structure.

2.9 Impression Creep

2.9.1 Evolution of the Impression Creep Technique

Assessment of creep properties of materials from indentation test method has been a subject of great interest to several researchers worldwide for more than last fifty years. Although the indentation test method is employed for evaluating the hardness of materials, it is potentially attractive for studying the creep deformation behavior of materials. The application of this particular test methodology to study creep behavior of materials was first attempted in the 1960s. The earliest investigation concerning the study of creep behavior from a simple long time indentation hardness test was carried out in the year 1960 [157]. Subsequently, there have been continued attempts by several other researchers to obtain creep properties of materials from this long time indentation hardness test [158-166]. In this test, a constant compressive load is applied on the surface of the flat specimen through a suitable indenter such as spherical or pyramidal indenters, for a period which largely exceeds the duration of a standard hardness test. The variation of the indentation size, expressed as diameter in the case of Brinell test, diagonal length in the case of Vickers test, is measured as a function of time. Although some degree of success was achieved in these investigations, the major drawback in this methodology was the continuous decrease in the stress with the time of indentation. This is because of the geometry of the indenter employed in this test methodology. During the test, the contact area increases with time of indentation which results in continuous decrease in stress. Thus, no steady state is attained. In order to get a constant stress and thereby a steady-state speed of indentation, the indenter shape has to be changed from a pyramidal or spherical shape to a cylindrical indenter with a flat end [167]. This suggestion was not given due attention for a long time. In the mid-1970s the impression creep test technique using cylindrical indenters with flat end was introduced [19]. In the literature, generally one comes across two nomenclatures, namely, indentation creep and impression creep. The difference lies in the geometry of the indenter employed in the test. Indentation creep refers to creep tests using spherical or pyramidal indenters whereas impression creep refers to tests using a cylindrical indenter with flat end. Since the cross-sectional area of the indenter remains constant, a constant load applied to the punch implies a constant stress.

2.9.2 Impression Creep Test Technique

In an impression creep test, a constant load (L) is applied to the test specimen through a flat-ended cylindrical indenter at high temperature. This results in a compressive load on the specimen. A test specimen and the impression creep testing are schematically illustrated in Fig. 2.24.

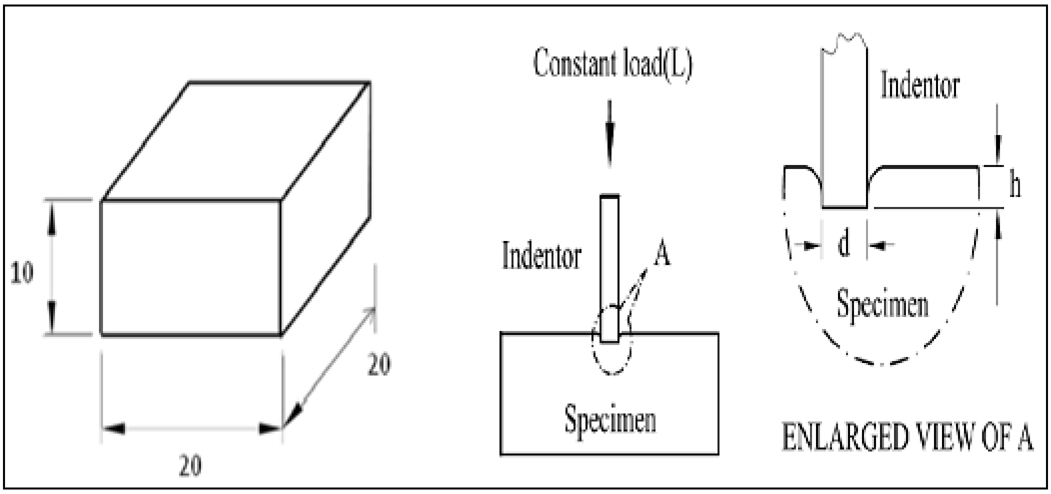

Fig. 2.24 Schematic of the Impression Creep Test Specimen (dimensions are in mm) and Impression Creep Testing [168]

During the test, the displacement of the cylindrical flat punch or the depth of penetration (h) is recorded as a function of the elapsed time. Initially, the penetration rate decreases with time and then reaches steady state after a transient period. During the steady state creep, depth of penetration increases linearly with test time. The plot of depth of penetration with elapsed test time yields the impression creep curve. Impression creep curves are similar to the conventional creep curves, but they exhibit only the first two characteristic stages of the creep curve namely, the primary creep and the steady state creep. A schematic of the impression creep curve is shown in Fig. 2.25. There is no tertiary creep stage in impression creep curve. This is because of the fact that in impression creep test, loading is compressive in nature. As a consequence, creep cracks and necking of specimen which occur during the tertiary creep stage leading to fracture do not take place in impression creep test.

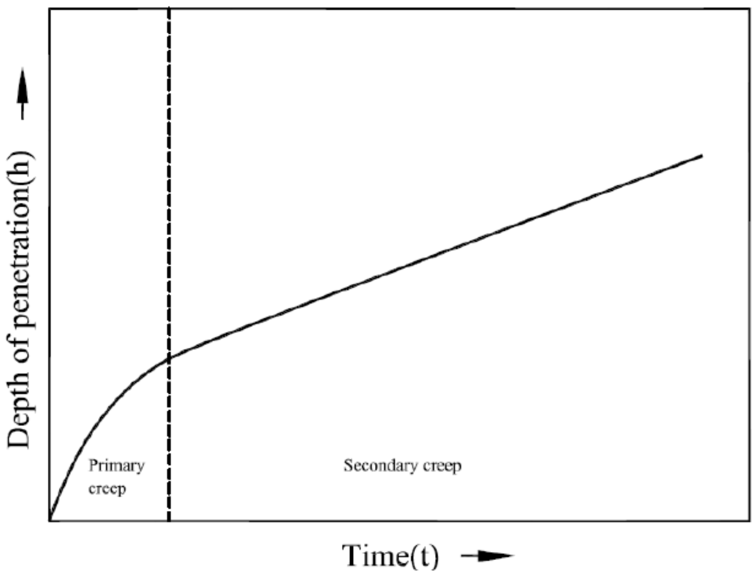

Fig.2.25 Schematic of the Impression Creep Curve [168].

2.9.3 Correlation Between Uniaxial and Impression Creep

In general, the creep rate obtained from uniaxial creep test and impression creep is in good agreement. Fig. 2.26. shows examples of the minimum creep strain rate data obtained from uniaxial and impression creep tests for a 316 stainless steel at 600^0C and a 2 ¼ Cr1Mo weld metal at 640^0C [169]. It can be seen that the data obtained from the two types of creep tests are in good agreement.

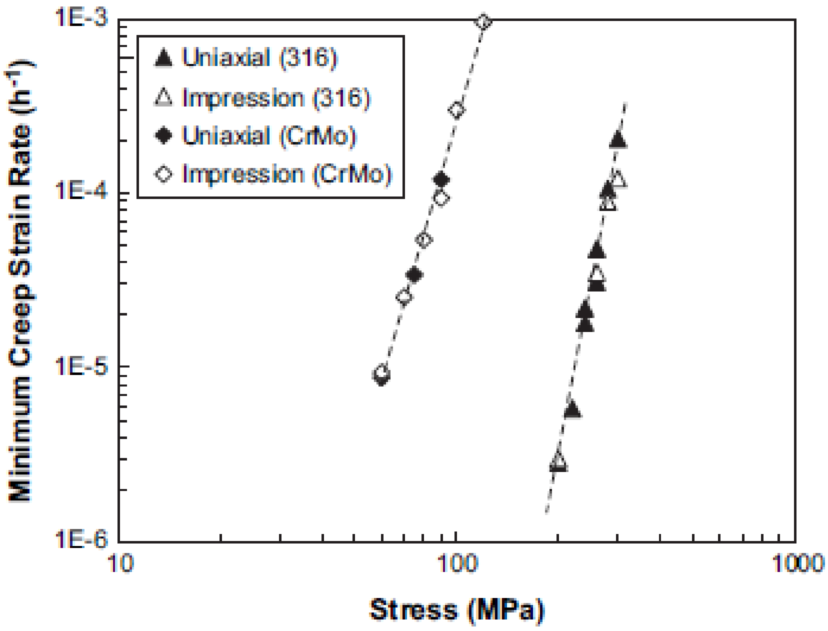

Fig. 2.26. Minimum Creep Strain rate Data for 316 SS at 600^{0}C and 2 ¼ Cr-1 Mo Weld Metal at 640^{0}C of Uniaxial and Impression Creep Tests [170].

2.9.4 Advantages and Applications of the Impression Creep Technique

Another important application is related to on-site, in-service assessment of high temperature components in power plant, where small button-shaped samples (w25 mm in diameter and 2–6 mm in thickness) are removed, for example, by a non-destructive sampling technique [146]. For these special applications, impression creep testing has become increasingly attractive since many power plant components are now operating beyond their original design life and economic, ‘‘non-invasive’’, small scale sampling and testing techniques are required for remaining life evaluation [163–165]. Impression creep testing technique has several advantages when compared with conventional creep testing. These are,

1. Impression creep technique is material non-invasive and hence requires a small specimen for the tests.

2. The ease of specimen preparation, since only two relatively parallel surfaces are required, one of which is well polished.

3. Due to the localized nature of the indentation stress field, a relatively large number of indentations may be made on a single specimen. Hence, a large amount of creep data can be collected from a single specimen which not only reduces the effort for specimen preparation, but also reduces the specimen to specimen scatter in properties.

4. The test time required is short when compared to conventional creep test. Hence, it enables rapid screening of creep properties of small laboratory heats for optimizing the chemical composition in alloy development programme.

5. Characterization of creep properties of different and narrow microstructural regions in the heat affected zone of weld joints, which is not possible to be determined in conventional creep tests.

6. Since the test requires small specimen, it is attractive for remnant life assessment studies [146-147] where it is not desirable to remove large amount of material from an operating component.

7. Because of the small indentation left in the specimen, the technique is in a sense nearly non-destructive; the small amount of compressive residual stresses remaining after the tests is not considered to be harmful.

8. Impression creep technique is useful for studying creep properties of ceramic materials, glass, composite materials where it is not possible to machine conventional creep specimens.

2.9.5 Limitations of the Impression Creep Technique

Despite these advantages, impression creep testing technique has few limitations. These are,

1. Type of loading is compressive unlike conventional creep tests in which the loading is tensile.

2. Rupture life cannot be determined by this technique because there is no fracture of the sample.

3. Since the test time is generally short, typically about a few hundreds of hours, creep behavior due to long time concurrent microstructural changes occurring in engineering alloys at high temperatures cannot be captured.

4. Although the test is relatively easy to perform and requires shorter time, interpretation of the results is difficult on account of the complex multi-axial nature of the stress beneath the indenter and the continuously varying amount of material under the indenter which is experiencing elastic, plastic and creep deformation.

2.10 Research Gap

The literature review discussed above suggests that A-TIG welding has many advantages over other conventional arc welding processes and it could become a promising welding process for welding of structural components in terms of enhanced productivity, improvement in mechanical properties and significant cost savings. Though the use of A-TIG welding for overcoming the limitations of TIG welding and enhancing the mechanical properties of various metals and alloys has been the subject of recent investigations, only limited literature is found on the effect of A-TIG welding on the microstructure and mechanical properties of 9Cr-1Mo steel. Therefore, development of A-TIG welding process for 9Cr-1Mo steel and studying the effect of A-TIG welding process on the microstructure and mechanical properties in comparison with the existing arc welding processes assumes significance. For setting up of the process parameters of A-TIG welding of 9Cr-1Mo steel, optimization of welding process parameters is required. Therefore, it becomes necessary to develop a convenient tool for optimizing the process parameters to achieve the target DOP in 9Cr-1Mo steel produced by A-TIG welding. It has been known that ferritic martensitic (FM) steels exhibit significant variations in microstructure and mechanical properties zone wise across its weld joint. Gradient in microstructure and mechanical properties have been reported to significantly influence the failure of structural components made from ferritic martensitic steels. Limited information is only available in the literature on the zone wise evaluation of mechanical properties of ferritic martensitic weld joints. Small specimen testing techniques like ABI and Impression creep testing have been found to be best suited for zone wise evaluation of strength and creep properties respectively. Therefore, zone wise evaluation of strength and creep properties using the above testing techniques and correlation with zone wise variations in microstructure is very important for 9Cr-1Mo steel weld joints.

CHAPTER 3

OBJECTIVES AND SCOPE

3.1 Objectives

- To study the effect of welding processes on the microstructure evolution, strength properties and creep behavior across the various zones of 9Cr-1Mo steel weld joint and also the residual stresses across the weld joints.
- To optimize the A-TIG welding process parameters using RSM and GA and compare their performances.
- To assess the residual stresses across the weld joint of 9Cr-1Mo steel to be fabricated by different welding processes using X-ray diffraction measurements
- To characterize the microstructural properties using optical, SEM and TEM across the various zones of 9Cr-1Mo steel weld joint fabricated by different welding processes.
- To evaluate the tensile and impact properties of weld joints fabricated by different welding processes using cross weld specimens and compare them.
- To evaluate the strength property across the various zones of 9Cr-1Mo steel weld joint fabricated by different welding processes using ABI technique.
- To evaluate of creep behavior across the various zones of 9Cr-1Mo steel weld joint fabricated by different welding processes using Impression creep testing technique.
- To compare the effect of welding processes on the microstructure and mechanical properties and recommend the best suited welding process for 9Cr-1Mo steel welding.

3.2 Scope

The scope of the present work is defined below to achieve the above mentioned objectives. Important considerations behind the definition of scope have also been outlined.

Material: 9Cr-1Mo steel is a promising candidate material for use in petro-chemical, chemical plants, thermal power plants and as nuclear fission reactor components. P9 steel is extensively used as steam generator and structural material in high temperature applications to improve the power plant efficiency. Most importantly 9Cr-1Mo steel is suitable for application as fuel element components, such as wrappers and also in the steam circuitry in the sodium-cooled fast breeder reactors. Hence the above steel is chosen for this study.

Welding Processes: Three arc welding processes, viz., SMAW, TIG welding and A-TIG welding processes were considered in the present study. Generally SMAW and TIG are the two processes which are extensively used in the fabrication of 9Cr-1Mo steel components. In order to improve the productivity, reduce the cost and fabrication time and improve the strength and creep properties, A-TIG welding process is proposed for welding of 9Cr-1Mo steel for the first time.

Optimization of A-TIG Welding: It is required to set up process parameters for A-TIG welding in order to achieve the required DOP during autogenous welding. The welding parameters Viz., current, torch travel speed, arc gap and electrode tip angle are required to be optimized. Optimization schemes such as DOE using RSM and GA are considered in this study. It is proposed to carry out optimisation of A-TIG welding process parameters for welding of 9Cr-1Mo steel using both the above schemes and compare their performance.

Residual Stress Measurements: Measurement of residual stress variation across the 9Cr-1Mo steel weld joints were considered using X-ray diffraction measurements. Effect of welding processes on the variation of residual stresses across the 9Cr-1Mo steel weld joints is proposed to be studied.

Mechanical Property Evaluation: Root Bend and side bend tests were considered for evaluating the integrity of the 9Cr-1Mo steel A-TIG weld joint. Microhardness measurements were considered across the various zones of the weld joints. Tensile tests at room temperature and impact toughness at room temperature and -40^{0}C were considered in cross weld specimens in the scope of mechanical property evaluation as these are the well known testing methods for evaluating the weld joints. Tensile and Impact tests were proposed to carried out on cross weld samples as per ASTM- E8 and ASTM-E23 respectively.

Microstructural Characterization: Zone wise microstructural characterization employing Optical, SEM, TEM were considered across the 9Cr-1Mo steel weld joints. The above microstructural studies were intended to examine the grain size, precipitates, dislocation substructure and correlate it with the zone wise variation in mechanical properties such as hardness, strength, impact toughness and creep of 9Cr-1Mo steel weld joints fabricated by various welding processes.

Zone wise evaluation of Strength Properties: ABI technique was considered for assessing the zone wise variation in strength properties such as YS, UTS, strain hardening exponent across the weld joints. However, good correlation between ABI testing and full scale tensile testing needs to be established first. It is proposed to assess the variation of strength properties across the various zones like weld metal, HAZ, ICHAZ and base metal in 9Cr-1Mo steel weld joints fabricated by various welding processes.

Zone wise evaluation of Creep behaviour using Impression creep testing: Zone wise evaluation of creep rates by impression creep testing was considered. Steady state impression velocities determined using impression creep testing will be converted into uniaxial creep rates using conversion factor and indenter diameter. Then using the uniaxial creep rates, it is proposed to determine activation energy for creep deformation zone wise employing Arrhenius equation for the 9Cr-1Mo steel weld joints fabricated by various welding processes.

CHAPTER 4

EXPERIMENTAL PROCEDURE

The experimental programme followed in this study is shown in the flow diagram (Fig 4.1). The Plain 9Cr-1Mo steel was chosen for this study. The chemical composition of the steel is given in Table 4.1. Three arc welding processes namely SMAW, TIG Welding and A-TIG welding have been employed for fabricating 9Cr-1Mo steel weld joints.

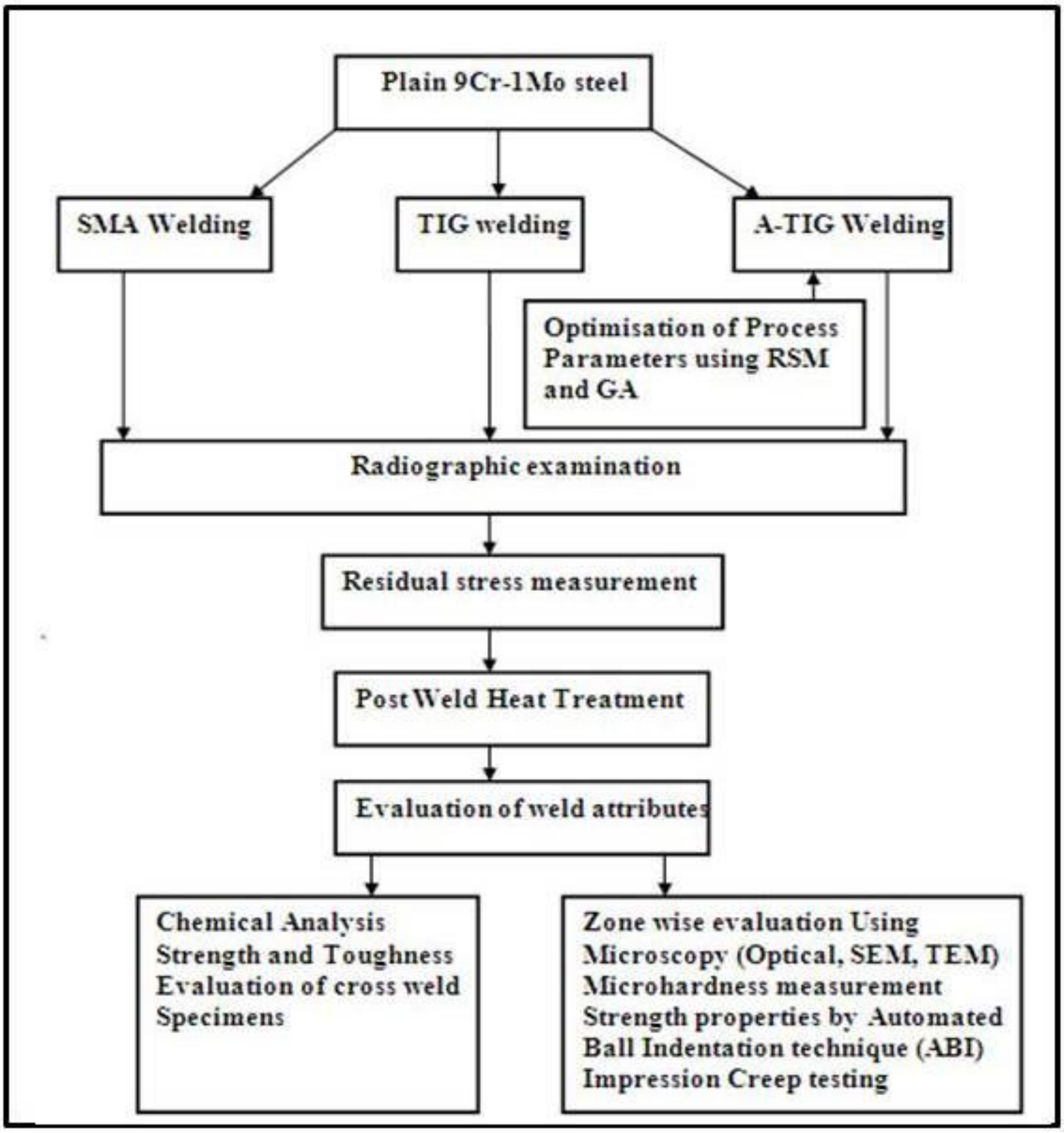

Fig.4.1 Flow Sheet of Experimental Scheme

Table 4.1 Chemical Composition of the 9Cr-1Mo Steel

Elements	Cr	Mo	C	Mn	Ni	Si	P	S
Base metal	9.1	0.94	0.102	0.46	0.1	0.50	0.009	< 0.01

SMA and TIG welding processes are carried out manually using welding consumables in multiple passes. A-TIG welding is an autogenous welding process whose process parameters need to be optimised prior to welding. Optimization was carried out employing RSM of DOE approach and GA.

4.1 Generation of Data for Correlating Process Parameters with Weld Bead Shape Parameters

The process variables which have important influence on the weld bead profile of A-TIG welds were defined. The process variables considered were welding current, travel speed, electrode tip angle and arc gap. First time electrode tip angle is included for the analysis as it is expected to influence the DOP. The four welding process parameters viz Current, Torch Speed, Tip angle and Arc Gap were considered over a predetermined range as shown in Table 4.2.

Table 4.2 Welding Process Parameters

SNo.	Process Parameters	Unit	Range
1	Current	A	100 to 300
2	Torch Speed	mm/min	630 to 180
3	Arc Gap	mm	1 to 3
4	Tip Angle	Degree	60-120

The multi component specific activated flux developed at IGCAR [171-173] is used for these experiments. The prepared mixtures of oxide powders were mixed with acetone and binder material to form a paste. The flux in the form of paste was manually applied on the joint surface using a brush prior to welding. A-TIG bead-on-plate welds are made with single pass on the 10mm thick 9Cr-1Mo steel plates.The welding was carried out using an automatic TIG welding machine (Fig 4.2) with a direct current electrode negative (DCEN) Lincoln electric power source (Model: Precision TIG 375).

Fig 4.2 Automated TIG Welding Machine

A 2% thoriated tungsten electrode of diameter 3.2 mm with and argon as shielding gas with a flow rate of 10 liters/min was used. The objective was to reduce the number of experiments and still determine the optimum process parameters. Therefore, DOE has been used to generate the design matrix. The range of process parameters has been defined based on our experience in using A-TIG welding process on different alloys. The experiments were carried out as per the design matrix generated by the Central Composite Design (CCD) methodology of RSM. The CCD are first order designs involving 2^N points where N is the number of variables augmented by additional central and 2 N axial points. In our case four input variables result in 2^4 i.e 16 base points with six central points and 2x4 i.e. 8 axial points. Therefore, totally 30 numbers of designs were generated and the same number of bead on plate welds were made (Fig. 4.3) to generate the data.

Table 4.3 Experimental Design Matrix and the Measured Responses

	Factor 1	Factor 2	Factor 3	Factor 4	Response 1	Response 2	Response 3
Run	A:Current	B:Travel Speed	C:Tip Angle	D:Arc Gap	DOP	Bead Width	HAZ width
	A	mm/min	Degree	mm	mm	mm	mm
1	150	75	67.5	1.5	4.241	7.191	1.72
2	200	90	105	2	4.298	8.243	1.831
3	250	75	67.5	1.5	4.337	9.422	2.244
4	200	90	105	2	4.303	7.379	1.928
5	250	75	142.5	2.5	5.277	9.263	2.286
6	250	105	142.5	2.5	4.771	8.764	2.097
7	100	90	105	2	1.913	3.724	1.539
8	250	105	67.5	2.5	5.139	9.766	2.034
9	300	90	105	2	6.13	11.45	2.577
10	250	105	67.5	1.5	5.342	9.114	1.954
11	200	60	105	2	4.433	7.432	2.029
12	200	90	30	2	4.387	8.761	1.901
13	150	75	67.5	2.5	3.637	7.165	1.985
14	150	105	142.5	2.5	2.776	5.519	1.732
15	250	105	142.5	1.5	4.527	7.604	1.852
16	150	105	67.5	2.5	3.392	6.649	1.95
17	200	90	105	3	4.131	9.714	1.936
18	150	75	142.5	1.5	3.17	5.358	1.663
19	200	90	105	2	4.467	7.449	1.724
20	200	90	105	1	4.309	6.673	1.62
21	200	90	180	2	4.094	7.642	1.753
22	150	105	142.5	1.5	2.807	5.435	1.492
23	200	90	105	2	4.237	7.96	1.95
24	150	105	67.5	1.5	3.111	6.267	1.675
25	200	120	105	2	4.139	7.492	1.703
26	250	75	67.5	2.5	5.399	11.502	2.605
27	250	75	142.5	1.5	4.966	8.877	2.5
28	200	90	105	2	4.128	7.615	1.62
29	200	90	105	2	4.355	7.567	1.75
30	150	75	142.5	2.5	3.329	6.696	1.785

Generated data will be used for developing regression models correlating process parameters with the weld bead shape parameters. Five number of A-TIG welds were made based on the determined optimum process parameters using RSM and GA approaches for validating the accuracy of the optimized process parameters in achieving the target weld bead shape parameters.

Fig. 4.3 Weld Bead Profiles of Experimental Runs

The welded samples were cut in the transverse direction, polished and etched using vilela's reagent (1 g picric acid, 5ml Hcl and 95 ml ethanol).The weld bead shape parameters such as DOP, weld bead width and HAZ width were measured using an optical microscope. The process variables and the responses were entered in to the statistical software Design Expert v7 for analysis. The design matrix with the measured response values are given in Table 4.3.

4.2 Fabrication of Weld Joints

The work pieces of 9Cr-1Mo steel (P9) in normalized and tempered (760^0C for 2 h) condition was used for the current study. The plates were machined to 250 mm x 125 mm x 10 mm thick rectangular dimensions. The surfaces of the two weld plates were cleaned with acetone to remove surface contaminations. The joint configuration used for A-TIG welding was closed square butt joint and for TIG and SMAW process were V groove joint which are shown in Fig. 4.4 (a, b) respectively. The schematic of A-TIG weld specimen is shown in Fig. 4.4(c). For carrying out A-TIG welding, the flux ingredients were mixed in the right proportion and made in to a paste form by using acetone as solvent. Activated flux in the form of paste was applied on the surface of the joint using paint brush before the welding. The thickness of the flux coating was in the range of 15–20 μm. A-TIG welding was carried out on 10 mm thick plates using double side welding technique.

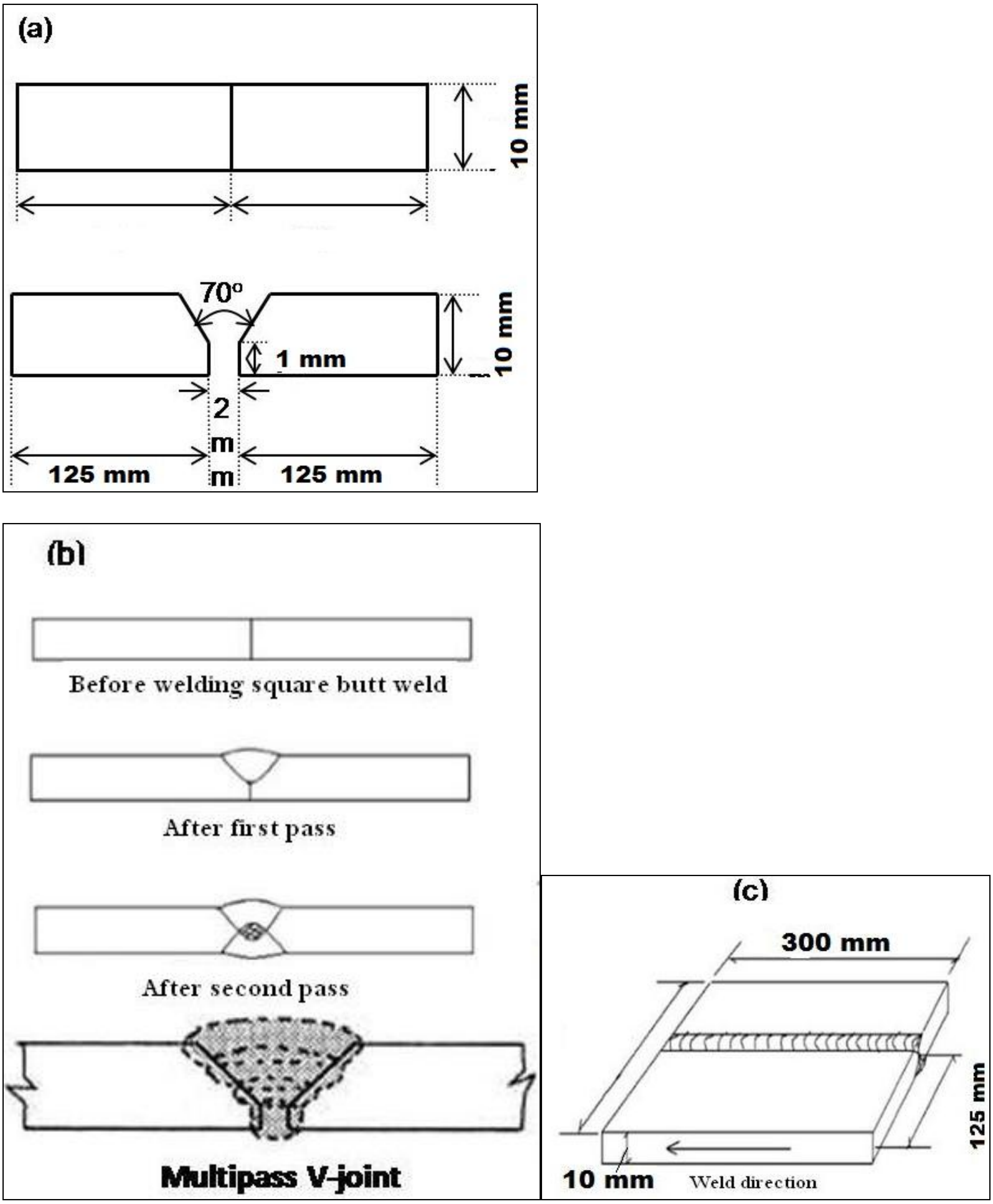

Fig. 4.4 Weld Joints (a) Square and V Edge Preparation (b) Square-Double Pass and V-Multi Pass (c) Welded Specimen (schematic)

Table 4.4 Welding Parameters Used for all the Processes

Welding Process	Current (A)	Voltage (V)	Torch speed (mm/min)	Shielding gas (Argon L/min)	Electrode Dia/Angle (mm/deg)	Arc gap (mm)	Heat Input per pass (kJ/mm)	No of Passes
SMAW root pass	100	12.3	83	---	3.15	-	0.89	1
SMAW remaining passes	130	13.5	96	---	3.15	-	1.1	7
TIG root pass	92	13	38	10	2.4 / 60°	-	1.89	1
TIG remaining passes	140	14	36	10	2.4 / 60°	-	3.27	12
A-TIG	270	17.4	120	10	45°	1.0	2.35	2

The welding parameters used for SMAW, TIG and A-TIG welding are given in Table 4.4. SMAW weld joint was made using E9018-B9 electrodes in 13 passes. TIG weld joint was made using ER 80 S B8 filler wire in 13 passes. The photographs of the weld joints fabricated by all the three process are shown in Fig. 4.5.In all the three welding processes the joints were preheated to a temperature of 250^{0}C before welding. In multi pass welding (TIG & SMAW) the inter pass temperature was maintained at 250^{0}C.


a)
23 7 2014
1b) TIG
b)
15 7 2014

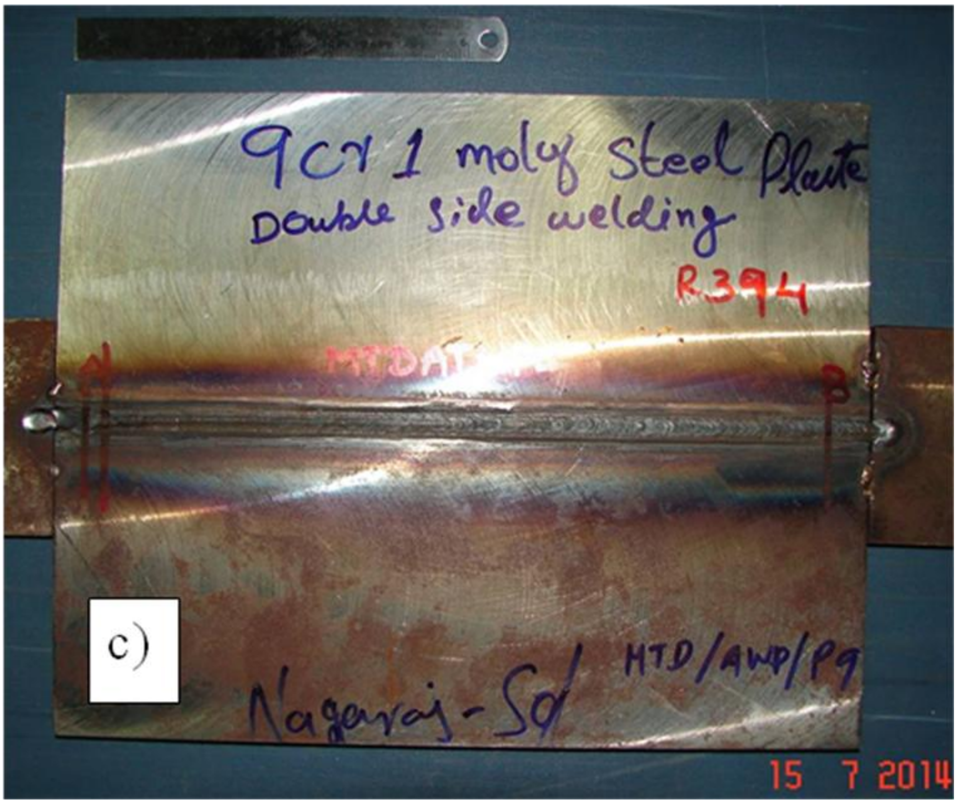

Fig.4.5 Photograph of Weld Joints Fabricated by (a) SMAW (b) TIG (c) A-TIG Welding Processes

4.3 Residual stress measurement

Residual stress measurements were carried out using XRD technique. Residual stress was measured using RIGAKU STRESS ANALYZER model MSF-2M with back reflection type goneometer. The parameters used for residual stress measurements are given in Table 4.5

Table 4.5 Experimental Parameters Setup for Residual Stress Measurements

Operating Voltage	30 kV
Current	7 mA
X-ray radiation	Chromium K_{α}
Wavelength	2.2896 Å
ψ range	0° to 45°
2θ range	148°-163°
Step Width	0.2°
Dwell Time	3 s
Aperture	2×4 mm
Filter	Vanadium
Soller slit	1 °
Plane	(211)

4.4 Radiography

All the weld joints were subjected to X-Ray Radiographic examinations for ensuring the soundness of the welds. ASME Section III class I specification was followed during the examination.

4.5 Bend Test

To check the integrity of autogenous A-TIG weld joints, bend tests were carried out. Root and side bend test was carried out as per the ASTM E190 procedure. Dye Penetrant test was carried out to check for cracks after test.

4.6 Chemical Analysis

Chemical analysis results of the weld metals of the three 9Cr-1Mo steel weld joints are given in the Table 4.6.

Table 4.6 Chemical Composition of the Weld Metals in wt%

Elements	Cr	Mo	C	Mn	Si	P	S	O
SMAW weld	9.2	1.0	0.099	0.459	0.359	0.02	0.019	0.09
TIG weld	9.15	1.11	0.108	0.494	0.394	0.008	0.010	0.04
A-TIG weld	9.01	1.18	0.122	0.468	0.468	0.002	0.011	0.05

4.7 Post Weld Heat Treatment

The defect free weld joints were subjected to PWHT of 760^{0}C for a soaking temperature of 2 hours. Fig. 4.6 gives the PWHT procedure followed. The heating rate was controlled at 200^{0}C per hour and air cooling after the soaking time was followed.

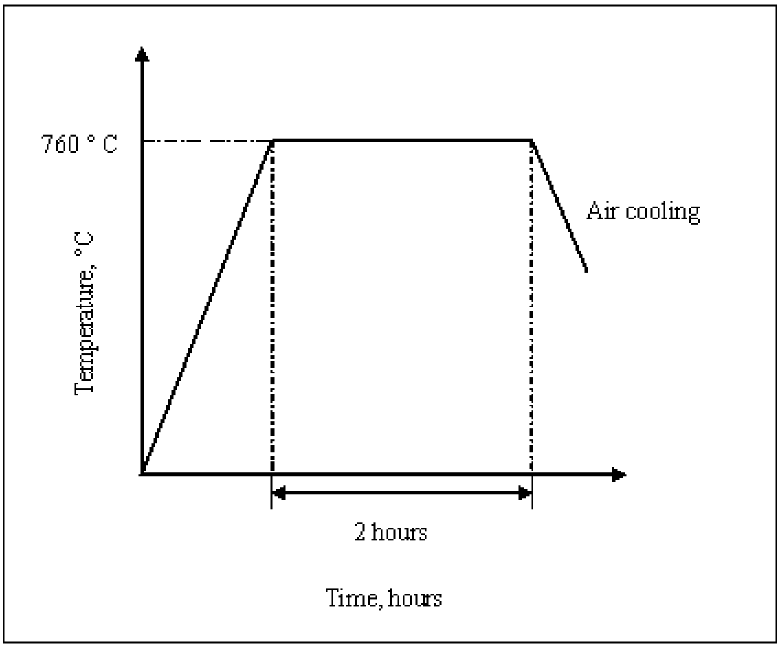

Fig. 4.6 PWHT Procedure

4.8 Microscopy

The weld joints were sectioned transversely mechanically polished from 80,220,320, 400,600,800 and 1000 grit SiC paper followed by 3 and 1 μm diamond paste to obtain mirror finish on the surface. Then the samples were etched with villela's reagent (1 g picric acid, 5 ml HCl acid and 95 ml ethanol) for microstructural investigations. This procedure was carried out for both as welded and PWHT samples.

Optical Microstructure images of the weld joints were taken using OLYMPUS GX51 microscope. Grain size measurement was carried out using the built in measurement software in OLYMPUS microscope. First the magnification used in the microscope is set in the software. Snapshot of the micrograph is taken; measurement bar appears in the bottom left side. Line tool is selected from the measurement bar and two lines were drawn intersecting each other perpendicularly inside the grain touching the boundary. After drawing the lines the length and width of the grains appears automatically in µm. The same procedure is repeated for all the grains in the snapshot. The average grain size is obtained directly and reported.

SEM images was taken using CAM SCAN 3200 LaB6 Filament gun model microscope.Thin foils from the heat-treated samples were prepared by cutting 1 mm thickness sample using diamond cutter followed by mechanical thinning (various size of grit papers and diamond paste) and punching out 3 mm dia area of the region to be investigated. Further thinning up to 6 to 8 micron thickness was carried out using STRUERS TENUPOL electrolytic polishing machine. The solution used was 20% perchloric acid and 80% methanol mixer and the temperature maintained at -35^{0}C and 17 Volts during the thinning and creating a hole for TEM examination. The TEM images were taken using LIBRA 200 FE high resolution TEM. This microscope is 200KV field emission gun type with a info limitation of 0.13 nm.

4.9 Mechanical Properties Measurement

Vickers micro hardness (HV) measurements were carried out across the weld joint using BOWERS make W423DAT model micro vickers tester. The range of the tester is 0.1 to 1 kgf. The test was carried out at 500 g load and 15 seconds dwell time.

Tensile test measurement was carried out using HUNGTA make 2402 model screw driven tensile tester machine. The maximum capacity of the machine is 100 kN. The strain rate was kept at 3 x 10^{-4} S^{-1}. YS and tensile strength of base metal and weld joints were evaluated using cylindrical tensile specimen as per ASTM standard E8 at room temperature. The typical cylindrical small specimen used for this test is shown in Fig. 4.7. Two specimens each were tested in all cases and average values were reported.

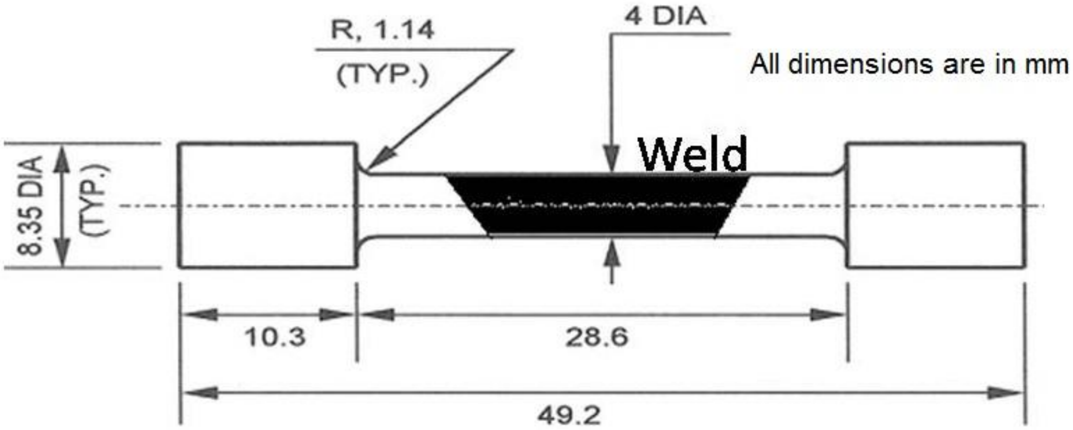

Fig. 4.7 Schematic Diagram of Tensile Test Specimen

Impact toughness was measured TINIUS OLSEN make 358J capacity make Charpy impact testing machine. Charpy V-notch impact test was carried out at room temperature and at -40° C on full size (55 mm x 10 mm x 10 mm) (Fig 4.8) transverse specimen with a notch orientation such that the crack propagates in the weld metal along the welding direction. The test was carried out as per ASTM E23 standard. Two specimens each were tested in all cases and average values were reported. The fractographs of the fractured surfaces were characterized using SEM and analyzed for identifying the mode of fracture.

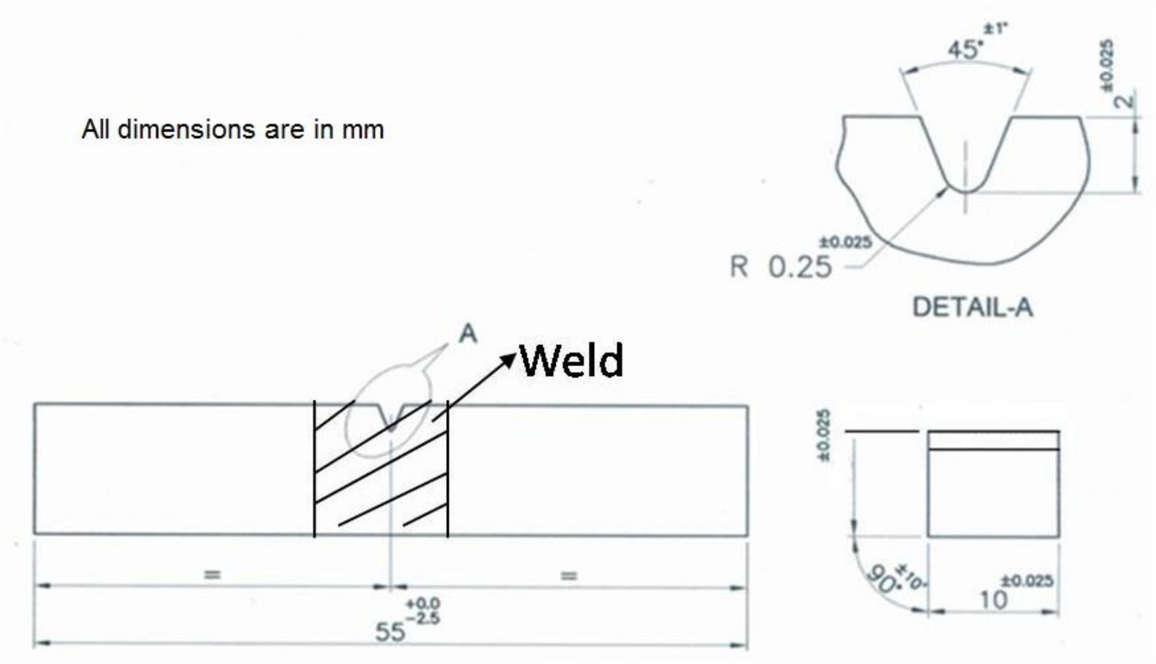

Fig 4.8 Schematic Diagram of V-Notch Charpy Impact Test Specimen

4.10 Strength Property Measurement by ABI Test

The metallographic samples from all the three weld joints were prepared (Polished and etched) and used for the ABI tests. The stress strain microprobe (SSM) system based on ABI technique [146,174] was employed for these tests. The testing machine was made by Advanced Technology corporation (ATC) USA and the model is B4000 (Fig. 4.9).In that system ABI tests can be conducted using tungsten carbide spherical indenters of various diameters such as 0.25, 0.51, 0.76 and 1.57 mm. Considering the approximate size of HAZ formed in the investigated weld joints and to avoid overlapping of different zones in a test, tungsten carbide indenter of diameter 0.25 mm was used for all the tests. The indenter, swivel mount for holding specimen, linear variable differential transformer (LVDT), etc. used for performing ABI test is shown in Fig. 4.9. The penetration depth of the spherical indenter into the test surface is measured with a displacement transducer such as a spring-loaded LVDT.

The force required to indent the material to increased depth values is measured with a force transducer such as a load cell. The various parameters used in ABI tests are given in Table4.7

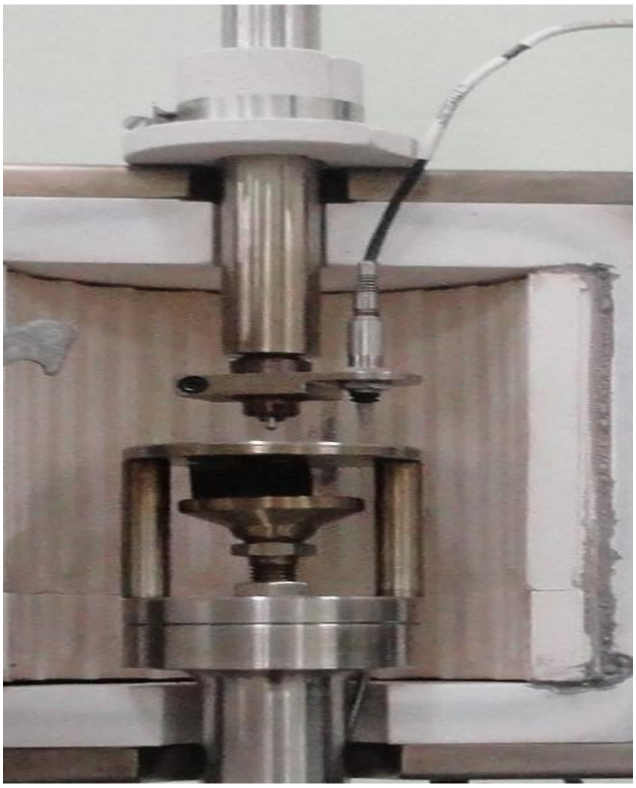

Fig. 4.9 Indenter and Specimen Fixture Assembly of ABI Testing Machine

ABI tests were conducted across various zones of 9Cr-1Mo steel weld joint fabricated by A-TIG, SMAW and TIG processes at room temperature. Two tests were conducted on each zone of the weld joint to check consistency in results and the extent of scatter. In case of large scatter between those tests, third test was conducted and out of the pair of tests showing closer values (within 5% variation) one set of results was taken for further analysis. The data acquisition system connected to the computer records the load and depth of indentation for further processing.

Table 4.7 ABI Parameters

Atmosphere	Air
Indenter Young`s modulus (GPa)	635GPa
Sample Young`s modulus (GPa)	210 GPa
Indenter radius used (%)	24%
Unload (% of max. load)	40 %
Number of cycles	7
Pre-load (N)	13.3
Indenter speed (mm/sec)	0.008

The typical ABI tested specimen and typical impression image are shown in Fig. 4.10 (a,b)

a)

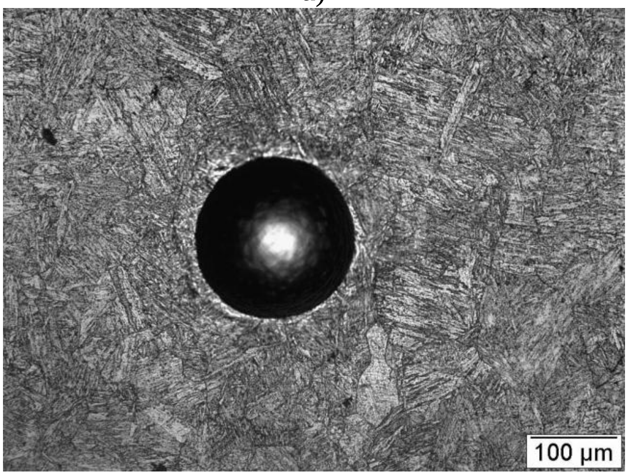

b)

Fig. 4.10 a) Typical ABI Tested Specimen b) Typical Optical Image of the Impression

4.11 Creep property Measurement by Impression Creep Test

Rectangular strips of approximately 30 x 20x 10 mm thick section were cut from all the three weld joints. The samples were prepared (Polished and etched) and used for the impression creep tests. The impression creep testing surfaces of the specimens were polished up to 1 μm diamond finish. Care was taken to maintain the parallelism of the surfaces while polishing the surface manually. The Impression creep testing machine (SPRANKTRONICS make 100 Kg capacity) is shown in Fig. 4.11. The vacuum chamber is maintained at 10^{-6}mbar pressure during the test. The Fig. 4.12 shows the typical impression creep test specimen employed in the present investigation.

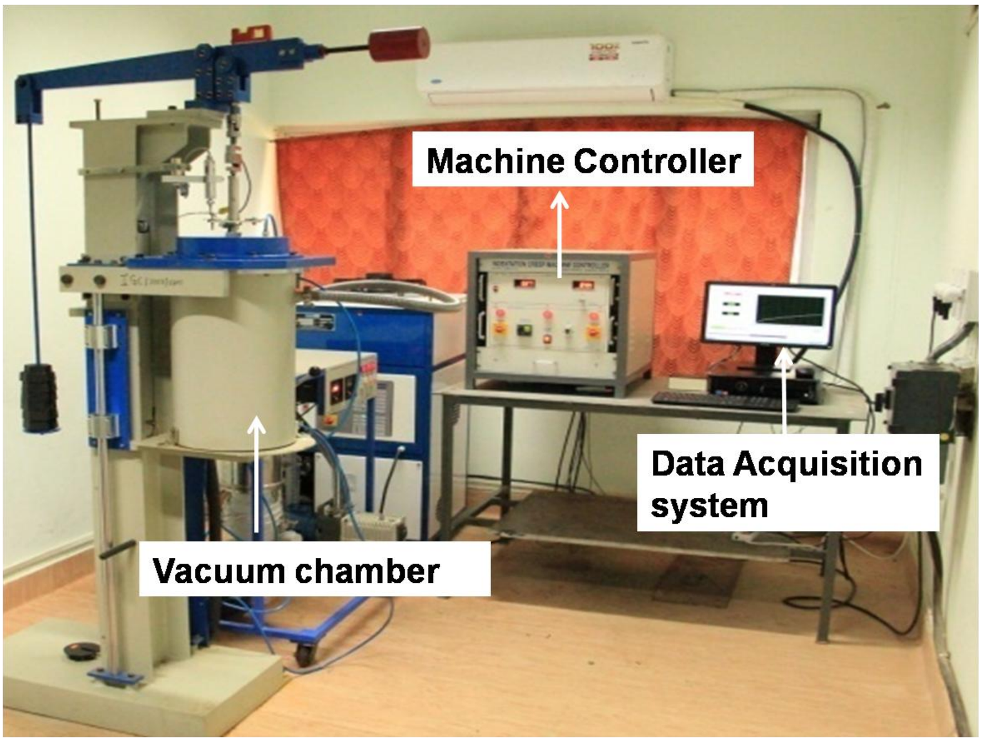

Fig. 4.11 Photograph of the Impression Creep Testing Machine

Fig.4.12 Typical Impression Creep Tested Specimen

The sample was loaded in the sample holder of the vacuum chamber with furnace for heating the specimen. The tests were carried out at 3 different temperatures (848 K, 873 K, 898 K). Once the required vacuum is obtained ($\simeq 5x10^{-6}$mbar) constant punching stress applied on the specimen (102 – 321 MPa). The time Vs indentation depth is recorded in the computer through the data acquisition system.

Post impression test, the specimens were cut as shown in the Fig. 4.13 for optical micro structural evaluation.

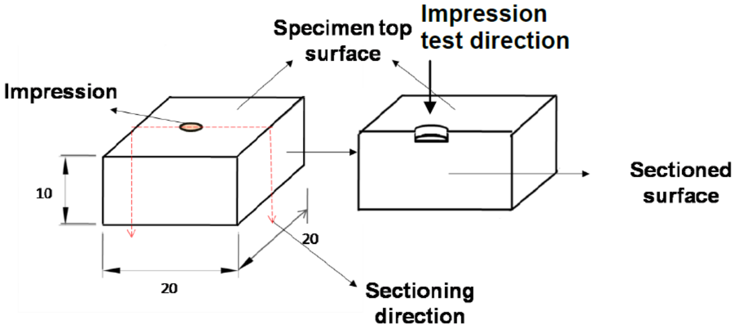

Fig. 4.13 Schematic Illustration of Sectioning the Tested Specimen for Cross-Sectional Optical Microstructural Analysis.

CHAPTER 5

RESULTS AND DISCUSSION

The results obtained from the optimization and experimental studies on the 9Cr-1Mo steel weld joints are presented and discussed in detail in four different sections.

In section 5.1, the optimization of A-TIG welding of 9Cr-1Mo steel using RSM and GA and their performance comparison in terms of optimized process parameters is presented and discussed. The effect of various welding processes on the macrostructure, microstructure, mechanical properties and residual stresses of the 9Cr-1Mo steel weld joints is discussed in detail by correlating microstructural variations with that of the mechanical properties of the cross weld specimens. Effect of welding processes on the residual stresses of the 9Cr-1Mo steel weld joints is also discussed in section 5.2. In section 5.3, zone wise evaluation of strength properties using ABI across the 9Cr-1Mo steel weld joints is presented and discussed in detail. Zone wise evaluation of creep behavior of 9Cr-1Mo steel weld joints using impression creep testing and the determination of activation energy for creep on various zones of the weld joints and the mechanism of creep is discussed in section 5.4.

5.1 Optimization of A-TIG Welding Process Parameters for 9Cr-1Mo Steel

5.1.1 Response Surface Methodology

RSM is one of the most extensively used methods for welding process parameter optimization. RSM is defined to build up the relationship between the controllable input welding process parameters and the desired responses. It is employed here because it requires a minimum number of experimental runs when compared with other methodologies. The analysis will provide information about the interaction between various welding process parameters and how it affects the output responses. The response can be viewed as three-dimensional response surface plots. The most popular design methodology within RSM designs is the CCD. CCDs are factorial designs augmented by the additional center and axial points to allow estimation of the tuning parameters of a model. In the present work, CCD method of RSM has been used to determine the optimum A-TIG welding process parameters to achieve the desired DOP and HAZ width. Bead on plate welding experiments were carried out as per the design matrix suggested by CCD of RSM. Numerical and graphical optimization is performed using RSM to obtain the desired DOP and HAZ width using desirability approach.

5.1.1.1 Development of Mathematical Model

Design expert v7 software is used for the analysis. The adequacy of the model is tested using the sequential F-test, lack of the fit test and the analysis of the variance (ANOVA) technique to obtain the best fit model. RSM has been applied for developing the mathematical relationships between the factors and the responses for determining the desired factors which give optimum weld bead dimensions. In applying the RSM, the independent variables are viewed as a surface to which a mathematical model is fitted. A second order polynomial expression as given in equation (5.1) is used to represent the response surface ‘Y’

$$Y = C + c_1 X_1 + c_2 X_2 + c_3 X_1^2 + c_4 X_2^2 + c_5 X_1 X_2 \qquad (5.1)$$

Whereas C is the intercept representing the arithmetic averages of all the quantitative outcomes of all runs; c_1 to c_5 are coefficients. The terms $X_1 X_2$ and x_i^2 (i = 1 and 2) represent the interaction and quadratic terms respectively. It is a general equation describing the relation between the process variables and the responses for a two variable case.

5.1.1.2 Development of Mathematical Model for DOP using RSM

ANOVA is applied for estimating the significance of the model at 95% significance level. The objective of ANOVA is to investigate whether the A-TIG welding process parameters and the interaction of these parameters have significant effects on the weld bead geometry and to recognize whether the model developed is significant. The ANOVA for DOP is shown in Table 5.1. The associated p-value < 0.05 for the model (95% confidence level) indicates that the model terms are statistically significant. The significance test of regression model and the lack of fit test are carried out by design expert software. The lack of fit value of 0.0704 implies that it is not significant. The adequacy measures adj. R^2 is close to 1, as it is desirable, which shows the adequacy of the model. The analysis shows that the value of adequate precision is 28.475, which represents the signal to noise ratio and is greater than 4 which indicates the adequate model discrimination.

Current (A), Travel speed (B), Tip angle (C) and Arc gap (D), the interaction factors of C and D, are favoured to be the significant model terms. The R-squared is 0.9772 and The Predicted "R" squared of 0.8741 is in reasonable agreement with adjusted "*R*" Squared of 0.9558. The interaction effect of current with arc gap is more compared to the interaction effect of current with travel speed and travel speed with arc gap. The final regression model derived in terms of process variables for DOP is given below.

$$DOP = + 4.54233 + 0.023325 * x1 - 0.040043 * x2 - 0.015615 * x3 - 0.85258 * x4 + 7.17097E\text{-}005 * x1 * x2 - 1.74409E\text{-}006 * x1 * x3 + 9.46292E\text{-}004 * x1 * x4 + 8.13692E\text{-}005 * x2 * x3 + 4.27903E\text{-}003 * x2 * x4 + 5.16608E\text{-}003 * x3 * x4 - 2.92837E\text{-}005 * x2^2 - 3.14855E\text{-}005 * x3^2 - 3.00469E\text{-}005 * x3^2 - 0.094337 * x4^2 \quad (5.2)$$

Where x1 is current, x2 is torch speed, x3 is tip angle and x4 is arc gap.

Using the above equation, the DOP values were predicted and compared with that of the actual DOP values as shown in Fig. 5.1. There was good agreement between the two values. The above model equation (5.2) will be used in the desirability analysis for carrying out multi-objective optimization.

Analysis of variance (ANOVA) is a collection of statistical models used to analyze the differences among group means and their associated procedures (such as "variation" among and between groups). In the ANOVA setting, the observed variance in a particular variable is partitioned into components attributable to different sources of variation. In its simplest form, ANOVAs are useful for comparing (testing) three or more means (groups or variables) for statistical significance.

Degree of freedom (DF) is the number of values in the final calculation of a statistics that are free to alter. The number of independent ways by which a dynamic system can move, without disrupting any restraint imposed on it, is called a number of degrees of freedom. The common rule for any set is that if n equals the number of values in the set, the degrees of freedom equal to n – 1.

According to ANOVA analysis the process variables welding current, travel speed, arc gap and tip angle have significant effects on DOP. The interaction effect of the process parameters is discussed below. When an interaction effect between any two process parameters is being examined the other parameters will be on their centre level.

Table 5.1 ANOVA Analysis for the DOP

	Sum of		Mean		p-value	
Source	Squares	DF	Square	F-Value	F	Source
Model	24.69	14	1.76	45.83	<0.0001	Significant
Current (A)	21.67	1	21.67	563.10	<0.0001	Significant
Travel speed (B)	1.02	1	1.02	26.38	<0.0001	Significant
Tip Angle (C)	0.84	1	0.84	21.73	0.0003	Significant
Arc gap (D)	0.071	1	0.071	1.84	0.1947	
Current-Travel speed	0.044	1	0.044	1.15	0.3006	
Current- Tip angle	2.15E-004	1	2.15E-004	5.597E-003	0.9414	
Current-Arc gap	8.559E-003	1	8.559E-003	0.22	0.6440	
Travel speed- Tip angle	0.042	1	0.042	1.10	0.3116	
Travel speed-Arc gap	0.016	1	0.016	0.41	0.5320	
Tip angle-Arc gap	0.19	1	0.19	4.91	0.0426	Significant
Current^2	0.15	1	0.15	3.85	0.0685	
Travel speed^2	1.38E-003	1	1.38E-003	0.036	0.8519	
Tip Angle^2	0.050	1	0.050	1.31	0.2705	
Arc gap^2	0.015	1	0.015	0.40	0.5367	

Residual	0.58	15	0.038			
Lack of Fit	0.51	10	0.051	3.98	0.0704	Not significant
Pure Error	0.064	5	0.013			
Cor Total	25.27	29				

Std. Dev.	0.20	R-Squared	0.9772
Mean	4.21	Adj R-Squared	0.9558
C.V. %	4.66	Pred R-Squared	0.8741
PRESS	3.18	Adeq Precision	28.475

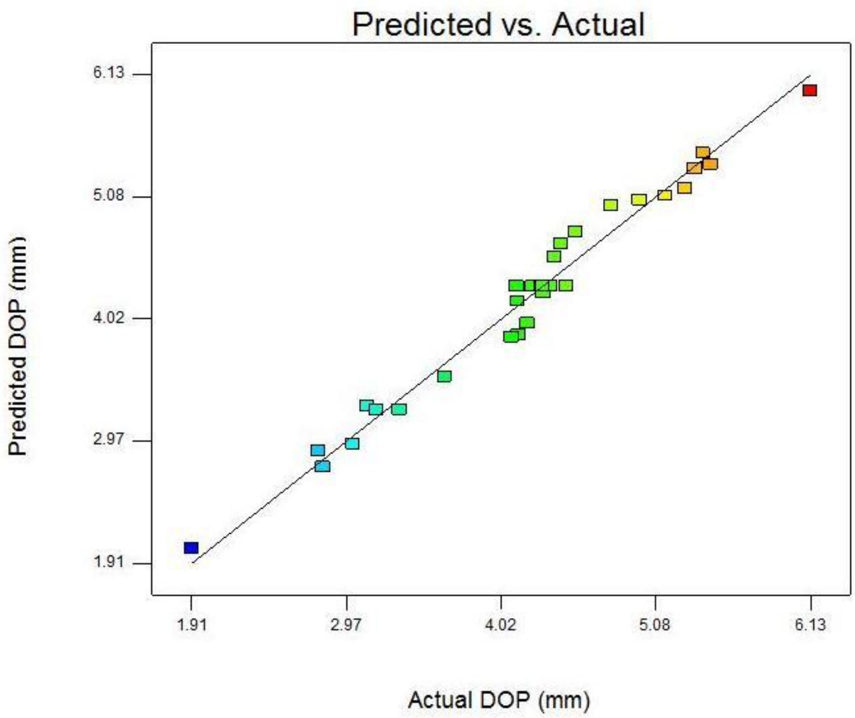

Fig. 5.1 Comparison of Predicted and Actual DOP

5.1.1.3 Interaction Effect of Process Parameters on DOP

The interaction effect of the current, travel speed, tip angle and arc gap on DOP are shown in Fig. 5.2 (a-d).

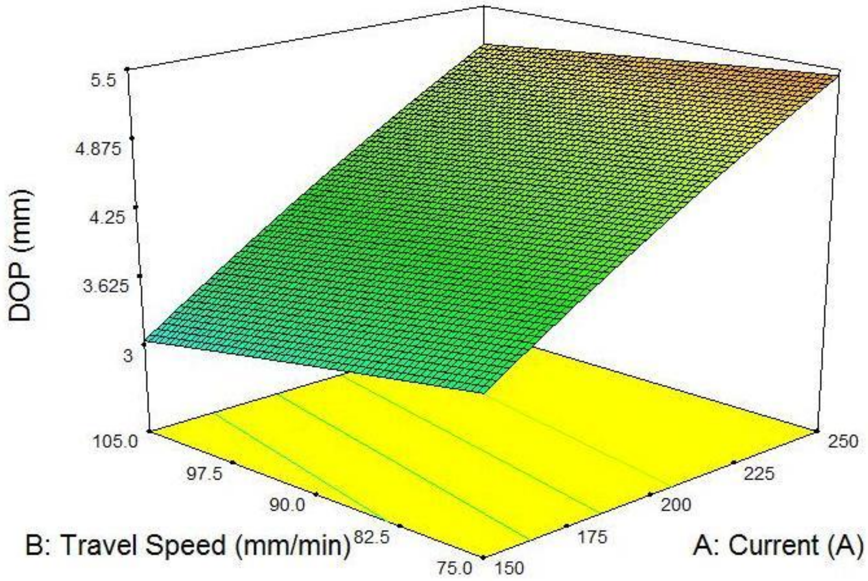

Fig. 5.2a. Interaction Effect of Travel Speed & Current on DOP

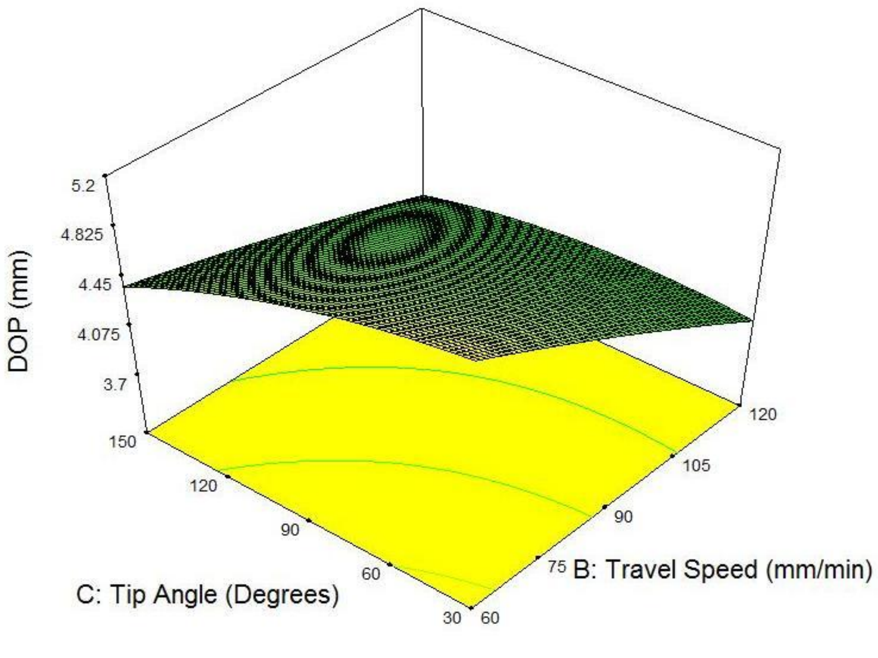

Fig. 5.2b. Interaction Effect of Travel Speed & Tip Angle on DOP

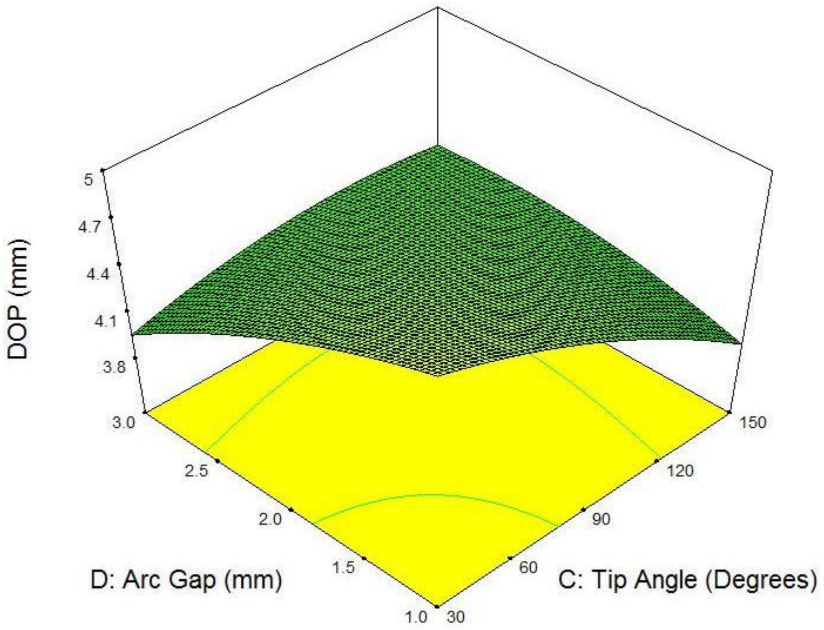

Fig. 5.2c. Interaction Effect of Arc Gap and Tip Angle on DOP

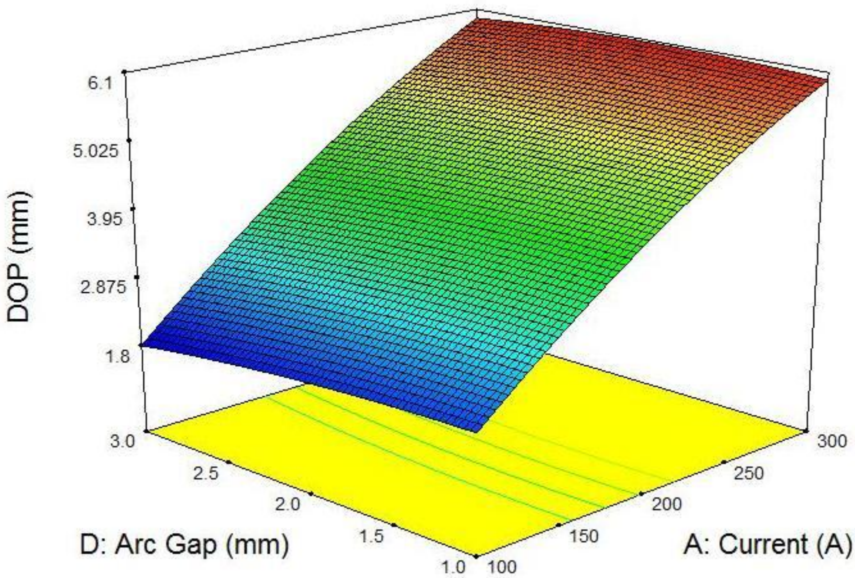

Fig. 5.2d. Interaction Effect of Arc Gap and Current on DOP

It is clear from the plots that higher current, lower travel speed, lower arc gap and lower tip angle results in maximum DOP during A-TIG welding of 9Cr-1Mo steel.

5.1.1.4 Development of Mathematical Model for HAZ Width using RSM

The ANOVA for HAZ width is shown in Table 5.2. The associated p-value < 0.05 for the model (95% confidence level) indicates that the model terms are statistically significant. The significance test of regression model and the lack of fit test are carried out by design expert software. The lack of fit value of 0.0692 implies that it is not significant. The adequacy measures adj. R^2 is close to 1, as it is desirable, which shows the adequacy of the model. The analysis of the ANOVA shows that the value of adequate precision is 13.315, which represents the signal to noise ratio and is greater than 4 which indicates the adequate model discrimination. In the present analysis Current (A) and Tip angle (C), the interaction factors of Tip angle and arc gap CD, are favored to be the significant model terms. The R-squared is 0.9188 and The Predicted "R" squared of 0.6835 is in reasonable agreement with adjusted "*R*" Squared of 0.8430. The final regression model derived in terms of process variables for HAZ is given in equation 5.3.

Table 5.2 ANOVA Analysis for the HAZ Width

	Sum of		Mean		p-value	
Source	Squares	DF	Square	F-Value	F	Source
Model	2.23	14	0.16	12.12	<0.0001	Significant
Current (A)	1.21	1	1.21	92.40	<0.0001	Significant
Travel speed (B)	0.28	1	0.28	21.58	0.0003	
Tip Angle (C)	0.062	1	0.062	4.75	0.0457	Significant
Arc gap (D)	0.16	1	0.16	12.19	0.0033	Significant
Current-Travel speed	0.12	1	0.12	9.37	0.0079	Significant
Current- Tip angle	0.011	1	0.011	0.85	0.3710	
Current-Arc gap	0.013	1	0.013	1.01	0.3315	
Travel speed- Tip angle	6.111E-004	1	6.111E-004	0.047	0.8320	
Travel speed-Arc gap	7.159E-003	1	7.159E-003	0.55	0.4713	
Tip angle-Arc gap	0.010	1	0.010	0.78	0.3916	Significant
$Current^2$	0.17	1	0.17	12.69	0.0028	
Travel $speed^2$	0.024	1	0.024	1.84	0.1947	
Tip $Angle^2$	0.015	1	0.015	1.14	0.3034	
Arc gap^2	1.579E-003	1	1.579E-003	0.12	0.7334	
Residual	0.20	15	0.013			

Lack of Fit	0.12	10	0.012	0.72	0.6920	Not significant
Pure Error	0.081	5	0.016			
Cor Total	2.42	29				

Std. Dev.	0.11	R-Squared	0.9188
Mean	1.91	Adj R-Squared	0.8430
C.V. %	5.98	Pred R-Squared	0.6835
PRESS	0.77	Adeq Precision	13.315

$$HAZ = +1.94967 +4.05638E\text{-}003 * x1 - 0.014072 * x2 -5.68211E\text{-}003*x3 +0.15042*x4 - 1.19515E\text{-}004 * x1*x2 +1.25504E\text{-}005*x1*x3 -1.17546E\text{-}003*x1*x4 +9.79248E\text{-}006*x2*x3+2.88486E\text{-}003*x2*x4 - 1.20027E\text{-}003*x3*x4 +3.10221E\text{-}005*x1^2 + 1.31357E\text{-}004* x2^2 +1.63376E\text{-}005 * x3^2 +0.030221 *x4^2 \quad (5.3)$$

Where x1 is current, x2 is torch speed, x3 is tip angle and x4 is arc gap.

Using the above equation, the HAZ width values are predicted and compared with that of the actual values as shown in Fig. 5.3. There is good agreement between the predicted and actual values. The equation (5.3) will be used in the desirability analysis for carrying out multi-objective optimization.

According to ANOVA analysis the factors welding current, travel speed, arc gap and tip angle have significant effects on HAZ width. The interaction effect of the process parameters is discussed below. When an interaction effect between any two process parameters is being examined the other parameters will be on their centre level.

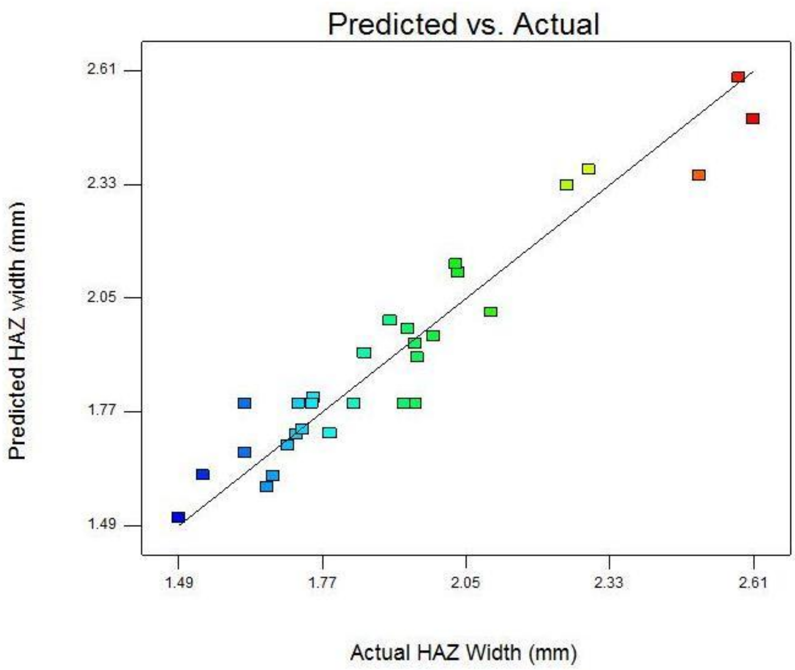

Fig. 5.3 Comparison of Predicted and Actual HAZ Width

5.1.1.5 Interaction Effect of Process Parameters on HAZ Width

The interaction effect of the current, travel speed, tip angle and arc gap on HAZ width are shown in Fig. 5.4(a-d). It is clear from the plots that during A-TIG welding process lower current, lower arc gap, higher speed and higher tip angle result in decreasing HAZ width.

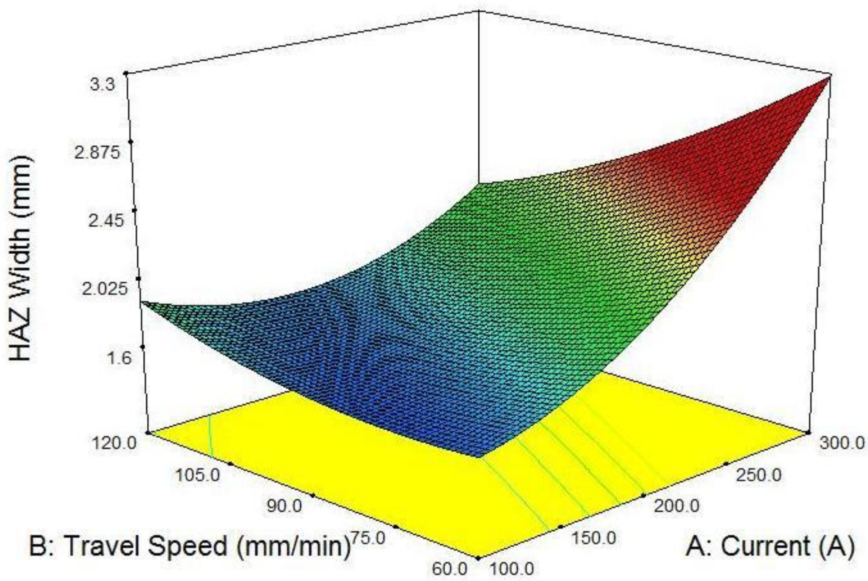

Fig. 5.4a. Interaction Effect of Travel Speed & Current on HAZ

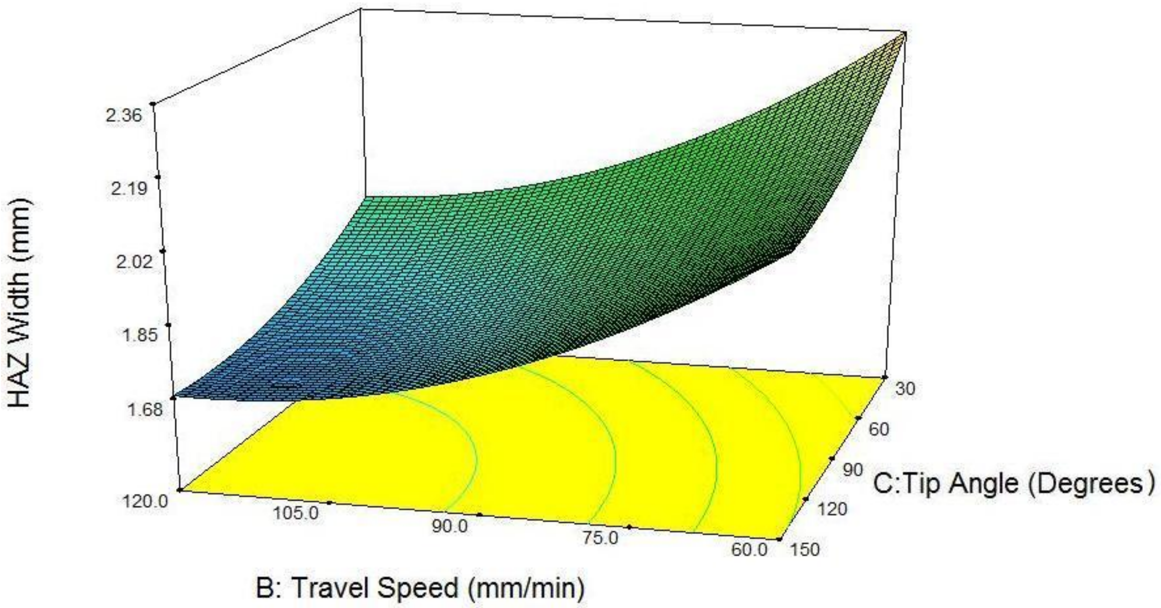

Fig. 5.4b. Interaction Effect of Travel Speed & Tip Angle on HAZ

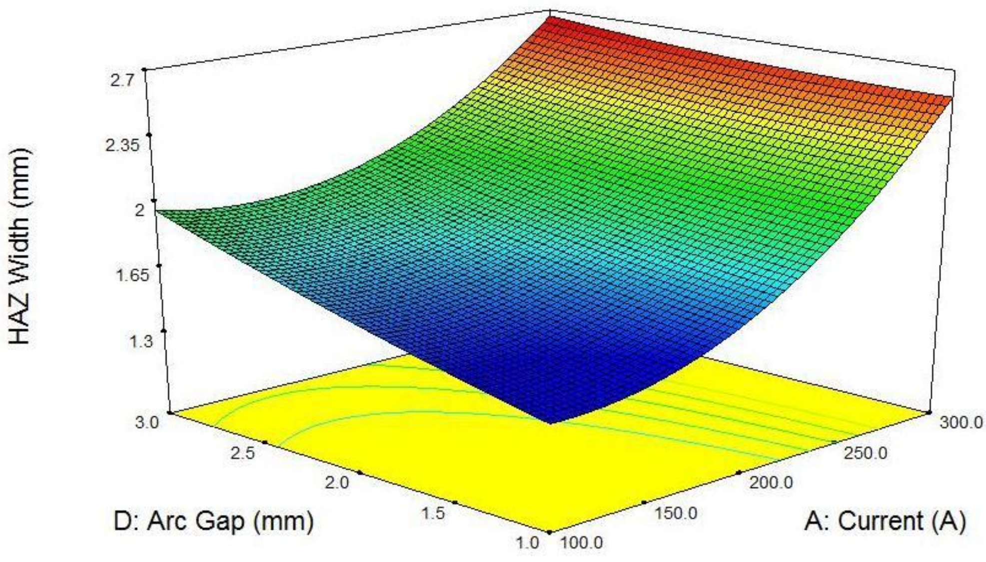

Fig. 5.4c. Interaction Effect of Arc Gap & Current on HAZ

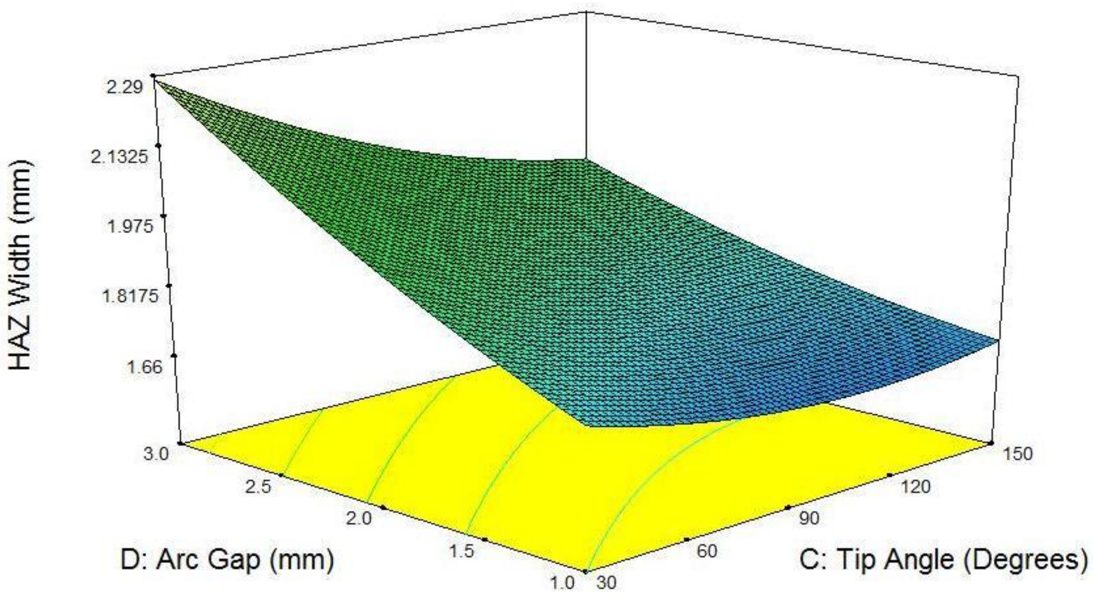

Fig. 5.4d. Interaction Effect of Arc Gap & Tip Angle on HAZ

5.1.1.6 Optimization using RSM

During A-TIG welding of 9Cr-1Mo steel, the main objective was to achieve the desired DOP and HAZ width. As there are two responses to be optimized, the problem becomes a multi-objective optimization. In the present case, the desired DOP is set as 6 mm and the desired HAZ width is set as 2 mm. Simultaneous study of multiple responses requires first building an appropriate response surface model for each response and then trying to find a set of optimized operating condition; which optimizes all responses or at least keeps them in desired ranges. Solving multiple response optimization problems utilizing this approach starts with using a method for combining multiple responses into a dimensionless measure of performance called the Overall Desirability Function, D = (d1.d2….dm)1/m where m is the number of the responses.

The higher value of D is more desirable and greatest functions of the system, which is recognized as the optimal solution. The optimum values of factors are identified from the value of desirable individual functions (d) that maximizes the Overall Desirability Objective

Function (D). Optimization of welding process parameters in design expert software determines for a combination of factor levels or ranges that concurrently satisfy essential optimization criteria on each one of the response and process parameters. In desirability function approach Optimization, the value of each response for a given combination of controllable factors is first translated to a number between zero and one known as individual desirability. Individual desirability functions are different for different objective types which might be Maximization, Minimization or Target. In this study desirability type used is target type (DOP = 6 mm, HAZ = 2 mm). Optimization criteria used in this study is shown in Table 5.3.

Table. 5.3 Optimization Criteria Used in the Study

Process Parameters	Goal	Lower Limit	Upper Limit	Lower Weight	Upper Weight	Importance
Current	is in range	150	300	1	1	3
Travel Speed	is in range	60	120	1	1	3
Tip Angle	is in range	60	160	1	1	3
Arc Gap	is in range	1	3	1	1	3
DOP	is target = 6	1.62	6.13	0.1	1	5
Bead Width	is in range	3.724	11.502	1	1	1
HAZ	is target = 2	1.492	2.5	1	0.1	5

Optimal solutions were generated based on the above criteria.

Table 5.4 gives the optimal solutions given by RSM. In the multi objective optimization (Target DOP is 6mm and Target HAZ width is 2 mm) the RSM provides best possible 52 solutions. In single objective optimization the desirability will be always one. However, in multi objective optimization, some solutions exhibit the desirability value less than one. However, while finalizing the optimum process parameters for achieving the target DOP and HAZ width, we consider the solutions with desirability value one only. From the optimal solutions (Table 5.4), only first 24 solutions exhibit desirability values of one. Optimum parameters are taken from the first 24 solutions only.

Table 5.4 Optimal solutions obtained by RSM

Number	Current	Travel Speed	Tip Angle	Arc Gap	DOP	Bead Width	HAZ Width	Desirability
1	299.98	118.41	60.00	1.00	5.92	9.51	2.00	1.00
2	300.00	118.65	61.06	1.03	5.92	9.48	2.00	1.00
3	299.98	119.58	60.01	1.14	5.91	9.46	2.00	1.00
4	299.71	118.41	64.69	1.02	5.90	9.43	2.00	1.00
5	299.39	120.00	63.00	1.21	5.89	9.39	2.00	1.00
6	296.48	118.09	60.00	1.18	5.88	9.50	2.00	1.00
7	297.64	119.99	60.01	1.30	5.87	9.43	2.00	1.00
8	299.98	119.92	68.58	1.17	5.87	9.31	2.00	1.00
9	300.00	118.50	70.67	1.00	5.87	9.33	2.00	1.00
10	300.00	119.91	61.14	1.22	5.90	9.44	2.01	1.00
11	299.99	119.95	76.13	1.16	5.83	9.19	2.00	1.00
12	299.23	120.00	79.01	1.21	5.81	9.14	2.00	1.00
13	279.42	107.64	60.00	1.00	5.79	9.74	2.00	1.00
14	293.09	119.99	62.76	1.51	5.79	9.38	2.00	1.00
15	292.66	120.00	60.25	1.52	5.79	9.41	2.00	1.00
16	291.09	120.00	60.01	1.58	5.76	9.41	2.00	1.00
17	275.84	105.55	60.04	1.00	5.78	9.77	2.00	1.00
18	268.46	102.03	60.01	1.00	5.72	9.77	2.00	1.00
19	269.15	102.30	60.00	1.00	5.73	9.77	2.00	1.00
20	291.96	120.00	95.63	1.59	5.67	8.98	2.00	1.00
21	289.56	117.52	91.67	1.50	5.67	9.07	2.00	1.00
22	291.90	120.00	60.00	1.65	5.77	9.47	2.02	1.00
23	255.58	95.99	60.11	1.00	5.62	9.71	2.00	1.00
24	251.16	93.28	60.06	1.00	5.61	9.70	2.00	1.00
25	295.57	114.88	82.29	1.00	5.79	9.29	2.02	0.99
26	247.34	91.29	60.00	1.00	5.58	9.67	2.00	0.99
27	281.01	120.00	60.01	1.90	5.56	9.38	2.00	0.99

28	288.97	120.00	113.30	1.67	5.56	8.79	2.00	0.99
29	241.72	88.58	60.00	1.00	5.54	9.60	2.00	0.99
30	289.70	120.00	120.90	1.55	5.51	8.62	2.00	0.99
31	230.03	82.09	60.04	1.04	5.46	9.45	2.00	0.99
32	273.08	117.69	60.00	2.00	5.45	9.42	2.00	0.99
33	233.69	84.17	66.82	1.00	5.44	9.35	2.00	0.99
34	226.84	81.26	60.01	1.00	5.44	9.36	2.00	0.99
35	227.14	81.21	62.07	1.00	5.43	9.33	2.00	0.99
36	224.44	80.16	60.01	1.01	5.42	9.32	2.00	0.99
37	274.62	119.99	131.90	2.25	5.36	8.95	2.00	0.99
38	211.14	73.50	60.00	1.00	5.33	9.01	2.00	0.99
39	270.70	120.00	134.32	2.38	5.31	9.03	2.00	0.99
40	208.71	72.47	60.00	1.00	5.31	8.94	2.00	0.99
41	274.20	120.00	151.22	2.14	5.26	8.67	2.00	0.99
42	265.37	120.00	61.72	2.25	5.23	9.27	2.00	0.99
43	265.96	119.99	159.99	2.42	5.16	8.85	2.00	0.99
44	256.55	119.95	160.00	2.72	5.06	9.13	2.00	0.99
45	188.48	61.55	67.82	1.00	5.11	8.11	2.01	0.99
46	279.77	119.06	160.00	1.45	5.04	7.99	2.00	0.99
47	198.41	65.34	89.86	1.00	5.00	7.99	2.00	0.99
48	221.49	77.14	118.98	1.00	4.85	8.02	2.00	0.98
49	242.97	99.78	159.94	2.35	4.83	8.88	2.00	0.98
50	214.40	73.28	119.33	1.00	4.78	7.82	2.00	0.98
51	201.91	71.43	159.99	2.40	4.39	7.93	2.00	0.98
52	193.61	120.00	99.46	3.00	3.68	7.91	2.00	0.96

In order to represent the results in simple way, graphical optimization was carried out which provided results in the form of overlay contour plots. The overlay plots allow quick visual inspection of the area of feasible response values in the process variables space to choose the optimum process parameter combination. The bright areas on the overlay plots in Fig. 5.5 are the regions that meet the proposed criteria. Therefore, the operating window in terms of the current and the torch speed to achieve the target DOP and HAZ width is identified as the yellow region in the overlay plot.

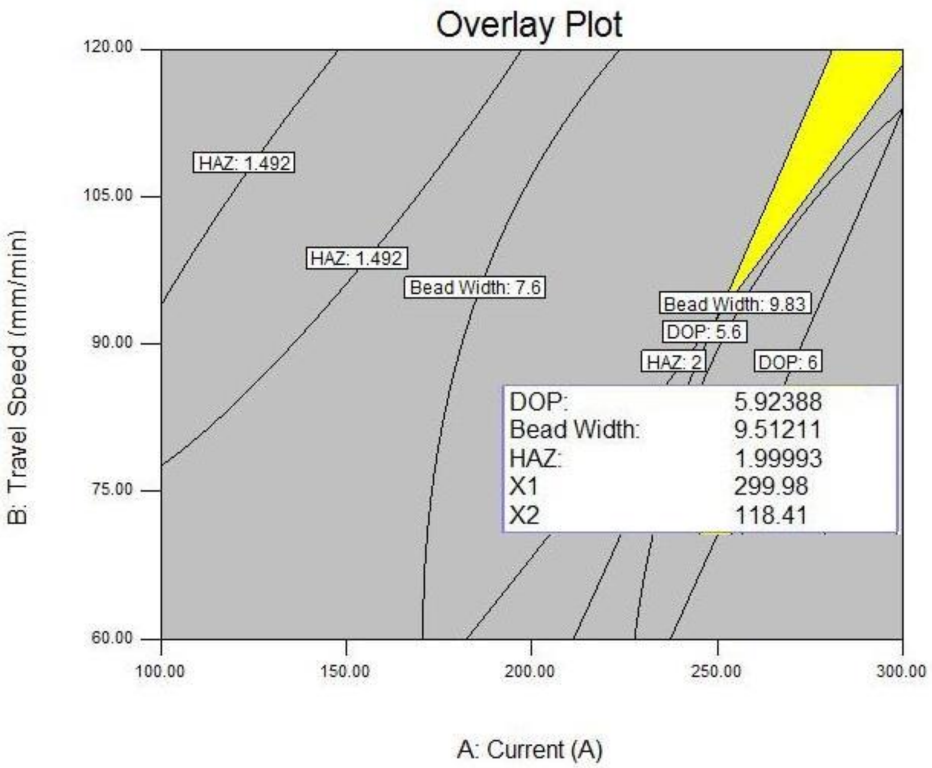

Fig. 5.5 Overlay Plot

5.1.2 Genetic Algorithm

GA is a family of computational techniques inspired by natural evolution process and is an efficient technique for optimisation [175,176] of welding process parameters. It is a random search process and employs random selection to direct the search through parametric space. It is based on the mechanics of natural selection and natural genetics. It is an iterative optimization procedure and it is a global optimization technique proposed by Holland in 70's and developed later by Goldberg. The beginning step of GAs involves representation of individuals for solution of the problem and is composed of a string of genes. The strings are created either in binary or real format. The solutions are evaluated based on an objective function and are then assigned a fitness value. Once the proper representation has been finalised for individuals, then initial population is created randomly. The size of the population is the number of individuals which are created by population. Then each individual is evaluated for its suitability against the objective function with highest rank of fitness. Then the individuals are selected from the current population for reproduction. Selection of individuals is based on their fitness value. The higher the fitness value the higher the probability of that individual being selected for reproduction. The selected individuals are then subjected to crossover and mutation operators to produce off springs which form the new population. The above described steps are carried out in an iterative procedure till the optimum solutions are determined. Optimization of the welding process for obtaining the desired DOP and HAZ width involves more than one objective function and hence the task of finding optimal solutions involve multi-objective optimization.

5.1.2.1 Development of Model by GA

The various functions (Initialization, Selection, Crossover, Reproduction and Mutation) of GA code were developed in Matlab software package to determine the optimum welding process parameters in order to achieve the desired DOP and HAZ width during A-TIG welding of 9Cr-1Mo steel. To achieve the desired DOP and HAZ width during A-TIG welding of 9Cr-1Mo steel plates, an objective function given in equation 5.4 is defined. The chosen objective function should facilitate convergence of solutions. Therefore, least square method is adopted as objective function for error minimization as in equation (5.4).

$$\mathrm{ObjV} = ([\mathrm{DOPT}-\mathrm{DOP}\,(i)]^2 / [\mathrm{DOPT}] + [\mathrm{HAZT}-\mathrm{HAZ}\,(i)]^2 / [\mathrm{HAZT}]) \qquad (5.4)$$

Where ObjV: Objective function

DOPT: Target values of DOP

DOP: Depth of penetration value of the i^{th} individual

HAZT: Target values of heat affected zone width

HAZ: Width of heat affected zone value of the i^{th} individual

Multiple regression models for correlating DOP and HAZ width with the process variables have been developed and are used to compute DOP and HAZ width individuals in the above equation. The equation 5.5 defines the DOP as s function of process variables and their interactions. Equation (5.5) has been used in equation (5.4) for calculating the DOP values as a function of process parameters. Similarly equation (5.6) defines the HAZ width as a function of process parameters and their interactions. Equation (5.6) has been used for calculating the HAZ width in equation (5.4).

$$DOP = 4.54233+0.02333*x1 + (-2.93E-05)*x1^2 + (-0.04004)*x2 + (-3.15E-05)*x2^2 + (-0.01562)*x3 + (-3.00E-05)*x3^2 + (-0.85258)*x4 + (-0.09434)*x4^2 + 7.17E-05*x1*x2 + (-1.74E-06)*x1*x3 + 9.46E-04*x1*x4 + 8.14E-05*x2*x3 + 0.00428*x2*x4 + 0.00517*x3*x4 \quad (5.5)$$

$$HAZ = 1.94967+0.00406*x1 + 3.10E-05*x1^2 + (-0.01407)*x2 + (1.31E-04)*x2^2 + (-0.00568)*x3 + 1.63E-05*x3^2 + 0.15042*x4 + 0.03022*x4^2 + (-1.20E-04)*x1*x2 + 1.26E-05*x1*x3 + (-0.00118)*x1*x4 + 9.79E-06*x2*x3 + 0.00288*x2*x4 + (-0.0012)*x3*x4 \quad (5.6)$$

Where x1 is current, x2 is torch speed, x3 is tip angle and x4 is arc gap.

Even though the objective function is minimized, the GA code is written for maximising the solution. Hence, the suitable fitness values are assigned to each solution for each iteration such that lower the value of objective function correspond to higher fitness value for that solution. The solutions are chosen based on their fitness index value.

5.1.2.2 Selection of GA Parameters

The fast convergence of GA depends on the best selection of GA parameters i.e. size of population, number of generations, selection of cross over type and rate and mutation rate. To achieve best optimum parameters, a trial and error method was adopted to execute the GA by varying the population size from 50 to120, number of generations from 80 to 200, crossover rate from 0.5 to 0.95 and mutation rate from 0.001 to 0.1. The GA parameters which provided optimum solutions are given in Table 5.5. The selection operator is also varied by employing roulette wheel selection and tournament selection.

5.1.2.3 Execution of GA Code

The ranges of input variables (welding current, travel speed, tip angle and arc gap) were specified as an input to the GA code. During the first iteration, the initial population was chosen randomly and each individual represented one set of process variables. The member of each individual was encoded with 16 bit binary string and the total length of the individual is (4x16) 64 bits. In one case, the roulette wheel selection is used to select the individuals in population, and parents are selected based on their fitness index value. Then multipoint crossover method is adopted with a crossover probability of 0.65 as it supports fast convergence. In multipoint crossover, crossover position and number of variables of individuals are selected randomly without duplicates and sorted in ascending manner. The variables between successive crossover points are exchanged between the two parents to generate new offspring. In another case, tournament selection is used with single point cross over. In GA tournament selection is most popular selection method due to its efficiency and simple implementation. In this tournament selection, number of individuals is selected randomly from the population and the selected individuals compete against each other. The individual with highest fitness wins and will be carried forward as one of the next generation population. It is found that during the case of tournament selection, the solutions exhibited a better convergence. After crossover, mutation operation was carried out on the offspring with a mutation probability value of 0.001. The off springs are sorted as per rank of fitness index value. The newly selected 100 chromosomes were reinserted for the next iteration. The iterative procedure continues till it reached the convergence criteria. The desired value for DOP was set as 6 mm and HAZ width was set as 2 mm. For each iteration, the GA code generates different set of process parameter to achieve the same target DOP and HAZ width values. Therefore, GA provided a number of solutions in terms of process parameters for achieving the target DOP and HAZ width in 9Cr-1Mo steel. The parameters given in Table 5.5 are the GA parameters identified to achieve the target DOP and HAZ width specified in the present work.

5.1.2.4 Validation of the Optimized Solutions by RSM and GA

Both the RSM and GA provided a number of solutions in terms of process parameters for achieving the target DOP and HAZ width during A-TIG welding of 9Cr-1Mo steel. In order to validate the solutions provided by RSM and GA, 5 solutions were randomly chosen for each method. For RSM method, all the 5 chosen solutions are not the optimized solutions as two of the solutions exhibited desirability values less than one. Therefore, the two solutions included in the validation experiments for RSM are not the optimized process parameters. For validation experiments, in order to ensure that it covers the entire range of solution, randomly pickup desired number of solutions from the generated 52 solutions by RSM were chosen. Validation experiments are performed to check and compare both RSM and GA models. The solutions were in the form of process parameters. Bead on plate weld experiments were carried out on the recommended process parameters. The metallographic samples were prepared and polished and etched to measure the DOP and HAZ width values. The measured response variable values and the corresponding process parameter values are given in Table 5.6 to Table 5.8 for RSM and GA based models with roulette wheel selection and tournament selection strategies respectively. RMS error is determined for comparing the performance of the RSM and GA based models. To achieve the target DOP and HAZ width, GA based model employing tournament selection strategy is found to be more accurate for optimizing the A-TIG welding process parameters. This is also in agreement with the literature report that tournament selection outperformed the roulette wheel selection process [177].

The process parameters determined are very realistic in terms of their values. In the industries A-TIG welding is carried out in the identified range of process parameters only for achieving the target DOP and HAZ width. Therefore, the optimized parameters determined by GA can be successfully employed in the fabrication industries for achieving the DOP required for good overlap during double side welding of 10 mm thick plates of plain 9Cr-1Mo steel.

Table 5.5 Best GA Parameters Chosen for Optimizing the Welding Process Parameters Generated by GA

Parameters	Roulette Wheel Selection Strategy	Tournament Selection Strategy
No. of variables	4	4
Size of population	100	100
No. of generations	100	100
Crossover rate	0.65	0.65
Crossover type	Multi point (two point)	Single point
Mutation rate	0.001	0.001
Type of selection	roulette wheel	Tournament selection
Individual chromosome size in bits	16	16

Table 5.6 Results of Validation Experiments for RSM Method

Current A	Travel speed mm/min	Tip Angle Degree	Arc gap, mm	DOP Target mm	Actual DOP measured, mm	RMS Error	HAZ Target mm	Actual HAZ measured mm	RMS error
300	118	60	1	6	6	1.005	2	2.367	0.6109
256	96	60	1	6	5.898		2	2.64	
230	82	60	1	6	5.579		2	2.424	
198	65	90	1	6	4.491		2	2.542	
202	71	160	2.4	6	4.391		2	2.921	

Table 5.7 Results of Validation Experiment for GA with Roulette Wheel Selection

Current A	Travel speed, mm/min	Tip Angle Degree	Arc Gap, mm	DOP Target mm	Actual DOP measured, mm	RMS error	HAZ Target, mm	Actual HAZ measured, mm	RMS error
268	114	60	1	6	5.329	0.5856	2	2.678	0.6895
240	100	60	1	6	5.192		2	2.433	
270	117	60	1	6	6		2	2.589	
276	120	30	1	6	5.219		2	3.032	
256	99	60	1	6	5.96		2	2.564	

Table 5.8 Results of Validation Experiment for GA with Tournament Selection

Current A	Travel speed, mm/min	Tip Angle Degree	Arc Gap, mm	DOP Target, mm	Actual DOP measured, mm	RMS error	HAZ Target, mm	Actual HAZ measured, mm	RMS error
265	110	60	1	6	5.645	0.5504	2	2.658	0.5916
258	102	60	1	6	5.794		2	2.101	
269	113	45	1	6	5.814		2	2.428	
275	120	45	1.2	6	5.049		2	3.013	
266	111	60	1	6	5.362		2	2.312	

5.1.3 Summary

Optimization has been carried out employing RSM and GA based models employing different selection operators involving roulette wheel selection and tournament selection. During the analysis based on DOE second order quadratic models have been developed correlating process and the response variables to predict the DOP and HAZ width as a function of process variables. Using RSM methodology, current is identified as the most significant process variable influencing the DOP and HAZ width during A-TIG welding of 9Cr-1Mo steel. Both RSM and GA based models provided number of solutions in terms of process parameters to achieve the target DOP and HAZ width. However, GA based model employing tournament selection operator is found to the accurate model based on validation experiments. Optimum A-TIG welding process parameters have been successfully determined in order to achieve the target DOP and HAZ width for 9Cr-1Mo steel.

5.2 Microstructure Examinations, Mechanical Properties Evaluation on Cross Weld Specimens and Assessment of Residual Stresses on 9Cr-1Mo Steel Weld Joints

9Cr-1Mo steel plates of 10 mm thick have been fabricated by three different welding processes. Depending on the welding process employed and the heat input, the number of passes required to complete the weld joint varied. The microstructure evolution, mechanical properties of the weld joints and the residual stresses generated in the weld joints all depend on the type of welding process, filler metal used, number of passes and the welding process parameters employed. It is therefore necessary to characterize the weld metal composition, study in detail evolution of microstructures, evaluate the tensile and impact toughness of cross weld specimens and measure the residual stresses of the 9Cr-1Mo steel weld joints.

5.2.1 Bend Test on A-TIG weld joint

A-TIG welding being an autogenous process for welding 10 mm thick plates of 9Cr-1Mo steel, it is desired to check the integrity the weld joint by bend test. Dye penetrant test was carried out on the bend tested specimens. After the test, no crack or defects are noticed on the surfaces of the bend tested samples. This observation confirms that the integrity of the A-TIG weld joint is good (Fig. 5.6).

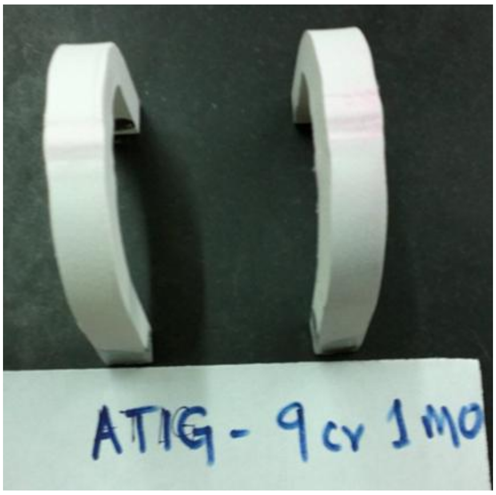

Fig. 5.6 Photograph of Bend Tested Cross Weld Specimen

5.2.2 Macrostructure

The cross sections of the weld samples of SMA, TIG and A-TIG weld joints are shown in Fig. 5.7 (a-c) respectively. Weld metal and HAZ regions are clearly visible in the macrographs. A clear overlap between top and bottom pass can be seen in A-TIG macrostructure. The weld metal and HAZ regions are wider in SMA weld joint and narrower in A-TIG weld joint.

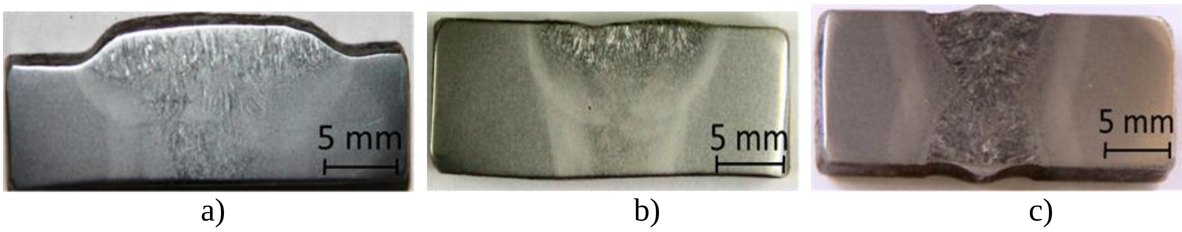

Fig. 5.7 Macrostructures of a) SMA, b) TIG c) A-TIG Steel Weld Joints

5.2.3 Chemical and Oxygen Analysis

Chemical analysis of the weld metal produced by SMAW, TIG and A-TIG welding process are given in Table 4.6. The chemical analysis of the weld metal was carried out by Radio frequency glow discharge optical emission spectrometer. The oxygen content in the weld metals were determined by inert gas fusion method. It is observed that the chemical composition of weld metal is slightly varied with the base metal composition. In general, the chemical analysis reported may have some scatter. In addition to that, the minor variation in the composition of SMAW and TIG welds could be due to filler wire addition. In case of A-TIG weld, there is no filler addition and the chemical composition difference could be due to vaporization losses during welding. The Carbon content in A-TIG weld is higher than that of the other joints and the oxygen content is higher in SMA weld than that of the other weld joints.

5.2.4 Microstructural Evaluation

Fig. 5.8(a) shows the optical micrograph of base steel exhibiting tempered martensite and

Fig. 5.8(b), shows the SEM microstructure exhibiting stable precipitates along the prior austenite grain boundaries formed during normalizing and tempering. Prior Austenite grain boundaries (PAGB) are clearly visible in the microstructure. Fig. 5.8(c) shows TEM microstructure of P9 steel base metal showing lath boundaries and precipitates.TEM images of P9 base metal clearly shows lath martensite structure. Fine carbide precipitates were seen along the lath boundaries. In the normalized and tempered condition, the precipitates are visible along and within the laths as shown in Fig. 5.8(c). The lath width varies from 700 to 1000 nm. Fig. 5.9(a-c) shows the microstructure of SMAW weld, coarse and fine HAZ in PWHT condition. PWHT microstructure reveals tempered martensitic microstructural features and carbide precipitates. Grain size of weld metal was 110 – 115 μm (± 20μm), coarse HAZ was 55- 60 μm (± 10 μm) and fine HAZ was 24- 28 μm (± 10μm). Fig. 5.10(a-c) shows the microstructure of TIG weld joint in PWHT condition. In PWHT condition weld and HAZ regions showed tempered martensitic microstructure. Grain size of weld metal was 90 – 100 μm (± 20μm), coarse HAZ was 50- 55 μm (± 10 μm) and fine HAZ was 24- 27 μm (± 10μm). The difference between A-TIG and TIG weld joint is that the prior austenitic grains are coarser in A-TIG weld joint. Microstructures of the weld metal, coarse and fine HAZ of the weld joint produced by A-TIG welding process in PWHT condition are shown in Fig. 5.11(a-c). The weld joints produced by A-TIG welding process exhibited tempered martensitic microstructure in PWHT condition. The average grain size of weld metal in PWHT condition was 90 – 115 μm (± 20 μm) , coarse HAZ was 50- 55 μm (± 10 μm) and fine HAZ was 23- 27 μm (± 10 μm) was measured in optical microscope. The measured average grain size values of all 3 weld joints are given in Table 5.9.

Table 5.9 Measured Average Grain Size of Various Zones and Length of Zones of 9Cr-1Mo Steel Weld Joints

	Base metal (µm)	ICHAZ (µm)	Fine HAZ (µm)	Coarse HAZ (µm)	Weld (µm)	Weld width (mm)	HAZ width (mm)
SMA Weld joint	11	13	24	58	113	20	5
TIG weld joint	11	14	26	53	91	15	3
A-TIG weld joint	11	12	25	53	100	10	2.7

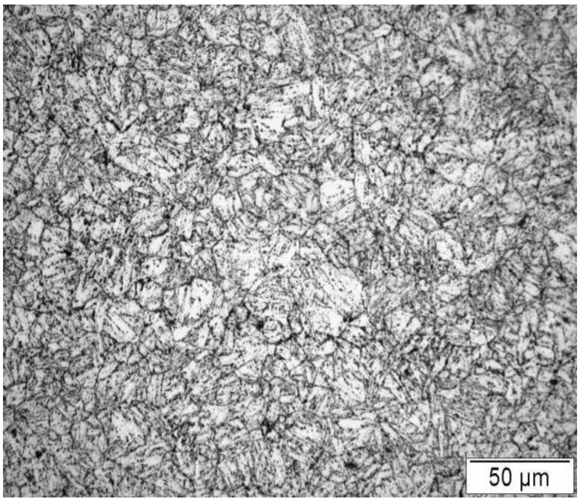

a)

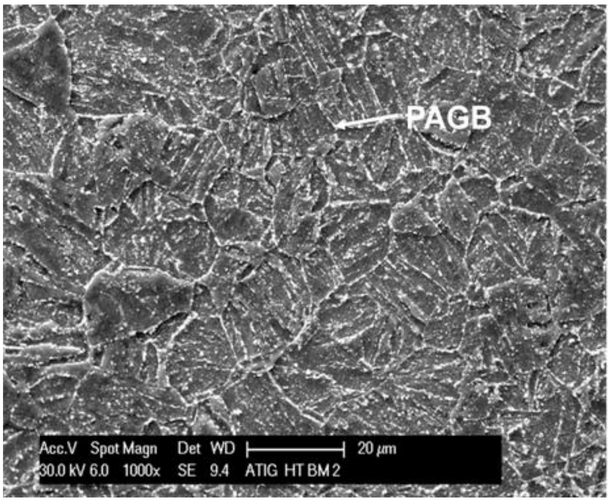

b)

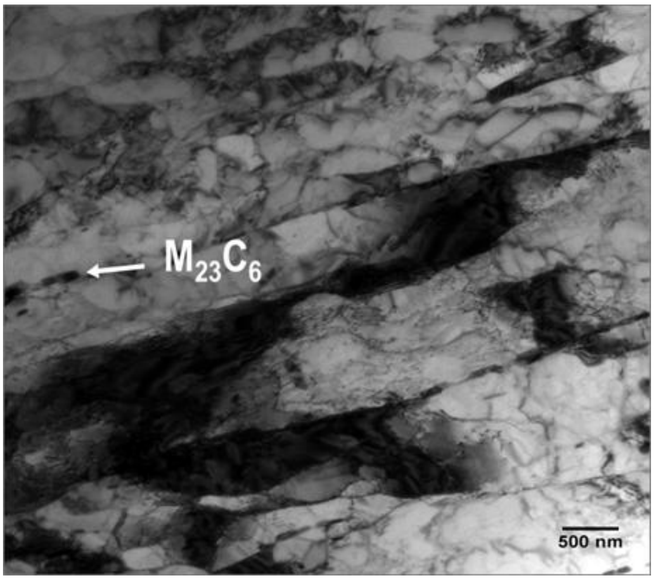

c)

Fig. 5.8 9Cr-1Mo Steel Base Metal in the Normalized and Tempered condition (a) Microstructure from OM (b) Microstructure from SEM c) Microstructure from TEM

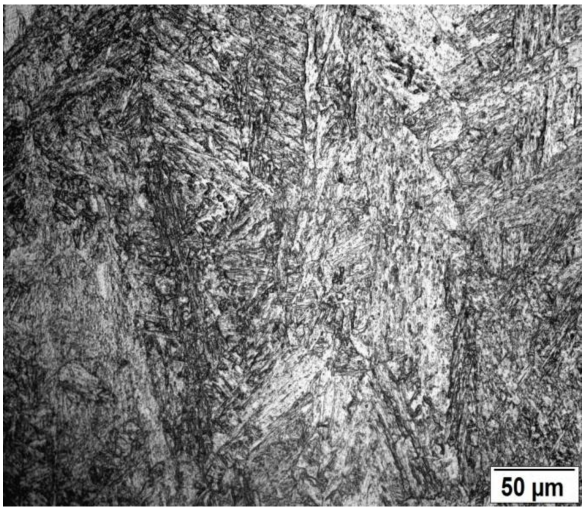

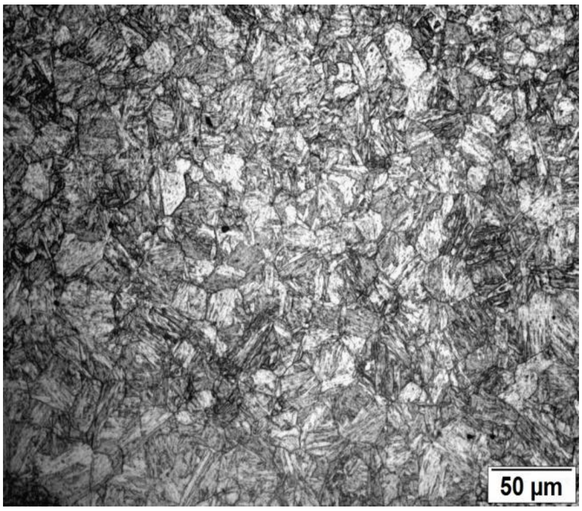

a) SMA weld metal b) SMA weld coarse HAZ

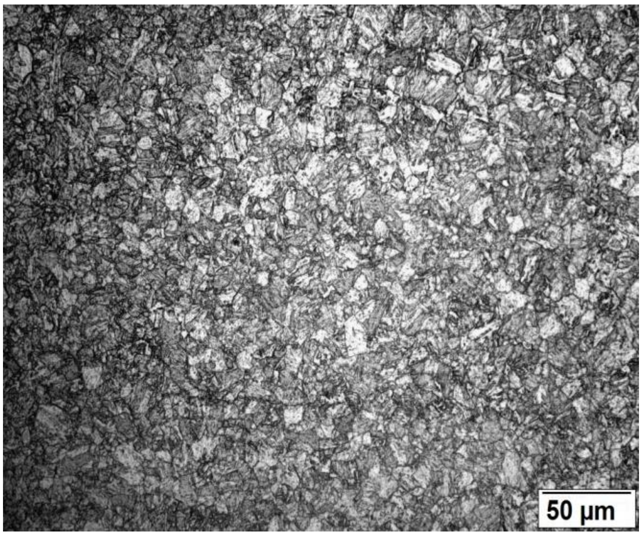

c) SMA weld fine HAZ

Fig. 5.9(a-c). Microstructures of SMA Weld metal, Coarse HAZ and Fine HAZ in PWHT Condition

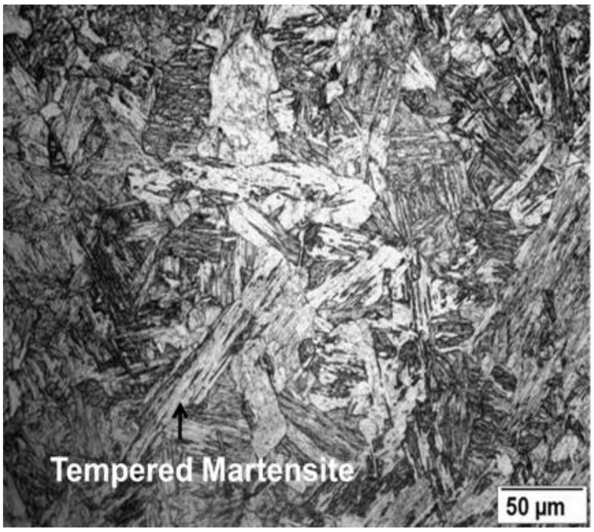

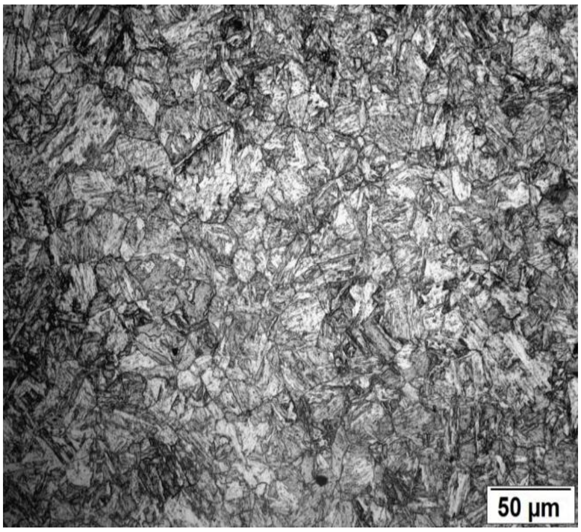

a) TIG weld metal b) TIG weld coarse HAZ

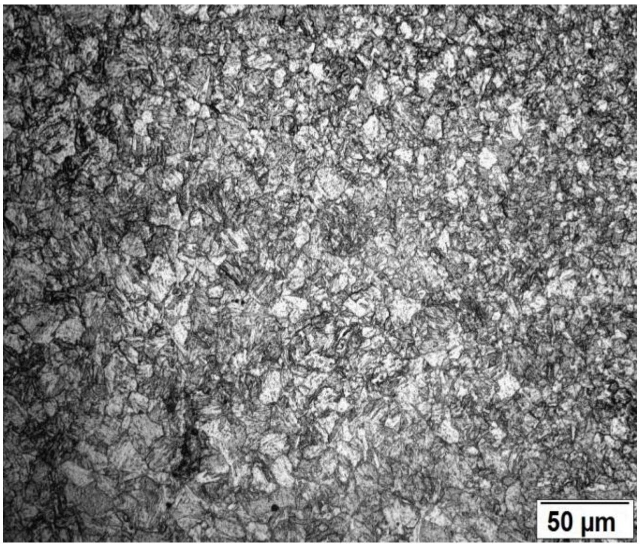

c) TIG weld fine HAZ

Fig. 5.10 (a-c). Microstructures of TIG Weld Metal, Coarse HAZ and Fine HAZ in PWHT Condition

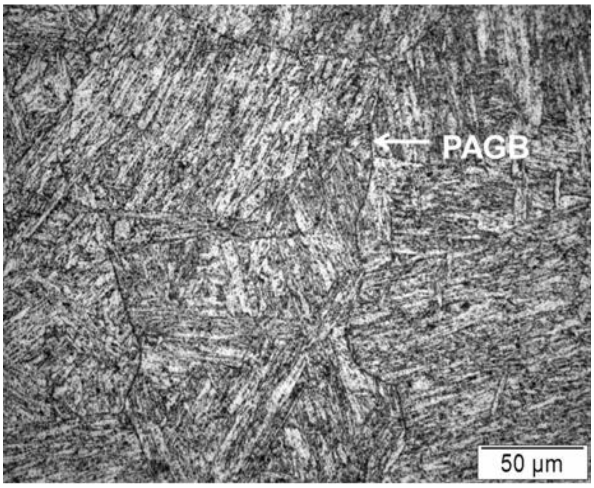

a) A-TIG weld metal

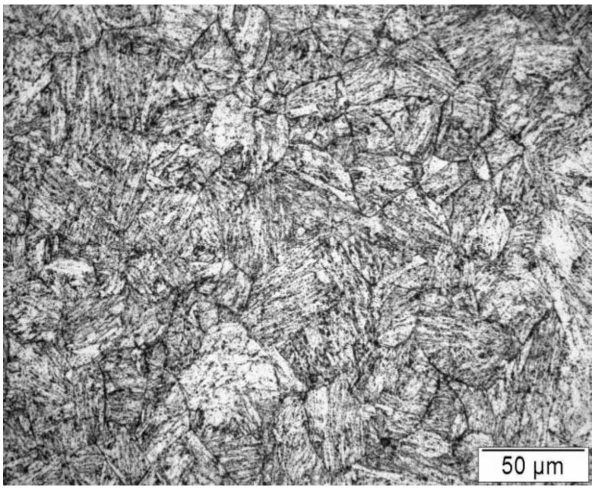

b) A-TIG weld coarse HAZ

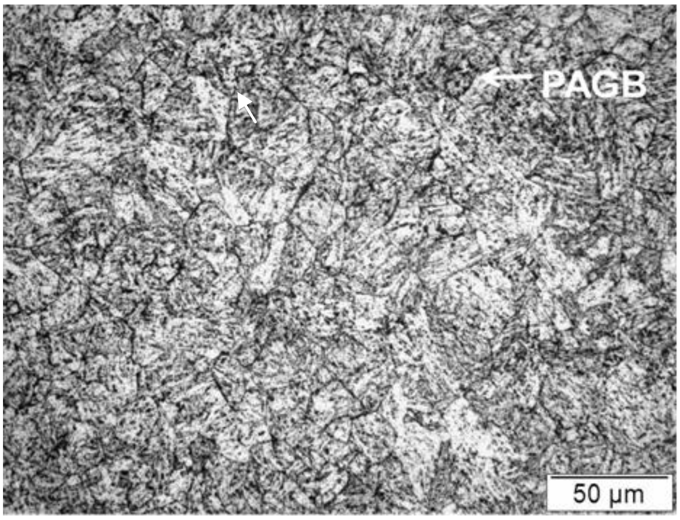

c) A-TIG weld fine HAZ

Fig. 5.11 (a-c). Microstructures of A-TIG Weld Metal, Coarse HAZ and Fine HAZ in PWHT Condition

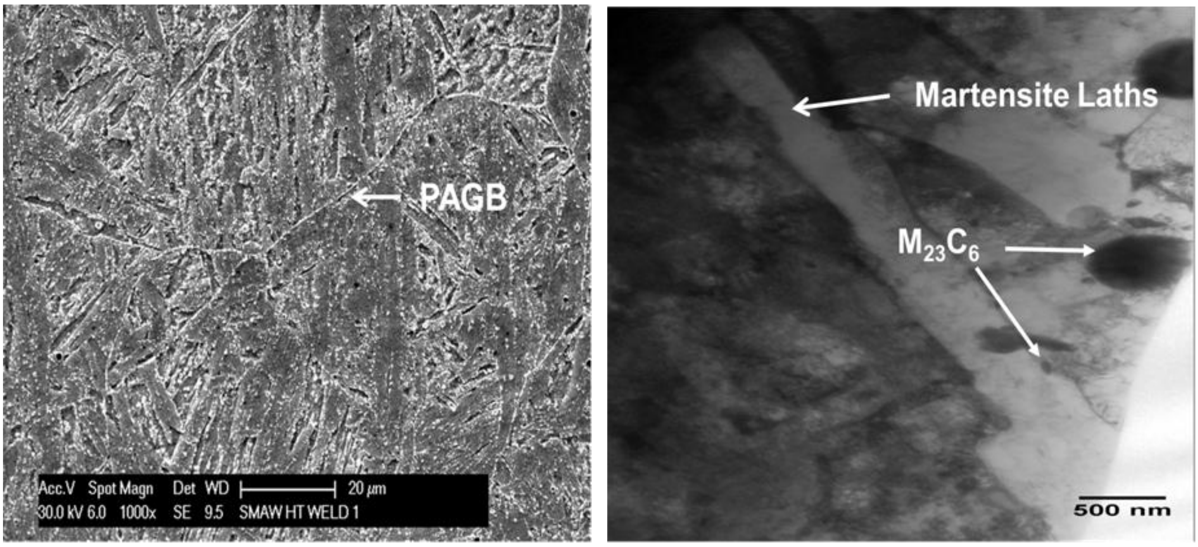

a) SMA weld metal

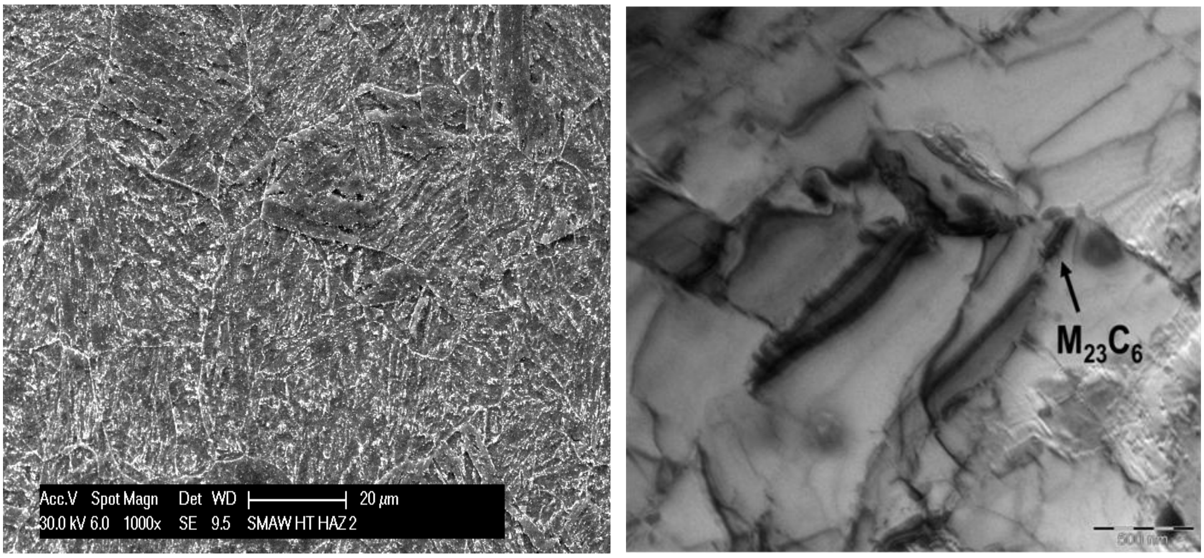

b) SMA weld HAZ

Fig. 5.12(a-b) SEM & TEM Images of SMA Weld and HAZ in PWHT Condition

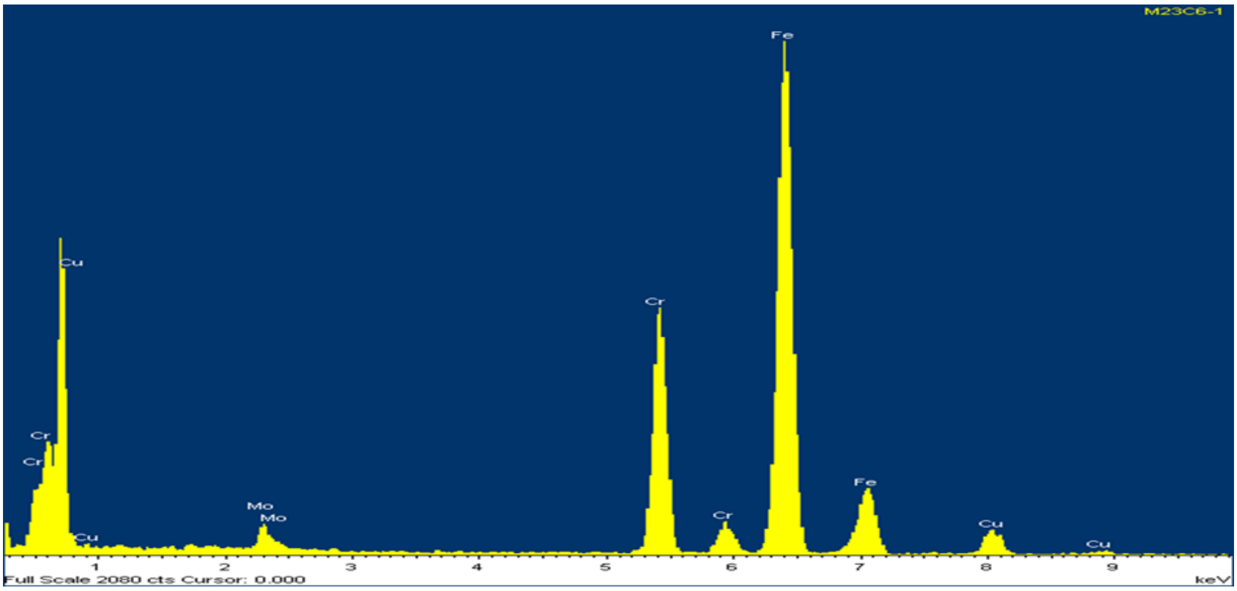

Fig. 5.13 TEM-Energy Dispersive Spectroscopy (EDS) Analysis of Precipitates in SMA Joint Weld

Fig. 5.12(a,b) shows the SEM & TEM micrographs of the SMAW weld zone and HAZ region in PWHT condition. In PWHT condition micrograph revealing tempered martensitic microstructure with precipitation of carbides along the prior austenitic grain boundaries. Coarser precipitates of size 580 nm are seen and also finer precipitates of 150 nm are seen along the lath boundaries. Fig. 5.13 shows TEM-EDS spectra showing chromium rich precipitates ($M_{23}C_6$) in the weld metal. It shows that precipitates are rich in Fe and Cr.

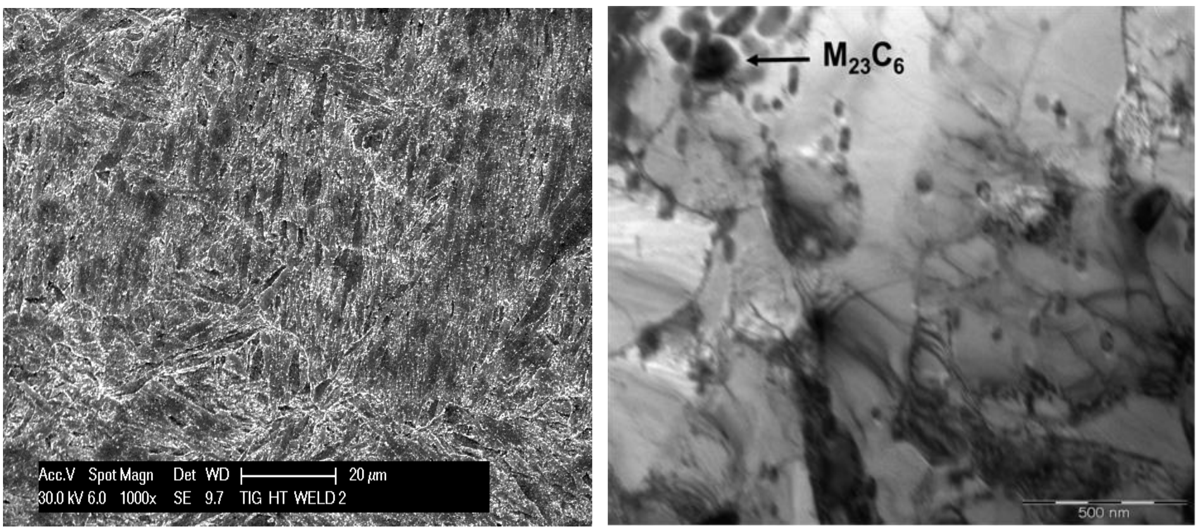

a) TIG weld metal

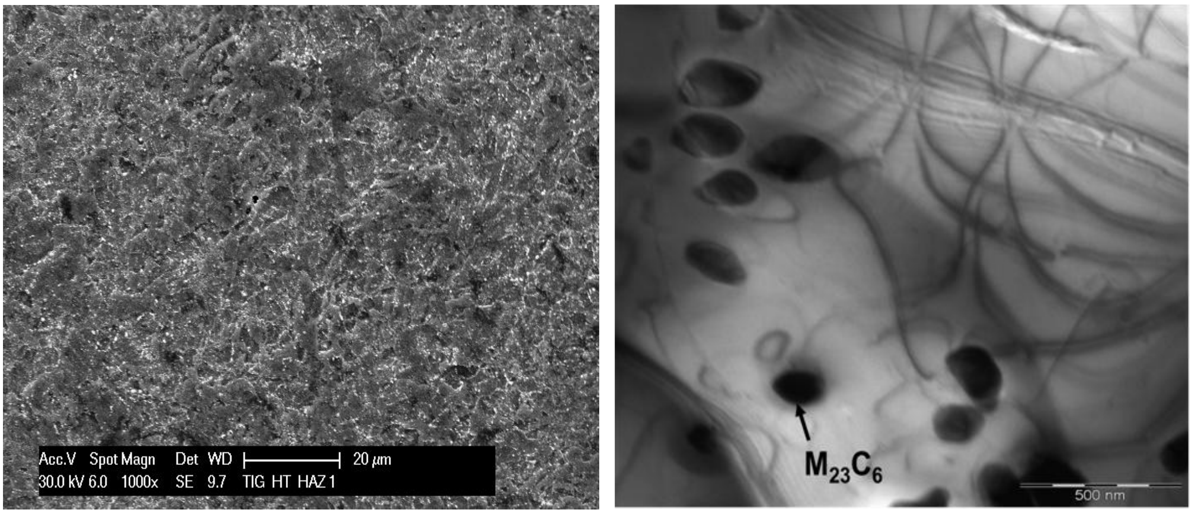

b) TIG weld HAZ

Fig. 5.14(a,b). SEM and TEM Images of TIG Weld and HAZ in PWHT Condition

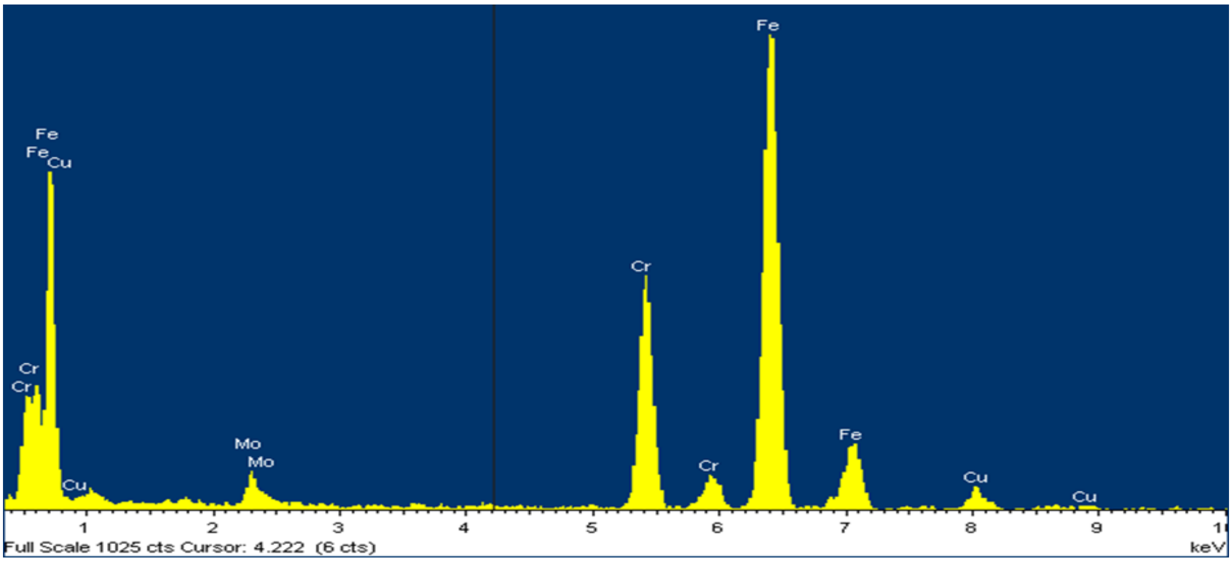

Fig. 5.15 TEM-EDS Analysis of Precipitate in TIG Weld

Fig. 5.14(a, b) shows the SEM and TEM micrographs of the TIG weld zone and HAZ region in PWHT condition. PWHT condition shows the microstructure of weld and HAZ depicting tempered martensitic microstructure with precipitates decorating the grain boundaries. Fig. 5.14(b) shows dislocation density is relatively lower. Lath boundaries are well decorated by $M_{23}C_6$ precipitates. Fig. 5.14 shows coarser carbide precipitates in the range of 230 to 280 nm. This may be due to repeated thermal cycles encountered by multiples passes of the TIG weld joint. The profile clearly reveals that it is Fig. 5.15 shows the TEM EDS spectra of the $M_{23}C_6$ carbide precipitates which are rich in Cr and Fe. .

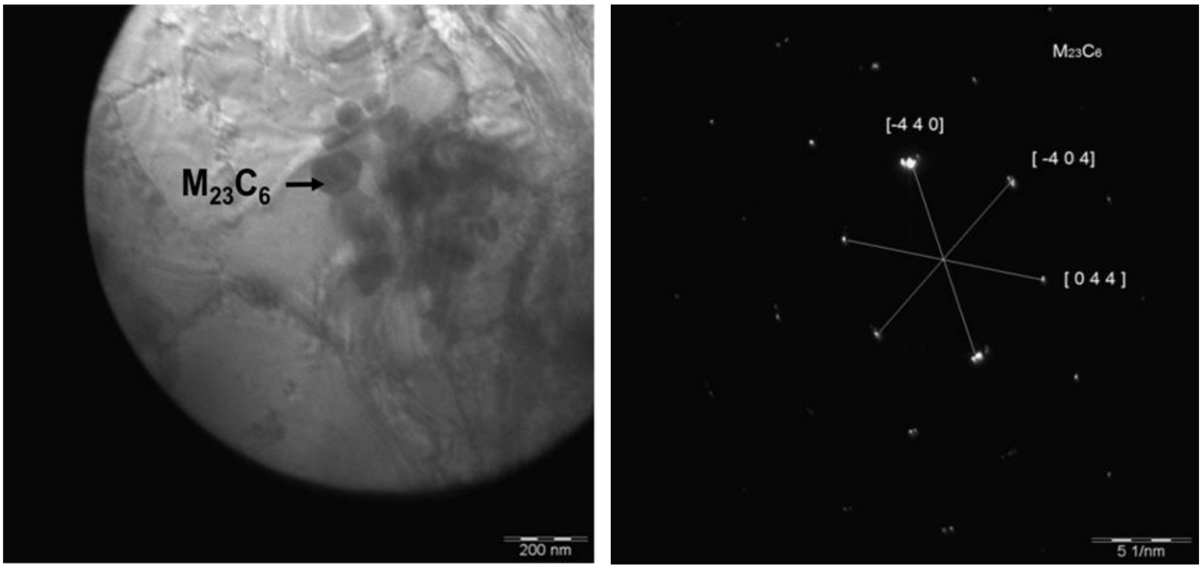

Fig. 5.16 Selected Area Diffraction (SAD) Pattern of Precipitates

The SAD pattern of the precipitate in TIG weld is shown in Fig. 5.16. The SAD pattern clearly shows that the precipitate is $M_{23}C_6$ with zone axis of [044].

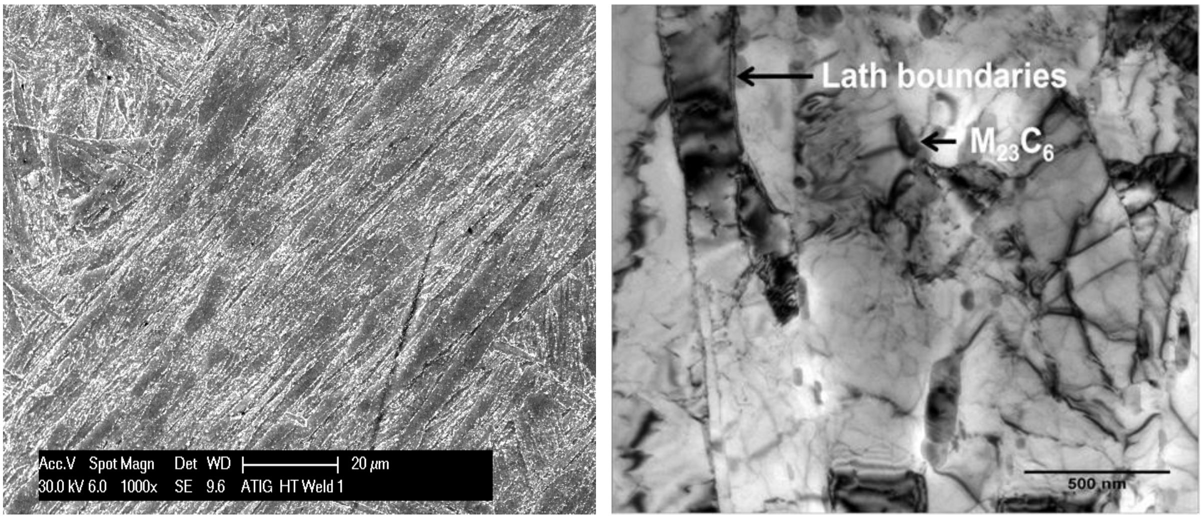

a) A-TIG weld metal

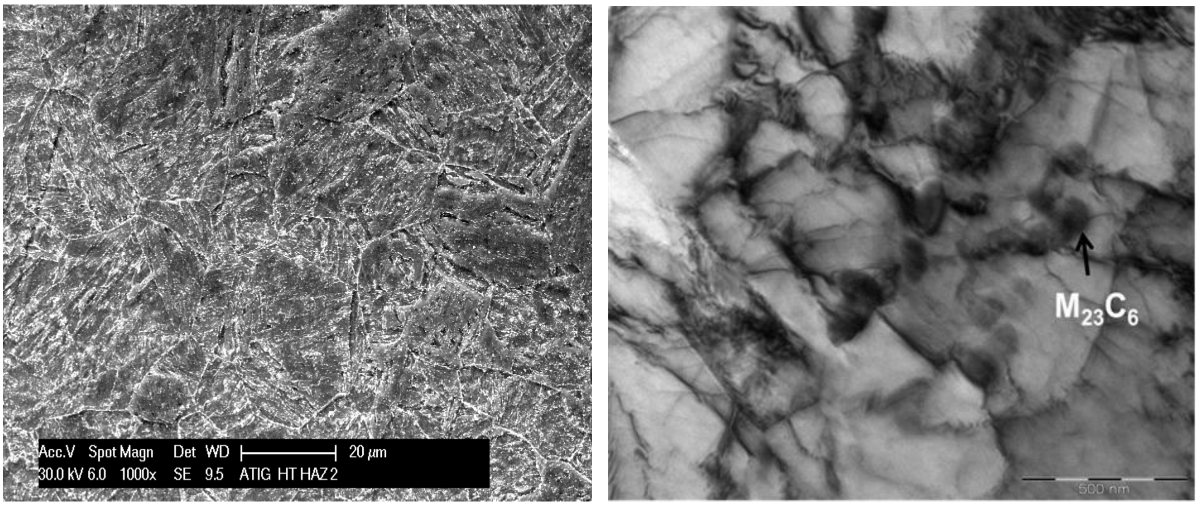

b) A-TIG weld HAZ

Fig. 5.17(a,b). SEM & TEM Images of A-TIG Weld and HAZ in PWHT condition

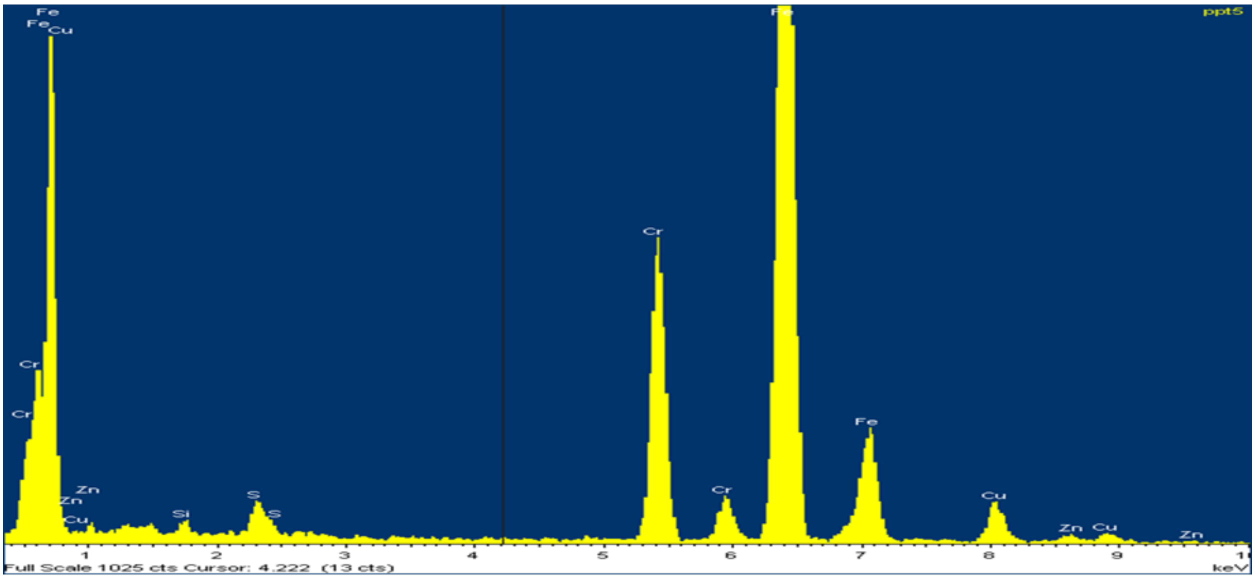

Fig. 5.18 TEM-EDS Analysis of Precipitate in A-TIG Weld

Fig. 5.17(a,b) compares the SEM and TEM micrographs of the weld zone and HAZ region of A-TIG weld joint in PWHT condition. These micrographs in PWHT condition reveals tempered martensitic microstructure with carbide precipitates. Lath width of A-TIG weld is finer and at high temperatures it will give better properties. TEM images of samples in the PWHT condition showed that the lath structure had broken up and sub grains had formed; see for example Fig. 5.17(a) taken from weld metal. Most of the precipitates formed on tempering were rich in iron, chromium, and molybdenum and were presumably of the $M_{23}C_6$

type. These were often found on both prior austenite and sub grain boundaries. Fig 5.17 (b) shows the precipitates decorating the sub grain boundaries.Fig. 5.18 show the TEM EDS analysis of the precipitates. The spectra clearly reveal that it is $M_{23}C_6$ carbide precipitates rich in Cr and Fe.

5.2.5 Evaluation of Mechanical Properties

Mechanical properties of the 9Cr-1Mo steel weld joints including microhardness, tensile properties and impact toughness were evaluated on cross weld specimens and the effect of welding processes on the above weld attributes were compared.

5.2.5.1 Hardness Evaluation

HV was measured across all three weld joints with 500 g load and dwell time of 15 seconds. All three welds (SMAW, TIG, A-TIG) in the as welded state exhibited higher hardness in the range of 350 to 470 VHN. Some variations were also observed in weld and HAZ region. This variation can be attributed to variations in peak temperature and cooling rate. It can also be observed from the Fig. 5.19(a-c) that in as welded state all weld joint exhibit a sharp transition in hardness from HAZ to base metal which is not desirable. It implies that the weld joint cannot be used in the as welded condition and PWHT is mandatory. Fig. 5.20 shows the hardness profile of all three weld joints in PWHT condition. However after PWHT of 760^0C for 2 hours the hardness values were found in the range of 200 to 260 HV in weld and HAZ region and also the transition is relatively smooth. After PWHT, the weld metal of the A-TIG weld joint exhibited more uniform hardness across the weld metal in comparison to that of the other two weld joints. After tempering A-TIG weld joint exhibited higher hardness in the range of 240 – 260 HV. TIG weld zone exhibited hardness in the range of 220 -230 HV. SMAW weld region exhibited hardness in the range of 210 – 220 HV. Hardness variations correlate very well with the microstructural observations described earlier for all the three weld joints. Higher hardness observed in the weld metal of A-TIG weld joint is attributed to higher carbon dissolved in martensite.

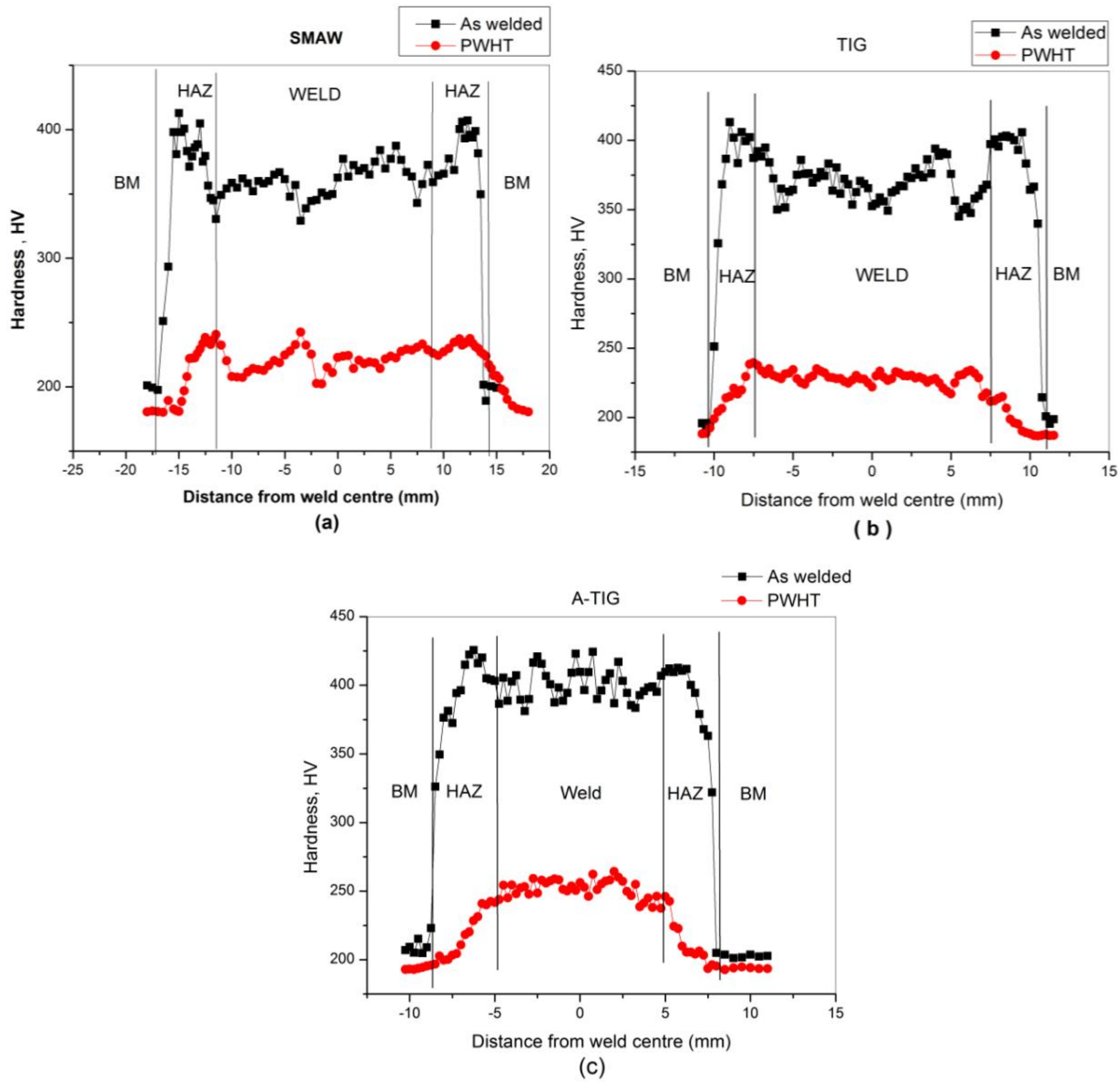

Fig. 5.19 Hardness Profile of a) SMA b) TIG and c) A-TIG Weld Joints

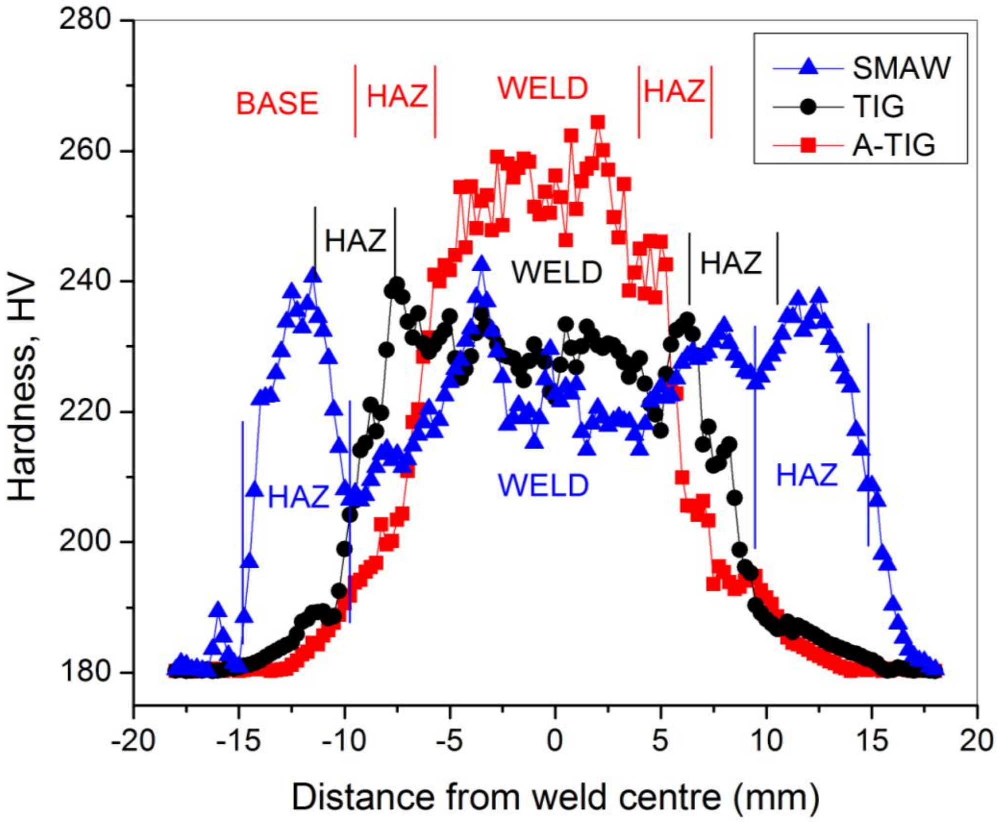

Fig. 5.20 Hardness Vs Distance Plots for SMA, TIG, A-TIG Weld Joints in PWHT Condition

5.2.5.2 Tensile Properties

Cylindrical tensile specimens with weld metal located in the centre of gauge length were fabricated in accordance with ASTM standards E8. Tensile tests were performed at room temperature at a nominal strain rate of 3 x 10^{-4} S^{-1}. The YS, tensile strength, % elongation and % reduction in area values are given in Table 5.10. Fig. 5.21 shows the comparison of stress strain plots of cross weld samples of the three weld joints. The base steel in the normalized and tempered condition exhibited higher YS and UTS compared to that of weld joints in the PWHT condition. The ductility of the all the weld joints are similar and lower than that of the base metal. TIG weld joint exhibited lower YS because of multiple thermal cycles seen during fabrication involving 13 passes. The Fig. 5.22(a-c) shows the photographs of all the tensile tested samples. The location of the failure is in the base metal region confirming the strength of weld metal is higher than that of the base metal. The tensile properties are average of three readings each. The SD values are ± 10, ± 8 and ± 15 for A-TIG, TIG and SMAW respectively. The higher YS reported for SMAW in table 5.9 is higher than other two weld joints.

Table 5.10 Tensile Properties of SMA, TIG and A-TIG Weld joints

Material	YS, MPa	UTS, MPa	% Elongation	% Reduction in area
SMAW weld joint	500	635	18	72.80
TIG weld joint	460	630	18	72.30
A-TIG weld joint	486	637	18	73.24

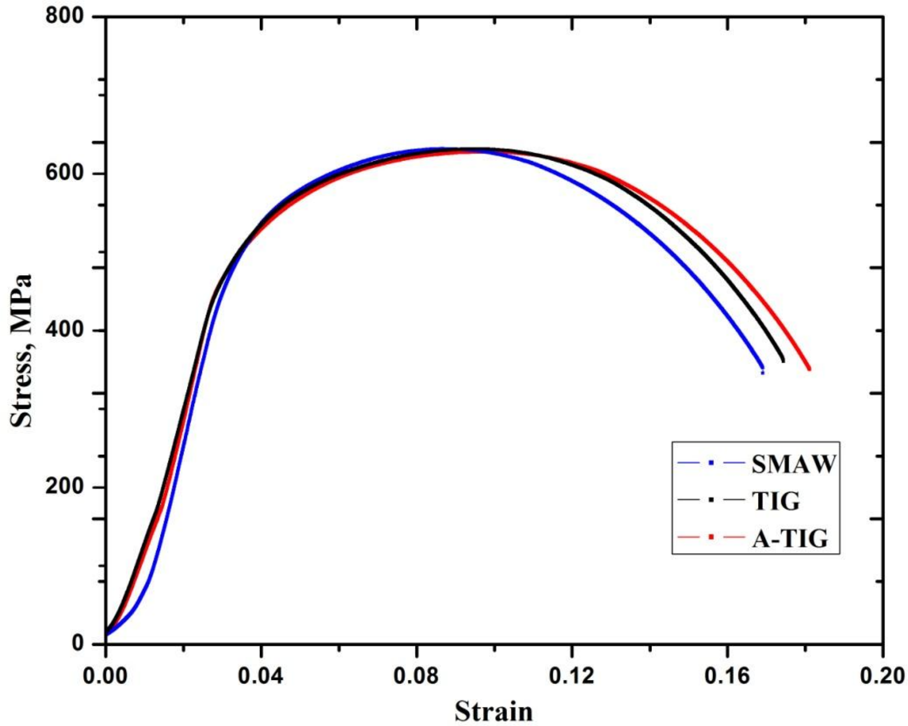

Fig. 5.21 Stress Strain Curves of 9Cr-1Mo Steel Weld Joints

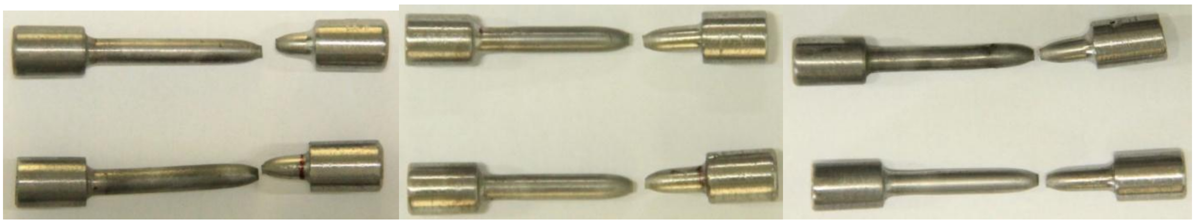

a) SMA weld joint b) TIG weld joint c) A-TIG weld joint

Fig. 5.22 Photographs of Tensile Tested Samples

5.2.5.3 Impact Toughness

The Charpy V-notch impact specimens were fabricated in accordance with ASTM standard E23. The impact test for base metal and all weld joints was carried out at room temperature and at sub zero (-40° C) temperature. The impact energy values obtained from the test are given in Table 5.11. The base metal and TIG weld exhibited higher toughness values of 241 J. A-TIG weld exhibited better impact toughness compared to SMA weld. All three weld joints exhibited toughness values more than the minimum toughness requirement of 47J. A minimum average of 47 J for the tempered weld metal (minimum single value of 38 J) has to been assured as per the European specification EN1599:1997 [178].

Table 5.11 Impact Toughness of BM, SMA, TIG and A-TIG Weld Joints in PWHT condition

Material	Impact Energy (J) at 20° C	Impact Energy (J) at -40° C
Base metal	241	18
SMAW joint	70	8
TIG weld joint	241	16
A-TIG weld joint	112	7

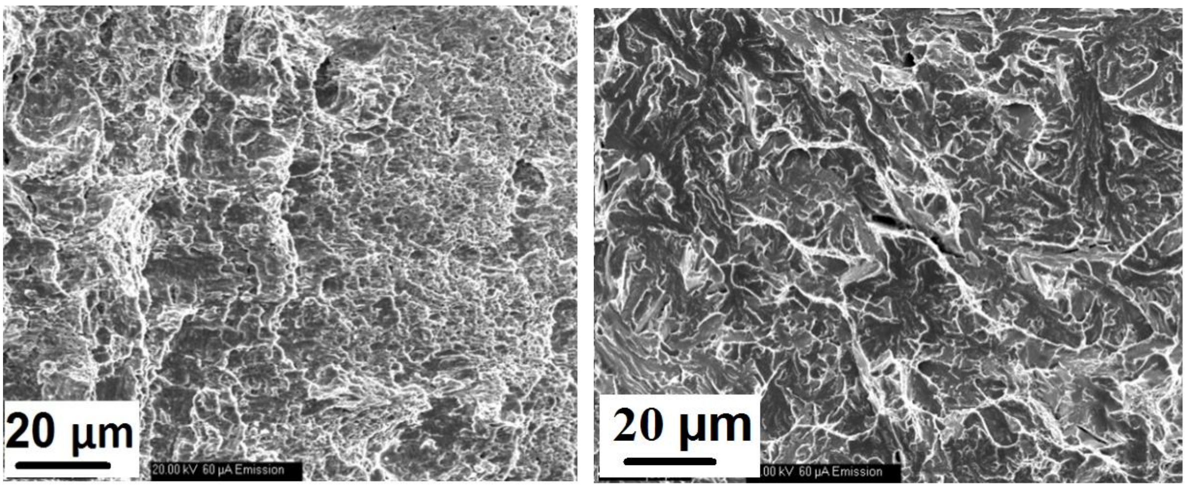

a) Room temperature b) at-40° C

Base metal

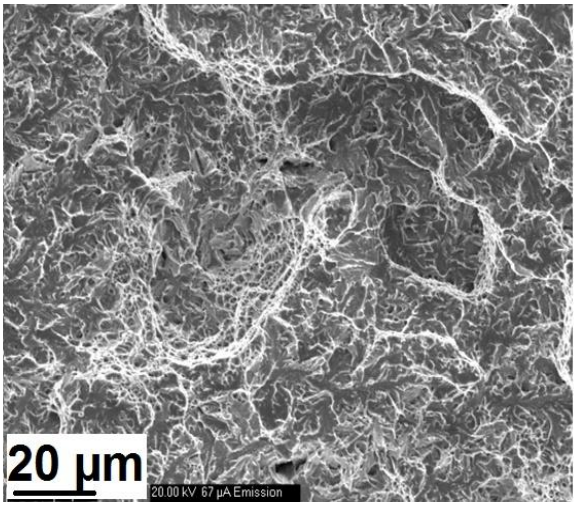

c) Room temp

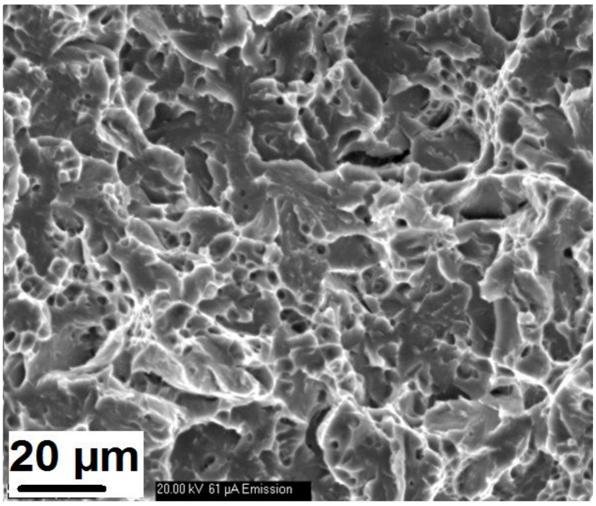

d) at -40° C

SMA weld

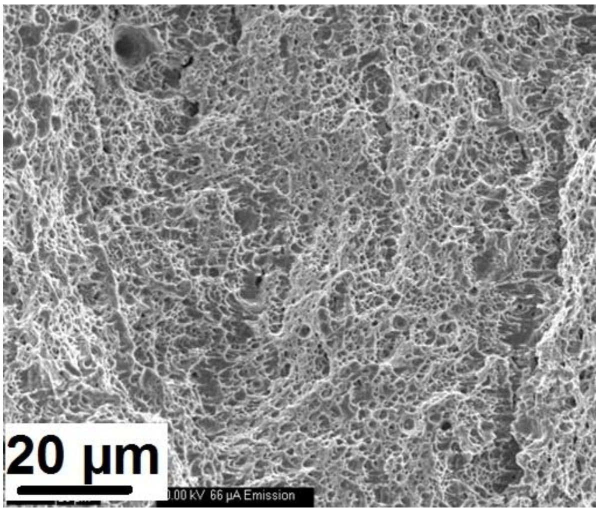

e) Room temp

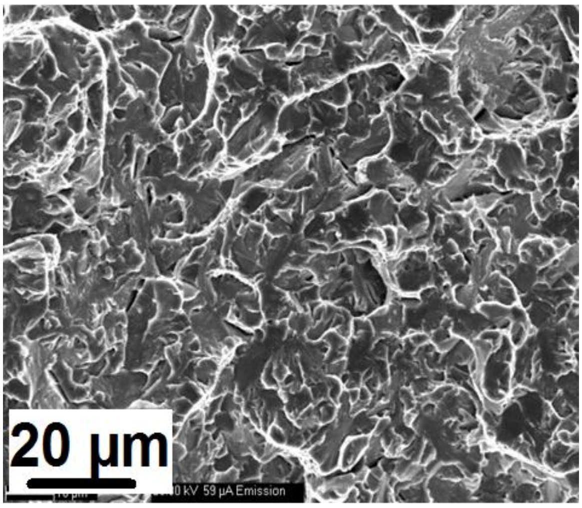

f) at -40° C

TIG weld

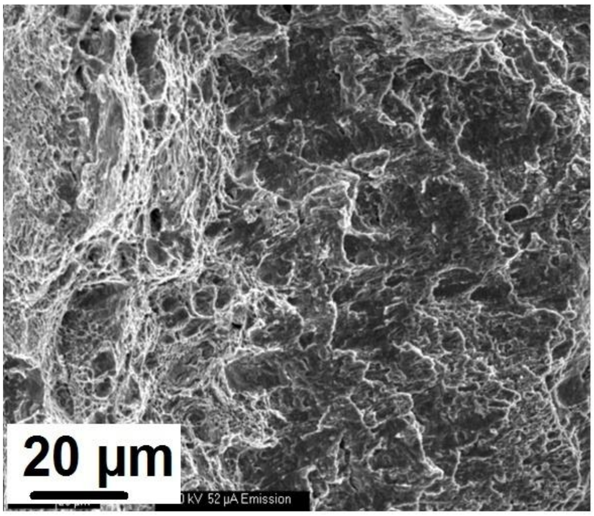

g) Room temp

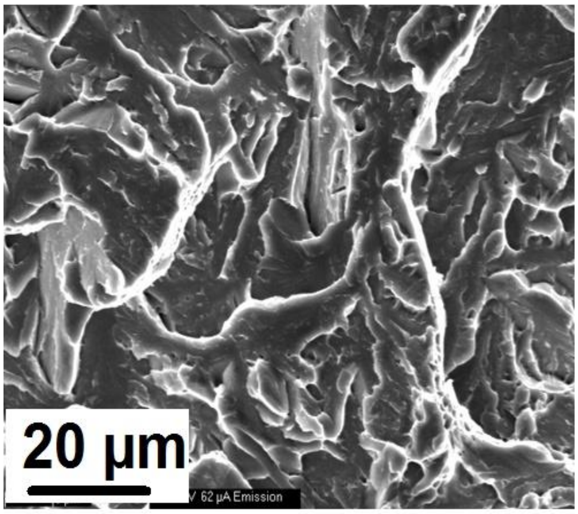

h) at -40° C

A-TIG weld

Fig. 5.23 Fractographs of Impact Tested Samples (a,b) Base Metal (c,d)SMA Weld (e,f) TIG Weld and (g, h)A-TIG Weld at RT and -40ºC

The Impact fractograph images at room temperature and at -40° C are shown in Fig. 5.23 (a-h). Fig. 5.23 (a, b) shows fractographs of impact tested samples of base metal at room temperature and subzero temperature (-40ºC) respectively. Fig. 5.23 (c, d) shows fractographs of SMA weld Joint at room temperature and at -40° C respectively. Fig. 5.23 (e) TIG weld Joint exhibit ductile fracture with an impact toughness value of 241 J. Fig. 5.23 (c) shows the quasi cleavage mode of fracture. Fig. 5.23(g) shows mixed mode of failure. At subzero temperature of -40° C, base metal and all the weld joints failed by cleavage mode of fracture, which is shown in Fig. 5.23 (b, d, f, h).

5.2.6 Residual Stress Measurement

Non uniform heating during welding produces in-compatible strain and remains after cooling, resulting in residual stress [179]. Due to this stress the atoms position and inter planner spacing gets shifted. By XRD technique we can find out the peak shift and planner spacing can be measured using Brags law and residual stress can be calculated. Residual stress can significantly affect the performance and reliability of components and structures [180-182]. Various NDT methods used to measure the residual stress. XRD is one of the finest methods. Residual stress measurement procedures and calculations are discussed in detail in the references [183-184].

The residual stress measurements were carried out along the longitudinal direction on the welded plates across each of the weld joints using the experimental parameters listed in Table 4.5. Two sets of measurements were carried out at each of the locations at which the stresses are to be evaluated. The stress values were estimated by a combined analysis of the change in the peak location with varying ψ obtained from the two measurements. A Young's modulus of 210 GPa was used as the material property to estimate the residual stress.

The slag removal was carried out by mild wire brushing on all the weld joints. It is expected that mild wire brushing would not cause significant changes in the residual stresses distribution on weld joints. In the SMAW joint, the stresses were compressive at all measured locations up to 30 mm on both sides of the weld centre. A peak compressive stress of 280 MPa was observed at 7 mm from the weld centre. The presence of compressive stresses may be attributed to dominance of phase transformation (martensite formation) induced stresses over that of the shrinkage stresses [185]. The length and area of weld metal and HAZ the SMA weld joint is more compared to that of other weld joints. Therefore, weld metal volume and Martensite formation is more in the case of SMA weld joint. In the TIG joint, tensile stress of 75 MPa was observed at the weld centre which dropped to ~ zero at 10 mm form the weld centre. A peak tensile stress of 300 MPa was observed at 15 mm from the weld centre on both sides. In the A-TIG weld joint, the stresses were tensile up to 30 mm from the weld centre. A peak tensile stress of 520 MPa was observed at 10 mm from the weld centre. Additional RS measurements were taken along a line situated 20 mm away from weld centre line (WCL) at 0, 2.5, 5 & 10 mm to confirm the higher stress gradient between the weld centre and HAZ. All the three weld joints showed typical 'M' shaped characteristic residual stress profile across the line of measurement with an elevation at the weld centre. Similar profiles were reported in V-butt joints of modified 9Cr-1Mo steel joints [186]. The peak tensile residual stresses were found to exist just beyond the heat affected zone of the weld joints. The narrow and wider stress affected zones observed in the joints are correlated to the individual bead widths of the various joints. The distribution of the hardness profiles is consistent with the bead width of the joints. The A-TIG weld joint showed tensile stress profile distribution while the SMA weld joint showed complete compressive stress profile distribution. Fig. 5.24 shows the residual stress profile of all weld joints.

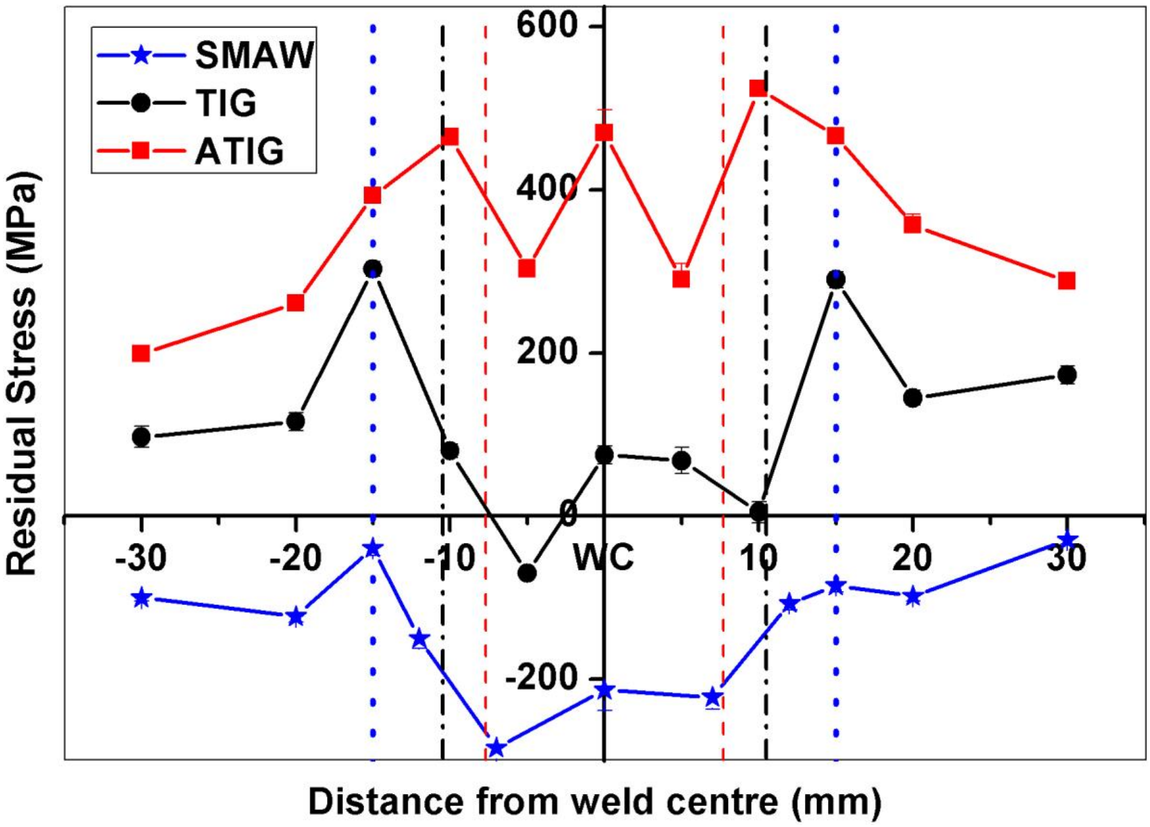

Fig. 5.24 Residual Stress Profiles of all Weld Joints

Among the three 9Cr-1Mo steel weld joints studied in the present work, SMA weld joint exhibited lower hardness, lower toughness, adequate strength and ductility values. Lower toughness could be attributed to coarser grain size and higher oxygen in the weld metal causing weld metal inclusions. 9Cr-1Mo steel SMA weld joint with lower toughness is not desired for applications. TIG weld joint exhibited higher toughness, adequate strength and ductility values. However the weld joint fabrication required 13 passes and V-groove edge preparation was also required. A-TIG weld joint exhibited higher hardness, adequate toughness, strength and ductility values. Fabrication required only two passes and no edge preparation was required. In order to improve the toughness in A-TIG weld joint, PWHT duration shall be increased from 2 to 4 h [187]. Between TIG and A-TIG weld joint, A-TIG weld joint may be preferred for applications from the point of view of ease of fabrication and reduced cost.

5.2.7 Summary

All the three weld joints exhibited tempered martensitic microstructure with $M_{23}C_6$ precipitates in the weld metal and HAZ. The SMA weld joint exhibited coarser prior austenite grain size and while the TIG weld metal exhibited finer prior austenite grain size. TEM studies showed that after PWHT, lath structure is broken up and substructures have formed in the weld metal and HAZ. A-TIG weld metal exhibited higher hardness value of 260 VHN while the TIG and SMA weld metals exhibited hardness values of 230 and 220 VHN respectively. The peak hardness value after PWHT for A-TIG weld joint is marginally higher compared to TIG and SMAW weld joint. Higher hardness in A-TIG weld metal is attributed to higher carbon in the martensite. Lower hardness in the TIG and SMA weld metals is due to multiple thermal cycles seen by the joint during welding. Strength and ductility values are similar for all three weld joints. TIG weld joint exhibited higher impact toughness values compared to A-TIG and SMAW weld joints. The higher toughness may be attributed to multiple thermal cycles involved in TIG weld joint fabrication which caused complete tempering of martensite. All the three weld metals and base metal exhibited ductile to brittle transition at -40ºC. All the three weld joints showed typical 'M' shaped characteristic residual stress profile found in ferritic-martensitic steel weld joints. In the SMAW joint, residual stresses were compressive, this may be attributed to domination of phase transformation (martensite formation) induced stresses over the shrinkage stresses. In the TIG weld joint, the residual stress varied from low compressive to tensile. In the A-TIG joint, residual stresses at the weld centre were found to be tensile at all the locations of measurement. In the case of A-TIG weld joint, shrinkage stresses dominate over phase transformation induced stresses.

5.3 Zone Wise Evaluation of Strength Properties 9Cr-1Mo Steel Weld Joints using ABI.

ABI technique has been used to characterize the gradient in strength properties of wide range of weld joints. A non-destructive technique such as ABI is best suited for assessment of strength property variations across 9Cr-1Mo steel weld joint in service. ABI test can also generate and supply tensile data on the various zones of 9Cr-1Mo steel weld joint for use in finite element analysis on a model of the fabricated component. The technique has many advantages like requirement for small volume of sample and it can be used in-situ. However, detailed investigation on the use of ABI for evaluating the strength variations across the 9Cr-1Mo steel weld joints is required before recommending the ABI for testing the component in service. The objectives of the present study involve assessing the effect of different arc welding processes on the strength property variation across the 9Cr-1Mo steel weld joint using ABI technique. The generated strength property data on the various zones of weld joint will also find application during finite element analysis of the weld joint.

5.3.1 ABI Analysis

The analysis makes use of elasticity and plasticity theories and semi-empirical relationships that govern the material performance under indentation loading [188]. The spherical shape of the indenter causes an increasing strain with increased indentation depth up to a maximum of 0.2 or 20% true-plastic-strain. A true strain of 20% corresponds to a penetration depth equal to the indenter radius. The current strain produced is a function of the penetration depth. The current stress at any time is a function of the current indentation force. Periodic partial unloading during the test is used to determine the plastic strain. The elastic depth is subtracted from the total depth to give the plastic depth. The schematic of applied force versus indentation depth during various cycles and determination of plastic depth is shown in Fig. 5.25(a). The incremental values of the true-stress and true-plastic-strain are calculated from the indentation force-depth data (based on elasticity and plasticity theories). Other properties, including the strain-hardening exponent (*n*), and ultimate strength (UTS) are derived from Holloman equation.

The indentation geometry during force application and after force removal (complete unloading) is shown in Fig. 5.25(b). Each loading cycle of ABI, the total depth of indentation (h_t) and load applied (P) are measured. The depth is converted to total indentation diameter (d_t) using the equation 5.7.

$$d_t = 2\,(Dh_t - h_t^2)^{½} \qquad (5.7)$$

where 'D' is the diameter of the indenter.

From the plastic depth h_p, the plastic diameter d_p is calculated by iterating in the equation 5.8,

$$d_p = \sqrt[3]{(2.735\ P\ D)\ \frac{\left[\frac{1}{E_S} + \frac{1}{E_I}\right]\left[4\,h_p^2 + d_p^2\right]}{4h_p^2 + d_p^2 - 4h_p D}}$$

(5.8)

where, E_S and E_I are the Young's modulus of the specimen and indenter respectively.

The true stress (σ_t) and true plastic strain (ε_p) values are calculated using the equations 5.9 and 5.10 respectively,

$$\sigma_t = \frac{4P}{\pi d_p^2 \delta} \qquad (5.9)$$

$$\varepsilon_p = 0.2\,(d_p/D) \qquad (5.10)$$

where, δ is a constant correlated to the constraint effect for plastic deformation for a given class of materials and given as (using equation 5.11 and 5.12),

$$\delta = \begin{cases} (i) & 1.12 & \phi \le 1 \\ (ii) & 1.12 + \tau \cdot \ln \phi & 1 < \phi \le 27 \\ (iii) & 2.87 \cdot \alpha_m & \phi > 27 \end{cases}$$

$$where \quad \tau = \{ (2.87 \cdot \alpha_m - 1.12) / \ln(27) \}$$

(5.11)

Where, α_m parameter is material dependent and is held at a constant value between 1.10 and 1.25 for various structural steels [189, 190] and

$$\phi = \varepsilon_p E_{spec} / 0.43 \sigma_t$$

(5.12)

The total indentation diameter (d_t) is used to approximately relate the rate of displacement of indenter (V_i) with the ball indentation strain rate ($\acute{\varepsilon}$) using the following equation 5.13 [191],

$$\acute{\varepsilon} \approx 0.4 \left(\frac{Vi}{dt}\right) \quad (5.13)$$

Data points from all cycles are fit by linear regression analysis to the equation 5.14

$$P/d_t^2 = A(d_t/D)^{m-2}, \quad (5.14)$$

Where m is the Meyer's coefficient and A is yield parameter obtained from the regression analysis. On finding yield parameter A, the YS (σ_y) is calculated from the equation 5.15,

$$\sigma_y = B + \beta_m A, \quad (5.15)$$

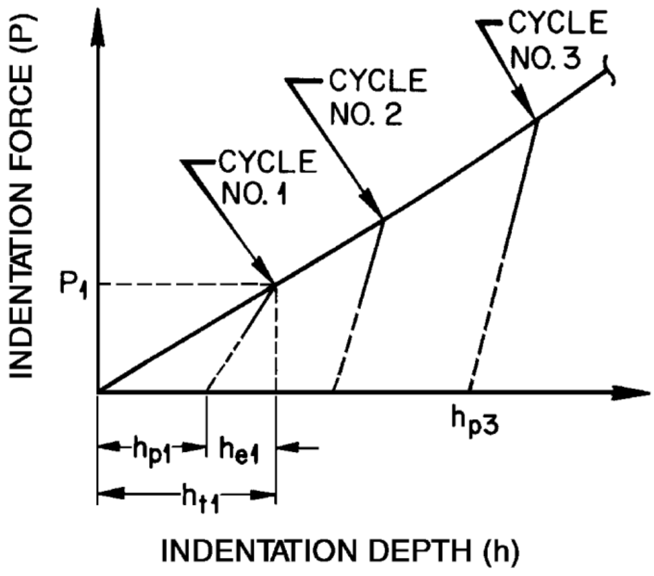

a)

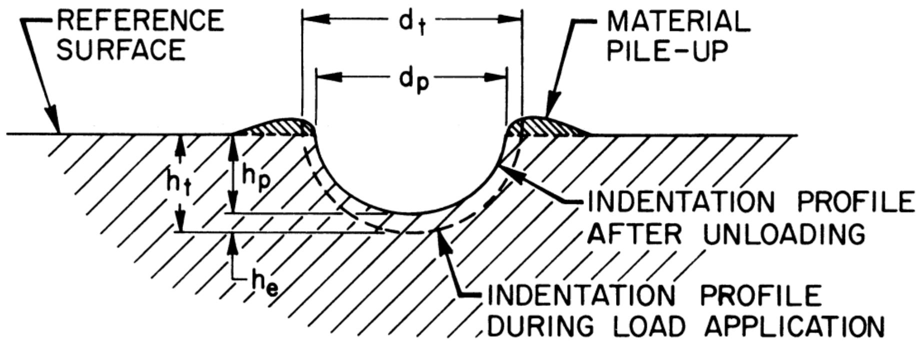

b)

Fig. 5.25 (a) Applied Force versus Indentation Depth, (b) Indentation Geometry during Loading and Complete Unloading [146].

Where β_m is material yield slope and is a constant for a given class of materials; B is yield offset constant (in MPa). The engineering UTS (σ_{UTS}) can be obtained by taking ε_u=n in Holloman equation (5.16) as,

$$\sigma_{UTS} = K\left(\frac{\varepsilon_u}{e}\right)^n = K\left(\frac{n}{e}\right)^n, e \approx 2.71 \tag{5.16}$$

where, K is the strength coefficient.

ABI analysis involves certain approximations and limitations. The analysis relies on empirical correlation of ABI data with uniaxial tensile test data. The UTS can be derived from equation 10 only for material whose stress-strain curve obeys Holloman equation. The constant value of ‘n’ as reported is merely an average value taken over some specific strain interval on stress-strain plot.

5.3.2 Applied Load and Indentation Depth Relations

Applied load-depth of indentation of raw data obtained on the weld metal, HAZ and base metal of SMAW, TIG and A-TIG weld joints at 300 K are respectively shown in Fig. 5.26(a,b,c). For the same depth of indentation, the applied load was higher at weld metal followed by HAZ when compared to base metal. It implies that the resistance to deformation was higher in the weld followed by HAZ. Base metal exhibited the least resistance to deformation. A-TIG weld metal exhibited maximum resistance to deformation compared to various other zones in different weld joints. This is in agreement with hardness values obtained for the various zones in different weld joints. This is attributed to the high carbon in martensite exhibited by A-TIG weld metal. The load-depth of indentation data that were obtained from various weld joints were analyzed according to equation (5.7 – 5.16). On the basis of empirical correlation with uniaxial test results, the constraint factor and the material yield slope were taken as 3.5 and 0.232 respectively in the analyses.

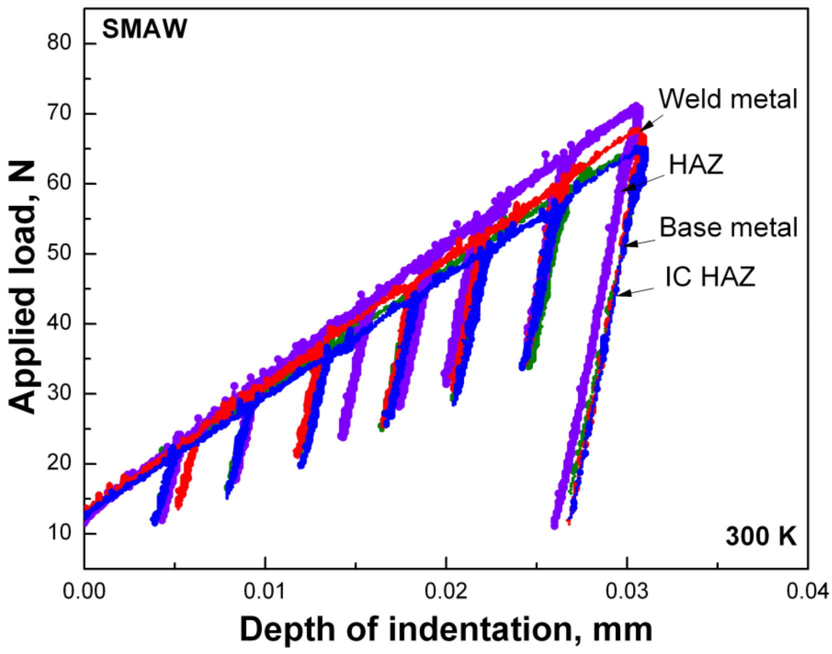
SMAW
Applied load, N
Depth of indentation, mm
Weld metal
HAZ
Base metal
IC HAZ
300 K
80
70
60
50
40
30
20
10
0.00
0.01
0.02
0.03
0.04

a)

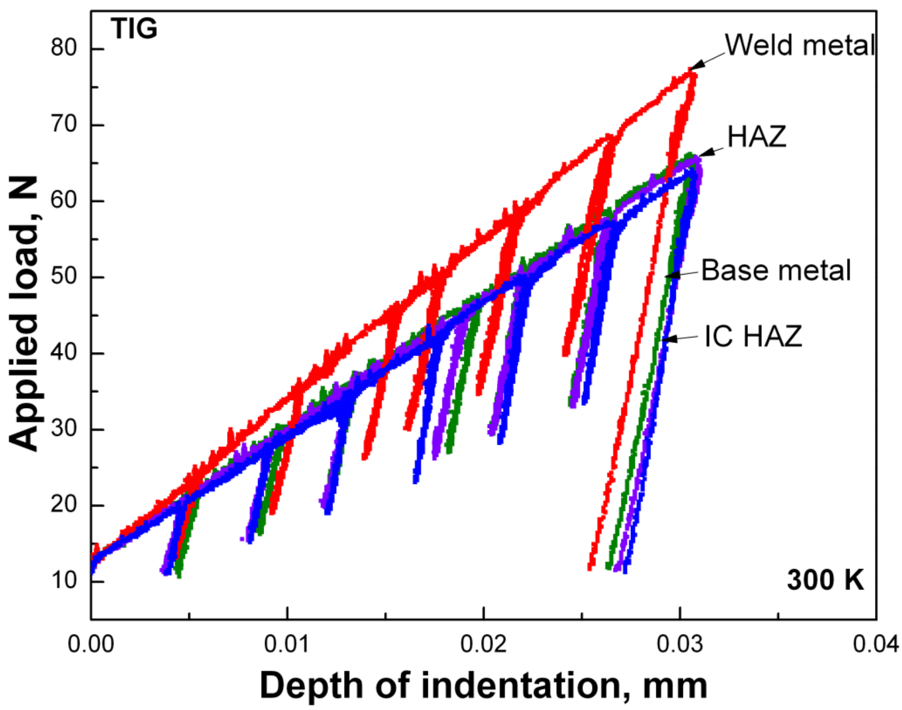
TIG
Applied load, N
Depth of indentation, mm
Weld metal
HAZ
Base metal
IC HAZ
300 K
80
70
60
50
40
30
20
10
0.00
0.01
0.02
0.03
0.04

b)

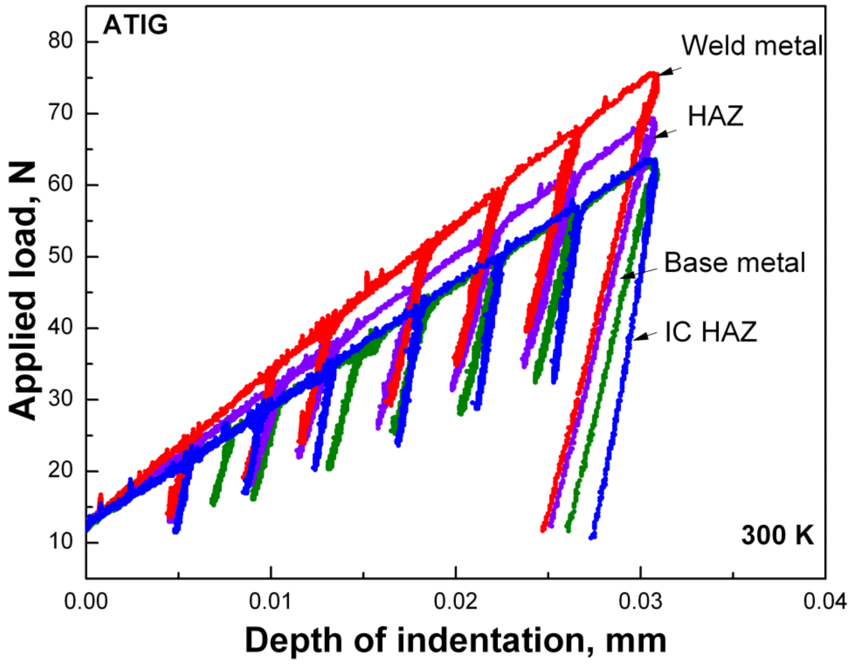

c)

Fig. 5.26 Applied Force Vs Indentation Depth of (a) SMAW (b) TIG and (c) A-TIG Weld Joints

5.3.3 Correlation Stress Strain between Uniaxial and ABI Method

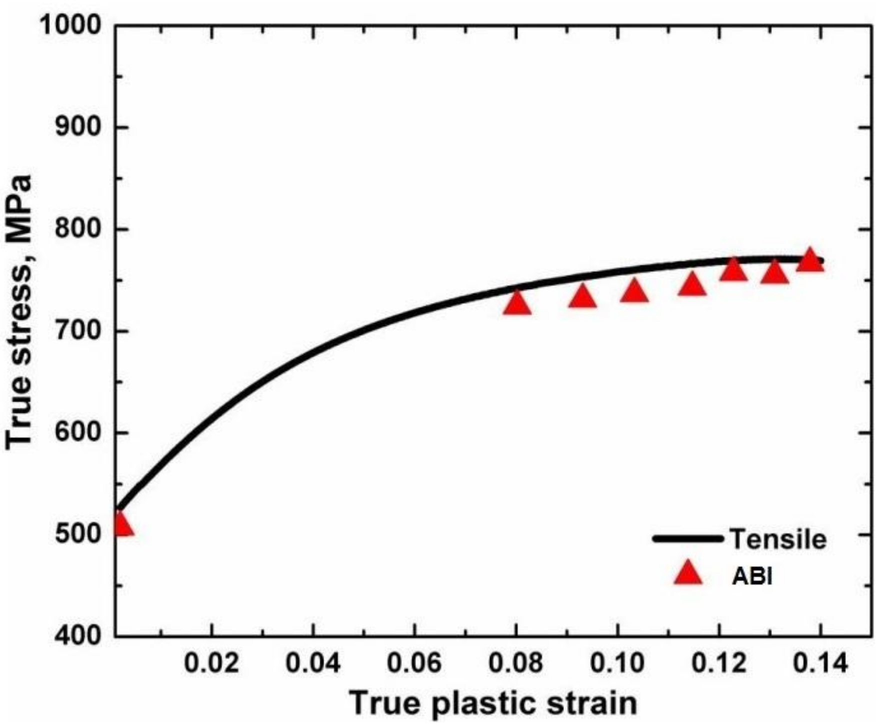

Fig. 5.27 Correlation of True Stress-True Plastic Strain Data for Base Metal Determined from Uniaxial Tensile Test with ABI Test

The true stress in uniaxial tensile test result versus ABI test tensile test result plot in Fig. 5.27

shows that the ABI calculated values are in line with the uniaxial tensile test results. ABI and uniaxial test results were similarly correlated for base metal and weld metal of SA-533B steel welds [191], 316LN stainless steel weld joint [192], etc. ABI and uniaxial test results exhibited close agreement in the above studies also.

5.3.4 Comparison of True Stress Vs True Strain of Weld Joints

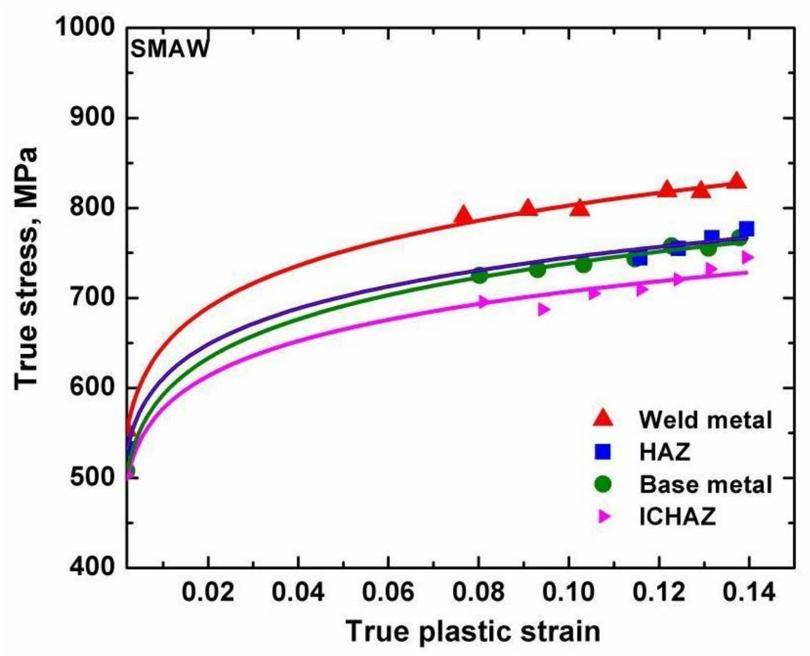

Fig.5.28 Flow Curves for Various Zones of SMAW Weld Joint

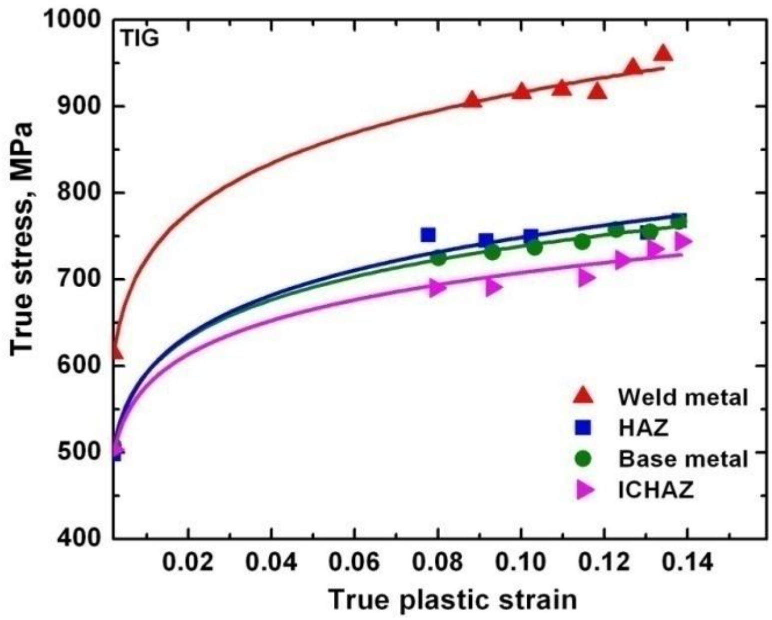

Fig. 5.29 Flow Curves for Various Zones of TIG Weld Joint

The flow curves plotted in Fig. 5.28 to Fig. 5.30 shows that weld metal region exhibits higher tensile strength that that of HAZ and base metal in all three 9Cr-1Mo steel weld joints. The high dislocation density during solidification from the molten weld pool and transformation to harder martensite resulted in increase of hardness and strength of the weld metal. Higher carbon content in A-TIG and TIG weld metal caused the formation high strength martensite in the A-TIG and TIG weld joint. The SMAW weld metal exhibited lower strength due to lower carbon content in martensite and coarser grain size.

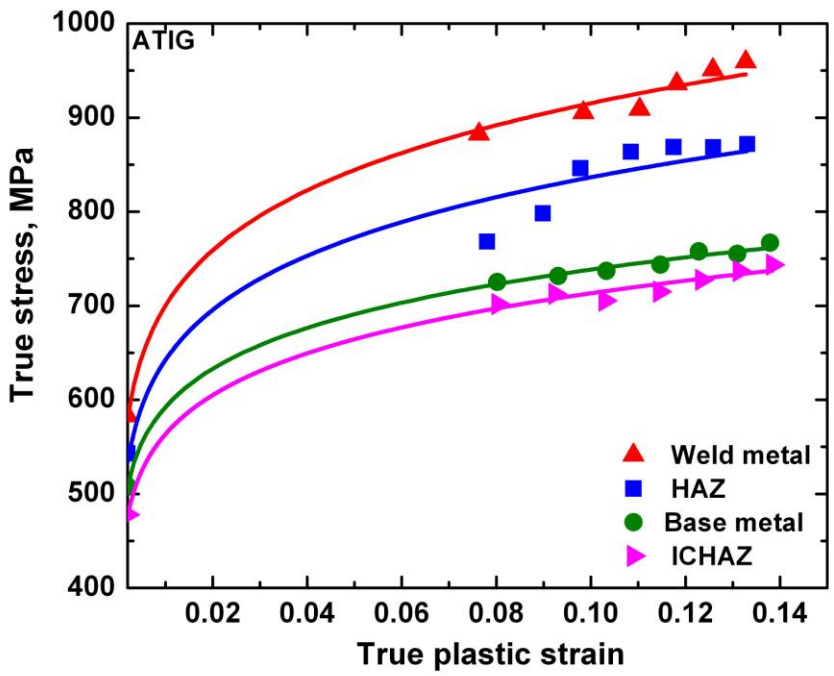

Fig. 5.30 Flow Curves for Various Zones of A-TIG Weld Joint

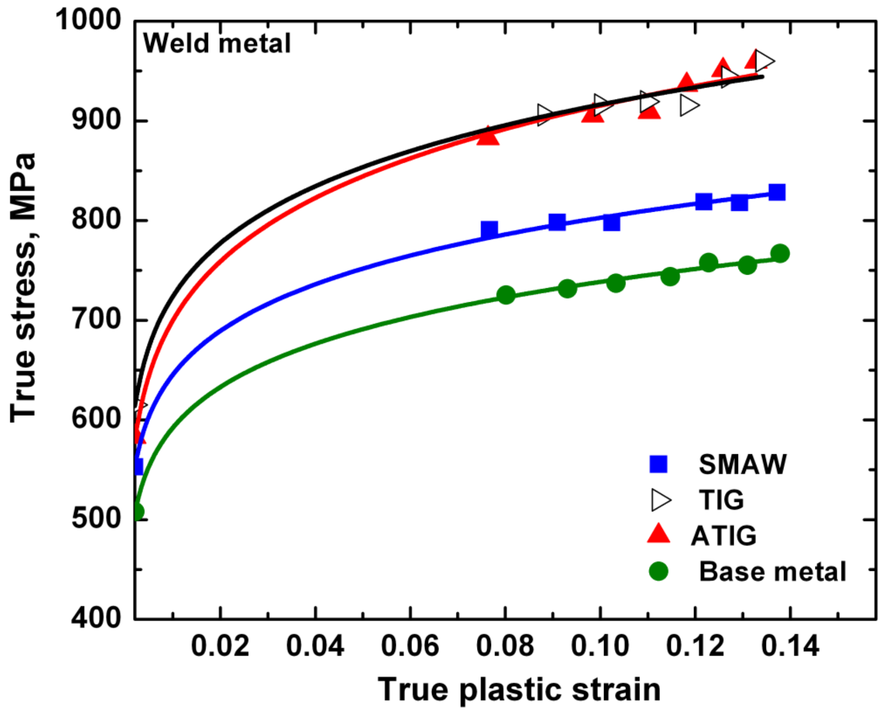

Fig. 5.31 Comparison of Flow Curves of Weld Metals of Joints Fabricated by Different Welding Processes and the Base Metal

From the ABI analysis on all the three welding processes (Fig. 5.31) shows that weld joints of A-TIG and TIG having similar tensile strength followed by SMAW joint. In Fig. 5.32 the HAZ region of A-TIG process is having higher tensile strength. The higher strength in the HAZ is attributed to high carbon martensite. Higher carbon in martensite is due to high heat input during A-TIG welding process which in turn causes higher austenitizing temperature in the HAZ region. Higher austenitization temperature could dissolve more precipitates formed during tempering into the austenite matrix. Austenite with dissolved carbon transformed into high carbon martensite in the HAZ region. Therefore, dissolved carbon was more in the HAZ of A-TIG weld joint due to higher austenitization temperature compared to that of other two weld joints. SMAW and TIG HAZ region are having similar tensile strength values. This is again attributed to high carbon martensite formed in the HAZ of the A-TIG weld joint. Fig. 5.33 shows the flow curves for the Inter critical HAZ of all the three weld joints. It is observed that IC HAZ exhibits lower strength compared to weld metal, coarse HAZ and base metal in all the three weld joints. This is attributed to partial phase transformation during weld thermal cycle which caused the softening in the ICHAZ. The optical micrographs could not reveal the partial phase transformations clearly. TEM analysis has been carried out on the ICHAZ and shown in Fig. 5.34 clearly shows tempered ferrite (TF) and martensite transformed zones. The incomplete phase transformation during the weld thermal cycle caused the softening in the ICHAZ of the weld joints. Since the strength is lowest at ICHAZ, this value should be taken for designing components.

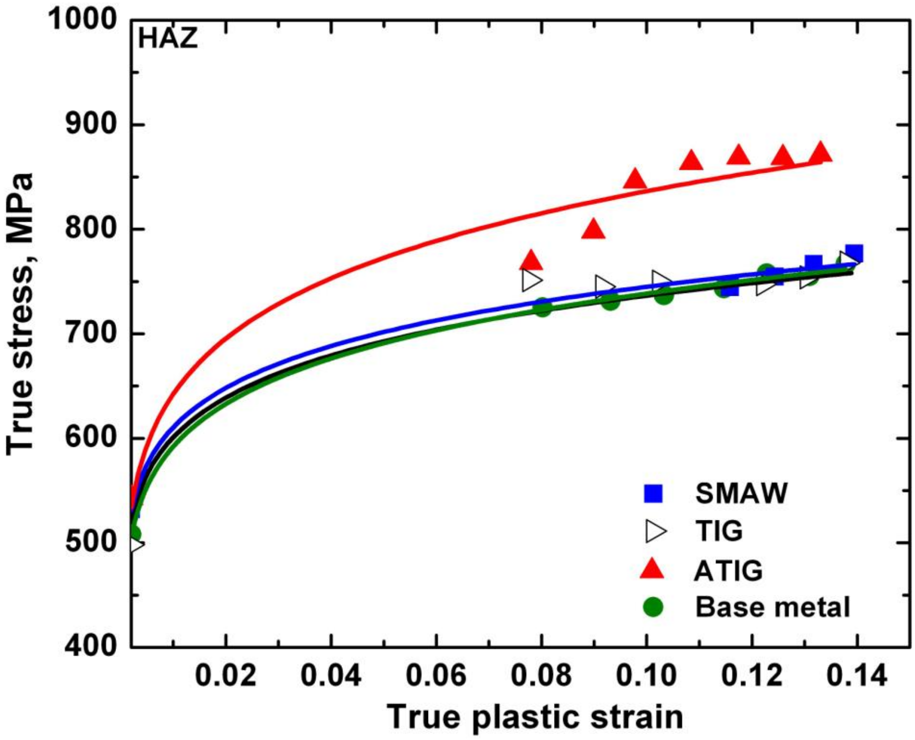

Fig. 5.32 Comparison of Flow Curves of HAZ of Joints Fabricated by Different Welding Processes and the Base Metal

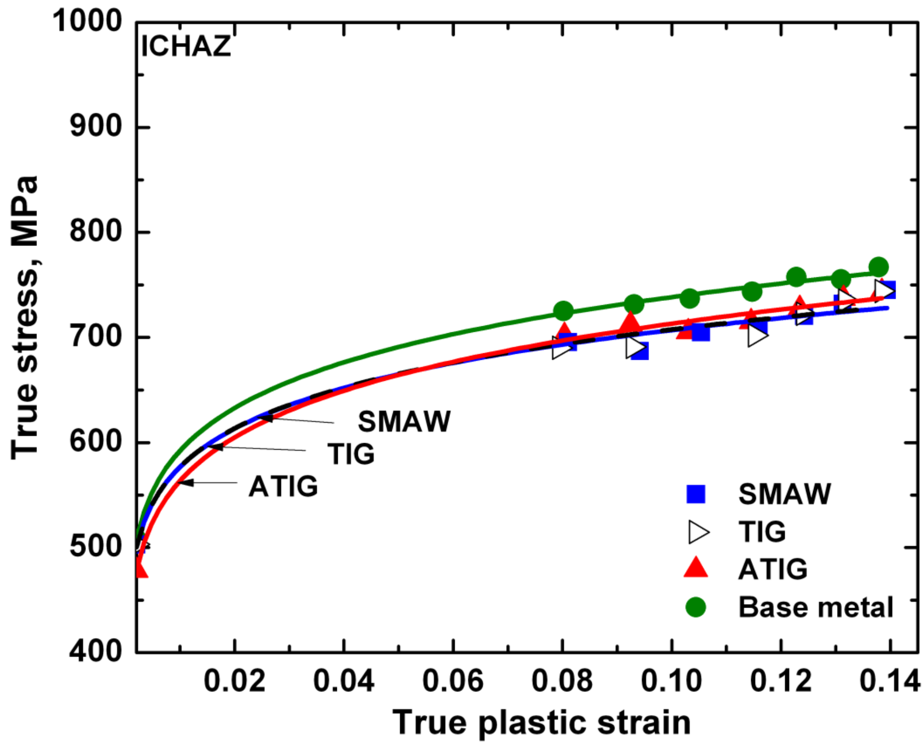

Fig. 5.33 Comparison of Flow Curves of ICHAZ of Joints Fabricated by Different Welding Processes and the Base Metal

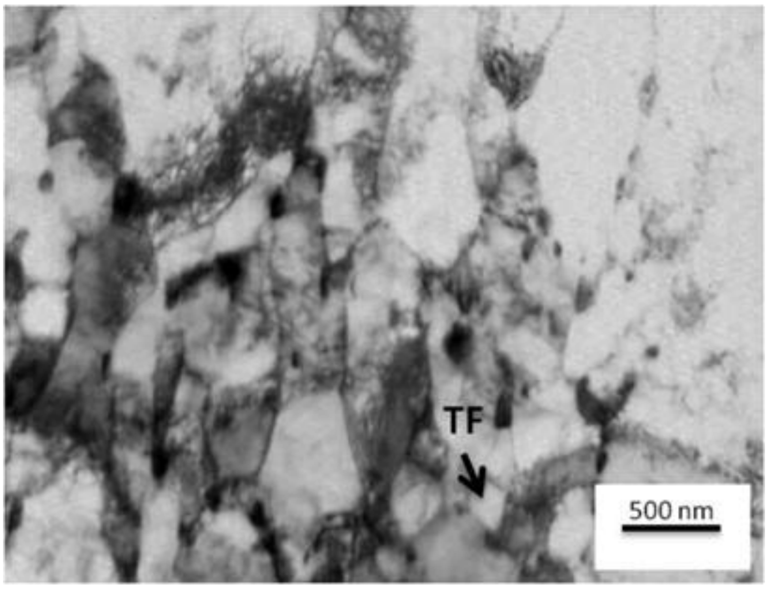

Fig. 5.34 Typical TEM Microstructure from ICHAZ

5.3.5 Comparison of Strength (YS & UTS) and Strain Hardening Coefficients

The variation of YS across various zones of weld joints as determined from ABI tests on all the three welding processes shown in Fig. 5.35. It was observed that weld joint fabricated

TIG welding showed higher YS at weld metal, followed by A-TIG and SMAW process joints. This may be due to finer prior austenite grains in the weld metal of TIG weld joint. However in HAZ region, the YS values observed to be higher in A-TIG and SMAW than TIG process. The variations of UTS across various regions of A-TIG, SMAW and TIG weld joints are shown in Fig. 5.36. The UTS curves showed that strength is higher in A-TIG compared to TIG and SMA weld joints. This is again attributed to high carbon martensite in the A-TIG weld metal and HAZ. The values of strain hardening exponent across various zones of SMAW,TIG and A-TIG weld joints is shown in Fig. 5.37 as bar chart. The strain hardening exponent exhibited slight variation across the zones for all the weld joints (ranging from 0.095 - 0.115). Strain hardening exponent is a measure of the increase in strength of materials due to plastic deformation. The strain hardening of materials is reported to depend on the microstructure, grain size, temperature and strain rate [193]. In the present case the slight variation in the strain hardening across the weld joints is attributed to variation in grain size and the carbon content in the martensite. A-TIG weld metal exhibited a carbon content of 0.122 while TIG weld metal exhibited a carbon content of 0.108 and SMA weld metal exhibited a carbon content of 0.099. Higher carbon is dissolved in the martensite of the A-TIG weld metal. Higher the carbon content, there is enhanced interaction between the dislocations and the carbon atoms. Carbon atoms play the role of obstacles to dislocation movement. More stress is required to move the dislocations and hence the A-TIG weld metal exhibits higher strain hardening exponent. The peak temperature seen during A-TIG welding is higher in the weld metal region as well as HAZ region. This is also clear from the coarser grain size observed in the weld and HAZ of A-TIG weld joint. As more precipitates dissolve in to the matrix during weld thermal cycle, carbon content in solid solution is higher in the weld and HAZ martensite of the A-TIG weld joint. Therefore, strain hardening exponent is higher across all the regions of the A-TIG weld joint.The lower strain hardening exponent in the SMAW weld metal is attributed to coarser grain size and lower carbon content in the martensite. The TIG weld metal exhibited carbon content in between that of the A-TIG and SMA weld metals. Hence strain hardening values exhibited by TIG weld joint is in between that of A-TIG and SMAW weld joints. The same interpretation can be substantiated using UTS/YS ratio shown in Fig. 5.38 UTS/YS ratio is a measure of uniform elongation and the toughness of a material and can delay the onset of necking. Therefore higher UTS/YS ratio is beneficial. Regardless of welding process, ICHAZ has the lowest value. The austenite formed on intercritical heating has lower carbon content in solution than normally found with other regions [194]. The transformation of low carbon austenite into bainite/martensite leads to softening of ICHAZ during the welding process which might have lowered UTS/YS ratio.

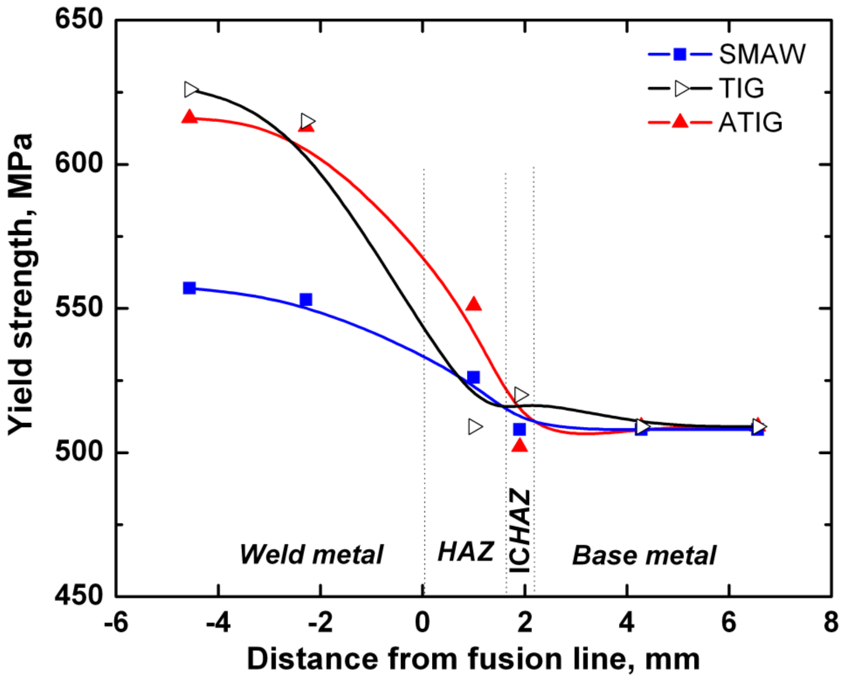

Fig. 5.35 YS variation Across the 9Cr-1Mo Steel Weld Joints

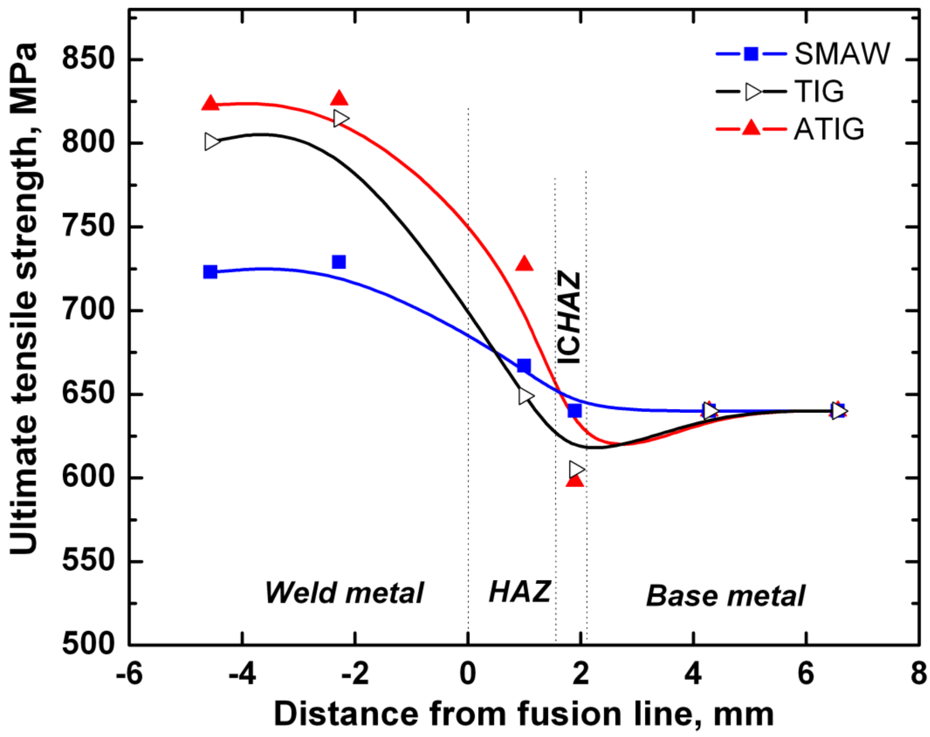

Fig. 5.36 UTS variation Across the 9Cr-1Mo Steel Weld Joints

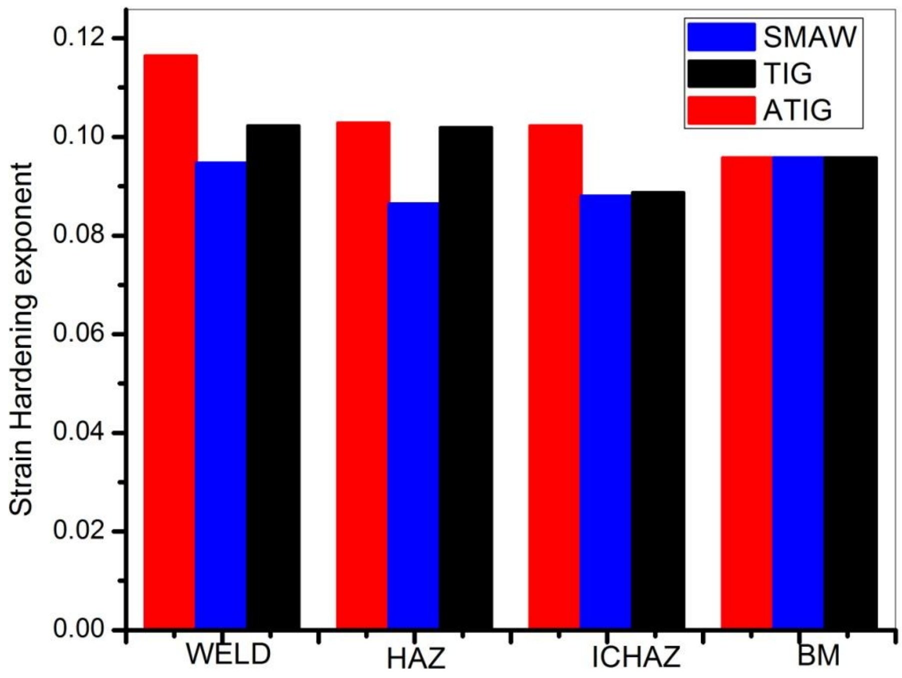

Fig. 5.37 Strain Hardening Exponent Values for Various Zones of 9Cr-1Mo Steel Weld Joints

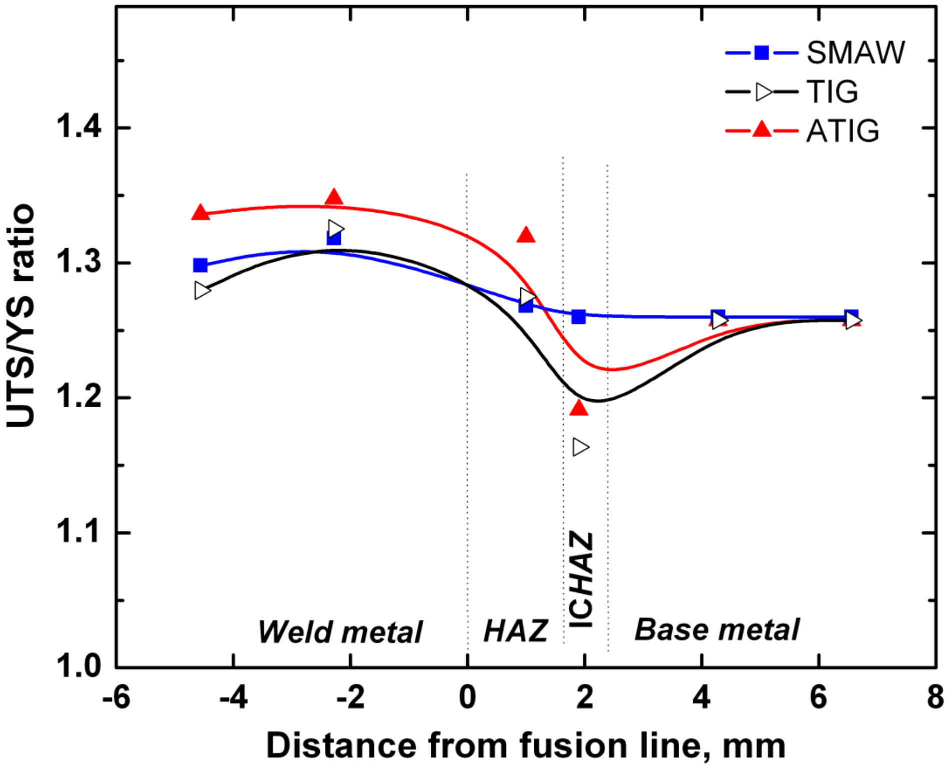

Fig. 5.38 Variation of UTS/YS Ratio Across the Weld Joints

Among the various welding processes, A-TIG showed the highest UTS/YS ratio. This can be correlated with the formation of harder martensite in the A-TIG weld metal. Low carbon martensite in TIG weld metal and coarser grain size and low carbon martensite in SMA weld metal resulted in lower UTS/YS ratios. However, among the various welding processes, A-TIG weld joint showed higher UTS/YS ratio in weld metal and HAZ region. SMAW showed slightly higher UTS/YS ratio in ICHAZ region.

Hence, among the three welding processes used for welding of 9Cr-1Mo steel, weld joint fabricated by A-TIG welding process exhibited the higher strength and strain hardening exponent values and similar ductility values compared to that of the weld joints fabricated by TIG and SMA welding processes. It is recommended that A-TIG welding process shall be used for fabricating the hexcan subassembly wrapper component made of 9Cr-1Mo steel.

5.3.6 Summary

The YS and tensile strength were observed to vary significantly across the 9Cr-1Mo steel weld joints. The YS and UTS decreased systematically from weld metal to base metal except at ICHAZ which exhibited least strength values. The incomplete phase transformation during the weld thermal cycle caused the softening in the ICHAZ of the weld joints. The A-TIG weld metal exhibited higher strength values followed by TIG and SMA weld metals respectively. A-TIG weld joint exhibited higher strain hardening values while SMA weld joint exhibited the least strain hardening values. High carbon martensite in the weld metal and HAZ of the A-TIG weld joint caused the higher strength and strain hardening values compared to that of the other two weld joints in 9Cr-1Mo steel. Hence, among the three welding processes used for welding of 9Cr-1Mo steel, weld joint fabricated by A-TIG welding process exhibited the higher strength and strain hardening exponent values compared to that of the weld joints fabricated by TIG and SMA welding processes. In terms of strength properties, A-TIG welding process is found to be a better for fabricating components made of 9Cr-1Mo steel.

5.4 Zone Wise Evaluation of Creep Behavior of 9Cr-1Mo Steel Weld Joints using Impression Creep Testing Technique

The material during impression creep exhibits the same stress and temperature dependence as a uniaxial tensile creep test. Impression creep tests therefore can be used to produce reliable creep strain rates equivalent to those obtained from a uniaxial creep test. IC testing requires shorter testing times typically 300 hrs. Also localized testing on the individual zones of the weld joint such as the weld metal or HAZ can be carried out. Impression creep curves exhibited primary and secondary creep stages similar to uniaxial creep curves. However, the tertiary stage was absent. The steady state creep rates determined from impression velocities were found to be in good agreement with the steady state creep rates obtained from uniaxial creep tests. Equivalence between applies stress and steady-state impression velocity with uniaxial creep stress and steady state creep rate respectively has been established based on the laws of mechanics for time-dependent plasticity. Characterization of creep properties of narrow microstructural regions such as HAZ of weld joints which is impossible to determine in uniaxial creep test is possible by IC testing. Therefore, zone wise evaluation of creep behavior of 9Cr-1Mo steel weld joints fabricated by different welding processes using impression creep testing has been carried out in the present study.

5.4.1 Analysis of Impression Creep Parameters

Punching stress and impression velocity:

In impression creep test, a constant load L is applied to the test specimen through a cylindrical punch of diameter d. The mean pressure under the punch is referred to as the punching stress and is given by the equation 5.17,

$$\sigma_{imp} = 4L/\pi d^2 \qquad (5.17)$$

Under the punching stress σ_{imp}, the cylindrical punch penetrates into the surface of the test specimen to a depth h in time t. The rate at which the cylindrical punch penetrates the specimen surface is referred to as impression velocity and is given by the equation 5.18,

$v_{imp} = dh/dt$ (5.18)

5.4.1.1 Correlation between Impression Creep Parameters and Conventional Uniaxial Creep Parameters:

For the characterization of creep behaviour of materials using impression creep test, it is essential to establish correlations between the impression creep parameters (σ_{imp}, v_{imp}) and uniaxial creep parameters (σ_{uni}, ε_{uni}). The steady state strain rate ε_{uni} in uniaxial creep test correlates with the ratio of impression velocity v_{imp} to the punch diameter d used in the impression creep test. Empirically, there is a factor, about 0.33, which converts the punching stress σ_{imp} to an equivalent stress σ_{uni} in conventional uniaxial creep tests. These relations have been established numerically by finite element calculations [195] and verified experimentally [155,196-197]. It is generally accepted that for materials obeying power-law creep, the steady state strain rate

ε_{uni} is related to the uniaxial stress σ_{uni} by the equation 5.19,

$\varepsilon_{uni} = A\, \sigma^n_{uni}$ (5.19)

where n is the stress exponent and A is the power law coefficient which incorporates the temperature dependence of steady state strain rate. Li and co-workers [155,195,198] carried out finite element analysis for materials obeying power-law creep. The impression creep experiment was simulated by considering power law constitutive equation for the deformation of each finite element. This power law defines the relation between the creep rate and the Von Mises stress. The Von Mises flow rule was used to calculate the various strain components. The calculation was done for many time intervals until a trend toward a steady state was clearly indicated. It was found that the impression velocity v_{imp} was proportional to the punch diameter ($v_{imp}/d \; \alpha \; \sigma^n_{imp}$) and had the same stress dependence as was observed in the conventional uniaxial creep test. Hence, where, v_{imp} is the impression velocity, σ_{imp} is the punching stress, d is the diameter of the punch and n is the stress exponent value. Researchers have generally resorted to trial-and-error method to correlate σ_{imp} and v_{imp}/d in impression creep to σ_{uni} and ε_{uni} in conventional uniaxial creep. The general forms of these correlations are given by the equations 5.20 and 5.21,

$$\sigma_{uni} = \alpha\, \sigma_{imp} \qquad (5.20)$$

and $$\varepsilon^{\circ}_{uni} = v_{imp} / \beta d \qquad (5.21)$$

where, α and β are the correlation factors.

Experimentally determined values of α range from 0.26 to 0.36 for a range of materials such as Pb, TiAl alloys, Mg–8Zn–4Al–0.5Ca alloy, Zn, cast Mg–5Sn–xCa alloys, 316 stainless steel [155,198–203]. Equation (5.22) is often used with β = 1 [155,196,199,200,202]. For the present analysis, we used the conversion factors α = 0.33 and β = 1, determined by finite element calculation reported by researcher in Ref. [195] to transform the creep data from impression creep testing to that of the conventional uniaxial creep testing for 9Cr-1Mo steel weld joints.

5.4.2 Microstructures of Impression Creep Tested Specimen

The typical optical microstructure of the impression creep tested samples of weld metals is given in Fig. 5.39 (a,b,c). Three distinct regions were observed which are labelled with number 1, 2, and 3. In order to distinguish these three distinct regions clearly, curved lines are drawn. In region 1 no significant changes in grain shape were observed. This shows that the stress in this region may be hydrostatic in nature and hence there is no plastic deformation. In region 2 extensive plastic deformation is visible as evident from the elongated grains. No change in shape of grains in the region 3 which is far away from the indentation indicates absence of plastic deformation in this region. This clearly demonstrates the localized nature of deformation in impression creep test.

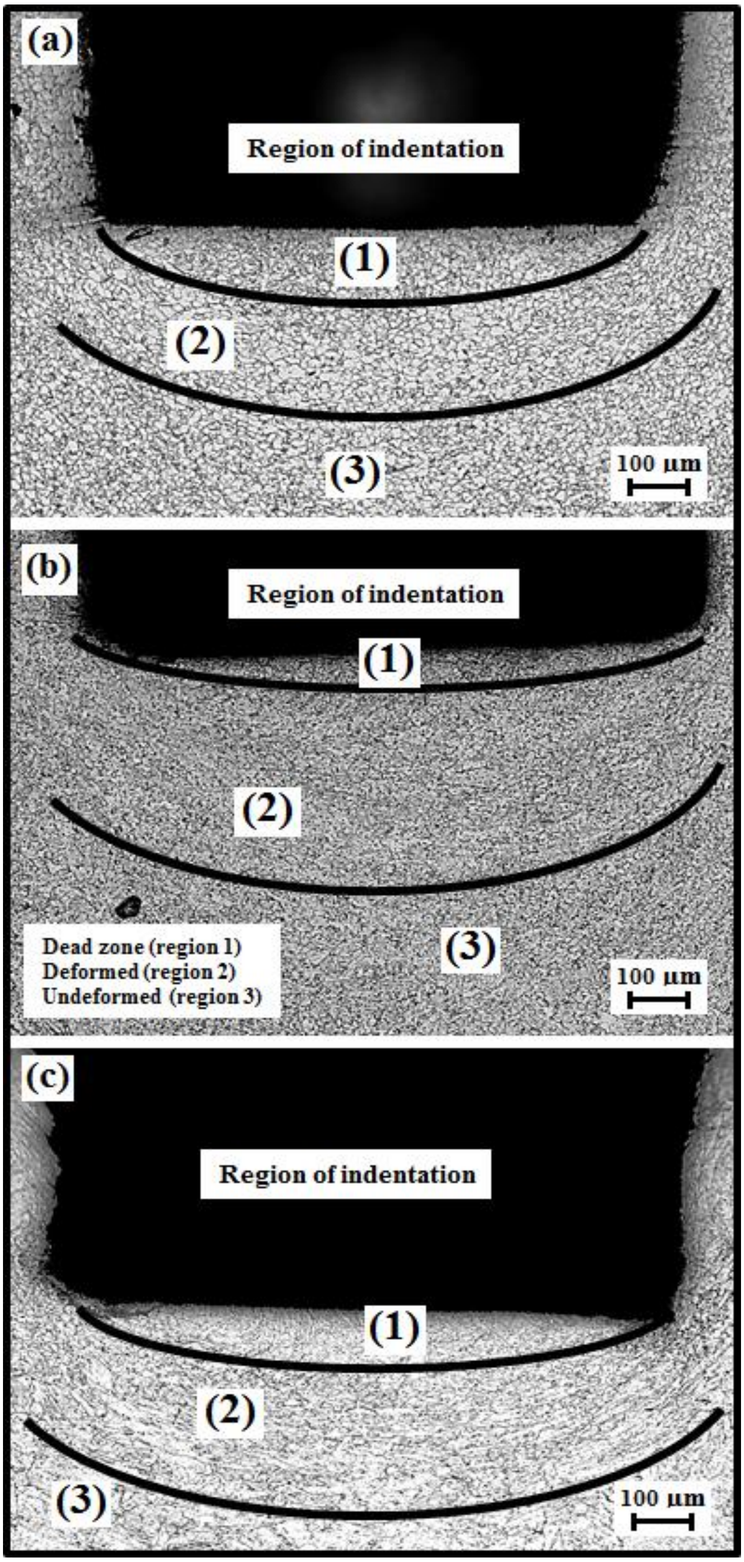

Fig. 5.39 Optical Images of Impression Creep Tested Specimen (a) SMAW weld (b) TIG weld (c) A-TIG weld

5.4.3 Impression Creep Curves

Fig. 5.40 (a-f) depict the typical impression creep curves obtained zone wise for 9Cr-1Mo steel weld joints under punching stress range of 100 to 300 MPa. Impression creep curves displayed two characteristic creep stages, i.e., primary creep stage and secondary creep stage. However, the tertiary creep regime that is clearly visualized in the conventional creep curves do not appears in impression creep. This is due to the nature of loading, which is compressive in impression creep testing. As a consequence, creep cavities and local damage of specimen in terms of necking that occur in the tertiary creep regime of tensile creep, do not manifest in impression creep at smaller strains. It can be observed that with increase in temperature at a nearly constant punching stress resulted in higher indenter penetration rates. This is in line with the observation of uniaxial creep curves, i.e., with the increase in temperature the creep rate increases.

In general, at all the test temperatures of 848, 873 and 898 K, base metal region exhibited higher resistance to creep deformation than that of the HAZ of the 9Cr-1Mo steel weld joints fabricated by all the three welding processes as observed from the depth of indentation against time plots (Fig. 5.40 b, d and f). HAZ of the A-TIG weld joint exhibited better resistance to creep compared to that of the HAZ of the weld joints fabricated by SMAW and TIG welding processes. At 848 K SMAW weld metal exhibited better resistance to creep deformation compared to that of base metal and other weld metals. Among all welds TIG weld metal exhibited the least resistance to creep deformation at all test temperatures.

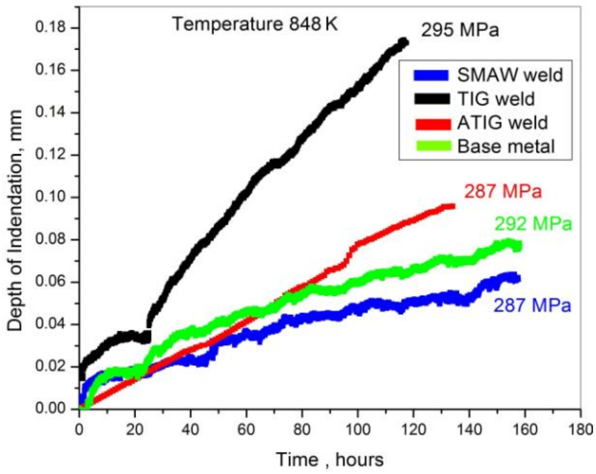

a)

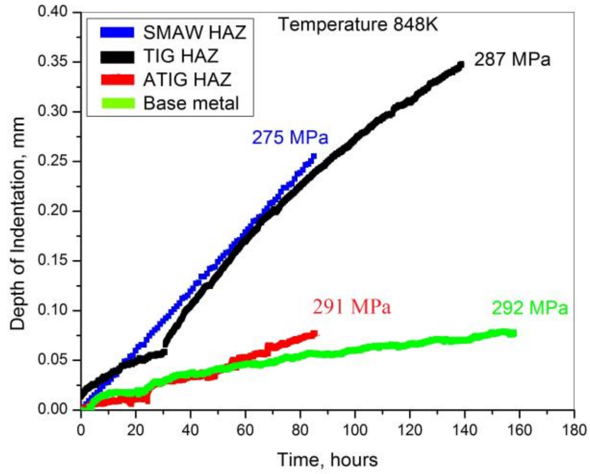

b)

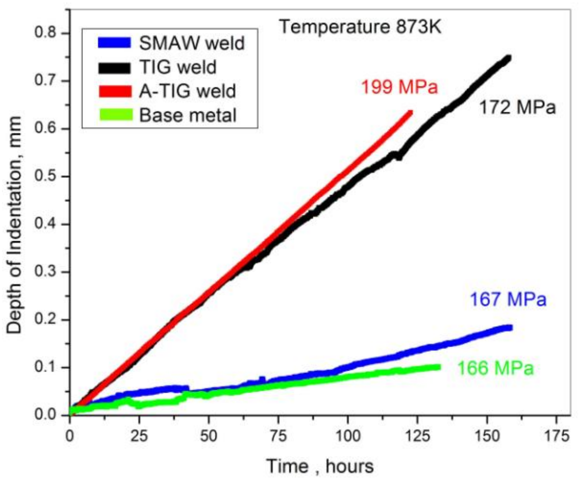

c)

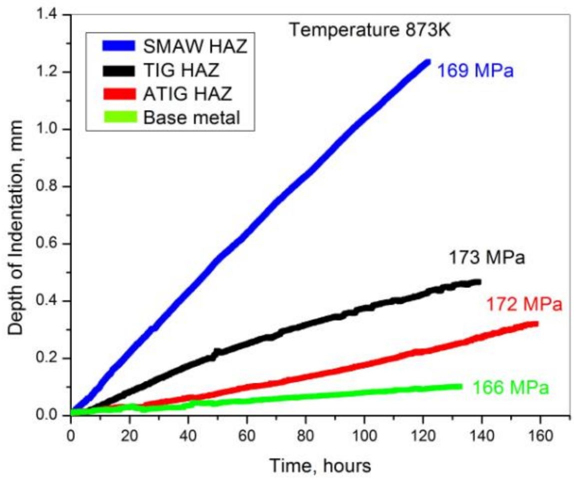

d)

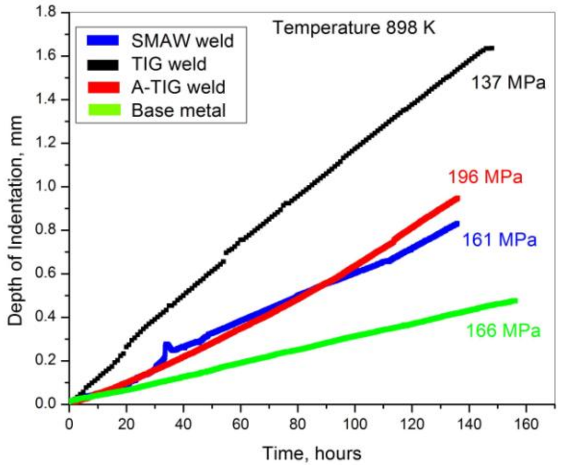

e)

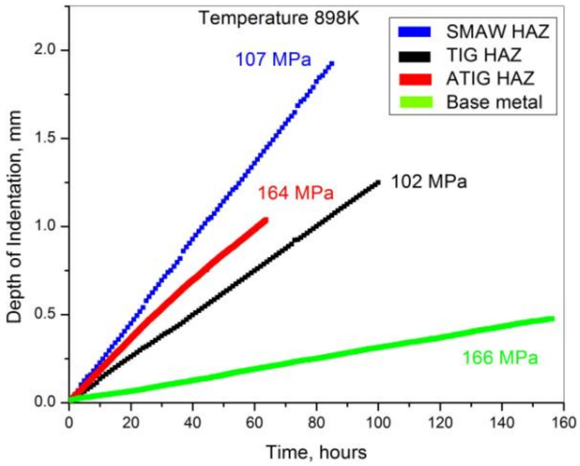

f)

Fig. 5.40 (a-f). Impression Creep Plots of Base Metal, SMAW, TIG and A-TIG Weld Metal and HAZ in 3 Different Temperatures (848, 873, 898 K)

5.4.4 Analysis of Activation Energy for Creep

The steady state creep rate of the material depends on the stress and temperature. When the stress is constant, creep rate depends on the temperature according to Arrhenius rate equation 5.22 which is given by,

$$\varepsilon^{\circ}_{ss} = A\ \sigma^{n} \exp(-Qc/RT) \qquad (5.22)$$

where ε°_{ss} is the steady state creep rate, *A* is the constant, *Qc* is the apparent activation energy for rate controlling process, *R* is the universal gas constant (8.314 Jmol-1K-1), *T* is the absolute temperature.

To determine the apparent activation energy for creep deformation during impression creep testing technique, a similar methodology which we generally use in conventional creep technique was followed here. The steady state impression velocities were plotted against the reciprocal of the absolute temperature on a semi-logarithmic scale as shown in Fig. 5.41. The graph illustrates the temperature dependence of the steady state impression velocity at constant punching stress of 166 MPa. Arrhenius rate equation was found to be operative between the steady state impression velocity and the temperature. Hence, Arrhenius rate equation in impression creep can be stated by the equation 5.23,

$$\frac{v_{imp}}{d} = A\ \sigma_{imp}^{n} \exp\left(-\frac{Q_c}{RT}\right) \qquad (5.23)$$

where, v_{imp} is the steady state impression velocity, *d* is the diameter of the punch, *Qc* is the apparent activation energy for rate controlling creep deformation process, *R* is the universal gas constant and *A* is the constant.

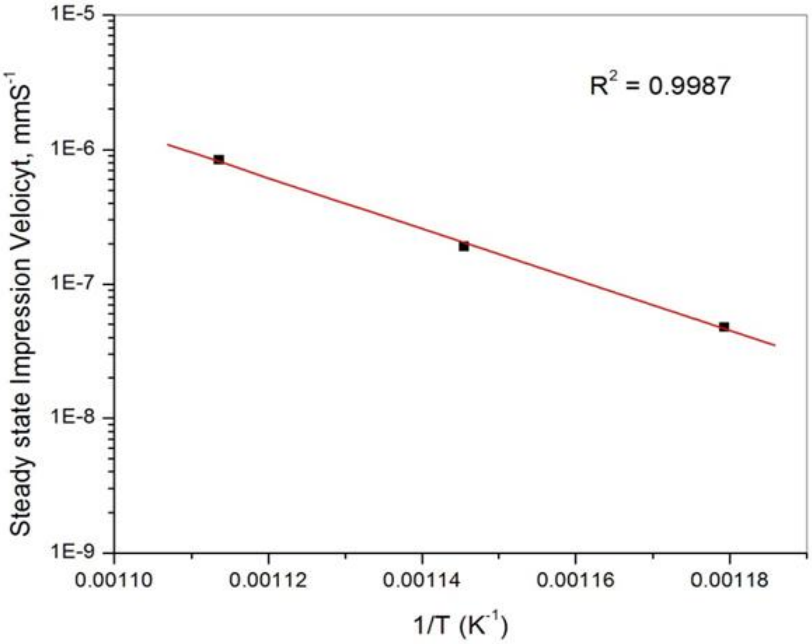

Fig. 5.41 Arrhenius Type Relationship between the Steady State Impression Velocity and the Testing Temperature for 9Cr-1Mo Steel

Table 5.12 Steady State Creep Rate and Activation Energy

	Temp (K)	**Base metal**	**SMAW Weld**	**SMAW HAZ**	**TIG weld**	**TIG HAZ**	**A-TIG Weld**	**ATIG HAZ**
Steady state creep rate /sec	848	4.780×10^{-8}	4.712×10^{-8}	5.374×10^{-7}	2.551×10^{-7}	3.871×10^{-7}	9.139×10^{-8}	2.30×10^{-7}
	873	1.907×10^{-7}	3.831×10^{-7}	2.749×10^{-6}	1.191×10^{-6}	8.806×10^{-7}	1.179×10^{-6}	5.862×10^{-7}
	898	8.389×10^{-7}	1.629×10^{-6}	9.391×10^{-6}	3.586×10^{-6}	5.671×10^{-6}	2.088×10^{-6}	3.989×10^{-6}
Activation energy KJ/mol		362 ± 13	448 ±25	362 ± 20	334 ± 20	338 ± 25	398 ± 13	359 ± 18

Following equation (5.23), the steady state impression velocities were plotted against the reciprocal of the absolute temperature on a semi-logarithmic scale as shown in Fig. 5.41 for 9Cr-1Mo steel. The graph illustrates the temperature dependence of the steady state impression velocity at constant punching stress of 166 MPa. The apparent activation energy for the 9Cr-1Mo steel was evaluated from the slope of the straight line; i.e.,$-Qc/2.3R$ was 362 KJ/mol. Similarly, the activation energy evaluated for various zones as a function of welding processes is given in table 5.12 SMAW weld joint exhibited activation energy of 448 KJ/mol in the weld metal and 362 KJ/mol in the HAZ. A-TIG weld joint exhibited activation energy of 398 KJ/mol in the weld metal and 359 KJ/mol in the HAZ. TIG weld joint exhibited activation energy of 334 KJ/mol in the weld metal and 338 KJ/mol in the HAZ.

5.4.5 Microstructural Characterization of Impression Creep Samples

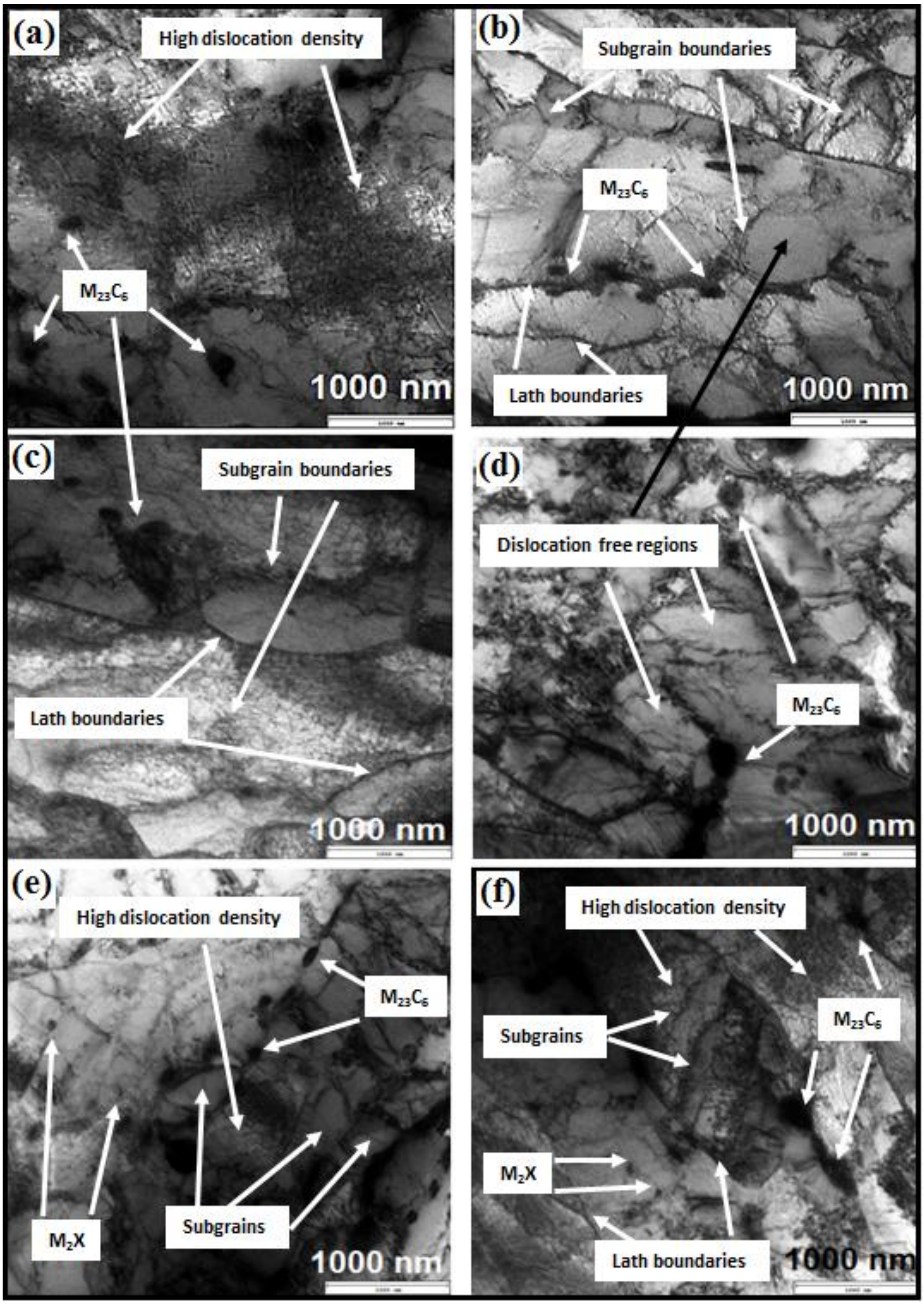

Fig. 5.42 (a-f). TEM Images of Deformed Region of the Impression Creep Samples
a) SMAW Weld b) SMAW HAZ c) TIG Weld d) TIG HAZ e) A-TIG Weld f) A-TIG HAZ

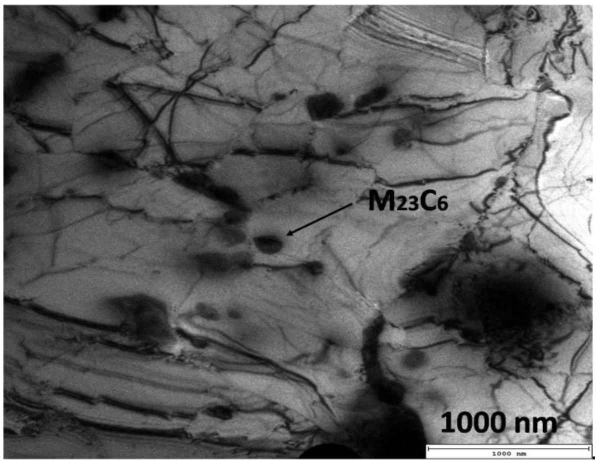

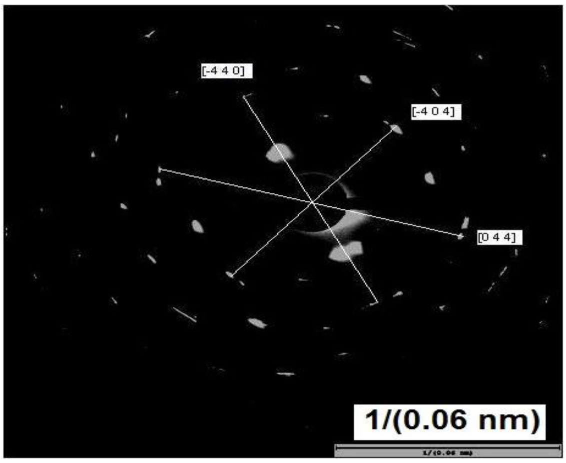

Fig. 5.43 TEM Image and SAD Pattern

The TEM microstructures of deformed weld and HAZ zones are shown in Fig. 5.42(a-f). Fig. 5.42a depicts the presence of high dislocation population in forms of tangles in SMAW weld region after the impression creep.

The dislocation density is relatively lower in case of crept HAZ of SMAW shown in Fig. 5.42 b. HAZ of SMAW also shows that more polygonized subgrain and dislocations free regions after creep. There are two main reasons for this difference. First, the initial dislocation density is relatively high in case of welds compared to HAZ due to the difference in peak temperature of both zones and thus it is also reflected even after the impression creep of the weld. However, the formation of subgrains, polygonization and dislocation free regions indicate that recovery rate of HAZ is relatively high compared to weld metal. The observations of Figs. 5.42 c-f reveal that, also for the other two processes TIG and A-TIG, the HAZ is recovered more compared to weld metal and resulted in dislocation free regions and subgrains formation. Fig. 5.42 d depicts that the TIG welded HAZ is having more dislocation free regions as well as coarse subgrains compared to all other tested conditions. The presence of coarse $M_{23}C_6$ carbides precipitates can be visualized along with the lath and subgrain boundaries of all tested specimens. Figs. 5.42 e and f show the substructure developed after the impression creep of A-TIG weld and HAZ, respectively. It can be observed that fine M_2X

nitrides are distributed throughout the matrix of A-TIG weld and HAZ. It can be also visualized that the relative precipitate density of M_2X is high in case A-TIG weld and HAZ compared to other two welds and their HAZ. The recovery of substructure is relatively low in case of A-TIG weld and HAZ resulted in smaller subgrains compare to TIG weld and HAZ, and SMAW HAZ.

As an example, TEM selected area diffraction pattern (SAD) of the SMAW weld metal crept at 898 K is shown in Fig. 5.43. Indexing of SAD pattern identified that the precipitate is $M_{23}C_6$.

In an impression creep test the material underneath the indenter undergoes a complex heterogeneous deformation. In order to find out the strain localization and deformation behaviour EBSD analysis near the impression of crept weld metals was carried out. The IPF map that represents the orientation of different grainsof SMAW weld region at low magnification of 250X and step size of 2.0 µm,to cover the whole area of deformation,is shown in the Fig. 5.44. The inverse pole figure map shows that there are 3 distinct regions of deformation those are separated with black curved lines. Region 1 shows the dead zone of the crept weld metal with no deformation and thus having no effect of loading. Region 2 is maximum deformed region and grain are bulged due to the applied indentation stress. The region marked as 3 in Fig. 5.44 is unaffected by impression stress. This is due to the fact that, stress is exhausted after the region 2, hence no deformation can be observed in region 3. The region immediate under the punch shows an insignificant change in strain accumulation, but shear deformation is induced at a distance below this region 1. Similar observation was found in case of TIG weld metal. The IPF map of TIG weld zone with step size of 2.0 µm and 0.6 µm is shown in Fig. 5.45 a and b, respectively. Three distinct regions are marked as 1, 2 and 3 for dead zone, deformation zone and unaffected zone, respectively. The width of dead zone is narrowest in the case TIG weld metal and grains are bulged due to the influence of load in the deformation zone 2. The region in between the black lines shows the extensive plastic deformed area. Fig. 5.45 b is the enlarged view of the marked rectangular area in Fig. 5.45 a. It can be visualized that finer and well polygonized grains are formed in the deformed region 2 (Fig. 5.45 b).

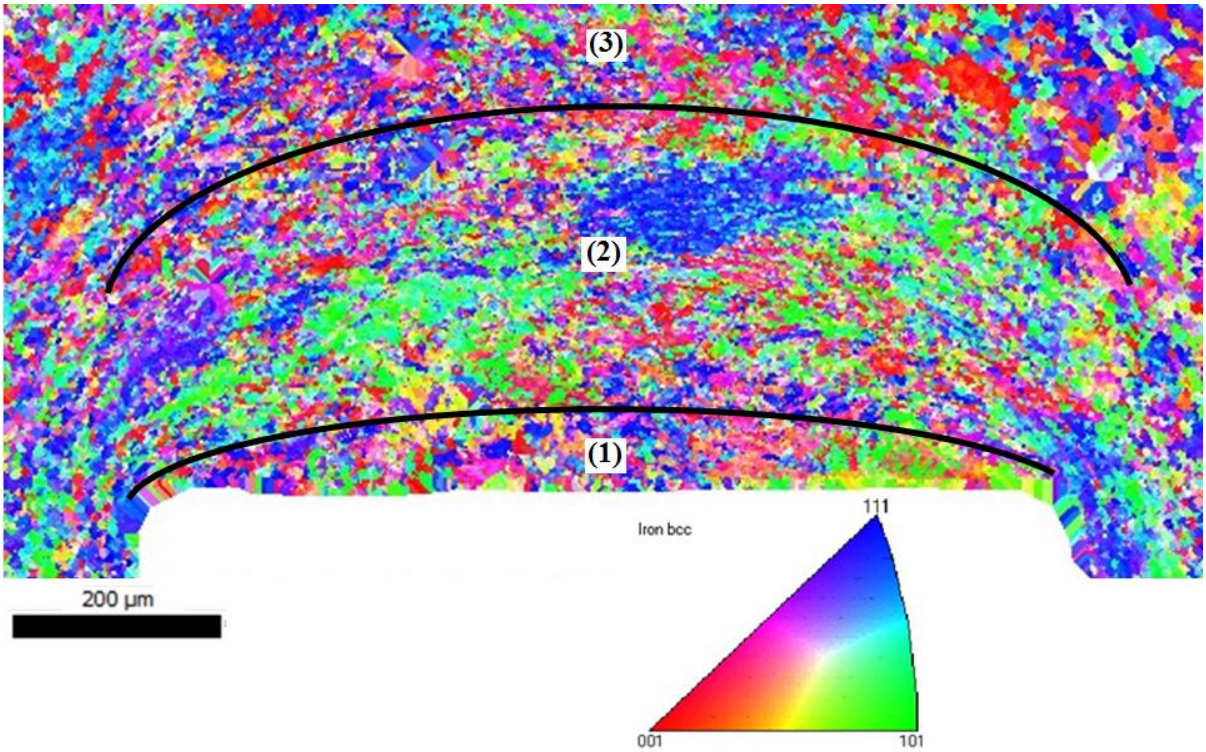

Fig.5.44 IPF map of SMAW weld region crept at 873 K / 168 MPa.

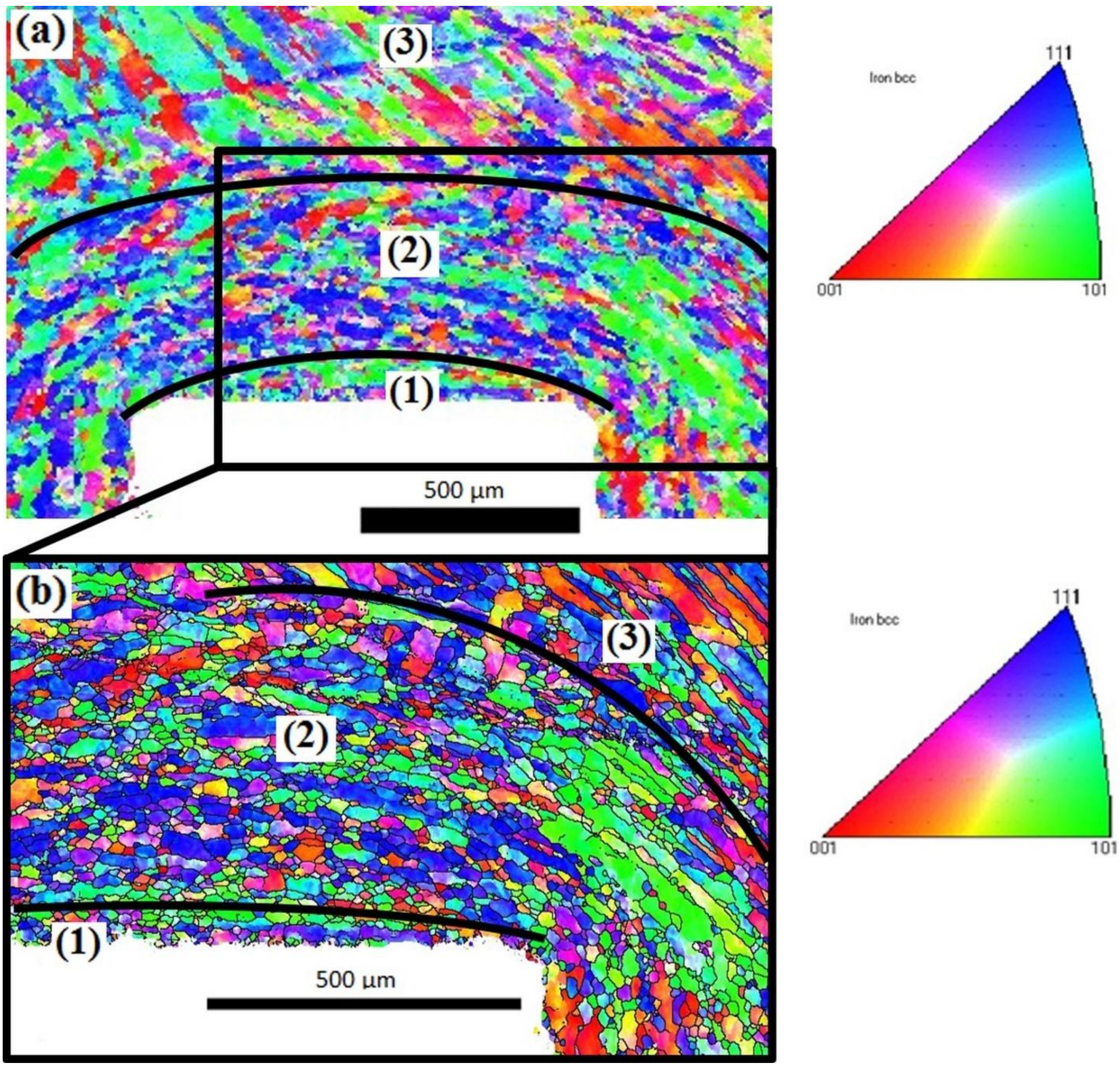

Fig.5.45 IPF maps of the TIG weld region crept at 873 K / 172 MPa(a) step size 2 µm and (b) step size 0.6 µm

Figs. 5.46 a and b depict the IPF map of A-TIG weld zone with step size of 2 µm and 0.6 µm, respectively.Similar to SMAW and TIG, A-TIG weld metal also exhibited three distinct regions. The dead zone 1 marked in Fig. 5.46 a is relatively thicker compare to SMAW and TIG welds and there is no significant change in the grains of the region just below the indenter. The region between the curved black lines is the plastically deformed region shown by the bulged grains under the influence of external indentation load. It can be visualized from the Fig. 5.46 b that, in comparison to TIG weld the grains in the deformation region of A-TIG welds are elongated and relatively less polygonised, suggesting less influence of stress.

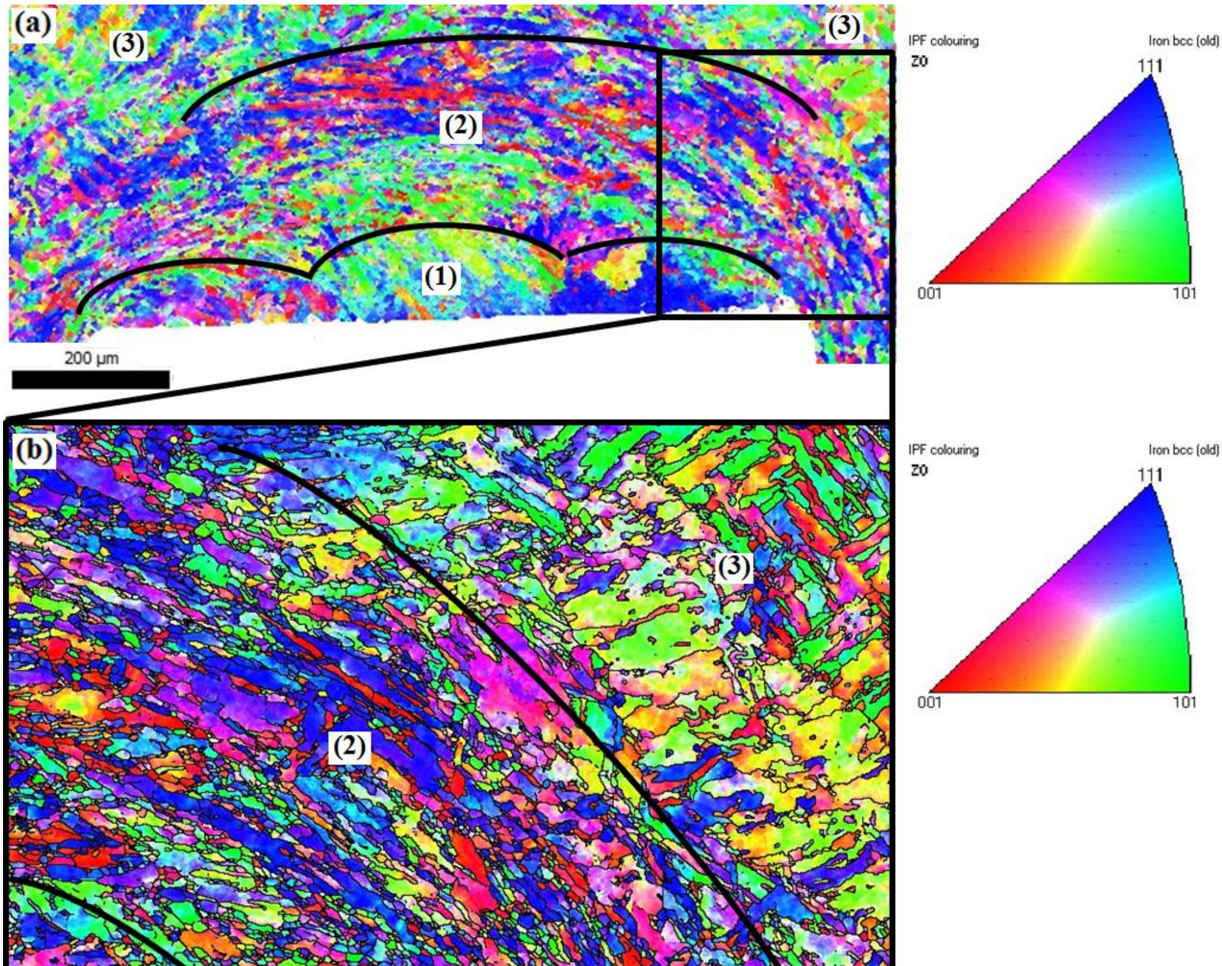

Fig. 5.46 IPF maps of the A-TIG weld region crept at 848 K / 275 MPa(a) step size 2 µm and (b) step size 0.6 µm

Based on the impression creep tests and the analysis, the activation energies for all zones are found in the range of 334 to 448 KJ/mol. These values of activation energy are higher than that of the glide energy of dislocations, i.e., 241.2 KJ/mol. Also, the range of energies lie within the reported values of dislocation creep [204]. This suggests that dislocation creep is the governing creep mechanism and deformation is assisted by the climb and glide motions of dislocations.

5.4.6 Summary

Impression creep technique and microstructural characterization were employed to characterize the creep behaviourand to identify the governing creep mechanism of distinct microstructural regions such as the weld metal, the heat-affected zone and the base metal of P9 steel weld joints fabricated by different welding processes.

Base metal exhibited better creep resistance compared to all HAZs and it was ascribed to the presence of high number density and small mean radius of precipitates compared to HAZs. Among all HAZs, A-TIG HAZ exhibited best creep resistance. This superior creep resistance was ascribed to relative high number density and small mean radii of strengthening precipitates. Resistance to creep deformation was least in the HAZ of the weld joints compared to the weld metal regions. This difference in creep resistance was due to the difference in prior austenitic size and dislocation density. It was found that SMA weld metal exhibited better creep resistance compare to other welds and base metal due to the presence of larger prior austenitic grain size. Activation energy for creep was in range of 334-448 KJ/mol for various zones and dislocation creep is identified as the governing creep mechanism in the tested range and the creep deformation is controlled by climb and glide motion of dislocations. Among all three welding processes A-TIG welding process is recommended for joining the power plant components because it results in strongest HAZ in terms of creep deformation.

CHAPTER 6

SUMMARY AND CONCLUSIONS

In an attempt to provide solutions to the problems associated with welding of 9Cr-1Mo steel a detailed study was undertaken to (a) optimize the A-TIG welding process parameters to achieve the target DOP and HAZ width in 9Cr-1Mo steel welds (b) study the effect of different welding processes on the microstructure and mechanical properties and residual stresses of 9Cr-1Mo steel weld joints (c) Zone wise evaluation of mechanical properties such as strength and creep on 9Cr-1Mo steel weld joints fabricated by different welding processes using small specimen testing techniques such as ABI and Impression creep testing techniques. Based on the detailed studies on the effect of various welding processes on the 9Cr-1Mo steel weld joints, the following conclusions are drawn.

1. Optimization has been carried out employing RSM and GA based models employing different selection operators involving roulette wheel selection and tournament selection. Optimum A-TIG welding process parameters have been successfully determined in order to achieve the target DOP and HAZ width for 9Cr-1Mo steel. During the analysis based on DOE second order quadratic models have been developed correlating process and the response variables to predict the DOP and HAZ width as a function of process variables. Using RSM methodology, current is identified as the most significant process variable influencing the DOP and HAZ width during A-TIG welding of 9Cr-1Mo steel. Both RSM and GA based models provided number of solutions in terms of process parameters to achieve the target DOP and HAZ width. RSM provided 22 number of solutions for achieving the target DOP and HAZ width while GA provided 100 solutions. However, GA based model employing tournament selection operator is found to the accurate model based on

validation experiments.

2. All the three weld joints exhibited tempered martensitic microstructure with $M_{23}C_6$ precipitates in the weld metal and HAZ. The SMA weld joint exhibited coarser prior austenite grain size in the weld metal. The grain size of the TIG weld metal are relatively finer. TEM studies showed that after PWHT, lath structure is broken up and substructures have formed in the weld metal and HAZ for all the three weld joints. $M_{23}C_6$ precipitates are seen in the prior austenite grain boundaries and subgrain boundaries.
3. The peak hardness value after PWHT for A-TIG weld joint is marginally higher (260 VHN) compared to TIG weld joint (230 VHN) and SMAW weld joint (220 VHN). Higher hardness in A-TIG weld metal is attributed to higher carbon in the martensite. Strength and ductility values are similar for all three weld joints (SMAW, TIG and A-TIG) tested by the cross weld specimens.
4. TIG weld joint exhibited higher impact toughness values compared to A-TIG and SMAW weld joints. The higher toughness may be attributed to multiple thermal cycles involved in TIG weld joint fabrication which caused complete tempering of martensite. All the three weld metals and base metal exhibited ductile to brittle transition at -40ºC. Fractographs revealed complete cleavage fracture at subzero temperature.
5. All the three weld joints showed typical 'M' shaped characteristic residual stress profile found in ferritic-martensitic steel weld joints. The peak residual stresses were found just beyond the heat affected zone of the weld joints. In the SMAW joint, residual stresses were compressive at the locations of measurement. The compressive stresses may be attributed to domination of phase transformation (martensite formation) induces stresses over the shrinkage stresses. In the TIG weld joint, the

residual stress varied from low compressive to tensile. In the A-TIG joint, residual stresses at the weld centre were found to be tensile at all the locations of measurement. In the case of A-TIG weld joint, shrinkage stresses dominate over phase transformation induced stresses.

6. The YS and tensile strength were observed to vary significantly across the weld joints. The YS and UTS decreased systematically from weld metal to base metal except at ICHAZ which exhibited least strength values. The incomplete phase transformation during the weld thermal cycle caused the softening in the ICHAZ of the weld joints.
7. The A-TIG weld metal exhibited higher strength values followed by TIG and SMA weld metals respectively. A-TIG weld joint exhibited higher strain hardening values while SMA weld joint exhibited the least strain hardening values.
8. High carbon martensite in the weld metal and HAZ of the A-TIG weld joint caused the higher strength and strain hardening values compared to that of the other two weld joints in 9Cr-1Mo steel.
9. Impression creep technique has been employed to characterize creep behavior of distinct microstructural regions such as the weld metal, the heat-affected zone and the base metal of 9Cr-1Mo steel weld joints at 848, 873 and 898 K under punching stress levels in the range of 100 to 300 MPa.
10. Base metal exhibited better creep resistance compared to all HAZs and it was ascribed to the presence of high number density and small mean radius of precipitates compared to HAZs. Among all HAZs, A-TIG HAZ exhibited best creep resistance. This superior creep resistance was ascribed to relative high number density and small mean radii of strengthening precipitates.
11. Resistance to creep deformation was least in the HAZ of the weld joints compared to the weld metal regions. This difference in creep resistance was due to the difference

in prior austenitic size and dislocation density. It was found that SMA weld metal exhibited better creep resistance compare to other welds and base metal due to the presence of larger prior austenitic grain size.

12. Activation energy for creep was in range of 334-448 KJ/mol for various zones and dislocation creep is identified as the governing creep mechanism in the tested range and the creep deformation is controlled by climb and glide motion of dislocations.
13. Among all three welding processes A-TIG welding process is recommended for joining the power plant components because it results in strongest HAZ in terms of creep deformation.

CHAPTER 7

FUTURE DIRECTIONS

The current work on the effect of welding processes on the weld attributes of 9Cr-1Mo steel weld joints can be extended further to include the effect of irradiation of the 9 Cr-1Mo steel weld joints. The work on A-TIG welding can be further improved to make this technology suitable for variety of applications. Hence there is scope for extending the work to broaden the area of application and usage. The thoughts on the directions for future work are discussed below.

1. One of the applications of 9Cr-1Mo steel is for wrapper components of FBRs, and the effect of irradiation dose on the microstructure and mechanical properties of 9Cr-1Mo steel weld joints fabricated by different welding processes can be studied in detail.
2. Numerical modeling of A-TIG process can be carried out to understand the mechanisms contributing to the increased penetration in Cr-Mo steel welds. Detailed study can be carried out to understand the effect of activated flux on the residual stresses and distortion of 9Cr-1Mo steel weld joints produced by A-TIG welding.
3. The use of A-TIG welding of 9Cr-1Mo steel could be compared with other welding processes such as Laser or hybrid Laser-Arc welding processes in terms of cost effectiveness and suitability for welding large thickness components.
4. Small specimen testing technique shear punch creep can be employed to characterize creep behaviour of 9Cr-1Mo steel weld joints including the third stage in order to understand the failure mechanisms.
5. More mechanical property tests such as fatigue crack growth and creep crack growth at elevated temperatures is advisable before fully adapting A-TIG welding process for critical joints in FBRs.

CHAPTER 8

REFERENCES

1. A. Barnes, The Influence of Composition on Microstructural Development and Toughness of Modified 9%Cr-1%Mo Weld Metals, 1995, Report 509/1995, TWI, Abington, UK,
2. W.B. Jones, C.R. Hills and D.H. Polonis, Microstructural Evolution of Modified 9Cr-1Mo Steel, 1991, Metallurgical Transactions A, 22, (5), pp. 1049–1058.
3. B.J. Cane, R.S. Fidler, in: S.F. Pugh, E.A. Little (Eds.), Ferritic Steels for Fast Reactor Steam Generators, 1977, British Nuclear Energy Society, London, pp. 193–199.
4. V.K. Sikka, J.W. Davies and D.J. Michael (Eds.), Ferritic alloys for use in nuclear energy technologies, 1984,TMS-AIME, warrendale, PA, pp. 317–327
5. S.L. Mannan, S.C. Chetal, B. Raj, S.B. Bhoje, Selection of material for Prototype Fast Breeder Reactor, 2003, Transactions of Indian Institute of Metals 56 155–178.
6. R.L. Klueh, Elevated temperature ferritic and martensitic steels and their application to future nuclear reactors, 2005, International Materials Reviews, Volume50, pp. 287–310.
7. Standard specification for seamless ferritic and austenitic alloy-steel boiler, superheater, and heat-exchanger tubes, 2011, ASTM standards A213/A213M-11a, ASTM Inter., Pennsylvania, USA.
8. R.L. Klueh and A.T. Nelson, Ferritic/Martensitic Steels for next-generation reactors, 2007, Journal of Nuclear Materials, 371, pp. 37-52.

9. L.M. Wytt, The Performance of Cr-Mo Steel Boilers of CEGB Power Stations in Ferritic Steels for Fast Reactor Steam Generators, 1977, Ed. M. Pugh and E.A. Little, British Nuclear Energy Society, London, pp.27-34.

10. Baldev Raj, B.K. Choudhary and K. Velusamy (Eds.), Pressure Vessels and Piping: Codes, Standards, Design and Analysis, 2009, New Delhi, pp. 1–32.

11. P.F. Girouxa, F. Dallea, M. Sauzaya, J. Malaplatea, B. Fourniera and A.F.G. Lorenzon, Mechanical and microstructural stability of P92 steel under uniaxial tension at high temperature**,** 2010, Materials Science and Engineering A,527, pp. 3984–3993.

12. G.W. Cunningham, P. Patriarca and E.E. Hoffman, Ferritic steels as alternate structural materials for high-temperature applications, 1983, Proceedings of International Conference, Ferritic steels for high temperature application, ASM metals park, Ohio, 3-6.

13. M.Vasudevan, computational and experimental studies on arc welded austenitic stainless steels, 2006, Ph.D Thesis, Indian Institute of Technology Madras, Chennai.

14. V. Ravishanker, D.K. Dwivide and M. Vasudevan, Influence of M-TIG and A-TIG Welding Process on Microstructure and Mechanical Behavior of 409 Ferritic Stainless Steel, 2017, Journal of Materials Engineering and Performance, DOI: 10.1007/s11665-017-2538-5

15. M. Vasudevan, Effect of A-TIG Welding Process on the Weld Attributes of Type 304LN and 316LN Stainless Steels, 2017, Journal of Materials Engineering and Performance, DOI: 10.1007/s11665-017-2517-x

16. V. Arunkumar, M. Vasudevan, V. Maduraimuthu and V. Muthupondi, Effect of activated flux on the microstructure and mechanical properties of Plain 9Cr-1Mo steel weld joint, 2012, Materials and Manufacturing Processes, 27, (11), pp. 1-7.

17. T. Sakthivel , M. Vasudevan, K. Laha , P. Parameswaran, K.S. Chandravathi, S. Panneer Selvi, V. Maduraimuthu and M.D. Mathew, Creep rupture behavior of 9Cr–1.8W–0.5Mo–VNb (ASME grade 92) ferritic steel weld joint, 2014, Materials Science and Engineering A, Volume 591, 3, pp. 111–120.

18. K.L Murty, P.Q. Miraglia, M.D. Mathew, V.N. Shah, and F.M. Haggag, Characterization of gradients in mechanical properties of SA-533B steel welds using ball indentation, 1999, International Journal of Pressure Vessels Piping, 76, pp. 361–369.

19. S.N. Chu and J.C.M. Li, Impression creep- a new creep test, 1977, Journal of Material Science, 12, pp. 2200-2208.

20. S. Nagaraju, P. Vasantharaja, N. Chandrasekhar, M. Vasudevan and T. Jayakumar, Optimisation of A-TIG Welding Process parameters for 9Cr-1Mo steel using Response surface methodology and Genetic Algorithm, 2016, Materials and Manufacturing Processes, 31, 3, pp. 319-327,

21. R.W. Vanstone, Advanced (“700^{0}C”) PF Power Plant, 2001, Proceedings of 3rd conference on Advances in Materials Technology for Fossil Power Plants, The institute of materials. University of Wales Swansea, London, pp. 7 –14.

22. A.J. Turnell, Oil Refinery Process Plants Part 2- Refinery Process Units and Materials Selection, 1977, Metal Construction 9(12), p. 552.

23. C. Willby and J. Walters, Material Choices for Commercial Fast Reactor Steam Generators in Ferritic Steels for Fast Reactor Steam Generators, 1977, Ed., M. Pugh and E.A. Little, British Nuclear Energy Society, London, pp. 40-49.

24. W.L. Bell, T. Lauritez and S.Vaidyanathan, Ferritics for Breeder Reactor In-Core Applications: A Survey of Alloys, Properties and Microstructures in Proceedings of Topical Conference on Ferritic Alloys for use in Nuclear Energy Technologies, Ed.,

1984, J.W. Davis and D.J. Michel, The Metallurgical Society of AIME, Pennsylvania, pp.113-124.

25. F. Masuyama, in: Advanced Heat Resistant Steels for Power Generation, Ed., R. Viswanathan and J. Nutting, 1999, The Institute Of Materials, London, Book 708, p. 33.
26. Z. Briggs and T.D. Parker, The Super 12% Cr Steels, 1965, Climax Molybdenum Co., New York.
27. Anon, Super 12% Cr Steels-An Update, 1983, Climax Molybdenum Co., New York.
28. H. Brearley, Knotted String-Autobiography of a Steelmaker, 1941, Longmans, London.
29. J.H.G. Moneypenny, Stainless Iron and Steel, 1926, Chapman and Hall, London.
30. L. Egnell, in: High Temperature Properties of Steels, 1967, The Iron and Steel Institute, London, Publication 97, p. 153.
31. J. Orr, F.R.. Beckit and G.D. Fawres, Physical Metallurgy of Cr-Mo Steels for Fast Reactor Boilers in Ferritic Steels for Fast Reactor Steam Generators, 1977, Ed., M. Pugh and E.A. Little, BRITISH NUCLEAR ENERGY SOCIETY, London, pp. 91-109.
32. T. George, E.R. Parker and R.O. Ritchie, Susceptibility of Hydrogen Attack of Thick Section 3Cr- 1Mo-1Ni Pressure Vessel Steel- Role of Cooling Rate, 1985, Materials Science and Technology, 1, p. 198.
33. R.R. Hosbons, in: Topical Conference on Ferritic Alloys for Use in Nuclear Energy Technologies, 1984, Ed., J.W. Davis and D.J.Michel, Transactions of Metallurgical Society of AIME, Warrendale, PA, 91.

34. J. Orr and S. J. Sanderson, in: Topical Conference on Ferritic Alloys for Use in Nuclear Energy Technologies, 1984, Ed., J.W. Davis and D.J. Michel, Transactions of Metallurgical Society of AIME, Warrendale, PA, 261.
35. F.S. Dickinson, A.F. Taylor, P.W. Jackson and R.W. Smith, in: Topical Conference on Ferritic Alloys for Use in Nuclear Energy Technologies, 1984, Ed., J. W. Davis and D.J. Michel, Transactions of Metallurgical Society of AIME, Warrendale, PA, 269.
36. J.F.W. Bishop, in: Dimensional Stability and Mechanical Behaviour of Irradiated Metals and Alloys, 1984, Vol. 2, British Nuclear Energy Society, London, p. 115.
37. R. Gajapathy and K. Veluchamy, CFD investigations of helical wire-wrap fuel pin bundle and its comparison with straight wire bundle, 2016, Progress in Nuclear Energy, 89, pp. 57-68
38. D.R. Harries, J. Standring, W.D. Barnes, and G.J. Lloyd, in: Effects of Irradiation on Materials: Eleventh Conference, ASTM STP 782, 1982, Ed., H.R. Brager and J.S. Perrin, American Society for Testing and Materials, Philadelphia, PA, p. 1197.
39. C. Brown, R.J. Lilley and G.C. Crittenden, PFR's Contribution to Fuel Development, 1994, The Nuclear Engineer, 35, pp. 122-128.
40. M. Lippens, K. Ehrlich, V. Levy, C. Brown and A. Calza Bini, in: Materials for Nuclear Core Applications, 1987, Vol. I British Nuclear Energy Society, London, p. 177.
41. K.Q. Bagley, E.A. Little, V. Levy, A. Alamo, K. Ehrlich, K. Anderko and A. Calza Bini, European development of ferritic-martensitic steels for fast reactor wrapper applications, 1988, Nuclear Energy, 27(5), pp. 295-303.

42. C. Brown, V. Levy, J.L. Séran, K. Ehrlich, R.J.C. Roger and H. Bergmann, in: Fast Reactors and Related Fuel Cycles-FR '91, 1991, Vol. I, Atomic Energy Society of Japan, Tokyo, Paper 7.5.
43. A.J. Lovell, A.L. Fox, W.H. Sutherland and S.L. Hecht, in: Reliable Fuels for Liquid Metal Reactors, 1987, American Nuclear Society, LeGrange Park, IL, pp. 3-25.
44. D.S. Gelles, in: EUROMAT 96: 1996, Materials and Nuclear Power, The Institue of Materials, London, p. 281.
45. V.S. Khabarov, A.M. Dvoriashin and S.I. Porollo, in: Technical Committee Meeting on: Influence of High Dose Irradiation on Advanced Reactor Core Structural and Fuel Materials, 1998, IAEA-TECDOC-1039, IAEA, Vienna, 139.
46. V.M. Poplavsky and L.M. Zabudko, in: Technical Committee Meeting on: Influence of High Dose Irradiation on Advanced Reactor Core Structural and Fuel Materials, 1998, IAEA-TECDOC- 1039 IAEA, Vienna, 7.
47. S. Nomura, S. Shikakura, S. Ukai, I. Seshimo, M. Harada, I. Shibahara and M. Katsuragawa, in: Fast Reactors and Related Fuel Cycles-FR '91, 1991, Vol. I Atomic Energy Society of Japan, Tokyo, Paper 7.4.
48. K. Ehrlich and G. Mühling, in: Reliable Fuels for Liquid Metal Reactors, 1987, American Nuclear Society, 4-1.
49. E.M. Morris and K. Ehrlich, in: Proceedings. Technical Committee Meeting on: Influence of High Dose Irradiation on Advanced Reactor Core Structural and Fuel Materials, 1998, IAEATECDOC- 1039, IAEA, Vienna, 129.
50. E.A. Little, D.R. Harries, F.B. Pickering and S.R. Keown, Effects of heat treatment on structure and properties of 12%Cr steels, 1977, Metals Technology, 4 pp. 205-217.

51. Wada and G.D. Eldis, Transformation Characteristics of 2.25Cr-1Mo Steel, ASTM-STP 755, Applications of 2.25Cr-1Mo Steel for Thick Wall Pressure Vessels, 1982, Sangdahl and Semchyshen, Ed., American Society for Testing and Materials, Philadelphia, pp. 343-362.
52. T. lshiguro, Y. Murakawi, K. Ohnishi and J.A Watanabe, A 2.25Cr-1 Mo Pressure Vessel Steel with Improved Creep Rupture Strength, 1982, Ed., Sangdahl and Semchyshen, American Society for Testing and Materials, Philadelphia, pp. 129-147.
53. F.B. Pickering and A.D. Vassiliou, Effect of Austenitising Temperature on Constitution, Transformation and Tempering of 9Cr-1Mo steel, 1980, Metals Technology, 7, pp. 409-413.
54. P. Patriarca, S.D. Harkeness, J.M. Duke and L.R. Cooper, US Advanced Materials Development Program for Steam Generators, 1976, Nuclear Technology, 28, p. 516.
55. W.O. Forgeng and W.O. Forgeng Jr., Metals Hand Book 8 ASM, 1973, Metals Park Ohio, pp. 402-404.
56. C.E. Spaedar Jr. and W.O. Doty, Report No.2: ASME Post Weld Heat Treating Practices: An Interpretive Report, 1996, WRC Bulletin 407, pp 50-65.
57. S.J. Sanderson, Mechanical Properties and Metallurgy of 9%Cr 1%Mo Steel in Proceedings in the Conference of Ferritic Steels for High Temperature Applications, 1983, Ed., A.K. Khare, ASM, Metals Park, Ohio, pp. 85-99.
58. K. Easterling, Introduction to Physical Metallurgy of Welding, 1992, Butterworth.
59. N. Yurioka and H. Suzuki, Hydrogen Assisted Cracking in C-Mn and Alloy Steels Weldments, 1990, International Materials Reviews, 35(4), p. 214 .
60. http://schools-wikipedia.org/images/1210/121098.png.htm
61. https://commons.wikimedia.org/wiki/File:GTAW_broken.svg

62. W. Robert and Messler, Principles of Welding, 2009, Wiley-VCH.
63. K. Sindo , Welding Metallurgy, 2003. John Wiley & Sons Inc.
64. M.C. Tsai and K. Sindo, Heat transfer and fluid flow in welding arcs produced by sharpened and flat electrodes, 1990, International Journal of Heat and Mass Transfer, 33, pp. 2089-2098.
65. J. Haidar and A.J.D. Farmer, Large effect of cathode shape on plasma temperature in high-current free-burning arcs, 1994, Journal of Physics D, Applied Physics, 27, pp. 555-560.
66. S. Ukita, K. Kokubo and T.Masuko, Effects of electrode tip shape and torch angle on high speed DCEN TIG welding, 2002, Welding International, 16(10), pp.778-783.
67. K. Hiraoka, A. Okada and M. Inagaki, Effect of electrode geometry on maximum arc pressure in gas tungsten arc welding, 1985, Journal of the Japan Welding Society, 3(2), 10e6.
68. M. Ushio and M. Fukuhisa, Mathematical modelling of heat transfer of welding arc (part 1), 1982, Transactions of Japan Welding Research Institute, 11(1):7e15.
69. TWI GSP No. 5663, An evaluation of the A-TIG welding process, 1994, January, 1994.
70. W. Lucas and D. Howse, Activating flux - Increasing the performance and productivity of the TIG and plasma processes, 1996, Welding and Metal Fabrication 64 (1), pp. 11 - 17.
71. L.N. Lie, D.H. Cai and Z.D. Zhang, Gas tungsten arc welding of magnesium alloy using activated flux coated wire, 2007, Scripta materialia 57, pp. 695-698.
72. P.C.J. Anderson, and R.Wiktorowicz, A-TIG welding – The effect of the shielding gas, 1995, TWI Bulletin, July/August, pp. 76-77.

73. P.C.J. Anderson and R.Wiktorowicz, Improving productivity with A-TIG welding, 1996, Welding and Metal Fabrication, 64(3), pp. 108-109.
74. W. Lucas, D.S. Howse, M.M. Savitsky and I.V. Kovalenko, A-TIG flux for increasing the performance and productivity of welding processes, 1996, Proceedings of 49th IIW annual assembly, International Institute of Welding, Document XII –1448- 96.
75. T. Paskell, C. Lundin and H. Castner, GTAW flux increases weld joint penetration, 1997, Welding Journal, 76 (4), pp. 57-62.
76. M.M. Savitsky, B.N. Kushnirenko and O.I. Ploeinik, Features of A-TIG welding of steels, 1999, Paton Welding Journal, pp. 24-32.
77. P.J. Modenesi, E.R. Apolinario and I.M. Pereira, TIG welding with single-component fluxes, 2000, Journal of Materials Processing Technology, 99 (1-3), pp. 260-265.
78. M. Tanaka, T. Shimizu, H. Terasaki, M. Ushio, F. Koshi-ishi and C.L. Yang, Effects of activating flux on arc phenomena in gas tungsten arc welding, 2000, Science and Technology of Welding and Joining, 5(6), pp. 397-402.
79. W. Lucas, Activating flux – improving the performance of the TIG process, 2000, Welding and Metal Fabrication, 68(2), pp. 7-10.
80. D.S. Howse and W. Lucas, Investigation into arc constriction by active fluxes for tungsten inert gas welding, Science and Technology of Welding and Joining, 2000, 5(3), pp. 189-193.
81. K.A. Yushchenko, et al. A-TIG welding of carbon-manganese and stainless steels, 1993, Intl. Conference on Welding Technology, Paton Institute, paper 2, Cambridge, 13-14.

82. Shanping Lu, Hidetoshi Fujii, Hiroyuki Sugiyama, Manabu Tanaka and Kiyishi Nogi, Weld penetration and Marangoni convection with oxide fluxes in GTA Welding, 2002, Materials Transactions, 43 (11), p. 2926-2931.
83. P. Rishi, Effect of Arc Welding Processes on the Weld Attributes of Micro Alloyed HSLA Steel, 2016, Ph.D Thesis, HBNI, IGCAR.
84. S. Lu, H. Fujii, H. Sugiyama and K. Nogi, Mechanism and Optimisation of oxide fluxes for deep penetration in gas tungsten arc welding, 2003, Metallurgical and Materials Transactions A, 34 A, p. 1901-1907.
85. P. Pascal and S. Jacques, Effect of activating fluxes on the penetration capability of TIG welding arc: study of fluid flow phenomena in weld pools and the energy concentration in the anode spot of a TIG arc plasma, 2003, Materials Science Forum, 426-432, pp. 4087-4092.
86. F. Liu, C. Yang, S. Lin, L. Wu and Q. Zhang, Mechanism of increasing A-TIG penetration, 2003, Acta Metallurgica Sinica, 39(6), pp. 661-665.
87. B.E. Paton, V.N. Zamkov, V.P. Prilutsky and P.V. Poritsky, Contraction of the welding arc caused by the flux in tungsten-electrode argon arc welding, 2000, Paton Welding Journal, 1, pp. 5-11.
88. T. Sándor and J. Dobránszky: The experiences of A-TIG welding applied on 1.4301 type stainless steel plates, 2007, Materials Science Forum, Vols. 537-538 pp. 63-70.
89. C.R. Heiple and J.R. Roper, Mechanism for minor element effect on GTA fusion zone geometry, 1982, Welding Journal, 61(4), pp. 97s-102s.
90. M.M. Savitskii and G. Leskov, The mechanism of the effects of electrically negative elements on the penetrating power of an arc with a tungsten cathode, 1980, Avt. Svarka 9, pp. 17–22.

91. S. Leconte, P. Paillard and P. Chapelle, Effect of oxide fluxes on activation mechanisms of tungsten inert gas process, 2006, Science Technology for Welding and Joining, 11, pp. 389–397.
92. Rogers et al., Minor effects on super alloy weld pools, 1993, Proc., 3rd International Conference on Trends in Welding Research, Gatlinburg, TN, USA, pp. 709-712.
93. C. Yang, S. Lin, F. Liu, W.U. Lin and Q. Zhang, Research on the Mechanism of Penetration Increase by Flux in A-TIG Welding, 2003, Journal of Materials Science & Technology, 19(1), pp. 225-227.
94. A. G. Simonik, The effect of contraction of the arc discharge upon the introduction of electro-negative elements, 1976, Svar. Proiz. 3, pp. 49–51.
95. J. J. Lowke, M. Tanaka and M. Ushio, Mechanisms giving increased weld depth due to a flux, 2005, Journal of Physics D: Applied Physics, Volume 38, Issue 18, pp. 3438-3445.
96. S. Kou and Y.H. Wang, Weld pool convection and its effect, 1986, Welding Journal 65 (3), pp. 63s-70s.
97. F. Ding, R. Zhang, Y. Gu and M. Ushio, Effect of flux on A-TIG welding of mild steels, 2001, Transactions JWRI, 30, pp. 35-40.
98. C.R. Heiple, J.R. Roper, R.T. Stagner and R.I. Aden, Surface active element effects on the shape of GTA, laser, and electron beam welds, 1983, Welding Journal, 62(3), pp. 72s-77s.
99. B. Pollard, The effects of minor elements on the welding characteristics of stainless steels, 1988, Welding Journal, 67(9), pp. 202s-213s.
100. K.C. Mills and B.J. Keene, Factors affecting variable penetration, 1990, International Material Reviews, 35(4), pp. 185-216.

101. J.A. Lambert, Cast-to-cast variability in stainless steel mechanized GTA welds, 1991, Welding Journal, 70 (5), pp. 41-52.

102. J.F. Lancaster and K.C. Mills, Recommendations for the avoidance of variable penetration in gas tungsten arc welding, 1994, Abington Publishing, Cambridge, England.

103. S.W. Pierce, P. Burgardt and D.L. Olson, Thermocapillary and arc phenomena in stainless steel welding, 1999, Welding Journal, 78(2), pp. 45s-52s.

104. V. Arunkumar, Effect of activated flux on microstructure and mechanical properties of 9Cr-1Mo steel welds, 2008, M.Tech Thesis, National Institute of Technology.

105. M. Vasudevan, A.K. Bhaduri, Baldev Raj and K. Prasad Rao, Genetic Algorithm based Computational model for Optimizing the Process parameters in A-TIG welding of 304LN and 316LN Stainless Steels, 2007, Materials and Manufacturing Processes, Vol. 22, (5), pp. 641-649.

106. M. Vasudevan, V. Arunkumar, N. Chandrasekhar and V. Maduraimuthu, Genetic Algorithm for Optimization of A-TIG welding process for mod. 9Cr-1Mo steel, 2010, Science and Technology of Welding and Joining, vol. 15 (2), pp.117-123.

107. N. Chandrasekhar and M. Vasudevan, Intelligent modeling for optimization of A-TIG welding process, 2010, Materials and Manufacturing Processes, 25, (11), pp. 1341-1350.

108. K.N. Gowtham, M. Vasudevan, V. Maduraimuthu and T. Jayakumar, Intelligent modeling combining ANFIS and Genetic Algorithm for optimizing welding process parameters, 2011, Metallurgical and Materials Transactions B, Volume 42, Number 2, pp.385-392.

109. L. Subashini, P. Madhumitha and M. Vasudevan, Optimization of Welding Process for Mod. 9Cr-1Mo steel using Genetic Algorithm, 2012, Journal of Computational Materials Science and Surface Engineering, Vol. 5, No. 1, pp. 1-15.

110. Nandan Naik, M. Vasudevan and K.R. Balasubramanian, Multi-objective optimization of A-TIG welding of duplex stainless steel using response surface methodology, 2015, International Journal of Advanced Manufacturing Technology, 77, pp. 67-81.

111. F. Julien M. Vasudevan and V. Maduraimuthu, Optimization of Welding Process Parameters for Reduced Activation Ferritic-Martensitic (RAFM) Steel, 2016, Transactions of the Indian Institute of Metals, 69(8), pp. 1493-1499.

112. Nandan Naik, M. Vasudevan and K.R. Balasubramanian, Optimization of A-TIG welding of Duplex Stainless Steel Alloy 2205 based on Response Surface Methodology and Experimental Validation, 2016, Journal of Materials: Design and Appli cations, vol. 230 (4), pp. 837-846.

113. R. Fisher, The design of experiments, 1935, Oliver-Boyd, Edinburgh

114. D.C. Montgomery, Design and Analysis of experiments, 1997, 4th ed. John Wiley and Sons, New York.

115. A.K. Lakshminarayanan and V. Balasubramanian, Comparison of RSM with ANN in predicting tensile strength of friction stir welded AA7039 aluminium alloy joints, 2009, Transactions of Nonferrous Metals Society of China, Vol.19, pp. 9-18.

116. Z. Kocabaş, An Application and interpretation of second order response surface model, 2001, Ankara Üniversitesi Tarım Bilimleri Dergisi, Journal of Agricultural Sciences, 7, pp. 121- 128.

117. R.H. Myers and D.C. Montgomery, Response surface methodology process and product optimization using designed experiments, 2002, A Wiley- Interscience Publication, 2nd ed, Canada, John Wiley and Sons, pp. 17-85, 203-303.

118. K. Elangovan, V. Balasubramanian and S. Babu, Developing an Empirical Relationship to Predict Tensile Strength of Friction Stir Welded AA2219 Aluminum Alloy, 2008, Journal of Materials Engineering and Performance, Vol. 17(6), pp. 820-830.

119. A. Jawdat Al-Jarrah, Sallameh Swalha, Talal Abu Mansour, Masoud Ibrahim and Maen Al-Rashdan, Optimization of Friction Stir Welding Parameters for Joining Aluminum Alloys, 2013, Using RSM, Advances in Theoretical and Applied Mechanics, Vol. 6, no. 1, pp. 13-26.

120. I. Dinaharan and N. Murugan, Automation of Friction Stir Welding process to join Aluminium Matrix composite by Optimization, 2012, Procedia Engineering, Vol. 38, pp. 105-110.

121. H.M. Ibrahim and E.E. Elkhidir, Response surface method as an efficient tool for medium optimization, 2011, Trends in Applied Science Research, 6, pp. 121-129.

122. N. Chakraborti, Genetic algorithms in materials design and processing, 2004, International Material Reviews, 49 (3-4), pp. 246-260.

123. K. Deb, An introduction to genetic algorithms, 1999, Sadhana, 24 (4&5), pp. 293-315.

124. D.E. Goldberg, Genetic algorithms in search, optimization and machine learning, 1989, Addison Wesley.

125. Kerry Gallagher and Malcom Sambridge, Genetic Algorithms: A powerful tool for large scale nonlinear optimization problems, 1994, Computers & Geosciences, 20(7), pp. 1229-1236.

126. K. Deb, Multi-objective optimisation using evolutionary algorithm, 2001, Chichester, UK, Wiley.
127. D.B. Fogel, An introduction to simulated evolutionary optimization, 1994, Institute of Electrical and Electronics Engineers -Transactions on Neural Networks, 5 (1), pp. 3-14.
128. M.Gen and R. Cheng, Genetic algorithms and engineering design, 1997, John Wiley & Sons, Inc.
129. C.R. Reeves, Using genetic algorithm with small populations, 1993, Proceedings. of the Fifth International Conference on Genetic Algorithms, pp. 92-99.
130. D. Kim, and S. Rhee, Optimisation of arc welding process parameters using a genetic algorithm, 2001, Welding Journal, 80(7), pp. 184s-189s.
131. D. Kim, S. Rhee and H. Park, Modelling and Optimisation of GMA welding process by genetic algorithm and response surface methodology, 2002, International Journal of Production Research, 40 (7), pp. 1699-1711.
132. D. Kim and S. Rhee, Optimization of GMA welding process using the dual response approach, 2003, International Journal of Production Research, 41(18), pp. 4505-4515.
133. Cemal Meran, Prediction of the optimized welding parameters for the joined brass plates using genetic algorithm, 2006, Materials and Design, 27, pp. 356-363.
134. D.S. Correia, C.V. Gonclaves, S.C. Junior, and V.A.Ferraresi, GMAW welding optimisation using genetic algorithms, 2004, Journal of Brazilian Society of Mechanical Science and Engineering, 26 (1), pp. 28-33.
135. D.S. Correia, C.V. Gonclaves, S.C. Junior and V.A. Ferraresi, Comparison between genetic algorithms and response surface methodology in GMAW optimization, 2005, Journal of Materials Processing Technology, 160, pp. 70-76.

136. S. Mishra and T. Debroy, A heat transfer and fluid flow model to obtain a specific weld geometry through multiple paths, 2005, Journal of applied physics, 98, 044902 (1) – 044902(10).

137. A. Kumar, S. Mishra, J.W. Elmer and T. Debroy, Optimization of the Jhonson-Mehl-Avarami equation parameters for α- ferrite to γ- austenite transformation in steel welds using a Genetic Algorithm, 2005, Metallurgical and Material Transactions, A, 36 A (1), pp. 15-22.

138. A. Kumar and T. DebRoy, Tailoring complex weld geometry through reliable heat transfer and fluid flow calculations and a genetic algorithm, 2005, Metallurgical and Materials Transactions, A, 36 A (10), pp. 2725-2735.

139. M. Murugananth, S.S. Babu, and S.A. David, Optimization of shielded metal arc weld composition for Charpy toughness, 2004, Welding Journal, 83(10), pp. 267s-276s.

140. Feng and Zihli, Processes and mechanism of welding residual stress and distortion, 2005, Wood head Publishing limited, 1st Ed, Cambridge, England, Chap. 1-3, 5-9.

141. E. Macherauch and K.H. Kloos, Origin, measurements and evaluation of residual stresses, 1987, Residual Stress Science and Technology, pp. 3–26.

142. J. Lu et al., Handbook of Measurement of Residual Stresses, 1996, SEM, Fairmont Press, Inc.

143. A.N. Lari, Advances in Surface Treatments, 1987, Vol 4, International Guidebook on Residual Stresses, p. 3.

144. G.E. Totten, Handbook on residual stress, 2002, ASM International, Vol 1, p. 417.

145. V. Hauk, Structural and Residual Stress Analysis by Non Destructive Methods, 1997, Elsevier, Amsterdam.

146. F.M. Haggag, Field Indentation Microprobe for Structural Integrity Evaluation, 1989, U.S. Patent No. 4852397.

147. K.L. Murty, M.D. Mathew, Y.Wang, V.N. Shah and F.M. Haggag, Nondestructive determination of tensile properties and fracture toughness of cold-worked A36 steel, 1998, International Journal of Pressure Vessels Piping, 75, pp.831–840.

148. M.D. Mathew, K.L. Murty, K.B.S. Rao and S.L. Mannan, Ball indentation studies on the effect of aging on mechanical behavior of Alloy 625, 1999a, Material Science and Engineering A, 264, pp. 159–166.

149. M.D. Mathew, L.M. Lietzan, K.L. Murty and V.N. Shah, Low temperature aging embrittlement of CF-8 stainless steel, 1999b, Material Science Engineering, 269, pp.186–196.

150. D. Tabor, The Hardness of Metals, 1951, Oxford University Press, New York.

151. F.M. Haggag, In: W.R. Corwin, F.M. Haggag, W.L. Server, (Ed.), In Situ Measurement of Mechanical Properties Using Novel Automated Ball Indentation System, Small specimen Test Technique Applied to Nuclear Reactor Pressure Vessel Thermal Annealing and Plant Life Extension, 1993, ASTM STP 1204, ASTM, Philadelphia, PA, pp. 27–39.

152. C.H. Mok, The dependence of yield stress on strain rate as determined from ball-indentation tests, 1966, Experimental Mechanics, 87, pp. 87–92.

153. K.L. Murty and M.D. Mathew, Non-destructive Monitoring of Structural materials using Automated Ball Indentation (ABI) Technique, 2004, Nuclear Engineering and Design, pp 81-96.

154. M.D. Mathew, L.M. Lietzan, K.L. Murty and V.N. Shah, Low temperature aging embrittlement of CF-8 stainless steel, 1999, Low temperature aging embrittlement of CF-8 stainless steel, Mater. Sci. Eng. A, 269, pp.189-196.
155. F.M. Haggag and K.L. Murty, in: P.K. Liaw, O. Buck, R.J. Arsenault and R.E. Green Jr. (Ed.), Non-destructive Evaluation and Materials Properties III, 1997, TMS, Warrendale, PA, p. 101.
156. F.M. Haggag, in: W.R. Corwin, F.M. Haggag and W.L. Server (Eds.), Small Specimen Test Technique Applied to Nuclear Reactor Vessel Thermal Annealing and Plant Life Extension, 1993, American Society for Testing and Materials, Philadelphia, p. 27 ASTM STP 1204.
157. T.O. Mulhearn and D. Tabor, Creep and hardness of metals: A physical study, 1960, Journal of the Institute of Metals, 7, p. 89.
158. P.M. Sargent and M.F. Ashby, Indentation creep, 1992, Material Science and Technology, 8, pp. 594-601.
159. H.D. Merchant, G.S. Murty, S.N. Bahadur, L.T. Dwivedi and Y. Mehrotra, Hardness- Temperature Relationships in Metals, 1973, Journal of Material Science, 8, pp. 437-442.
160. O.D. Sherby and P.E. Armstrong, Prediction of activation energies for creep and self-diffusion from hot hardness data, 1971, Metallurgical and Materials Transactions B, pp. 3479-3484.
161. R.M. Hooper and C.A. Brookes, Incubation periods and indentation creep in lead, 1984, Journal of Material Science, 19, pp. 4057-4060.
162. G. Cseh, N.Q. Chinh, P. Tasnadi and A. Juhasz, Indentation test for the investigation of high-temperature plasticity of materials, 1997, Journal of Material Science, 32, pp.5107-5111.

163. G. Cseh, N.Q. Chinh and A. Juhasz, Indentation Curves and Viscosity Measurements on Glasses, 1998, Journal of Material Science, 17, pp. 1207-1209.

164. M. Fujiwara and M. Otsuka, Indentation creep of β-Sn and Sn–Pb eutectic alloy, 2001, Material Science and Engineering A, pp. 319-321, 929-933.

165. U.K. Viswanathan, T.R.G. Kutty, R. Keswani and C. Ganguly, Evaluation of hot hardness and creep of a 350 grade commercial maraging steel, 1996, Journal of Material Science, 31, pp. 2705-2709.

166. B.N. Lucas and W.C. Oliver, Indentation power-law creep of high-purity indium, 1999, Metallurgical and Materials Transactions A, 30A, p. 601.

167. J. Larsen-Badse, Indentation creep of soft metals, 1967, ORNL-TM-1862 Report.

168. Naveena, Understanding creep deformation behavior of 316LN Stainless steel and its weld joint using impression creep technique, 2013, Ph.D Thesis, HBNI.

169. T.H. Hyde and W. Sun. Multi-step load impression creep tests for a ½ CrMoV steel at 565 ^{0}C, 2001, Strain 2001, 37, pp. 99–103.

170. T.H. Hyde, C.J. Hyde and W. sun, A Basis for selecting the most appropriate small specimen creep test type, 2014, Journal of pressure vessels Technology, 136(2), pp. 1-6.

171. An international patent, Tungsten Inert Gas Welding Flux for enhancing Penetration in Single Pass for austenitic stainless steels, 2006, (patent no. PCT/IN06/00442 dt.8/11/06).

172. M. Vasudevan, A.K. Bhaduri and Baldev Raj, Microstructure and Mechanical Properties of Austenitic Stainless Steels, 2005, International Welding Congress, February 16 – 19, Mumbai.

173. M. Vasudevan, A.K. Bhaduri and Baldev Raj, Development and Evaluation of Activated Flux for TIG welding of Type 304 LN and Type 316 LN Stainless

Steels, 2008, International Institute of Welding, 2008, International Congress, January, 8-10, Chennai,.

174. F.M. Haggag, J.A. Wang, M.A. Sokolov and K.L. Murthy, Use of portable/in situ stress-strain microprobe system to measure stress strain behavior and damage in metallic materials and structures, 1997, Philadelphia, American Society for Testing and Materials. [ASTM STP 1318], pp. 85-98.

175. S. Datta and P.P. Chattopadhyay, Soft computing techniques in advancement of structural metals, 2013, International Materials Reviews, 58 (8), pp. 475-504.

176. N. Chakraborti, Critical assessment 3: The unique contributions of multi-objective evolutionary and genetic algorithms in materials research, 2014, Materials Science and Technology, 30 (11), pp. 1259-1262.

177. Noraini Mohd Razali and John Geraghty, Genetic algorithm performance with different selection strategies in solving TSP, Proceedings of the World Congress on Engineering, 2011, Vol II WCE July 6 – 8, London, U.K.

178. Z. Zhang, A.W. Marshall and J.C.M. Farrar, Present developments in welding consumables for P (T) 91 creep-resisting steels. Conference Proceedings, International Conference on Integrity of High-Temperature Welds, 1998, Nottingham, UK, 3-4 November, The Institute of Mechanical Engineers, London, pp. 77-91.

179. D. Deng, Y. Zhou, T. Bi and X. Liu. Experimental and Numerical investigations of welding distortion induced by $C0_2$ gas arc welding in thin-plate bead-on joints, 2013, Material and Design, 52, pp. 720-729.

180. H. Long, D. Grey, A. Carlier and P.G. Marpoulos. Prediction of welding distortion in butt joint of thin plates, 2009, Material and design, 30 (10), pp.4126-4135.

181. M. Seyyedian, M. Haghpanahi and M. Sedighil, Investigation of the Effect of Clamping on Residual Stresses and Distortions in Butt-Welded Plates, 2010, Transaction B Mechanical engineering, 17 (5), pp.387-394.

182. A.K. Vasudevan, K. Sadananda and G. Glinka. Critical parameters for fatigue damage, 2001, International Journal of Fatigue, Vol. 23, pp. 39-53.

183. I.C. Noyan and J.B. Cohen, Residual Stress Measurement by Diffraction and Interpretation, 1987, Springer-Verlag, New York.

184. B.D Cullity and S.R Stock, Elements of X-ray Diffraction, 2001, Prentice Hall, New Jersey.

185. Jonas Hensel, Thomas Nitschke-Pagel and Klaus Dilger, On the effects of austenite phase transformation on welding residual stresses in non-load carrying longitudinal welds, 2015,Welding in the World, Vol. 59(2), pp. 179-190.

186. A. Kundu, P.J. Bouchard, S. Kumar, K.A. Venkata, J.A. Francis, A. Paradowska, G.K. Dey and C.E. Truman, Residual stresses in P91 steel electron beam welds, 2013, Science and Technology in Welding and Joining, 18 (1), pp. 70–75.

187. V. Maduraimuthu, M. Vasudevan and P. Parameswaran, Studies on the improvement of toughness in modified 9Cr-1Mo steel A-TIG weld joint, 2015, Transactions Indian Institute of Metals, 68,(2), pp. 181-189.

188. K.L. Murthy, M.D. Mathew, P.Q. Miraglia, V.N. Shah and F.M. Haggag, Non-destructive evaluation of deformation and fracture properties of materials using stress-strain microprobe, Non-destructive characterization of materials in aging systems, 1998, (Eds. R.L. Crane, J.D. Chenbach, S.P. Shah, T.E. Matikas, P.T. KhuriYakub and R.S. Gilmore), 327; Pennsylvania, Materials Research Society.

189. H. Lee, J. H. Lee and G.M. Pharr, A numerical approach to spherical indentation techniques for material property evaluation, 2005, Journal of the Mechanics and Physics of Solids, 53, pp. 2037–2069.

190. D.P. Miannay, Time-Dependent fracture mechanics, 2001, New York. Springer-Verlag.

191. K.L. Murthy, P.Q. Miraglia, M.D. Mathew, V.N. Shah and F.M. Haggag, Characterization of gradients in mechanical properties of SA-533B steel welds using ball indentation, 1999, International Journal of Pressure Vessels and Piping, 76, pp. 361-369.

192. J. Ganesh Kumar, V.D. Vijayanand, M. Nandagopal and K. Laha, Evaluation of variation of tensile strength across 316LN stainless steel weld joint using automated ball indentation technique, 2015, Materials at High Temperatures., 32 (6), pp. 619-626.

193. Rishi Pamnani, V. Karthik, T. Jayakumar, M. Vasudevan and T. Sakthivel, Evaluation of mechanical properties across micro alloyed HSLA steel weld joints using Automated Ball Indentation, 2016, Material Science and Engineering A, 651, pp. 214-223.

194. K. Laha, K.S. Chandravati, P. Parameswaran and K. Bhanu SankaraRao,Type IV Cracking Susceptibility in Weld Joints of Different Grades of Cr-Mo Ferritic Steel, 2009, Metallurgical and Materials Transactions *A*., 40, pp. 386-397.

195. H.Y. Yu and J.C.M. Li, Computer simulation of impression creep by the finite element method, 1977, Journal of Material Science, 12, pp. 2214–2222.

196. S.N.G. Chu and J.C.M. Li, Impression creep of β-Tin single crystal, 1979, Journal of Material Science & Engineering, 39 , pp. 1–10.

197. D. Chiang and J.C.M. Li, Impression Creep of Lead, 1994, Journal of materials research, 9, pp. 903–908.

198. E.C. Yu and J.C.M. Li, Impression creep of LiF single crystals, 1977, Philosophical Magazine, 36, pp. 811–825.

199. K. Dorner, B. Roller, B. Skrotzki, Stockhert and G. Eggeler, Creep of a TiAl Alloy: A Comparison of Indentation and Tensile Testing, 2003, Material Science & Engineering A , 357A , pp. 346–354

200. L. Peng, F. Yang, J.F. Nie and J.C.M. Li, Impression Creep of a Mg-8Zn-4Al-0.5Ca Alloy, 2005, Material Science & Engineering A, 410–411, pp.42–47.

201. P.S. Gondavarti and K.L. Murty, Creep Anisotropy of Zinc Using Impression Tests, 1987, Journal of Material Science & Letters, 6, pp. 456–458.

202. G. Nayyeri and R. Mahmudi, The microstructure and impression creep behavior of cast, Mg–5Sn–xCa alloys, 2010, Material Science & Engineering A, 527, pp. 2087–2098.

203. M.D. Mathew, K. Laha and V. Ganesan, Improving creep strength of 316L stainless steel by alloying with nitrogen, 2012, Material Science & Engineering A, 535, pp. 76–83.

204. T. Shrestha, M. Basirat, I. Charit et al, Creep deformation mechanisms in modified 9Cr-1Mo steel, 2012, Journal of Nuclear Materials, 423, pp. 110-119.